



HAL
open science

Numerical and experimental studies of magnetic field effects on solidification of metallurgical silicon for photovoltaic applications

Mircea Cablea

► **To cite this version:**

Mircea Cablea. Numerical and experimental studies of magnetic field effects on solidification of metallurgical silicon for photovoltaic applications. Materials. Université Grenoble Alpes, 2015. English. NNT: 2015GREAI017 . tel-01204763

HAL Id: tel-01204763

<https://theses.hal.science/tel-01204763>

Submitted on 24 Sep 2015

HAL is a multi-disciplinary open access archive for the deposit and dissemination of scientific research documents, whether they are published or not. The documents may come from teaching and research institutions in France or abroad, or from public or private research centers.

L'archive ouverte pluridisciplinaire **HAL**, est destinée au dépôt et à la diffusion de documents scientifiques de niveau recherche, publiés ou non, émanant des établissements d'enseignement et de recherche français ou étrangers, des laboratoires publics ou privés.

THÈSE

Pour obtenir le grade de

DOCTEUR DE L'UNIVERSITÉ DE GRENOBLE

Spécialité : **Matériaux, Mécanique, Génie civil, Electrochimie**

Arrêté ministériel : 7 août 2006

Présentée par

« **Mircea CABLEA** »

Thèse dirigée par « **Annie GAGNOUD** » et
codirigée par « **Kader ZAIDAT** »
et « **Yves DELANNOY** »

préparée au sein du **Laboratoire SIMaP**
dans l'**École Doctorale I-MEP2**

Numerical and experimental studies of magnetic field effects on solidification of metallurgical silicon for photovoltaic applications

Thèse soutenue publiquement le « **13 mars 2015** »,
devant le jury composé de :

Mr, Anis, JOUINI

Directeur de Recherche CEA, (Président)

Mme, Nathalie, MANGELINCK

Chargée de Recherche CNRS, (Rapporteur)

Mr, Valéry, BOTTON

Maître de Conférences INSA Lyon, (Rapporteur)

Mr, Alain, JARDY

Directeur de Recherche CNRS, (Membre)

Mr, Mustapha, LEMITI

Professeur INSA Lyon, (Membre)

Mme, Annie, GAGNOUD

Directeur de Recherche CNRS, (Directrice de thèse)

Mr, Kader, ZAIDAT

Maître de Conférences Grenoble INP, (Co-directeur de thèse)

Mr, Yves, DELANNOY

Professeur Grenoble INP, (Co-directeur de thèse)



Abstract

The photovoltaic installed capacity worldwide is expected to increase in the upcoming years. A vast majority of the photovoltaic modules currently produced are based on silicon wafers, with no indications that another material will replace silicon in the near future. The modules efficiency is related to the wafer quality, therefore, to the silicon crystal ingots from which the wafers are made. The wafer quality is given by the amount of crystal defects, which is strongly related to the presence of various impurities in the final ingots. Both mono and multi crystalline silicon ingots are obtained as a result of crystallization (solidification) processes, where important parameters such as the crystal growth rate and thermal gradients are precisely controlled. A solidification process implies growing a crystal from melt by decreasing the temperature. During this process, impurities with a segregation coefficient $K_0 < 1$ are accumulating in the melt, being rejected by the solid-liquid interface. This chemical segregation process is greatly influenced by the fluid flow patterns present in the melt. The control of the fluid flow during the solidification can be achieved by using external magnetic fields. This approach will provide an elegant way to control the impurities segregation process, while growing silicon crystal ingots.

In this study, an experimental set-up (Bridgman type solidification furnace) was used and forced convection was induced by a travelling magnetic field (TMF) during the solidification process. As a result of the induced forced convection, the impurities rejected from the solid-liquid interface in the melt are redistributed. By decreasing the impurities concentration in the liquid near the interface (solute boundary layer), the chances for the impurities to be incorporated in the solid decrease as well. As a result, the impurities are relocated towards one end of the silicon ingot. Impurities distribution in the obtained silicon ingots is analysed in this study. Another impact of the forced convection in the liquid is the curvature of the solidification interface. The solid-liquid interface shape has an influence on the grain structure in the multi-crystalline silicon ingots. Most of the grain boundaries found in such ingots are associated to crystal defects with a negative impact on the solar cell efficiency. The influence of the applied travelling magnetic field on the solidification interface shape was analysed as well, by marking the interface during the solidification process.

In parallel to the experimental study, a numerical model was developed, using the commercial software ANSYS FLUENT. The model provides detailed temperature maps of the furnace as well as important information regarding the solidification process, flow patterns and liquid velocities. The information provided by the model is complementary to the experimental data and can be used to improve the experimental process. A new solidification module for ANSYS FLUENT, able to simulate the segregation process during the solidification, was developed in SIMaP/EPM laboratory and was also integrated in the model. The new module, which uses dynamic mesh technique provided by FLUENT, allows a complete separation of the solid domain from the liquid one, as well as imposing boundary conditions on the solidification interface.

Résumé

Dans les prochaines années, une augmentation significative des installations photovoltaïques est prévue. La plupart des modules photovoltaïques produits sont à base de silicium et aucun autre matériau ne pourra remplacer efficacement le silicium dans un avenir proche. L'efficacité électrique des modules photovoltaïques est reliée en grand partie à la qualité des plaquettes de silicium (ou wafers) utilisées, c'est-à-dire à la qualité du lingot dont elles sont issues. La qualité des lingots du silicium dépend fortement du taux de défauts cristallins et de la quantité d'impuretés présentes dans le lingot. Les lingots de silicium (monocristallins et multi-cristallins) sont élaborés à l'aide de procédé de croissance cristalline où les principaux paramètres tels que la vitesse de croissance et le gradient de température sont contrôlés avec précision. La solidification est un procédé de croissance à partir d'un bain fondu que l'on refroidit de manière contrôlée. Durant ce processus, les impuretés ayant un coefficient de ségrégation $K_0 < 1$ sont extraites du silicium grâce au phénomène de ségrégation chimique. L'écoulement dans le bain liquide influe fortement sur la ségrégation. L'utilisation d'un champ magnétique permet de contrôler l'écoulement dans la zone liquide durant la solidification des lingots de silicium.

Pour l'étude expérimentale, nous utilisons un four Bridgman équipé d'un brasseur électromagnétique qui permet de générer une convection forcée par champ glissant. Les impuretés rejetées à l'interface solide-liquide (rejet de soluté) sont redistribuées dans le liquide en présence de convection forcée. La décroissance du taux d'impuretés dans le liquide à proximité de l'interface, c'est-à-dire dans la couche limite, tend à diminuer la quantité d'impuretés incorporées dans le solide. Ainsi, les impuretés sont localisées dans la fin du lingot de silicium. La convection forcée a aussi un effet sur la courbure de l'interface solide-liquide. La forme de l'interface a une influence sur la structure de grains du lingot multi-cristallin. La plupart des joints de grains sont considérés comme des défauts cristallins réduisant l'efficacité des cellules solaires. L'interface de solidification a été marquée pendant les expériences pour analyser l'influence du champ magnétique glissant sur sa forme.

En parallèle avec l'étude expérimentale, le logiciel commercial ANSYS FLUENT a été utilisé pour développer un modèle numérique des phénomènes mis en jeu dans le procédé de solidification sous champ. Il permet, notamment, d'obtenir le champ de température dans le four et les vitesses dans

le liquide. Les informations obtenues par le modèle viennent compléter les résultats expérimentaux et peuvent être exploitées pour améliorer le processus expérimental. Pour simuler le procédé de ségrégation, nous avons conçu et développé dans ANSYS FLUENT un nouveau module de solidification. Ce nouveau module utilise la fonction de maillage dynamique de FLUENT. Cette approche permet de travailler avec deux domaines distincts (un pour le liquide et un pour le solide) et aussi de gérer les conditions aux limites à l'interface de solidification. Ensuite nous avons intégré ce module dans le modèle du procédé.

to my wife, Georgia
for her constant support

Acknowledgements

I would like to express my deep gratitude to my PhD advisers M. Kader Zaidat, Mme. Annie Gagnoud and M. Yves Delannoy for supporting me during these past three years. Thank you for your advice, trust and for the freedom you granted me. I remember with pleasure the early morning hours in the experimental room with Kader, the long afternoons in front of the computer with Yves and the balance between the two approaches provided by Annie. Thank you all for being there for me and for providing the valuable scientific support.

I would like to thank to M. Anis Jouini, Mme. Nathalie Mangelinck, M. Valéry Botton, M. Alain Jardy, M. Mustapha Lemiti, Mme. Annie Gagnoud, M. Kader Zaidat and M. Yves Delannoy for accepting to be part of the jury.

I would also like to thank M. Thierry Duffar for the highly valuable scientific advices during the years. You were the first to show me the beauty of material science and for that I shall remain forever grateful. I also want to say thank you to M. Yves Fautrelle for your advices. Your trust and support is highly appreciated.

A big thank you to M. Guy Chichignoud for teaching me how to safely operate in the chemistry room. Thank you M. Guy Chichignoud, M. Kader Zaidat and M. Thierry Duffar for helping me with the work I had to do in the chemistry room. I would equally want to thank M. Abdallah Nouri for the help provided in the analysis of the experimental results.

During these last years I had the pleasure to closely work with the technical team, from which I had the chance to learn so much. I would like to thank all of you, especially M. Christian Garnier, M. Ghatfan Hasan and M. Gabriel Fournier for your support and patience.

I would also like to express my appreciation for my colleagues from the SIMaP/EPM group, for their professionalism, friendship and for their efforts to help me improve my French. I would also like to mention the support provided to me by my friends outside the laboratory, with which I have shared

many happy moments during these past three years.

Last but not least, I want to thank my family for their help, support and unconditioned love. Especially my wife, Georgia Cablea, to whom I owe a great deal for encouraging me to choose this path and helping me to stay on it. Thank you.

Contents

Introduction	1
1 State of the art	3
1.1 Context	3
1.1.1 Photovoltaic industry	3
1.1.2 Photovoltaic solar cells	5
1.1.3 Purification of silicon feedstock	7
1.2 Directional solidification of silicon	9
1.2.1 Aspects of the directional solidification	9
1.2.2 Bridgman-Stockbarger technique	13
1.3 Melt stirring during the solidification	14
1.3.1 Influence on the shape of the solidification interface . . .	15
1.3.2 Effect on the segregation of impurities	16
1.4 Positioning of the thesis	17
2 Experimental set-up	19
2.1 General description	19
2.1.1 VB2 furnace	19
2.1.2 Bitter electromagnet	24
2.2 Performed experiments	26
3 Numerical model	31
3.1 Objectives	31
3.2 Description of the physical phenomena	32
3.2.1 Mass conservation and momentum equation	33
3.2.2 Heat transfer model	35
3.2.3 ANSYS FLUENT solidification and melting module . . .	37
3.3 SIMaP/EPM solidification module	39
3.3.1 Module description	39
3.3.2 Module validation	43

3.4	Boundary conditions, model geometry and mesh description . . .	50
3.5	Thermal model validation	53
4	Interface shape and crystal macro structure	59
4.1	Objectives and approach	59
4.2	Experimental and numerical results	62
4.2.1	Solidification interface shape during the solidification process	62
4.2.2	Interface marking by Peltier effect	68
4.2.3	Interface marking by TMF effect	72
4.3	Flow patterns and liquid velocity analysed in GaInSn	81
4.4	Conclusions	85
5	Segregation under travelling magnetic field (TMF)	87
5.1	Theoretical aspects of the segregation process	87
5.2	Experimental and numerical results	91
5.2.1	Overview of the analysis methodology	91
5.2.2	Results on experiments set I	93
5.2.3	Results on experiments set II	100
5.2.4	Results on experiments set III	109
5.3	Conclusions	117
	General conclusions and perspectives	119
	Bibliography	128
A	Multilayer thermal insulation	129
B	Silicon properties	131
C	Phase diagrams	133
D	Interface stability criterion	135
E	Simulation results for iron and phosphorus	139
F	Résumé	145

List of Figures

1.1	Evolution of global PV cumulative installed capacity 2000-2013	4
1.2	Global PV cumulative scenario until 2018	4
1.3	Levelised cost of PV electricity in Europe	5
1.4	Solar cells efficiency chart	5
1.5	Steps in the PV solar cell making process, using multi-crystalline silicon.	6
1.6	Directional solidification and Czochralski proceses	7
1.7	From metalurgical grade silicon to feedstock for PV. Silicon purification routes. DSS: Directional Solidification System . . .	8
1.8	Refining by directional solidification	8
1.9	Example of the temperature distribution in a silicon ingot . . .	10
1.10	Example of flow patterns and liquid velocity	10
1.11	Directional solidification with mono-crystalline seeds	11
1.12	Breakdown of the solidification front	13
1.13	Bridgman-Stockbarger technique, schematics	14
1.14	Snapshots of the velocity stream lines in a silicon melt exposed to TMF	15
1.15	Images with the liquid-solid interface deflection	16
1.16	Comparison of substitutional carbon and SiC particle distributions	17
2.1	Main components of VB2 experimental installation.	20
2.2	Close-up view of VB2 furnace central area	21
2.3	VB2 furnace control and command panel	22
2.4	Water panel installed on the furnace cooling system.	23
2.5	Flow patterns in the melt induced by the travelling magnetic field	24
2.6	Components of the Bitter type electromagnet	25
2.7	Image of the electromagnet used in the VB2 furnace and the magnetic field intensity variation as a function of the induced current	26

2.8	Example of thermocouples positioning and of temperature profiles recorded during one experiment. Imposed cooling rate for a fix position of the crucible.	27
3.1	Description of the elements considered by the SIMaP/EPM solidification module for Fluent	40
3.2	Description of the displacement of one node at the solidification front, for an unsteady case simulation.	42
3.3	Description of a Stefan problem.	44
3.4	Mesh evolution in time.	45
3.5	Solidification front position and thermal fluxes	46
3.6	Temperature distribution at different instants	46
3.7	Aluminium impurities at the solidification interface	48
3.8	Iron impurities at the solidification interface	49
3.9	Phosphorus impurities at the solidification interface	49
3.10	Numerical model geometry (3.10a). Zoom-in on the central area highlighting the main material components and regions of the numerical model (3.10b).	50
3.11	View on the central part of the model geometry	52
3.12	Numerical model mesh in different regions of the furnace and crucible. Total number of mesh cells is ≈ 20000	53
3.13	Measured dissipated powers and simulated ones	55
3.14	Measured temperatures and the simulated ones	55
4.1	Solidification interface shapes and flow patterns during the solidification process for various magnetic field orientations.	60
4.2	Grain structures obtained in experiment set I.	61
4.3	Experiment I.1. Numerical results of liquid velocity distribution	64
4.4	Experiment I.2. Numerical results of liquid velocity distribution	65
4.5	Experiment I.3. Numerical results of liquid velocity distribution	65
4.6	Experiment I.4. Numerical results of liquid velocity distribution	66
4.7	Grain macro-structure and interfaces on vertical slices of the obtained ingots for experiment set I	67
4.8	Principle of interface marking with Peltier effect.	69
4.9	Interface marked using Peltier effect	71
4.10	Grains macro-structure on vertical slices of the obtained ingots for experiment set III	73

4.11	Experiment III.1 macro-structure on vertical slice and interface at a given moment. Comparison between experimental and simulation results	74
4.12	Experiment III.1; Temperature and liquid velocity	75
4.13	Experiment III.2 macro-structure on vertical slice and interface at a given instant. Comparison between experimental and simulation results	76
4.14	Experiment III.2; Temperature and liquid velocity	77
4.15	Experiment III.3 macro-structure on vertical slice and interface at a given instance. Comparison between experimental and simulation results	78
4.16	Experiment III.3; Temperature and liquid velocity	79
4.17	Experiment III.4 macro-structure on vertical slice and interface at a given moment. Comparison between experimental and simulation results	80
4.18	Velocity measurement procedure in GaInSn	82
4.19	Computed liquid velocity of GaInSn, presented on a vertical cross section.	83
4.20	Axial liquid velocities in GaInSn.	84
5.1	Definition of the boundary layer thickness	88
5.2	Segregation process for a pure diffusive case	89
5.3	Segregation process for a perfect mixing case	90
5.4	Segregation process for a convecto-diffusive case	90
5.5	Vertical slice from the center of the ingot and cutting procedure	92
5.6	Aluminium axial segregation along the ingot centre for experiments in set I.	94
5.7	Iron axial segregation along the ingot centre for experiments in set I.	95
5.8	Phosphorus axial segregation along the ingot centre for experiments in set I.	96
5.9	Defects observed on the surface of a sample obtained from experiments in set I	97
5.10	Precipitates observed on the surface of a sample obtained from experiments in set I	98
5.11	EDS spectrum of Al and Si observed on samples from experiments in Experiment I.1 at the level of a dendrite like defect.	99

5.12	EDS spectrum of Al, Si and Fe observed on samples from experiments in Experiment I.1 at the level of a dendrite like defect.	99
5.13	Grain macro-structure on vertical slices for experiments from set II.	101
5.14	Aluminium axial segregation along the ingot centre for experiments in set II.	102
5.15	Iron axial segregation along the ingot centre for experiments in set II.	103
5.16	Phosphorus axial segregation along the ingot centre for experiments in set II.	104
5.17	Numerical results of liquid velocity distribution	105
5.18	The maximum computed liquid velocity at different positions of the solidification interface.	106
5.19	Column like traces observed on the surface of a sample obtained from experiments in set II (optic microscope)	107
5.20	Column like traces observed on the surface of a sample obtained from experiments in set II (SEM)	107
5.21	Precipitates observed on the surface of a sample obtained from experiments in set II	108
5.22	Precipitates observed on the surface of a sample obtained from experiments in set II	108
5.23	Aluminium axial segregation along the ingot centre for experiments in set III.	110
5.24	Iron axial segregation along the ingot centre for experiments in set III.	110
5.25	Phosphorus axial segregation along the ingot centre for experiments in set III.	111
5.26	Comparison of experimental and computed interfaces for experiment III.2	112
5.27	Evolution in time of the aluminium distribution in liquid silicon for Experiment III.1. Colour map values are expressed in mass fraction.	113
5.28	Evolution in time of the aluminium distribution in liquid silicon for Experiment III.2. Colour map values are expressed in mass fraction.	113
5.29	Simulated aluminium distribution in liquid silicon at the interface.	114

5.30	Computed K_{eff} for aluminium along the solidification interface.	115
5.31	Computed maximum values of aluminium at the interface for experiments in set III	116
5.32	Computed minimum values of aluminium axial segregation at the interface for experiments in set III	116
A.1	Multilayer insulation, dimations and perspectives.	130
C.1	Phase diagram for aluminium-silicon	133
C.2	Phase diagram for iron-silicon.	134
D.1	Computed critical velocity.	136
E.1	Evolution in time of the iron distribution in liquid silicon for Experiment III.1.	139
E.2	Evolution in time of the iron distribution in liquid silicon for Experiment III.2.	140
E.3	Iron distribution in liquid silicon at the interface.	140
E.4	Computed K_{eff} for iron along the solidification interface.	140
E.5	Computed maximum values of iron at the interface for experiments in set III	141
E.6	Computed minimum values of iron axial segregation at the interface for experiments in set III	141
E.7	Evolution in time of the phosphorus distribution in liquid silicon for Experiment III.1.	142
E.8	Evolution in time of the phosphorus distribution in liquid silicon for Experiment III.2.	142
E.9	Phosphorus distribution in liquid silicon at the interface.	143
E.10	Computed K_{eff} for phosphorus along the solidification interface.	143
E.11	Computed maximum values of phosphorus at the interface for experiments in set III	144
E.12	Computed minimum values of phosphorus axial segregation at the interface for experiments in set III	144

«Dans la vie, rien n'est à craindre, tout est à comprendre. »

— Marie Curie

Introduction

Global photovoltaic energy market forecasts indicate an increase of the installed capacity in the following years. Silicon remains the main material used in the photovoltaic (PV) solar cells production. Other base materials, such as cadmium telluride, are also used to produce solar cells, but without the perspective of a replacement of silicon as main material for PV module, in the near future. Various crystal growth techniques are used to produce silicon wafers for PV industry, using pure silicon as feedstock. In order to remain competitive on the market, the manufacturers must further decrease the production cost and/or increase the efficiency of the PV modules. Polysilicon wafers obtained from cast multi-crystalline silicon ingots are cheaper than the mono-crystals ones, at the cost of a slight decrease in performance. Recently, significant research efforts were made towards improving the quality of the polysilicon ingots obtained using a directional solidification process. Currently the research focuses on the grain structure, defects in the crystal and pollutant contamination.

A reduction in the PV module production cost can also be achieved by a decrease of feedstock material cost. The silicon feedstock for the photovoltaic industry must be at least of solar grade (SoG) quality. Currently the feedstock is generally obtained using expensive techniques such as chemical vapor deposition (i.e. Siemens process). Cheaper alternative purification methods, to transform metallurgical grade silicon to solar grade feedstock, are also developed. Directional solidification process can be used as a purification method especially for metallic impurities with a small segregation coefficient ($K_0 \ll 1$).

The objective of this study is to understand the segregation process under a travelling magnetic field in a directional solidification technique, as well as controlling the solidification interface shape in the process. By applying external forces, induced by the magnetic field, the fluid flow in the melt can be controlled, thus improving the efficiency of the segregation process (increased

concentration of impurities at the top of the ingot). This technique can be directly applied for the purification of silicon, on what was referred to as the alternative path purification method in the previous paragraph, aiming to further decrease the process cost by improving its efficiency. Another benefit of a more efficient segregation process, when used in the final crystallization, is that it allows the use of lower quality feedstock without compromising the quality of crystal ingots from which the wafers are made. However, the liquid stirring, beneficial for the segregation process, has an influence on the solidification interface shape as well, which produces changes to the crystal grain structure. The influence of the magnetic field on the interface curvature is also analysed in this work.

In the first chapter, the context of this study is detailed and a general review of the literature related to this work is presented. The second chapter will present details regarding the experimental installation used, as well as an overview of the performed experiments. In the third chapter, the numerical model developed for this research subject is presented. Commercial software ANSYS FLUENT was used to develop the model and a new proprietary solidification module for FLUENT was developed, especially for the segregation process modelling. The fourth chapter presents experimental results for experiments conducted in different conditions. The focus of this chapter is towards the solid-liquid interface shape. Results from the numerical model are presented along with the experimental ones in order to provide a more complete description of the involved phenomena. The solidification interface was marked during the solidification process, using two different techniques (Peltier technique and using the magnetic field), in different experimental conditions. The aim of these procedures is to provide relevant information on the influence of the magnetic field on the interface shape. The fifth chapter is dedicated to the segregation process. Some of the experiments already presented in chapter four are now analysed from this perspective, but new experiments are also introduced. In the last part of this chapter, numerical results regarding the impurities segregation obtained with the new solidification model are presented.

Chapter 1

State of the art

1.1 Context

1.1.1 Photovoltaic industry

New photovoltaic systems are installed every year world wide, reaching a cumulative installed capacity of $\approx 140GW$ in 2013 [1]. Figure 1.1 shows the evolution of the photovoltaic (PV) cumulative installed capacity in the world between the years 2000 and 2013. In 2013, Europe was leading with $\approx 80,000MW$ of installed capacity but in the later years a significant increase was observed in China, America and Asia Pacific. The European Photovoltaic Industry Association (EPIA) also estimates the installed capacity for the next few years, based on more or less favorable scenarios (Figure1.2). According to the EPIA most optimistic projection released in 2014, $400GW$ of global cumulative installed capacity can be reached by 2018.

The Levelised Cost of Energy (LCOE) for PV electricity has reached grid parity in some European countries in the last years. LCOE, represented in *Euro/KWh* (or $\$/KWh$), is an economical indicator of the cost of the energy generating system including all cost over its lifetime. The initial investment, operation cost and maintenance, cost of fuel and cost of capital are taken into account when computing LCOE. Joint Research Centre (JRC) of the European Commission presented a distribution map of PV LCOE across the European countries (Figure 1.3) [2]. In countries like Germany, Italy or Spain, the PV electricity price is already below the price of retail electricity.

Currently, the installed PV capacity is largely stimulated by Feed-in Tariff (FiT) schemes, a policy mechanism designed to accelerate investment on renewable energy technologies by offering a higher price per KWh, obtained

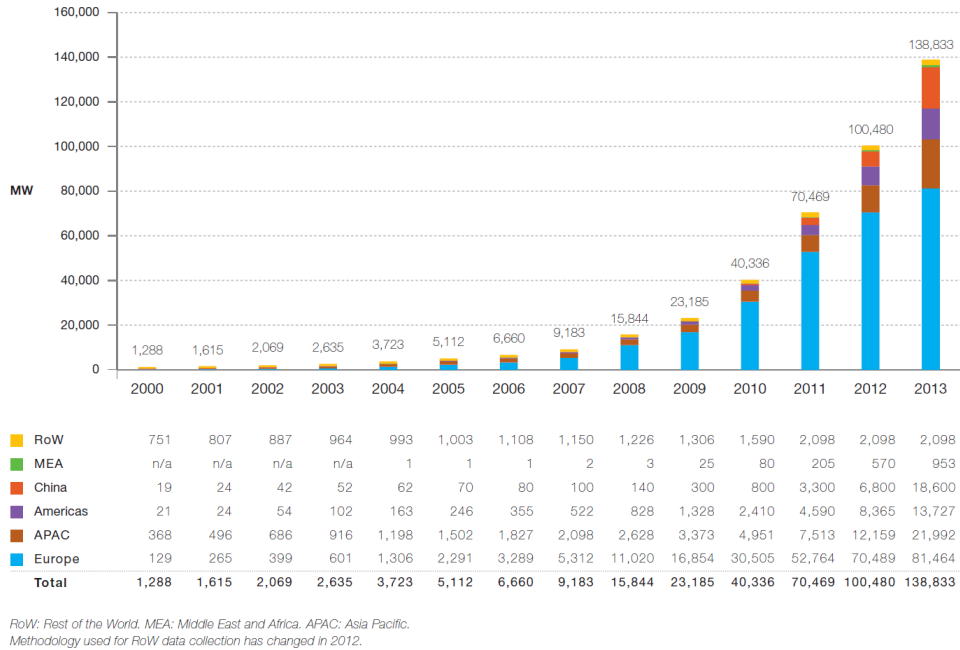


Figure 1.1: Evolution of global PV cumulative installed capacity 2000-2013. (Source: EPIA 2014) [1].

from renewable energy sources. More details about the support mechanisms for promoting PV systems in EU countries is presented in [3]. In order to be self sustainable and to compete with the conventional energy sources, the LCOE for PV energy must decrease further. To achieve that, the solar cells efficiency must be further increased and the production cost must be decreased. One way to reduce the cell production cost is to further decrease the cost of silicon, which remains the main material used in the PV cell production.

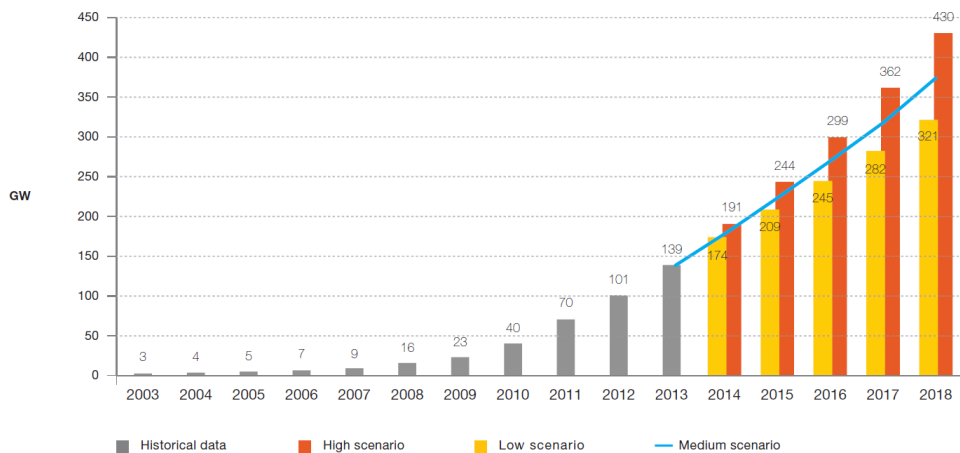


Figure 1.2: Global PV cumulative scenario until 2018. (Source: EPIA 2014) [1].

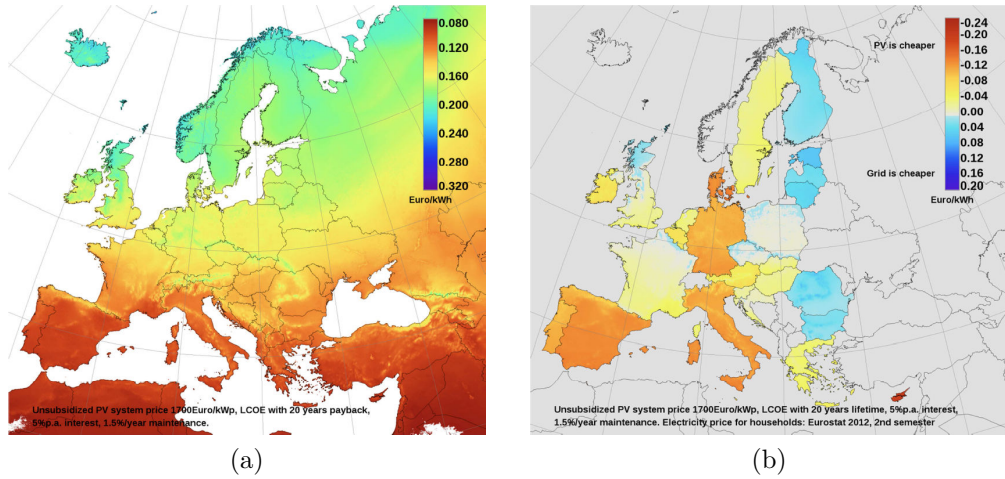


Figure 1.3: Distribution of the levelised cost of PV electricity in Europe (1.3a) and price difference between PV levelised electricity cost and household retail prices (1.3b). [2].

1.1.2 Photovoltaic solar cells

The Photovoltaic (PV) solar cell performance has continuously increased over the last years. Figure 1.4 depicts the efficiency recorded for different types of PV solar cells in laboratory conditions. While for single-crystalline silicon based cells the efficiency reaches $\approx 25\%$, for multi-crystal cells the maximum recorded efficiency is $\approx 20\%$. In normal operating conditions, both cell types are operating at lower efficiencies, depending on various environmental factors.

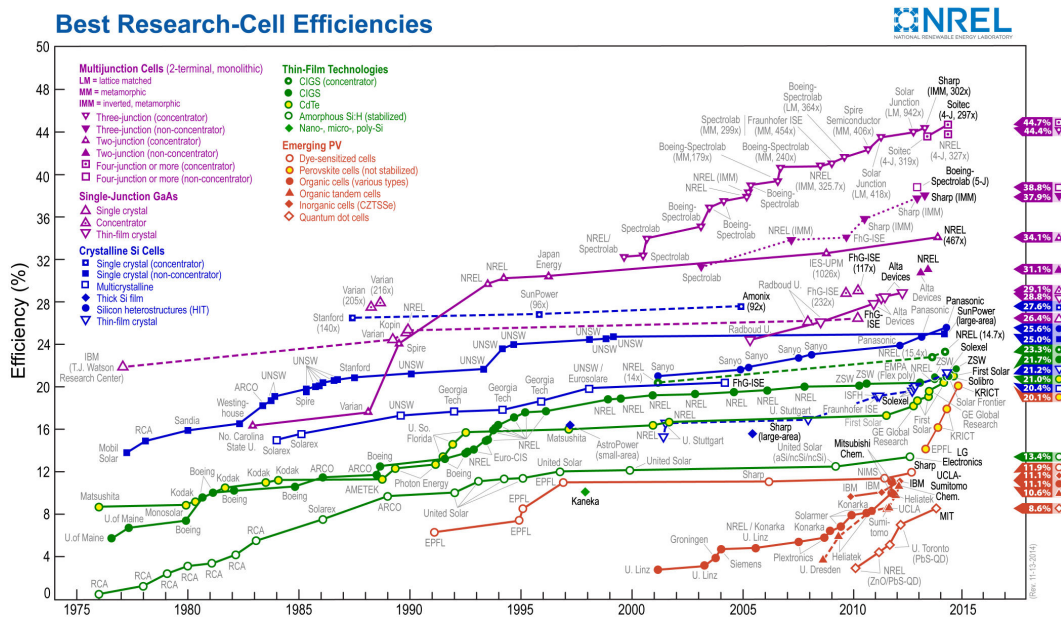



Figure 1.4: Solar cells efficiency chart. (Source: NREL) [4].

Silicon ingots are obtained as a result of a crystallization process where high quality multi-crystalline silicon (mc-Si) feedstock is used. The silicon ingots are then cut in wafers, from which the solar cells are made. The steps in the making process of PV modules, made from mc-Si wafers, are depicted in Figure 1.5. Ingots of different shapes and sizes are created using various types of controlled crystallization processes. The most common crystallization process used to obtain multi-crystalline silicon ingots is the directional solidification process (see Figure 1.6a). Mono-crystalline ingots can be obtained using various methods, Czochralski method (see Figure 1.6b) being the most common one. Another technique widely used to obtain mono-crystalline silicon ingots is the floating zone (FZ) process. Since a significant part of the material is lost due to cutting and slicing in order to obtain silicon wafers, other growth techniques, like ribbon growth, have been developed, in order to reduce the amount of wasted material. The goal of the solidification process at this stage is to obtain ingots with a minimum number of defects. These final ingots, once they reached the required quality, are cut and sliced into wafers. These wafers are used to produce the solar cells which are assembled into PV panels.


Silicon feedstock



Controlled solidification


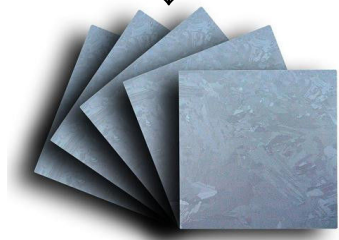
Silicon ingot



Cutting
and
sawing




Assembling

Silicon solar panel

Silicon wafers

Figure 1.5: Steps in the PV solar cell making process, using multi-crystalline silicon.

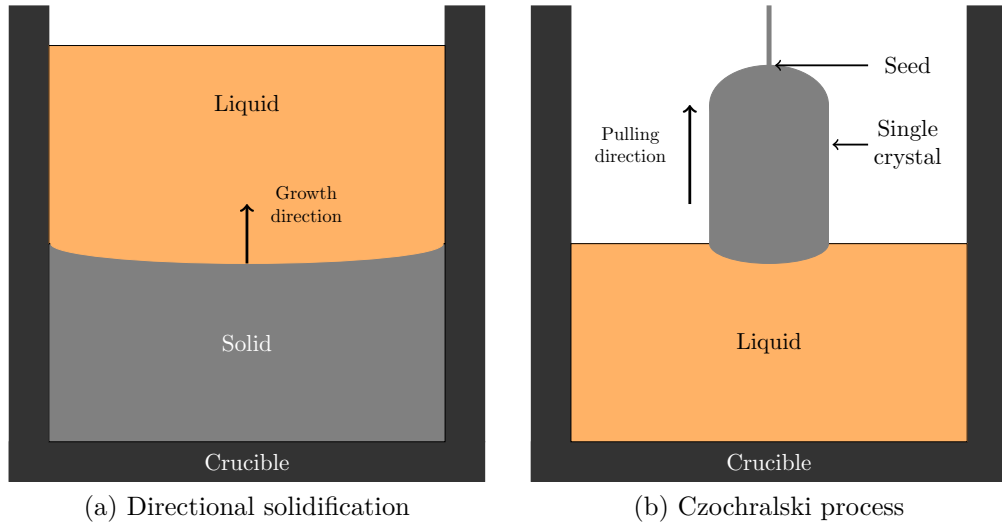


Figure 1.6: Two processes used to obtain silicon crystals. Directional solidification process (1.6a) is mainly used for multi-crystalline silicon ingots. Czochralski process (1.6b) is the most known crystal growth method for mono-crystals.

1.1.3 Purification of silicon feedstock

The silicon ingots, from which the wafers are made, need to have a purity below one part per million (ppm), in order to ensure a high efficiency of the final cells [5]. This generally implies a high purity of the silicon feedstock. Starting from a metallurgical grade silicon (MG-Si) with a 98.5% purity, different purification approaches are possible in order to increase the purity level such that the resulting solar grade silicon (SoG-Si) or electronic grade silicon (EG-Si) can be used as feedstock for the PV industry. There are different approaches considered for this purification step, and a comprehensive review of the main techniques used in silicon purification for feedstock is presented in [6, 7]. Figure 1.7 depicts the two main purification routes that are currently most used for silicon.

The most widely used technique to obtain high quality multi-crystalline silicon is the well known Siemens process, which implies a silicon deposition on pure silicon seed rods, from gaseous trichlorosilane, by chemical decomposition in a reaction chamber. Using this technique, multi-crystalline silicon (mc-Si) with a purity up to 9N or one part per billion (ppb) can be produced. A more recently developed process called fluidized bed reactor (FBR) can be used to produce high quality polysilicon using silane (SiH_4). These two processes are based on chemical purification of the metallurgical grade silicon, and belong to the chemical route depicted in Figure 1.7.

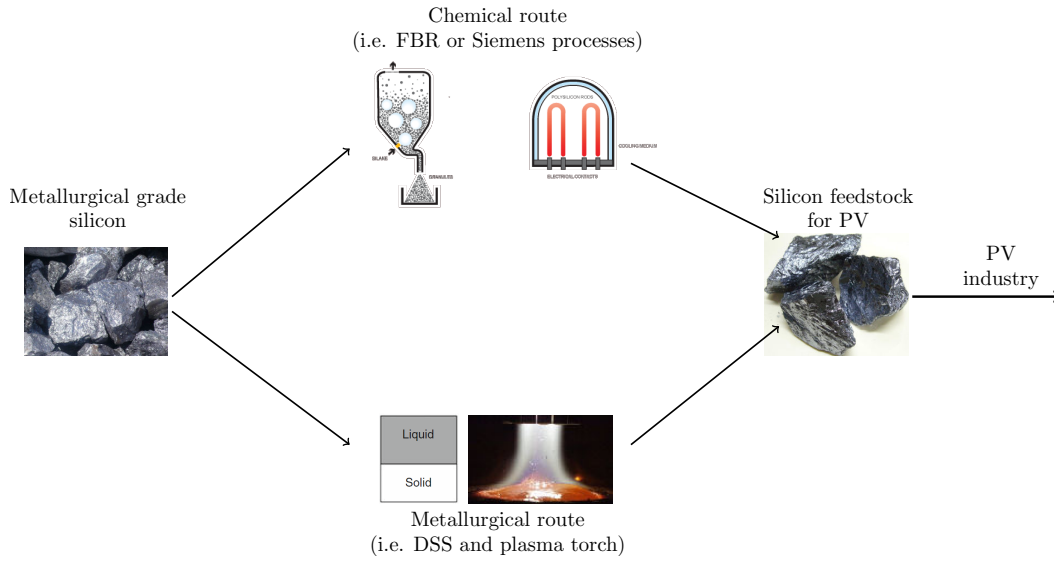


Figure 1.7: From metallurgical grade silicon to feedstock for PV. Silicon purification routes. DSS: Directional Solidification System

Another way to purify MG-Si is by employing metallurgical techniques. By directional solidification process, the heavy impurities (metals) are generally not incorporated in the solid, due to their small segregation coefficients ($K_0 \ll 1$, see Figure 1.8). The silicon obtained so far by this route is usually referred to as upgraded metallurgical grade silicon (UMG-Si) with impurities levels not low enough for PV industry. For impurities such as Boron, other purification processes like plasma torch [8] or slag refining [6] have been developed. The segregation coefficient K_0 for boron is also smaller than 1. However, it is higher than K_0 of metals. Solar grade silicon quality, with purity level below $1ppm$, can also be obtained by this metallurgical route. To reach purity level below $1ppm$, the directional solidification process must be repeated several times, which, as consequence, increases the production cost.

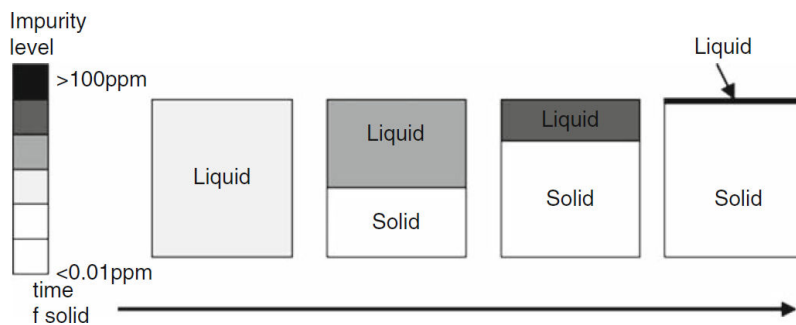


Figure 1.8: Refining by directional solidification for $K_0 \ll 1$. The dark color indicates level of impurity (white is $< 0.01ppm$ and black is $> 100ppm$) [6]

1.2 Directional solidification of silicon

Different techniques are used to obtain silicon crystals for PV applications. Directional solidification of silicon (Figure 1.6a) is the most widely used technique to obtain multi-crystalline silicon ingots. Czochralski method (Figure 1.6b) is the most commonly used one for mono-crystals production. Using this method, high quality crystals are produced, generally presenting a reduced amount of defects in the crystals. However, the disadvantages of the Czochralski method are the high price of the resulted ingots, the slow growth rates and the ingots cylindrical shape, which leads to important quantities of material losses (up to 50%), when square wafers are desired.

1.2.1 Aspects of the directional solidification

Temperature control

A directional solidification process is generally used to cast multi-crystalline silicon ingots. Silicon is molten in a crucible, generally made of quartz (SiO_2) and coated with boron nitride (Si_3N_4). A vertical thermal gradient is imposed in the melt, such that the liquid bottom is colder than the top. If the temperature at the crucible bottom is decreased below the melting temperature of silicon, the solidification process begins. Controlling the thermal gradients in the melt and the cooling rate is the key to control the solidification process. A first solidification layer must form at the crucible bottom and the crystal will grow towards the crucible top.

In directional solidification systems (DSS) the thermal gradients in the silicon are usually imposed by heating elements situated outside the crucible. Two heating/cooling systems enable to control separately the top and the bottom of the ingot. This configuration imposes a vertical thermal gradient in the silicon. A side thermal insulation is generally placed around the crucible, with the purpose of limiting the radial thermal gradient inside the crucible. In some furnace configurations, a separate heater is placed outside the crucible. An example of the temperature distribution computed inside an ingot is depicted in Figure 1.9 [9]. Due to the high temperatures in the ingot ($> 1600K$), experimental measurements of the temperatures are usually made using thermocouples or pyrometers. However, precise experimental measurements inside the melt are not easily available. Detailed temperature profile inside the ingots can be simulated using numerical models to compensate for the lack of precise experimental data.

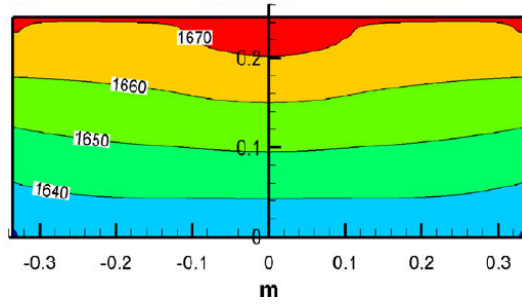


Figure 1.9: Example of temperature distribution (K) in a silicon ingot, for a classical directional solidification system.[9]

Natural convection

The radial thermal gradient in the melt and the liquid density variation with the temperature, leads to natural convection in the liquid silicon. Figure 1.10 [10] depicts computed flow patterns in the liquid silicon, during directional solidification process. Velocities up to $2 \cdot 10^{-3} m/s$ can be achieved due to the natural convection. The effects of convection on the ingots quality will be further discussed.

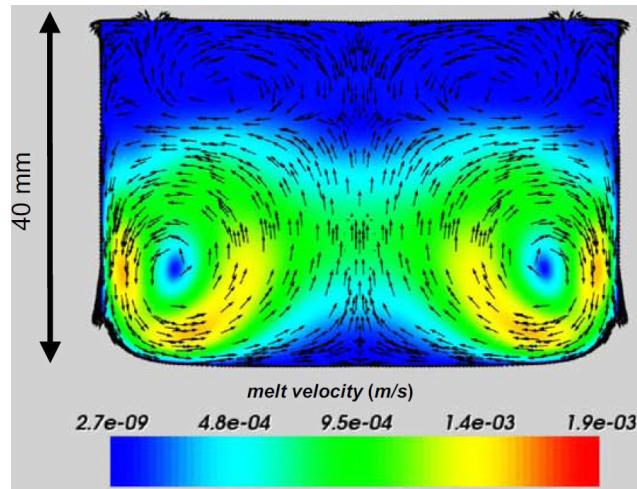


Figure 1.10: Example of flow patterns and liquid velocity computed in silicon melt.[10]

Grain structure and defects

Using a directional solidification method, multi-crystalline ingots are obtained. Single crystal grains, with different sizes and crystallographic orientations, are stacked together to form the mc-Si ingot. The grains boundaries are considered as crystal defects, most of them having a negative impact on the PV cells efficiency [11]. Other defects like dislocations clusters are present

inside the silicon grains. This type of defects are also present in single crystals and they also affect the solar cells efficiency by decreasing the minority carrier lifetime.

Attempts to grow mono crystals using directional solidification have been made. If one or multiple mono crystal seeds are placed at the crucible bottom (see Figure 1.11), and the temperature field in the silicon is well controlled, the silicon that will be solidified inside the crucible should take the crystallographic orientation of the seeds, forming a single crystal [12, 13]. However, new grains are created at the crucible wall, due to nucleation. These grains will advance towards the center of the ingot, corrupting the mono-crystalline structure (see Figure 1.11b). Due to the nucleation on the crucible walls, defects reducing the crystal quality are penetrating deep inside the ingot. The silicon grains nucleation on substrates has being investigated [14, 15], as well as different techniques that can be used to prevent these defects to advance into the ingot.

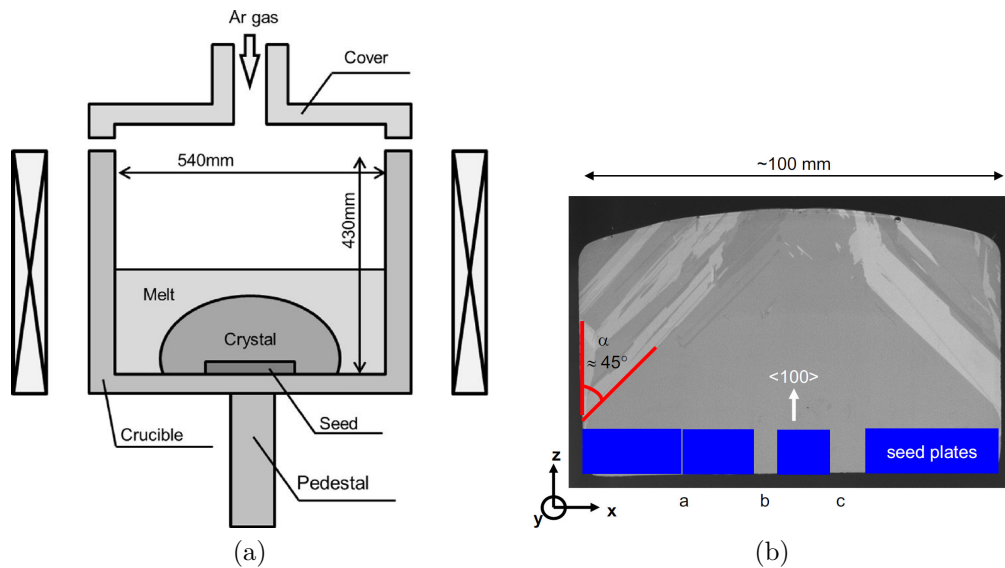


Figure 1.11: Schematic of a furnace where only one mono-crystalline seed was used (1.11a). [12]. Scan image of a vertical cut of an experiment with split seeds (1.11b).[13]

Impurity contamination

Due to the high melting temperature of silicon ($1687K$), the furnaces used for silicon crystal growth have to be able to cope with such temperatures. Therefore, most of the components in these furnaces (heaters, thermal insulation, etc...) are made from carbon based materials. This leads to a carbon rich environment, in which the crystal growth process is conducted. The presence

of carbon in the silicon ingot is known to lead to a series of defects in the crystallographic structure, reducing the crystal quality. If quartz crucibles are used, oxygen (O) from the crucible is likely to be also found in the silicon. The crucible coating is another source of impurities like nitrogen (N), that can be transferred in to the silicon [16]. None of these impurities are desired in the final ingot. The presence of carbon, oxygen and nitrogen pollutants in the silicon ingots is the most investigated type of contamination, due to their origin. Even if a solar grade quality silicon is used, these pollutants are likely to cause damage to the crystallographic structure and to decrease the crystal quality.

Moreover, if silicon feedstock coming from the metallurgical route is used, other impurities like iron, aluminium or phosphorus are already present in the initial silicon bulk. All these pollutants are generally segregating during DSS, so that they will be transported towards the top of the ingot, part that will be removed in the end (see Figure 1.8). However, for high levels of impurities a breakdown of the solidification front is possible [6] (see Figure 1.12) where the grain structure changes and the impurity segregation process is disturbed. A high level of contamination in the melt can cause the formation of different precipitates, which can create new grains, by nucleation, in the undercooled liquid in front of the solidification interface. If the nucleation site density became significant, for the given crystal growth parameters, the grains structure can change from columnar to equiaxed [17, 18]. Other parameters of the crystal growth process, such as the growth velocity, also influence the precipitates formation in the melt [10]. Aspects regarding impurity segregation in a directional solidification process are detailed in Section 1.3.



Figure 1.12: Picture that shows breakdown of the solidification front in MC Si [6].

1.2.2 Bridgman-Stockbarger technique

The Bridgman technique implies passing an ampule which contains the material to be solidified, from a hot zone where the temperature is above the melting temperature of the material to a colder zone below the melting temperature. In a classical Bridgman furnace only the temperature of the hot zone is controlled. The difference between Bridgman technique and Bridgman-Stockbarger technique is that in the second one, the colder zone temperature is also controlled. Figure 1.13 depicts the schematic principle of the Bridgman-Stockbarger technique. The solidification interface is always positioned between the two zones and the crystal growth rate is related to the pulling velocity of the crucible or ampule. For the experimental work presented in this study, a solidification furnace using Bridgman-Stockbarger technique was used. The description of the furnace and other related details are presented in Chapter 2.

A solidification furnace using Bridgman-Stockbarger technique can be used to perform directional solidification experiments. In such experiments, due to the temperature control of the hot and cold zone, different values for the vertical thermal gradient can be tested. In combination with a whole range of pulling velocities available, this system can easily become a tool for studying the solidification mechanisms.

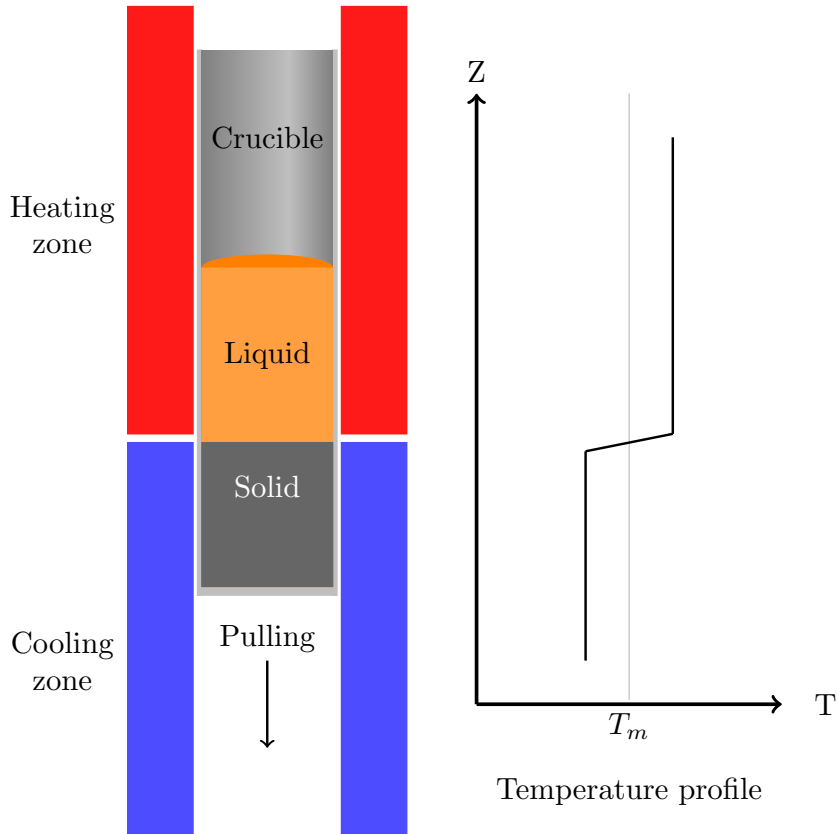


Figure 1.13: Bridgman-Stockbarger technique schematics on the left side and temperature profile along Z axis on the right side.

1.3 Melt stirring during the solidification

Natural convection appears in the melt due to a non uniform temperature distribution in the liquid. Due to natural convection, vortices are created in the silicon bulk. The generated flow patterns have an influence over the solidification interface shape [19] and also contribute to eventual pollutants redistribution in the bulk. It has been shown that an increased liquid velocity is beneficial for the segregation process [20, 16, 21]. However, for high concentrations of impurities in the melt, more than 1% in the case of MG-Si, the small liquid velocity generated by the natural convection is not sufficient to significantly influence the segregation process. Therefore, different attempts to increase the liquid velocity in the melt during the solidification have been made using different techniques. Mechanical stirring of the melt [22] is one of these methods, while other studies were concentrated around the magnetic field usage to induce forced convection in the liquid [23].

Melt stirring using magnetic field is possible in silicon due to the physical properties of the material. The electric conductivity of the silicon melt allows

a magnetic field to induce electrical currents, therefore, Lorentz forces in the melt, proportional to the magnetic field intensity. These forces generate a forced convection in the liquid, changing the flow patterns in the melt [24]. Different inductor geometries, generating different types of magnetic fields such as travelling (TMF), rotating (RMF) or alternating (AMF) magnetic fields have been analysed [23, 25]. Others types of magnetic fields, like carousel magnetic fields (CMF), have also being tested [25, 26]. All these different types of magnetic fields are ultimately creating different flow patterns in the liquid and with that, they produce different effects on the solid-liquid interface shape [27] and different pollutants redistribution in the melt.

Figure 1.14 depicts an example of computed velocity stream lines in a silicon melt for different magnetic field used [25].

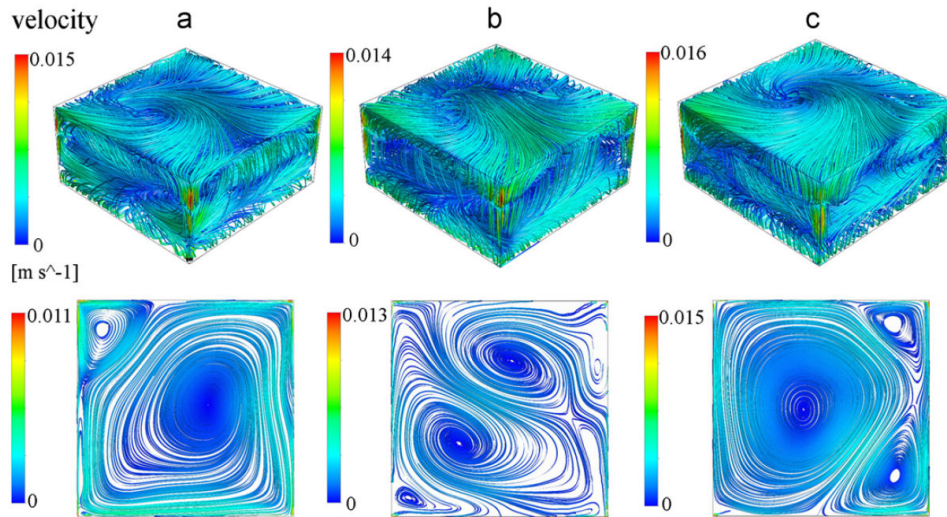


Figure 1.14: Snapshots of the velocity stream lines in a silicon melt exposed to:(a)TMF upward; (b)AMF lateral and(c)TMF downward: iso view and projection on mid-horizontal plane. [25].

1.3.1 Influence on the shape of the solidification interface

The forced convection in the melt, induced by various stirring methods, changes the temperature distribution in the liquid which results in a change of the solidification interface shape during the solidification process [28, 29]. Using a travelling magnetic field (TMF) to stir the melt can result in a concave or convex interface shape depending on the magnetic field orientation (see Figure 1.15) [30, 31]. The solidification front deflection has a significant influ-

ence on the ingot grains macro-structure. The grain boundaries are generally perpendicular to the solidification interface.

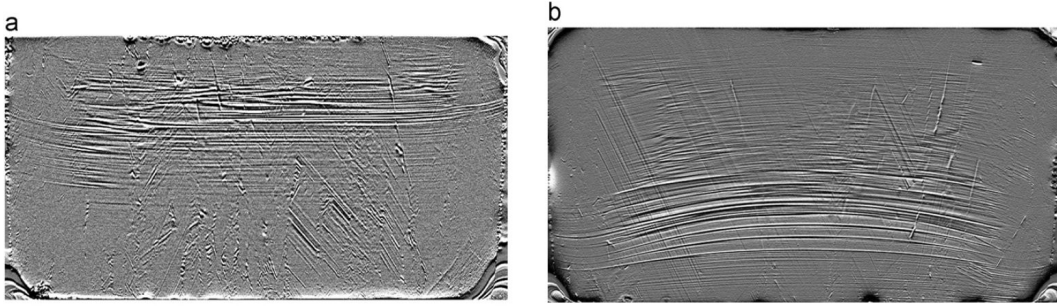


Figure 1.15: Example of images with the liquid-solid growth interface revealed from striation morphology analysis by Lateral Photo-voltage Scanning (LPS) on vertical cuts:(a) for upward directed TMF and (b) for downward directed TMF [30].

1.3.2 Effect on the segregation of impurities

Besides imposing the interface shape, the forced convection also mixes any pollutant present in the melt. The radial distribution of impurities along the interface is also influenced by the flow patterns directions and intensity. If these flow patterns are controlled by the magnetic field, the radial distribution of pollutants in the final ingot can be controlled as well.

Another important aspect of the effects induced by stirring is the impurity segregation along the ingot's height. The theoretical aspects of the pollutants segregation phenomena have been intensely studied for diffusive scenarios [32], as well as for convective ones [33, 34]. More details regarding the influence of the melt flow on the solute boundary layer are presented in Chapter 5 Section 5.1.

The axial distribution of impurities in the ingot is affected by the segregation coefficient (K_0) for different types of pollutants. For instance the carbon has a $K_0 < 1$ which results in an increasing concentration with the solid fraction. Figure 1.16 [6] depicts the carbon concentration and SiC particles along the ingot height for two different cooling rates. A solute boundary layer is formed in the melt, due to solute rejection at the interface. If the solubility limit ($\approx 10^{18} atoms/cm^3$ [35]) is reached, SiC particles are formed. SiC particles damage the crystal structure if they are to be incorporated in the solid [18]. The convection influences the solute boundary layer therefore the pollutant distribution in the ingot. Controlling the boundary layer using forced convection, leads to a control of solute axial segregation in the ingot.

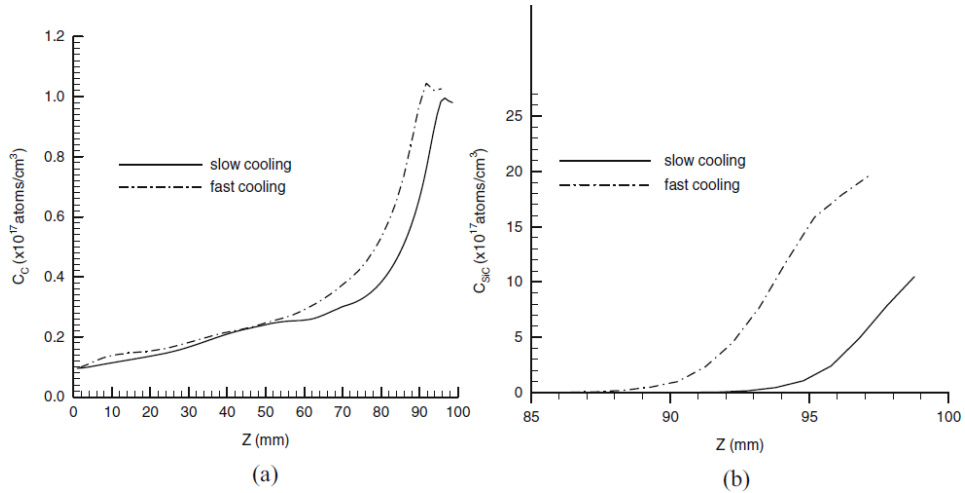


Figure 1.16: Comparison of substitutional carbon and SiC particle distributions along the center axis of ingot between two solidification processes with different cooling rates. (a) substitutional carbon; (b) SiC particles [6].

1.4 Positioning of the thesis

The work presented in this thesis is focused on studying the effect of using a travelling magnetic field (TMF) during the casting process of multi-crystalline silicon ingots. The purification process of silicon, on the metallurgical route, can also be improved by introducing new techniques such as segregation with electromagnetic stirring. The melt stirring has beneficial effects on the impurity segregation process and crystal macro-structure as well. In the following chapters experimental results obtained in a solidification furnace, using Bridgman-Stockbarger technique, will be presented. The effect of TMF over the solidification interface shape (see Chapter 4) and impurities segregation mechanisms (see Chapter 5) in the silicon ingots is analysed. A numerical model has been developed as well (see Chapter 3), in order to provide more details regarding phenomena such as fluid flow patterns, temperature fields and segregation.

These thesis objectives are to improve the segregation efficiency and the control of the solidification interface shape using a travelling magnetic field in a directional solidification process. Currently, the directional solidification process involved in the silicon purification, on the metallurgical route (see Figure 1.7), must be repeated several times to achieve solar grade quality. An improvement of the pollutant segregation efficiency by using a magnetic field can significantly reduce the number of required solidifications at this step. On the other hand, if this technique is applied in the casting of ingots from which

wafers are made (see Figure 1.5) less pure and cheaper silicon can be used as feedstock material. Controlling the solidification interface shape during the solidification is also a key point in controlling the grain macro-structure and defect distribution in the final ingots.

Chapter 2

Experimental set-up

2.1 General description

2.1.1 VB2 furnace

The SIMaP/EPM laboratory is equipped with a solidification furnace called Vertical Bridgman 2 Inches (VB2). It is a vertical cylindrical furnace where a directional solidification process can be conducted in order to create cylindrical ingots of 2 inches in diameter. The VB2 furnace was designed by the CYBERSTAR company in the early 1990s. At that time, the furnace was designed for growing crystals of GaAs. Due to the cylindrical shape of the furnace, a vertical symmetry axis can be considered. In the original design, the heating system of the installation was composed of two resistors (one upper resistor for the higher temperature and a bottom one for the lower temperature) and an "adiabatic" zone in the middle part.

In order to use the furnace for photovoltaic silicon growth, some modifications were made. In 2011, at the beginning of the study presented in this document, the furnace had the following configuration (Figure 2.1):

- Two resistive heaters made of graphite.
- A thermal insulation layer made of graphite foam.
- C type thermocouples were used in order to allow the recording of the high temperatures inside the furnace.
- A Bitter type electromagnet was already installed, allowing the control of the liquid flow inside the melt by creating a travelling magnetic field (TMF).

Since 2011, the furnace was further improved:

- The thermal insulation layer made of graphite foam, was kept only in

the upper and bottom part of the furnace (see Figure 2.1).

- A more efficient multilayer thermal insulation was designed for the solidification part of the furnace, surrounding the crucible. Details about this multilayer insulation are presented in Appendix A.
- An automatic system was developed in order to control the TMF intensity and orientation.
- Flow-meters and thermocouples were added to the cooling system in order to analyse the energy losses on different parts of the furnace.

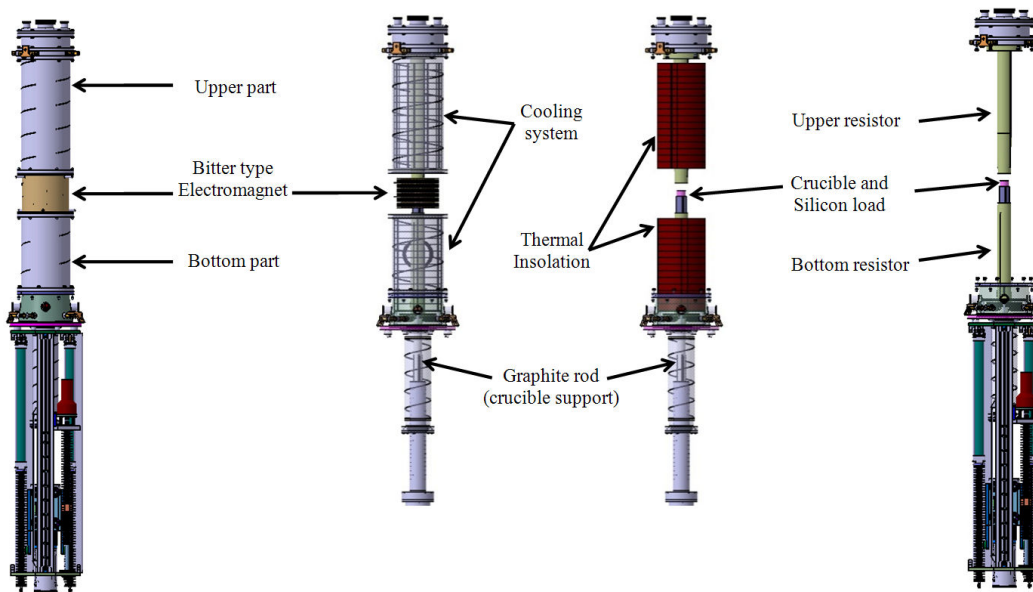


Figure 2.1: Main components of VB2 experimental installation.

The VB2 furnace is mainly used to obtain polycrystalline silicon by directional solidification. The middle part of the furnace, where the solidification process takes place, is depicted in Figure 2.2. The furnace is equipped with two resistive heaters (D and E) that provide a given thermal gradient in the silicon. A fused silica crucible (A) filled with silicon is positioned between the two heaters, in order to obtain an axial thermal gradient in the silicon bulk. The crucible is supported in this position by a cylindrical shaped graphite support (B) at the top of a vertical graphite rod (C). Surrounding the graphite support, a multilayer thermal insulation (G) is positioned in order to maintain a low radial thermal gradient in the silicon during the solidification. The multilayer thermal insulation is surrounded by the Bitter type electromagnet (H), consisting in multiple windings immersed in a water pool for cooling. The exterior walls of the furnace are also water cooled. Between the heaters and the cooled walls a graphite foam thermal insulation (F) was placed. Silicon load

is placed inside the crucible and only after a complete melting of the silicon, the crystallization process can begin.

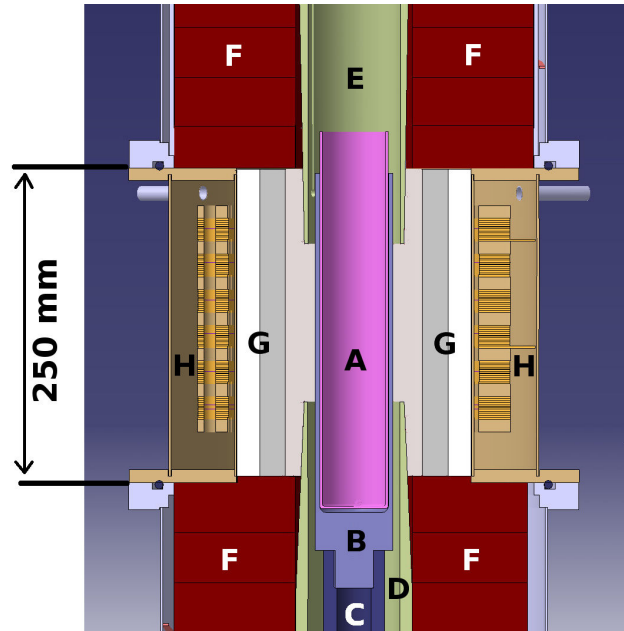


Figure 2.2: Close-up view of VB2 furnace central area. A: Crucible, B: Graphite support, C: Graphite rod, D: Bottom resistor, E: Upper resistor, F: Graphite foam thermal insulation, G: Multilayer thermal insulation, H: Bitter electromagnet.

The VB2 installation is completely automated. Software and hardware equipment offer the possibility to control the crystallization process through variations of different parameters. A temperature gradient along the crucible height is imposed by controlling the temperature of both heaters. A directional solidification of the melt can be obtained either by imposing a cooling rate in the two heaters or by pulling down the crucible with a precise velocity. The first method offers the advantage of avoiding to use a complex mechanical system in order to move the crucible during solidification. Pulling down the crucible offers the advantage of a constant temperature field in the fixed part of the furnace, minimizing the effect of thermal inertia. Connecting a step by step motor to the graphite rod offers the possibility to control the movement of the crucible inside the furnace. The direction (up/down) and the velocity of the crucible are easily controlled and can be changed at any moment in time.

The temperature of the two resistors is controlled by two regulators provided by EURO THERM. The EURO THERM 3504 model regulators are PID controllers compatible with many communication protocols (EIA232, EIA485, Ethernet protocol, etc.). A user interface which allows the configuration of

the regulators is ensured by the *iTools* software platform, also provided by EUROTHERM. To record the high temperature values of the heaters (above the silicon melting temperature), C type thermocouples are positioned near the two heaters. These thermocouples provide the feedback for the PID regulators. This type of thermocouples is capable to read temperatures up to 2320 °C.

A picture of the furnace command panel is given in Figure 2.3. This panel allows the user to set the experimental parameters like temperatures inside the furnace or crucible pulling velocity. The panel also enables the operating of the vacuum pump and control of the argon atmosphere inside the furnace. The computer present on the command panel runs different software, among which *iTools*, providing an even easier access to the temperature regulators, or *NetDAQ* software for the data acquisition system.

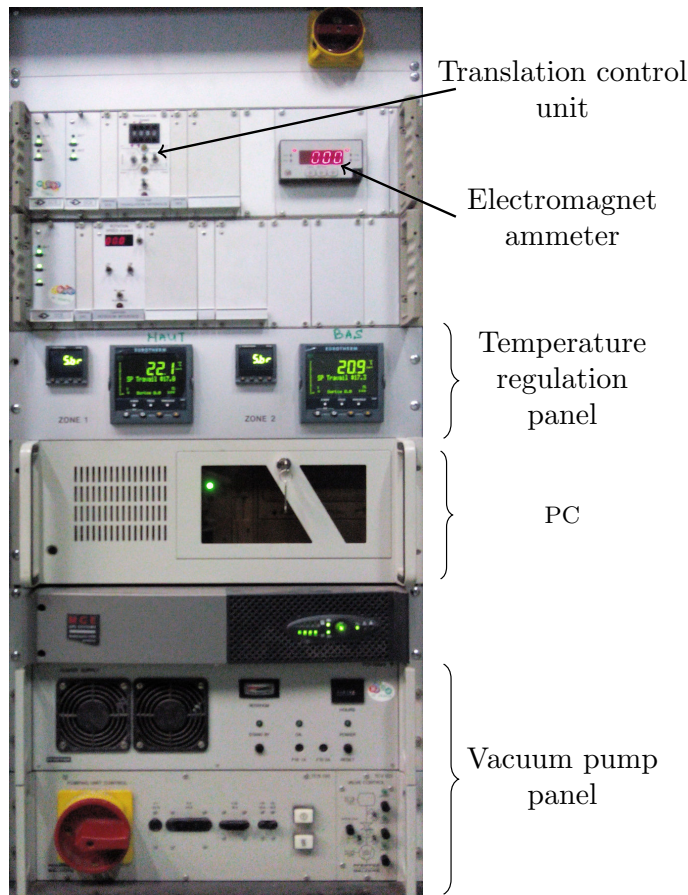


Figure 2.3: VB2 control and command panel including: a crucible translation control unit, an ammeter displaying the electrical current intensity in the electromagnet windings, temperature regulation panel equipped with EUROTHERM 3504 model PID regulators, a command panel for the vacuum pump.

A series of flow meters and thermocouples were connected to the furnace cooling system in order to provide information about the cooling efficiency of different parts of the furnace. Figure 2.4 depicts the panel on which the thermocouples and flow meters were installed on separate pipes. The flow meters were provided by *IFM electric* company. The flow rates and water temperatures are recorded during the experiments. The cooling of the electrical connections for the two heaters and the exterior walls is monitored through this system. This approach can provide information about the power losses in the different parts of the furnace. Moreover, the evolution in time of the thermal insulation quality could be monitored this way. In addition, the electrical power injected in the heaters at any moment in time is also recorded. This way, a power balance can be checked between the electric power injected in the heaters and the thermal power transferred to the water-cooled furnace walls. This system was successfully used to validate the numerical model. The validation process is fully described in Section 3.5. A data acquisition system is used to record the time variation of all the signals generated by this system, including the temperatures indicated by the thermocouples located inside the furnace.

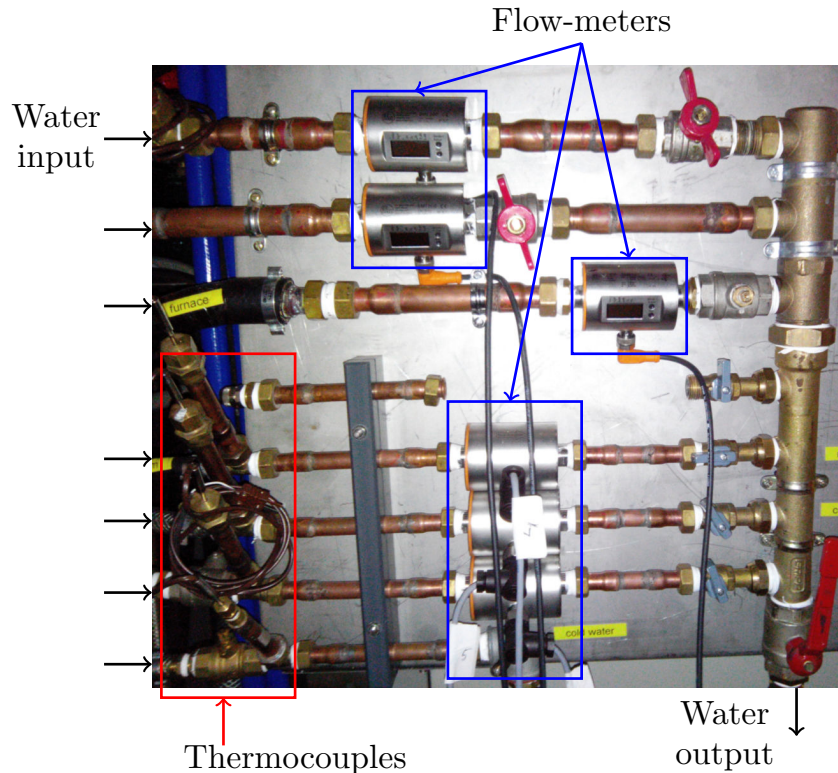


Figure 2.4: Water panel installed on the furnace cooling system.

2.1.2 Bitter electromagnet

The furnace is equipped with a Bitter type electromagnet positioned outside the multilayer insulation, around the crucible. The electromagnet is able to produce a travelling magnetic field (TMF) during the experiments. Different magnitudes and orientations can be selected for the magnetic field and as a result, different flow patterns at velocities up to $10^{-2}m/s$ [36] can be induced in the molten silicon. During the solidification process, a travelling magnetic field can control the shape of the solidification front and the segregation of impurity elements [23, 28] .

Figure 2.5 presents the theoretical flow patterns generated by different orientations of the travelling magnetic field. A predominant concave or convex shape of the solidification interface can be imposed by the different flow patterns. One must be aware that this type of flow patterns can be achieved and sustained only if no sources of flow instabilities exists. More details about this matter are presented in Chapter 4 Section 4.3.

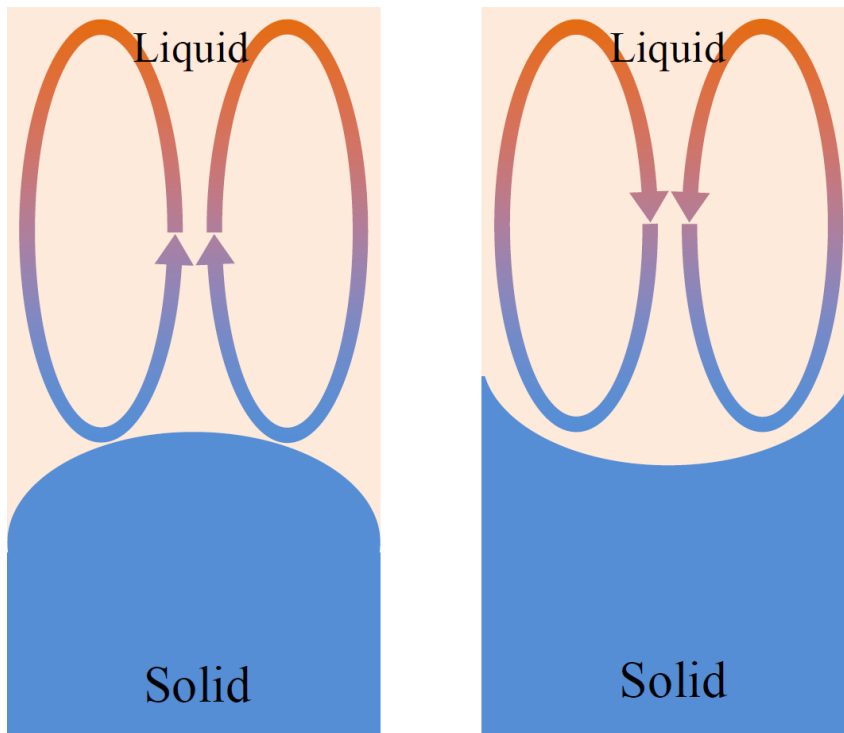


Figure 2.5: Flow patterns in the melt induced by the travelling magnetic field. Downward TMF (left) and upward TMF (right).

The Bitter type electromagnet (Figure 2.6c) is made of multiple windings separated by a ceramic insulator. Each winding (Figure 2.6b) is constructed from multiple circular copper plates (Figure 2.6a) and insulator separators.

The plates and the insulators are combined in a helical configuration such that the electrical current flows round across each disk before passing to the next one. A strong travelling magnetic field is generated in the axial direction of the electromagnet. Because very high electrical currents can pass through the coil, the cooling of the system becomes an important issue. The cooling is done by passing water through small perforation holes. These holes are perfectly aligned on each layer of both copper and insulation material forming vertical parallel channels. This configuration of many parallel cooling channels provides an efficient cooling method by forming a large thermal exchange surface [37].

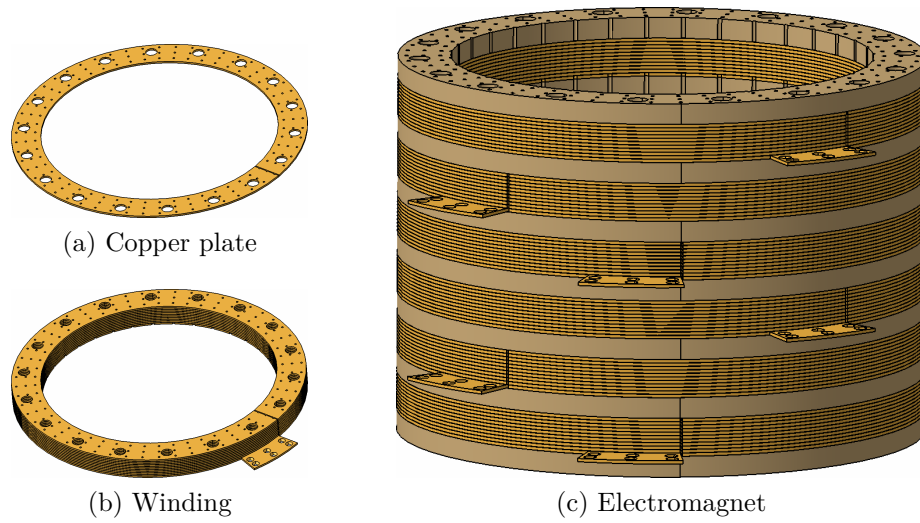


Figure 2.6: Components of the Bitter type electromagnet

The Bitter electromagnet on the VB2 installation (Figure 2.7a) has six windings supplied with three-phase currents at network frequency ($50Hz$). The phase shift between windings is $\pm 60^\circ$. Figure 2.7b presents the correlation between the electrical current sent through the electromagnet windings and the vertical component of the generated magnetic field. The electromagnet is placed around the crucible and the magnetic field directly introduces a Lorentz force which leads to the formation of different flow patterns in the melt (see Figure 2.5), depending on the orientation of the Lorentz force. The induced liquid velocity depends on the intensity of the generated magnetic field. For the magnetic field frequency of $50Hz$ and for the physical properties of liquid silicon, the electromagnetic skin depth was computed at $\delta = 6,24cm$.

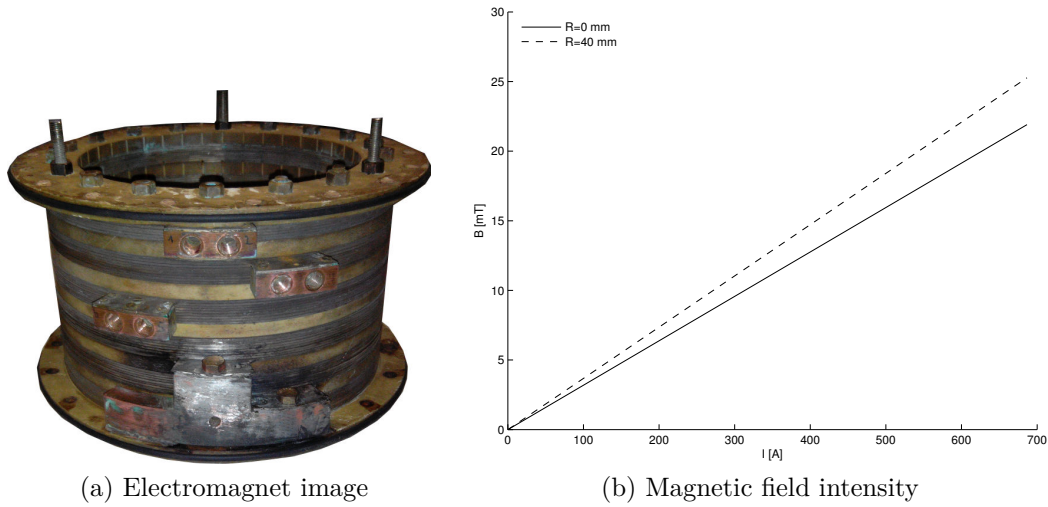


Figure 2.7: Image of the Bitter type electromagnet used in the VB2 furnace (2.7a). Magnetic field intensity variation as a function of the induced current in the mid-plane of the electromagnet (2.7b). (RMS amplitude of the vertical component. R represents the distance on horizontal plane from the geometrical center of the electromagnet. Measurements were performed using a coil designed in the laboratory. The thermal insulation was removed during the measurements.)

2.2 Performed experiments

Multiple series of experiments were performed using silicon contaminated with different levels of impurities as raw material. The main objective was to observe the effect of the travelling magnetic fields over the impurity distribution in the final ingot. Therefore, two different raw materials were used. The impurity concentrations for the raw materials used for these experiments are presented in Table 2.1. As shown in this table, the raw materials used in the experiments consist in silicon contaminated with different concentrations of aluminium, iron and phosphorus. The silicon labelled Si-A has low to moderate impurities levels, while Si-B is highly charged in aluminium.

Table 2.1: Impurities levels for the raw silicon used in the solidification experiments

Material reference	Aluminium [ppm]	Iron [ppm]	Phosphorus [ppm]
Si-A	6.8	10	9.6
Si-B	600	13.2	2.76

The directional solidification process for multi crystalline silicon implies

that the solidification begins at the bottom of the melt and the solidification front moves slowly towards the top of the crucible. This procedure implies a vertical thermal gradient in the molten silicon, created by the two heaters. A higher temperature is required for the top part of the melt and a lower temperature for the bottom part. This can be achieved by imposing different temperatures to the two heaters. C type thermocouples are placed around the crucible in order to record the temperature evolution during the solidification process. The temperature values recorded by the thermocouples outside the crucible, are different from the temperatures at the same height inside the crucible in the silicon melt. These differences can go up to $50K$, according to experimental observations. This phenomenon occurs because the crucible is made of quartz and is a thermal insulator. An example of the thermocouples positioning inside the furnace and of the recorded temperatures for one of the performed experiments is depicted in Figure 2.8.

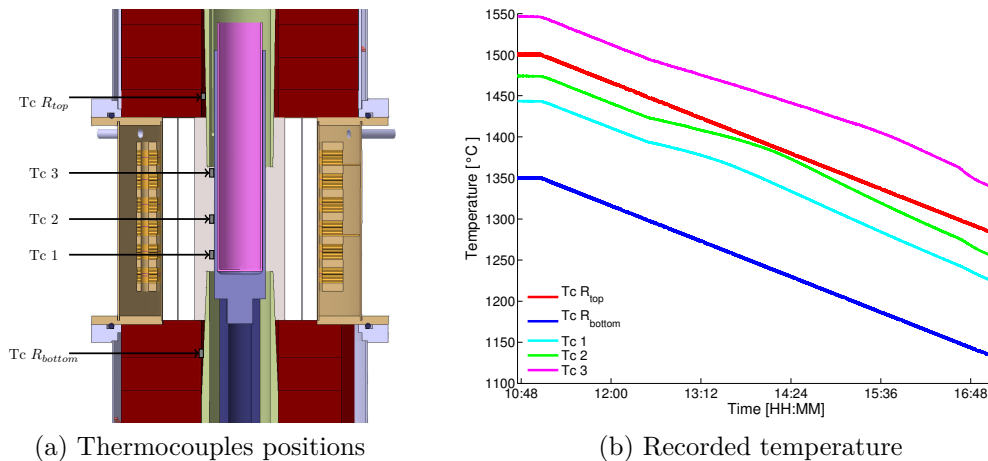


Figure 2.8: Example of thermocouples positioning and of temperature profiles recorded during one experiment. Imposed cooling rate for a fix position of the crucible.

The first step of the process consists in a complete melting of the material inside the crucible. Once the silicon is molten and a thermal gradient is stable inside the melt, the solidification process can begin. In order to initiate the solidification, the temperature at the bottom of the crucible must be decreased below the solidification temperature of the silicon and for that to happen, two possible solutions are available for VB2 furnace configuration. For the first option the solidification begins due to a temperature decrease of both heaters so that the temperature difference between them remains constant. While the crucible position remains unchanged during the solidification process, the im-

posed temperatures for the two resistors are decreased with constant cooling rate. An example of this scenario is shown in Figure 2.8b. The second solidification method available in VB2 is pulling down the crucible with a constant speed while the heaters temperatures remain unchanged.

Tables 2.2, 2.3 and 2.4 describe the main characteristics of the three sets of performed experiments: raw materials used, the imposed temperature difference between the heaters, cooling rate or pulling velocity and the TMF intensity and orientation. All the ingots obtained in these experiments have a diameter of $\approx 5\text{cm}$ (2 inches) and a height varying between 12 and 15cm. For the first two sets of experiments (Tables 2.2 and 2.3) the solidification process was started and conducted by decreasing the temperatures of the two resistors. The temperature difference between the two resistors was set for all experiments to 150K . A thermal gradient in the silicon ingot can be estimated to $\nabla T \approx 1000\text{K}/\text{m}$. For experiments in set III, the solidification was conducted by pulling the crucible downwards with a given velocity.

Table 2.2: Experiment set I

Experiment number	Raw material	Imposed ΔT	Cooling rate $[K/h]$	TMF Intensity $[mT]$	TMF orientation
I.1	Si-A	150	36	0	-
I.2	Si-A	150	36	4	Upward
I.3	Si-A	150	36	4	Downward
I.4	Si-A	150	36	4	Alternating

For the first set of experiments different orientations of the travelling magnetic fields were used. The two conventional orientations for a travelling magnetic field (upward and downward) were used. Alternating the TMF orientation, which implies interchanging upward and downward orientations at different time intervals, was also attempted. All alternating TMF experiments were conducted with a 30s period between the orientation interchanges. The 30s period was considered because numerical simulations indicated that the flow induced by TMF reaches a stable velocity after about 15s. For the experiments in this set, the mean growth velocity computed by the numerical model was between 10^{-5} and $1.5 \cdot 10^{-5}\text{m}/\text{s}$. The results obtained for this first set of experiments are detailed in Section 4.2.1 and 5.2.2.

For the second set of experiments only downward oriented TMF was used. Experiments I.1 and II.1 were conducted without magnetic field and they are used as reference experiments. Because the silicon Si-B was highly contamin-

Table 2.3: Experiment set II

Experiment number	Raw material	Imposed ΔT	Cooling rate [K/h]	TMF intensity [mT]	TMF orientation
II.1	Si-B	150	36	0	-
II.2	Si-B	150	36	7	Downward

ated with aluminium, for the Experiment II.2 the magnetic field intensity was almost doubled compared to experiments in set I. The liquid velocity is proportional to the TMF intensity. An increased liquid velocity decreases the solute boundary layer thickness and reduces the impurity concentration at the interface. Only downward oriented TMF was used in this experimental set because of technical limitations of the experimental set-up for 7mT TMF intensity. More details and results for these experiments are found in Section 5.2.3.

The third set of experiments (Table 2.4) was conceived similar to the set I regarding the silicon type, TMF orientations and intensities used. However, in this set the temperature difference between the two heaters was increased compared to the first set. Nonetheless, the major difference between set I and III is that for the latter a different procedure was used in order to initiate the solidification. If the first option was to gradually decrease the heaters temperatures by imposing a cooling rate, the second one was to keep the temperature field static and to pull down the crucible with a precise velocity. This velocity will be further referred to as pulling velocity and in the case of experiments III it was set constant at $4 \cdot 10^{-6} m/s$. The pulling velocity was chosen to be smaller than the growth rate computed for experiments in the set I. The reason for this choice was to study the segregation phenomena for the same raw material, at different growth rates. The results obtained for this set of experiments are presented in Section 4.2.3 and 5.2.4.

Table 2.4: Experiment set III

Experiment number	Raw material	Imposed ΔT	Pulling velocity [m/s]	TMF intensity [mT]	TMF orientation
III.1	Si-A	400	$4 \cdot 10^{-6}$	0	-
III.2	Si-A	350	$4 \cdot 10^{-6}$	4	Downward
III.3	Si-A	350	$4 \cdot 10^{-6}$	4	Upward
III.4	Si-A	350	$4 \cdot 10^{-6}$	4	Alternating

As in previous experiments, the impurity segregation during the solidific-

ation under TMF was still of interest. Only for the experiments considered in set III solid-liquid interface marking was attempted. For this procedure a different magnetic field intensity was used for a short time (few seconds) at different given moments during the solidification process. More details about the solidification interface marking procedure are presented in Section 4.2.3.

Additional solidification experiments were conducted, with the main objective of testing another interface marking procedure using Peltier effect. These experiments are presented in detail in Section 4.2.2.

Chapter 3

Numerical model

This chapter focuses on the numerical model developed to support and complete the experimental results. Firstly, the objectives of the developed model are presented. The main physical phenomena modelled are then presented and discussed in the second section of this chapter. The third section details the new solidification module for ANSYS FLUENT, developed at SIMaP/EPM laboratory. The solidification and melting module, provided by ANSYS FLUENT, can be used to compute the interface shape during the solidification of silicon, but cannot be used to simulate the solute segregation in silicon. Therefore, the aim for this new module is to provide the computation means for a solute segregation process during the solidification. A validation of this new module is presented at the end of this third section. After defining the numerical model core, further implementation details, like boundary conditions, model geometry and mesh structure, are presented in the fourth section. At the end of the chapter, a thermal validation of the global numerical model is presented. Several comparisons of the model with experimental results are presented in the following chapters.

3.1 Objectives

The comprehensive description of the experimental furnace, presented in Chapter 2, indicates some technical limitations to use the furnace as a research facility. Some important information, as the induced liquid velocity or flow patterns, are not available to the user. Regarding the temperature inside the crucible, the only available information is provided by the thermocouples positioned right outside the crucible. As explained in Chapter 2, these temperatures measured outside the crucible are different from the silicon tem-

perature, at the same height inside the crucible. Therefore, the user does not have accurate information about the temperature distribution in the silicon.

This lack of exact information can be a very important drawback to perform quality experiments. A numerical model can compensate for the missing experimental information and can provide more details related to the solidification process. Another benefit from developing a numerical model can be the prediction of quantities such as the solid-liquid interface shape for different experimental conditions. Therefore, developing a reliable numerical model became one of the main objectives of this work. A 2D axisymmetric model was developed using the commercial software ANSYS Fluent 14.5. The 2D axisymmetric geometry for the model was considered because of the cylindrical shape of the furnace as well as all the furnace components and crucible.

A 2D axisymmetric geometry allowed a reduced mesh size (≈ 20000 cells). The simulations were performed in transient mode with a time step of 5s. All these factors contributed to a robust numerical model, where the simulated time was only three times slower than the real time.

3.2 Description of the physical phenomena

In order to develop a numerical model that will correctly describe the behaviour of the real experimental furnace, firstly the physical phenomena involved must be determined. The main physical models considered in the development of the numerical model are heat transfer, fluid flow, solidification and impurity segregation. The corresponding physical models will be detailed in the following subsections [38].

In order to simulate the travelling magnetic field present in the real experiment, the numerical model must also integrate the previously developed *Induction* module. The *Induction* module, developed at SIMaP/EPM laboratory [39] is used, for 2D and 2D axisymmetric model, to compute the electromagnetic force density imposed as a volume source for momentum equations. This will induce a forced convection in the liquid during the simulations. The module was already successfully used in other research programs studying plasma torches, continuous casting of silicon, levitation of metal droplets and electromagnetic pumps.

3.2.1 Mass conservation and momentum equation

The equation solved by ANSYS FLUENT software for mass conservation is:

$$\frac{\partial \rho}{\partial t} + \nabla \cdot (\rho \vec{v}) = S_m \quad (3.1)$$

where ρ represents the material density, \vec{v} represents the liquid velocity and the source term S_m represents the mass added to the continuous phase from the dispersed second phase and any user-defined sources.

For 2D axisymmetric geometries, the continuity equation is given by

$$\frac{\partial \rho}{\partial t} + \frac{\partial}{\partial x} (\rho v_x) + \frac{\partial}{\partial r} (\rho v_r) + \frac{\rho v_r}{r} = S_m \quad (3.2)$$

where x is the axial coordinate, r is the radial coordinate, v_x is the axial velocity, and v_r is the radial velocity.

The momentum conservation equation computed by Fluent is

$$\frac{\partial}{\partial t} (\rho \vec{v}) + \nabla \cdot (\rho \vec{v} \vec{v}) = -\nabla p + \nabla \cdot (\bar{\bar{\tau}}_{eff}) + \rho \vec{g} + \vec{F} \quad (3.3)$$

where p is the static pressure, $\bar{\bar{\tau}}_{eff}$ is the stress tensor, $\rho \vec{g}$ is the gravitational body force and \vec{F} is the external body forces. The liquid silicon is assumed to be a Newtonian fluid and the stress tensor $\bar{\bar{\tau}}_{eff}$ is given by

$$\bar{\bar{\tau}}_{eff} = \mu_{eff} \left[(\nabla \vec{v} + \nabla \vec{v}^T) - \frac{2}{3} \nabla \cdot \vec{v} I \right] \quad (3.4)$$

where $\mu_{eff} = \mu + \mu_t$ is the effective viscosity, μ_t is the turbulent viscosity, I is the unit tensor, $\frac{2}{3} \mu_{eff} \nabla \cdot \vec{v} I$ is the effect of volume dilation (null for our incompressible fluid flow).

Natural convection is computed using the Boussinesq approximation, which allows to consider ρ constant in all terms except $\rho \vec{g}$. In this term, a linear variation of the fluid density with the temperature is assumed.

For 2D axisymmetric geometries, the axial and radial momentum conser-

vation equations are given by

$$\begin{aligned}
\frac{\partial}{\partial t}(\rho v_x) + \frac{1}{r} \frac{\partial}{\partial x}(r \rho v_x v_x) + \frac{1}{r} \frac{\partial}{\partial r}(r \rho v_r v_x) &= -\frac{\partial p}{\partial x} \\
&+ \frac{1}{r} \frac{\partial}{\partial x} \left[r \mu_{eff} \left(2 \frac{\partial v_x}{\partial x} - \frac{2}{3} (\nabla \cdot \vec{v}) \right) \right] \\
&+ \frac{1}{r} \frac{\partial}{\partial r} \left[r \mu_{eff} \left(\frac{\partial v_x}{\partial r} + \frac{\partial v_r}{\partial x} \right) \right] + F_x
\end{aligned} \tag{3.5}$$

and

$$\begin{aligned}
\frac{\partial}{\partial t}(\rho v_r) + \frac{1}{r} \frac{\partial}{\partial x}(r \rho v_x v_r) + \frac{1}{r} \frac{\partial}{\partial r}(r \rho v_r v_r) &= -\frac{\partial p}{\partial r} \\
&+ \frac{1}{r} \frac{\partial}{\partial x} \left[r \mu_{eff} \left(\frac{\partial v_r}{\partial x} + \frac{\partial v_x}{\partial r} \right) \right] \\
&+ \frac{1}{r} \frac{\partial}{\partial r} \left[r \mu_{eff} \left(2 \frac{\partial v_r}{\partial r} - \frac{2}{3} (\nabla \cdot \vec{v}) \right) \right] \\
&- 2 \mu_{eff} \frac{v_r}{r^2} + \frac{2}{3} \frac{\mu_{eff}}{r} (\nabla \cdot \vec{v}) + \rho \frac{v_z^2}{r} + F_r
\end{aligned} \tag{3.6}$$

In Equations 3.5 and 3.6 the axial and radial components of the force density F_x and F_r represent the source terms for external forces and buoyancy forces. The induction module, included into the numerical model, computes the Lorentz force induced by the travelling magnetic field and is added as an external forces using source terms. This force increases the liquid velocity with the TMF intensity and a forced convection is generated in the silicon melt. In simulations presented in Section 4.2 the computed liquid velocity reaches $3.4 \cdot 10^{-2} m/s$. For this level of velocity, crucible dimensions (1 inch in radius) and the physical properties of the silicon (Appendix B), Reynolds number can be computed at ≈ 2800 . For this value of the Reynolds number, laminar and turbulent flows are possible, therefore also the turbulence effect must be considered in the model. ANSYS FLUENT software offers the choice of several turbulent models. The Shear-Stress Transport (SST) $k - \omega$ turbulent model was chosen. The $k - \omega$ turbulent model is proposed by [40] and combines the accurate formulation of the $k - \omega$ model in the near-wall region with the free-stream independence of the $k - \epsilon$ model in the far field. The model computes the turbulence kinetic energy (k) and the specific dissipation rate (ω).

3.2.2 Heat transfer model

The model solves the energy equation where the heat transfer includes conduction, convection and radiation. ANSYS FLUENT solves the energy equation in the following form:

$$\frac{\partial}{\partial t}(\rho E) + \nabla \cdot (\vec{v}(\rho E + p)) = \nabla \cdot (k_{eff}\nabla T - \sum_j h_j \vec{J}_j + (\bar{\tau}_{eff} \cdot \vec{v})) + S_h \quad (3.7)$$

where E is the energy per unit mass, k_{eff} is the effective thermal conductivity ($k + k_t$, where k_t represents the turbulent thermal conductivity), and \vec{J}_j is the diffusion flux of species j . On the right-hand side of Equation 3.7 the term $\nabla \cdot k_{eff}\nabla T$ represents energy transfer due to conduction, $\nabla \cdot \sum_j h_j \vec{J}_j$ represents species diffusion, and $\nabla \cdot (\bar{\tau}_{eff} \cdot \vec{v})$ represents viscous dissipation. The S_h term includes the user defined volumetric heat sources.

In Equation 3.7

$$E = h - \frac{p}{\rho} + \frac{v^2}{2} \quad (3.8)$$

In Equation 3.8 the sensible enthalpy h is defined as:

$$h = \sum_j Y_j h_j \quad (3.9)$$

where Y_j is the mass fraction of species j , and

$$h_j = \int_{T_{ref}}^T C_{p,j} dT \quad (3.10)$$

where T_{ref} represents the reference temperature and $C_{p,j}$ represents the heat capacity of species j .

The model contains different regions of different materials like thermal insulators, liquid silicon or argon gas. The form of the energy equation (3.7) varies according to the different material phases. Therefore different equations are going to be solved for different regions in the model, depending whether they are solid, liquid or gas phase. Equation 3.11 is the energy equation solved for solid regions as thermal insulators, heaters or the crucible.

$$\frac{\partial}{\partial t}(\rho h) + \nabla \cdot (\vec{v}\rho h) = \nabla \cdot (k\nabla T) + S_h \quad (3.11)$$

where

ρ represents the density

h represents the sensible enthalpy
 k represents the thermal conductivity
 T represents the temperature
 S_h represents the volumetric heat source.

Considering that the furnace operates at high temperatures, radiative heat transfer must be considered in the numerical model and a radiation model must be used in argon volumes. The Discrete Ordinates (DO) radiation model was considered and it solves the radiative transfer equation (Equation 3.12) for a finite number of discrete solid angles, each associated with a direction vector \vec{s} fixed in the global Cartesian system (x, y, z) .

$$\begin{aligned}
 \frac{dI(\vec{r}, \vec{s})}{ds} + (a + \sigma_s) I(\vec{r}, \vec{s}) = an^2 \frac{\sigma T^4}{\pi} \\
 + \frac{\sigma_s}{4\pi} \int_0^{4\pi} I(\vec{r}, \vec{s}') \phi(\vec{s}, \vec{s}') d\Omega'
 \end{aligned} \tag{3.12}$$

where

\vec{r} represents position vector
 \vec{s} represents direction vector
 \vec{s}' represents scattering direction vector
 s represents path length
 a represents absorption coefficient
 n represents refractive index
 σ_s represents scattering coefficient
 σ represents Stefan-Boltzmann constant ($5.67 \times 10^{-8} \text{W/m}^2 - \text{K}^4$)
 I represents radiation intensity
 T represents local temperature
 Φ represents phase function
 Ω' represents solid angle.

The most important region of the model, where the most relevant information is recovered from, is the region where the silicon is found. This region must be totally or partially considered as fluid, depending on the solidification model that is used. If *ANSYS FLUENT solidification and melting* module (Section 3.2.3) is used the solidification region is totally considered as fluid and if *SIMaP/EPM solidification* module (Section 3.3) is used, the solidification region is separated in two, a fluid one and a solid one. In liquid silicon region, the convection takes part in the heat transfer process. Furthermore, if

heat is added to a fluid, a flow can be induced in the liquid due to the gravity force acting on the density variations (buoyancy force). As a result, a natural convection takes place in the fluid.

3.2.3 ANSYS FLUENT solidification and melting module

ANSYS FLUENT software provides a *solidification and melting* module that can be used to simulate the solidification process. The material enthalpy (Equation 3.13) is computed as the sum of the sensible enthalpy h and the latent heat content ΔH .

$$H = h + \Delta H \quad (3.13)$$

where

$$h = h_{ref} + \int_{T_{ref}}^T c_p dT \quad (3.14)$$

and

h_{ref} represents the reference enthalpy

T_{ref} represents the reference temperature

c_p represents the specific heat at constant pressure

For materials where $T_{solidus} \neq T_{liquidus}$, a liquid fraction β can be defined as

$$\begin{aligned} \beta &= 0 & \text{if } T < T_{solidus} \\ \beta &= 1 & \text{if } T > T_{liquidus} \\ \beta &= \frac{T - T_{solidus}}{T_{liquidus} - T_{solidus}} & \text{if } T_{solidus} < T < T_{liquidus} \end{aligned} \quad (3.15)$$

Equation 3.15 is generally used by the solidification module when dealing with alloys. If a pure material is used then $T_{solidus} = T_{liquidus}$ and the module uses a method based on enthalpy [41] to compute the liquid fraction β .

According to ANSYS FLUENT Theory Guide [38], once the liquid fraction β is defined, the latent heat content ΔH can be written as

$$\Delta H = \beta L \quad (3.16)$$

where L represents the latent heat of the material.

When the *solidification and melting* module is used, the energy equation in the fluid regions is written as

$$\frac{\partial}{\partial t}(\rho H) + \nabla \cdot (\rho \vec{v} H) = \nabla \cdot (k \nabla T) + S \quad (3.17)$$

H represents enthalpy

ρ represents density

\vec{v} represents fluid velocity

S represents source term

When this module is used to simulate the solidification process, the region filled with silicon must be considered as a fluid zone. Afterwards the module computes the liquid fraction β . Depending on the computed value for β the material is considered a liquid if $\beta = 1$, a solid if $\beta = 0$ or partially solidified if $0 < \beta < 1$. In certain cells in the solidification region the material is computed as partially solidified and this represents a mushy zone, describing the solidification interface. In ANSYS FLUENT the partially solidified region are treated as a porous medium and the porosity in each cell is set equal to the computed liquid fraction in that cell. According to ANSYS FLUENT documentation [38], the momentum sink term M_s takes the following form:

$$M_s = \frac{(1 - \beta)^2}{(\beta^3 + \epsilon)} A_{mush} (\vec{v} - \vec{v}_p) \quad (3.18)$$

where β is the liquid volume fraction, ϵ is a small number (10^{-3}), A_{mush} is the mushy zone constant (ANSYS FLUENT Users Guide recommends $A_{mush} = 10^6$ for non alloys materials), and \vec{v}_p is the solid pulling velocity (set to $\vec{0}$ for this numerical model). The momentum sink term is added as a source term in the momentum equation in order to make the velocity to vanish in the solid regions of the fluid.

Sinks are also added to the turbulence equations in the mushy zone and solidified zone to account for the presence of solid matter. For the turbulence equations, the sink term T_s in Equation 3.19 is very similar to the momentum sink term (Equation 3.18) and is also added as a source term in the momentum equation.

$$T_s = \frac{(1 - \beta)^2}{(\beta^3 + \epsilon)} A_{mush} \phi \quad (3.19)$$

where ϕ represents the turbulence quantity being solved (k, ϵ, ω).

As described above, the solidification and melting module provided by Fluent was initially conceived for alloys including a mushy zone. For a planar solidification front (no mushy zone), which is the case for silicon, this pseudo-mushy zone gives only an approximation of the near front phenomena (such as chemical segregation). However, the thermal balance is respected, making it a good solution to describe the shape of the solidification interface.

3.3 SIMaP/EPM solidification module

3.3.1 Module description

A solidification module for Fluent was developed at SIMaP/EPM laboratory. This module aims to describe precisely the solidification process in the "planar front" regime for materials with low concentration of impurities. By using a front tracking method, a detailed description of the front vicinity can be obtained, with first application to segregation phenomena. The same accuracy would be hardly reached with the front capturing method available in ANSYS FLUENT.

The solidification front is described as a boundary zone (wall), which allows a fine boundary layer mesh on the liquid side. The boundary conditions for the front include diffusive fluxes such as turbulent friction, turbulent heat transfer and turbulent mass transfer. Wall conditions are used in order to include turbulent wall functions, but User Defined Function (UDF) are needed to take into account additional convective fluxes due to the mass flow across the solidification front.

The front is crossed by a mass flow density q_{msol} equal to the mass solidified per second and per unit area, given by a thermal balance at interface. The mass flow density is used to define the crystal growth velocity (Equation 3.20) which is the normal component of the solidification front velocity with respect to the solid.

$$R = \frac{q_{msol}}{\rho_s} \quad (3.20)$$

where ρ_s represents the solid density.

By convention $q_{msol} > 0$ for the solidification regime and $q_{msol} < 0$ for melting. A pulling velocity \vec{v}_p with respect to the laboratory frame of reference

can be imposed. The solid will move with respect to the laboratory frame with a velocity equal to the pulling velocity. In this case, the solidification front velocity can be computed as:

$$v_i = \vec{v}_p \cdot \vec{n} + R \quad (3.21)$$

where \vec{n} represents the unit normal to the solidification front, directed out of the solid, along which R is computed.

If the pulling velocity (\vec{v}_p) will cause the solid to move at the same speed, with respect to the laboratory frame, the liquid has a velocity with a normal component \vec{v}_l that verifies:

$$\vec{v}_l \cdot -\vec{n} = \left(\frac{\rho_s}{\rho_l} - 1 \right) R - \vec{v}_p \cdot \vec{n} \quad (3.22)$$

where ρ_s and ρ_l represents the solid and liquid densities, respectively.

In order to avoid a volume change during the simulations and therefore free surface models, ρ_s and ρ_l are considered to be equal. As a result the same pulling velocity will be imposed in the liquid as well as in the solid and the Equation 3.22 can be rewritten as:

$$\vec{v}_l \cdot -\vec{n} = -\vec{v}_p \cdot \vec{n} \quad (3.23)$$

Figure 3.1 summarises, in the laboratory frame of reference, all the elements introduced above.

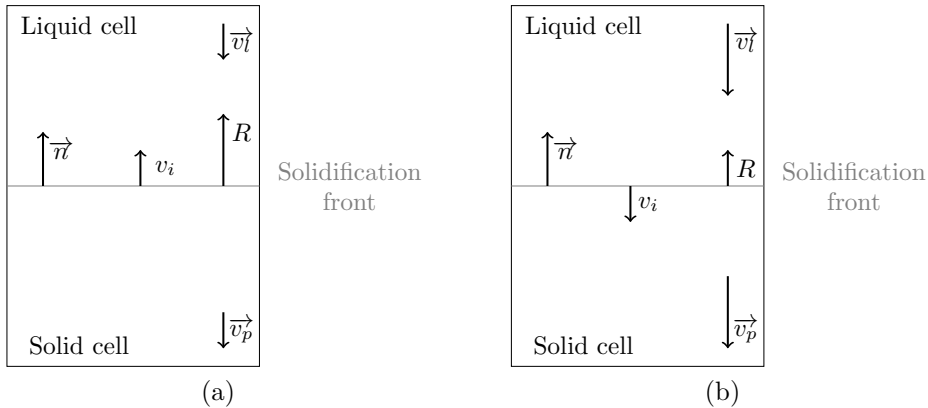


Figure 3.1: Description, in the laboratory frame of reference, of the elements introduced in the SIMaP/EPM solidification module for Fluent. Figure 3.1a depicts the scenario when the pulling velocity \vec{v}_p is smaller than the crystal growth rate R , while Figure 3.1b represents the reversed scenario.

The melting temperature T_m of the pure solvent is imposed at the solidification front and the thermal fluxes are calculated by the model at each time step. The module takes into account the flow across the front in transport equations, and computes the front shape from a thermal balance at the front. If the shape is imposed, the thermal balance will not be considered locally but globally, using a thermal balance on the whole front to get its global displacement. The thermal balance equation can be written as

$$\rho_s (\vec{v}_p \cdot \vec{n} - v_i) (h_l - h_s) = k_l \left(\frac{\partial T}{\partial \vec{n}} \right)_l - k_s \left(\frac{\partial T}{\partial \vec{n}} \right)_s \quad (3.24)$$

where h_s and h_l are the solid and liquid specific enthalpies at the interface (their difference is the latent heat), k_l is the liquid thermal conductivity and k_s represents the solid thermal conductivity.

The thermal balance equation is used to compute the crystal growth velocity $R = v_i - \vec{v}_p \cdot \vec{n}$. This can be replaced in Equation 3.20 and the equation for solidification front velocity, in the laboratory frame of reference, can be rewritten as:

$$v_i = \vec{v}_p \cdot \vec{n} + \frac{k_s G_s - k_l G_l}{\rho_s (h_l - h_s)} \quad (3.25)$$

where $G_s = \left(\frac{\partial T}{\partial n} \right)_s$ and $G_l = \left(\frac{\partial T}{\partial n} \right)_l$ are the thermal gradients in the solid and liquid, respectively.

For an unsteady case, in order to deform the interface according to the computed fluxes (based on thermal balance equation), a displacement value is computed for each node nd along the interface. The node displacement δZ_{nd} is computed as:

$$\delta Z_{nd} = \frac{\Delta t}{N_f} \sum_{f=1}^{N_f} \frac{R_f}{\vec{e}_c \cdot \vec{n}_f} \quad (3.26)$$

where Δt is the time step, N_f is the number of interface faces touching node nd , R_f is the solidification velocity (growth rate) of face f , \vec{n}_f is the unit normal to face f and \vec{e}_c is the unit vector in the crystallization direction.

Figure 3.2 depicts the principle for the displacement of a given node (nd) on the solidification front, described in Equation 3.26. On the solidification front, faces f_1 and f_2 are tangent to the node nd . For both faces their computed displacement $R_f \vec{n}_f$ is used to determine a mean value for the displacement δZ_{nd}

for node nd . This displacement is calculated for every node on the interface, at the end of each time step. Following, a complete re-meshing of the solid and liquid volumes is performed.

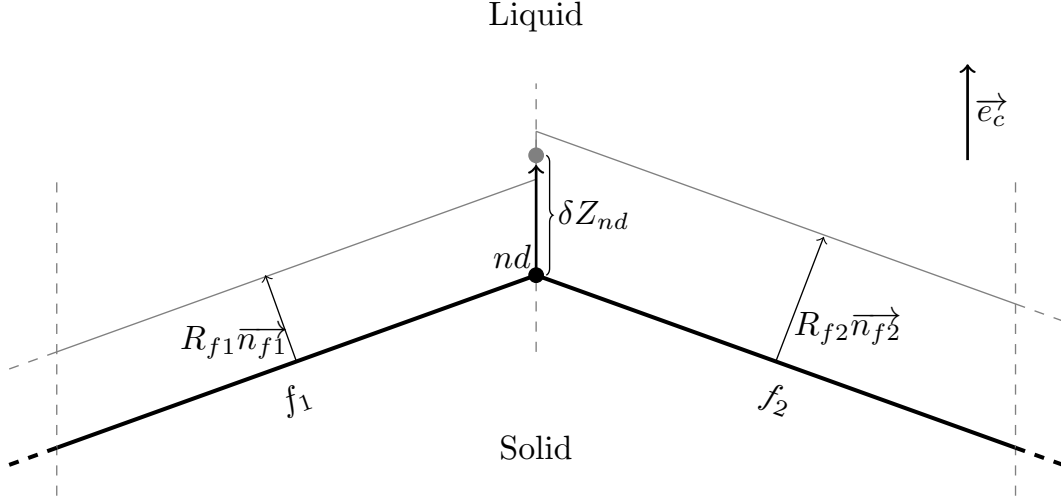


Figure 3.2: Description of the displacement of one node at the solidification front, for an unsteady case simulation.

The SIMaP/EPM solidification module also allows species segregation computations during the solidification process. During the solidification, for species i , the mass fraction at the interface, on the liquid side, is Y_l and is related to its value Y_s on the solid side, by the thermodynamic equilibrium condition:

$$Y_s = K_0 \cdot Y_l \quad (3.27)$$

where K_0 is the equilibrium partition coefficient (segregation coefficient). Because of the mass flow density q_{msol} across the solidification front, there is a convection flux density of solute $-\vec{n}q_{msol}Y_s$ from the interface to the solid, and $-\vec{n}q_{msol}Y_l$ from the liquid to the interface. Taking into account the diffusion flux density (Equation 3.28) from the liquid to the interface while neglecting diffusion in the solid, the balance of fluxes at the interface can be written as Equation 3.29

$$J_{diff} \cdot -\vec{n} = \rho_l D \left(\frac{\partial Y_l}{\partial \vec{n}} \right)_i \quad (3.28)$$

$$\left(\frac{\partial Y_l}{\partial \vec{n}}\right)_i = \frac{q_{msol}Y_l - q_{msol}Y_{si}}{\rho_l D} = \frac{1 - K_0}{\rho_l D} q_{msol}Y_l \quad (3.29)$$

where D represents the diffusion coefficient.

Equation 3.29 represents the boundary condition at the solidification front. This condition relates the derivative along the normal n of the solute fraction Y_l in the liquid to its value at the front. This derivative measures the "solute rejection" from the interface, and can be imposed as a diffusion flux density when the convection flux density $q_{msol}Y_l$ is also added to the interface. The total flux density that must be imposed on the solidification front is the sum of the convection $q_{msol}Y_l$ and diffusion $\rho_l D \left(\frac{\partial Y_l}{\partial \vec{n}}\right)_i$ from the liquid to the front.

3.3.2 Module validation

Thermal validation

In order to validate the SIMaP/EPM solidification module, a simulation for the two-phase Stefan problem was considered, where an analytical solution can be computed as well. A particular scenario for the Stefan problem was considered, where the solidification front propagation in a liquid environment, caused by a thermal shock is analysed. The detailed description as well as the analytical solution of the Stefan problem can be found in [42]. The geometry of the problem is depicted in Figure 3.3. A semi-infinite one-dimensional block of liquid initially at homogeneous temperature T_i is considered. At t_0 the temperature at $x = 0$ (left side) is dropped at $T = T_0 < T_m$. The thermal shock will create a solid layer at $x = 0$ and the solidification front will advance into the liquid. The solidification front is at a temperature T_m , where $T_0 < T_m < T_i$ and represents the boundary between the two phases.

According to [42] the temperature in the solid and in the liquid, at instance t , can be computed as:

$$T_s = A_1 + B_1 \operatorname{erfc}\left(\frac{x}{2\sqrt{\alpha t}}\right) \quad (3.30)$$

$$T_l = A_2 + B_2 \operatorname{erfc}\left(\frac{x}{2\sqrt{\alpha t}}\right) \quad (3.31)$$

where α is thermal diffusivity and

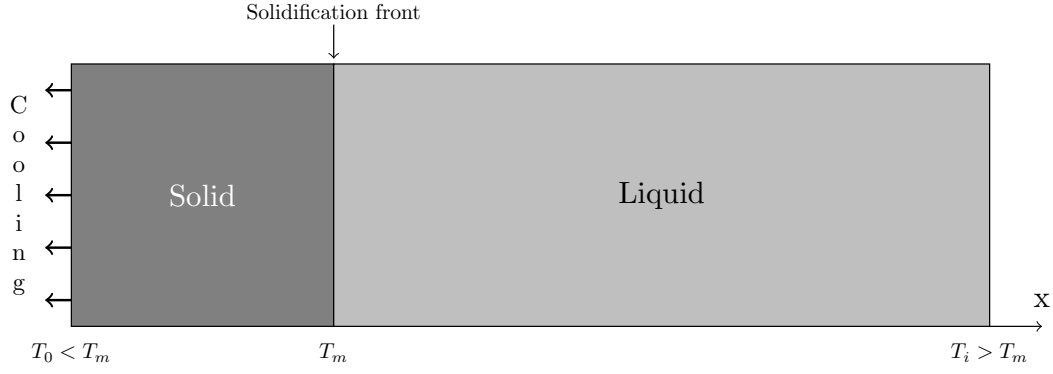


Figure 3.3: Description of a Stefan problem.

$$\begin{aligned} A_1 &= T_0 - B_1 & A_2 &= T_i \\ B_1 &= \frac{T_0 - T_m}{\text{erf}(\mu)} & B_2 &= \frac{T_m - T_i}{\text{erfc}(\mu)} \end{aligned}$$

According to the authors [42] the constant μ is given by:

$$\sqrt{\pi}\mu e^{\mu^2} = \left(\frac{(T_m - T_0)}{\theta_0 \text{erf}(\mu)} - \frac{(T_i - T_m)}{\theta_0 \text{erfc}(\mu)} \right) \quad (3.32)$$

where $\theta_0 = \frac{\Delta H}{c_p}$.

The theoretical solution proposed by the authors [42] considered the same physical properties of the liquid and solid silicon, for simplification. The position of the solidification front at instant t is computed as:

$$X(t) = 2\mu\sqrt{\alpha t} \quad (3.33)$$

In order to simulate the Stefan problem described above, a simple geometry model is considered, where only the solidification region (silicon) is described. The initial geometry contains two separate regions (solid and liquid) from the beginning. The total dimension (x direction) of the two regions is $H = 10^{-1}m$ while the width (y direction) is $W = 10^{-2}m$. The solid region (left side) has a thickness (x direction) of $10^{-4}m$ at t_0 . The initial temperature of the liquid is set to $T_i = 1737K$. The temperature $T_0 = 1637K$ is imposed at the cold boundary ($x = 0$). The temperature T_i imposed at the hot boundary ($x = H$) is $1737K$ with a null velocity. The melting temperature of the silicon, $1687K$, is imposed to the solidification front. Remaining walls are considered to be

adiabatic. In this simulation, the physical properties of the liquid silicon are considered to be the same as the ones of the solid silicon. The simulation is conducted in transient mode and the solidification is simulated for 1000 seconds. The time step for this particular simulation evolved from $0.01s$ at the beginning ($t = 0s$) up to $50s$ towards the end of the simulation ($t = 1000s$).

A triangular mesh is chosen for both regions. On the liquid side of the front a boundary layer was added. The triangular mesh was chosen because of the Fluent capability to completely re-mesh it, which is not the case for a quadrilateral mesh. The boundary layer was introduced for a better description of the solute boundary layer (described in Section 5.1). Figure 3.4 depicts the time evolution of the solidification front along the x direction as well as the changes in the mesh.

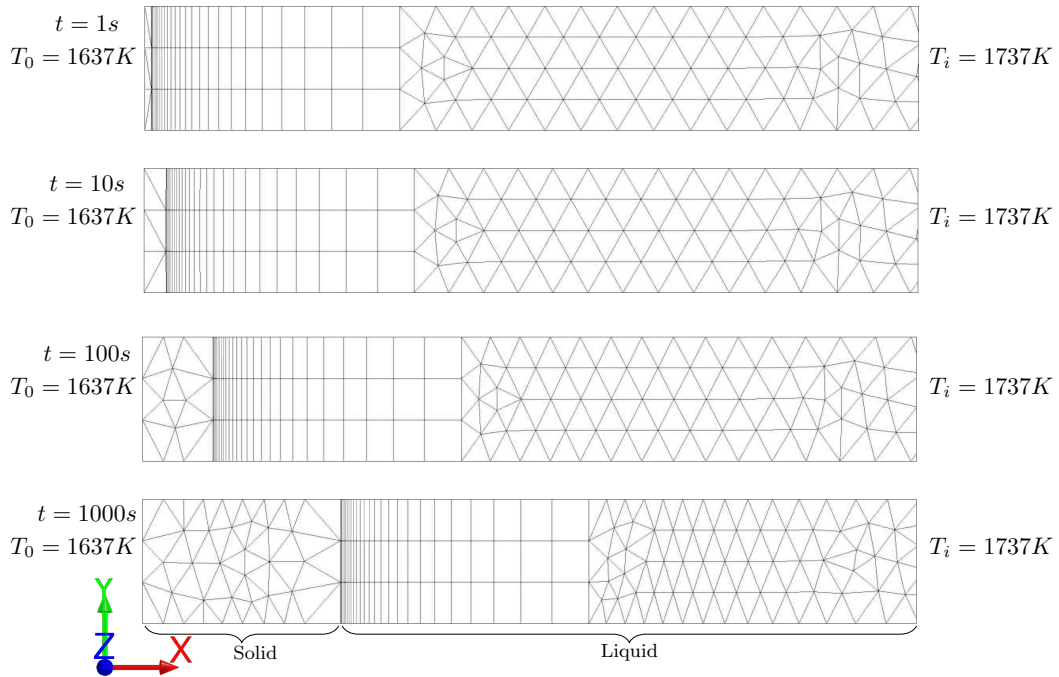


Figure 3.4: Mesh evolution in time.

The results obtained for this simulation are now compared with the analytical solution. Figure 3.5a presents a comparison between the simulated and theoretical values for the evolution of the front position in time. The theoretical result was obtained using Equation 3.33 for the same temperature (T_0 , T_m and T_i) as in the simulation. Up until $\approx 400s$, the simulation correctly describes the front position predicted by the theory. After $400s$, differences between the simulated and theoretical position of the front begin to appear. Moreover, the thermal flux was computed at the solidification front on the solid and liquid as

well. A comparison between theoretical and simulated values for the thermal flux is presented in Figure 3.5b. The model correctly computes the thermal flux for the first 100s of the simulation. After 100s, the computed thermal flux on the liquid side of the interface begins to differ from the theoretical values.

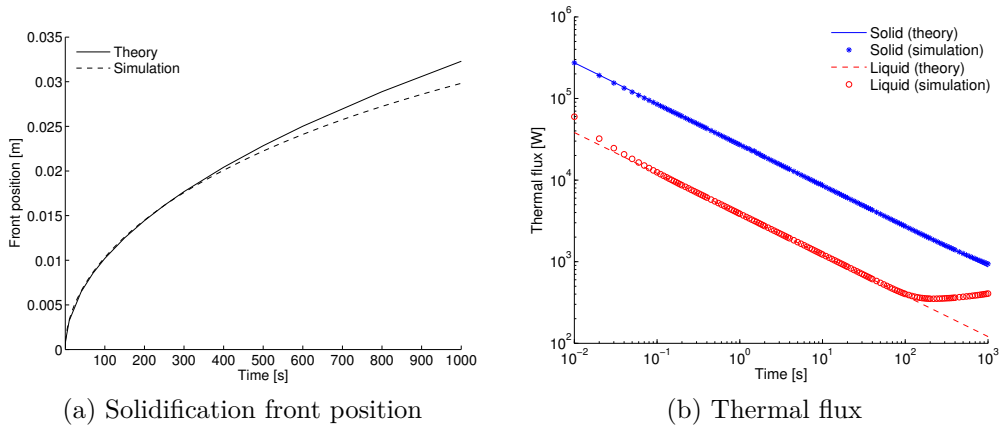


Figure 3.5: Comparison of theoretical and simulated values for the solidification front position and thermal fluxes at the interface.

The theoretical values for temperature in the x direction are computed using Equations 3.30 and 3.31 at different instants. A comparison between theoretical values and the ones obtained from the simulation is presented in

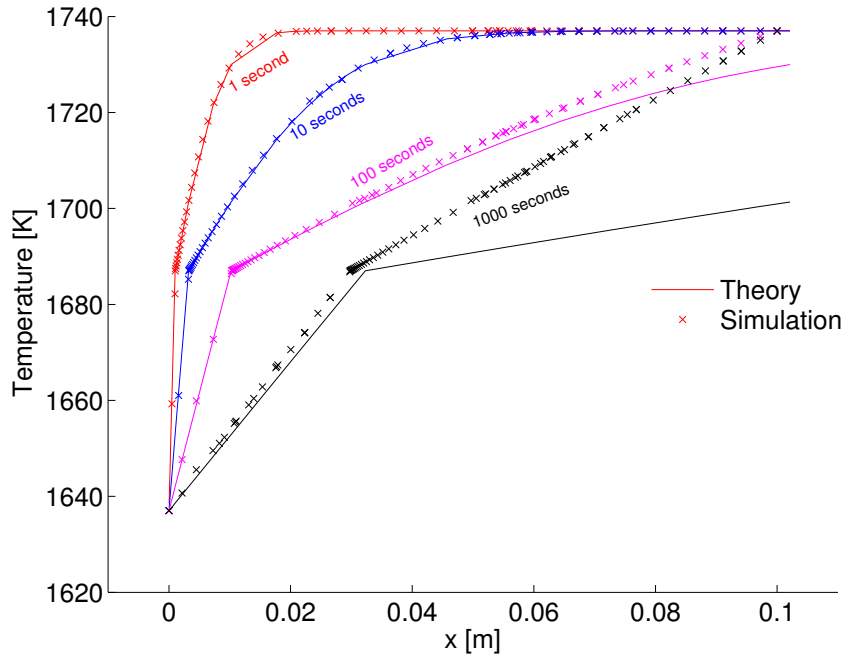


Figure 3.6: Comparison of theoretical and simulated values for temperature distribution at different instants.

Figure 3.6. In Figure 3.6, for each data set (*1second*, *10seconds*, *100seconds* and *1000seconds*), the comparison was made at the same instance. After 100s, the theoretical temperature in the far liquid ($x = 0.1m$) decreased below the initial temperature T_i , while it is fixed at T_i (boundary condition) in the simulation. These differences between the theoretical and computed temperature profiles after $\approx 100s$ came from the fact that the theory is for a semi-infinite domain, while the simulation was performed in a finite geometry ($x = 0.1m$). This can also explain the differences between numerical and theoretical values for the front position and thermal fluxes as well.

Segregation validation

The SIMaP/EPM solidification module is also able to compute the impurity distribution in the liquid. In order to completely validate the module another simulation was conducted with the same geometry as the one used for the Stefan problem with the same boundary conditions. In this new simulation, the only change from the Stefan problem simulation is the solidification front velocity, which was set constant this time. The chosen value for the front velocity was $10^{-5}m/s$, this value is close to the one observed in general in the performed experiments.

The module is capable of computing the impurity concentration values at the solidification interface on the liquid side, and for this simulation aluminium, iron and phosphorus were considered with an initial concentration $C_0 = 10^{-5}$ mass fraction (*10ppm*). A theoretical value for the impurity concentration at the interface on the liquid side during the initial transient is provided by [43].

$$C_L^* \simeq \frac{C_0}{K_0} \left[1 - (1 - K_0) \exp\left(-\frac{K_0 x R}{D}\right) \right] \quad (3.34)$$

where

C_L^* represents the impurity concentration at the interface on the liquid side

C_0 represents the initial concentration

K_0 represents the segregation coefficient

x represents the solidification front position on the X direction

R represents the solidification front velocity (growth rate)

D represents the impurity diffusion coefficient in the liquid solvent

Based on the impurity concentration on the liquid C_L^* and on the segrega-

tion coefficient K_0 , the level of the impurities concentrations in the solid can be computed using Equation 3.35.

$$C_S^* = C_L^* \cdot K_0 \quad (3.35)$$

The segregation coefficient K_0 has different values for each impurity types. For aluminium $K_0 = 2 \cdot 10^{-3}$, for iron $K_0 = 8 \cdot 10^{-6}$ and for phosphorus $K_0 = 3.5 \cdot 10^{-1}$ [44]. The value for the diffusion coefficient D was considered at $7 \cdot 10^{-8} m^2/s$.

A comparison of the theoretical and experimental results regarding the obtained impurities levels are presented in Figure 3.7 for aluminium, Figure 3.8 for iron and Figure 3.9 for phosphorus. The figures are depicting the impurity concentrations in the solid normalized to the initial concentration, for the solidification front position during the initial transient. For this simulation, $4 \cdot 10^{-2} m$ were solidified at a constant growth rate, after which only for phosphorus the initial transient regime is getting close to an end, as it can be observed in Figure 3.9. At the end of the initial transient, C_S^*/C_0 must reach the value of 1 for a diffusive case. For aluminium and iron, due to their smaller values of K_0 compared to phosphorus, the initial transient is still in the beginning phase. The initial transient duration [43] for the diffusive case is estimated at $4D/RK_0$. At a constant growth rate R and for smaller values of K_0 , the length of the initial transient increases.

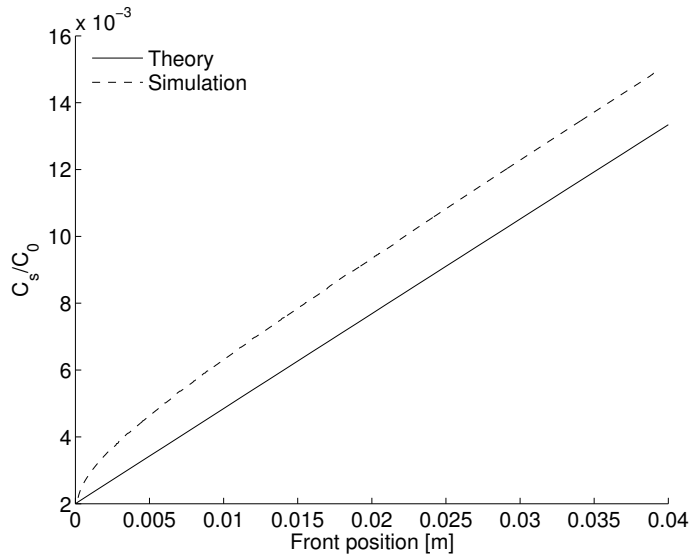


Figure 3.7: Comparison of theoretical and simulated values for aluminium impurities at the solidification interface on the liquid side.

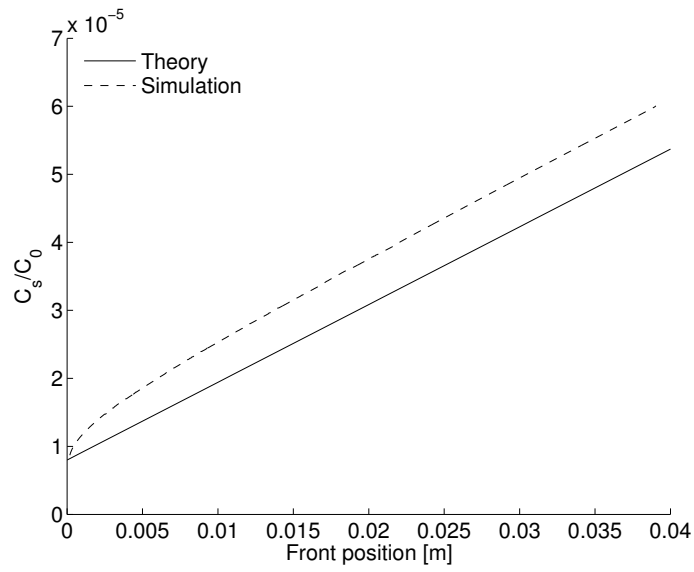


Figure 3.8: Comparison of theoretical and simulated values for iron impurities at the solidification interface on the liquid side.

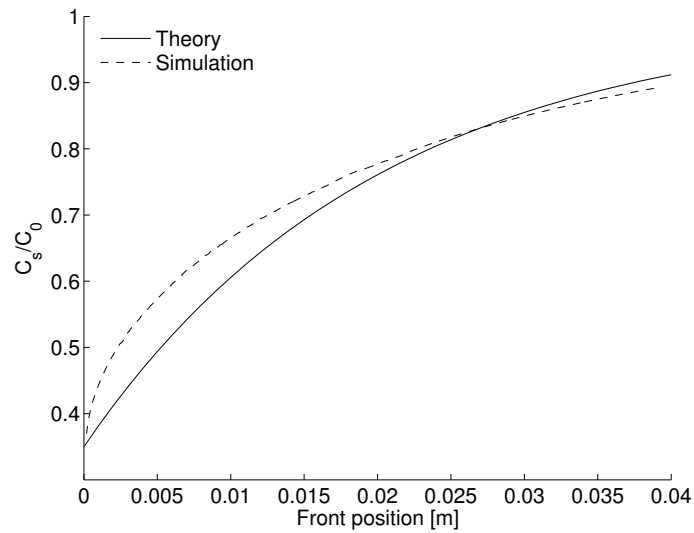


Figure 3.9: Comparison of theoretical and simulated values for phosphorus impurities at the solidification interface on the liquid side.

3.4 Boundary conditions, model geometry and mesh description

For models with minimal domains (only solidification regions with the surrounding crucibles) very accurate values of the boundary conditions would be required if proper results are to be expected. Considering that the experimental set-up cannot provide the precise information needed for the boundary conditions (e.g. exact temperature profiles on the crucible wall) for such a minimalist model, the entire furnace geometry was represented in the numerical model not only the solidification region. Figure 3.10a presents the complete model geometry. As it can be observed, a 2D axisymmetric model was developed due to the cylindrical shape of the furnace.

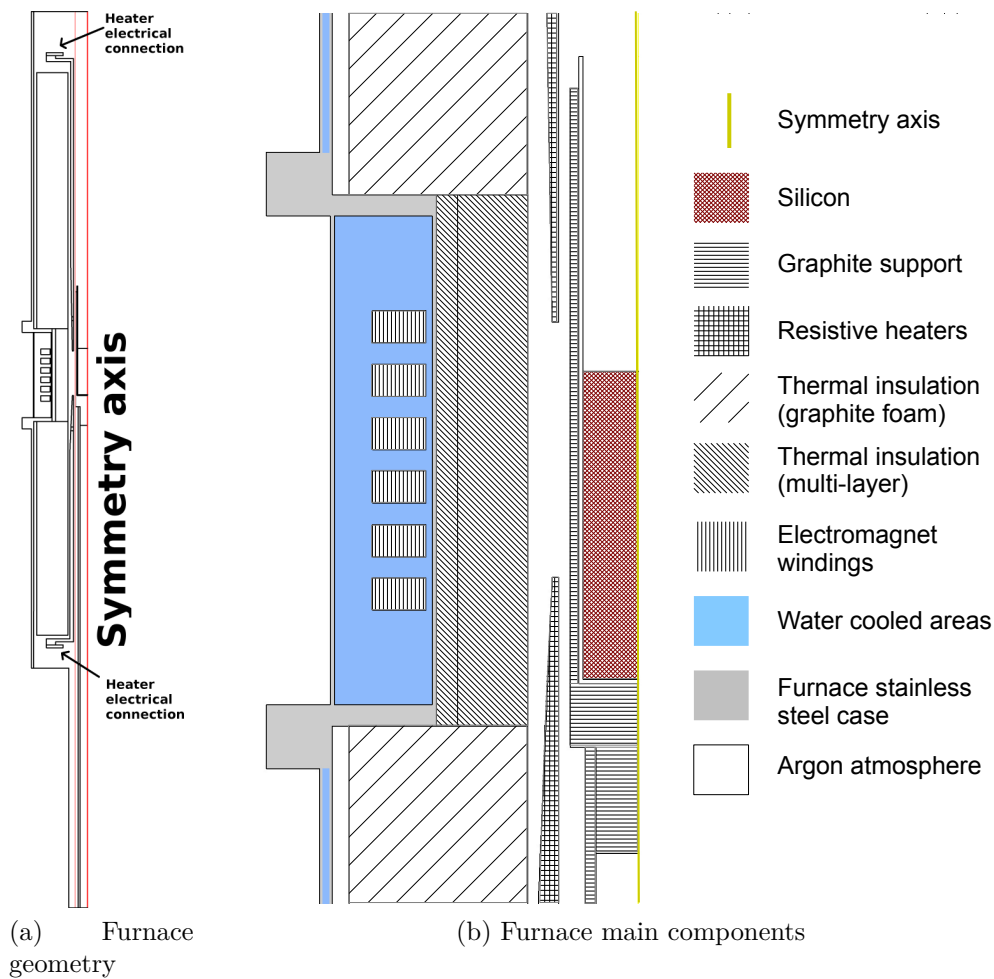


Figure 3.10: Numerical model geometry (3.10a). Zoom-in on the central area highlighting the main material components and regions of the numerical model (3.10b).

The model uses the same materials as the real furnace and Figure 3.10b presents the furnace main components. The heaters, as well as the crucible support and the rod, are made from solid carbon. Two different types of thermal insulation are used, a multi-layer insulation, in the hottest part of the furnace, surrounding the crucible, and graphite foam insulation is used in the rest of the furnace. The electromagnet windings are made from copper (see Section 2.1.2). The furnace case is made of stainless steel and is water cooled. The regions where the argon atmosphere is considered are also indicated in the figure.

Figure 3.11 depicts a close-up view on the central region of the furnace geometry, where the cold temperature boundary conditions, the heaters and the sliding interface are highlighted. Considering that all the exterior walls of the furnace are water cooled, a cold temperature condition ($T = 300K$) was set to all the boundaries, highlighted in blue in Figure 3.11. The electromagnet windings remain cold despite the Joule heating, included in the model. The electrical connectors for the heaters current supply are also water cooled, thus the same cold temperature condition was imposed in the model for the corresponding regions. Another important aspect is temperature profile of the two heaters. No temperature profile is imposed on the heater. Instead, a fixed power density distribution is imposed on the heating elements, deduced from the heater geometrical shape. The power density level imposed on the two heaters is computed as a volume source in order to provide the same temperatures (at the measurement position) as the temperature imposed in each experiment. For each heater, this power level is computed at every iteration using a thermal resistance to the cold environment, adjusted from the previous iteration. The model solves the energy equation (Equation 3.17) where the heat transfer includes radiation (in argon volumes), conduction (in solid and fluid volumes) and convection (in fluid volume). The silicon is the only fluid volume considered in the model. All the others, including the argon volume are considered solids. The model contains also a sliding mesh interface that allows the simulation of the experimental pulling system in the model. The sliding interface basically enables the geometry separation in two parts, a static one (outer part) containing the heaters and the thermal insulation, and a mobile one (inner part) containing the solidification region, the crucible and the supporting elements. The pulling system will impose a vertical translation of the mobile part with a constant speed, which will be further referred to as pulling velocity.

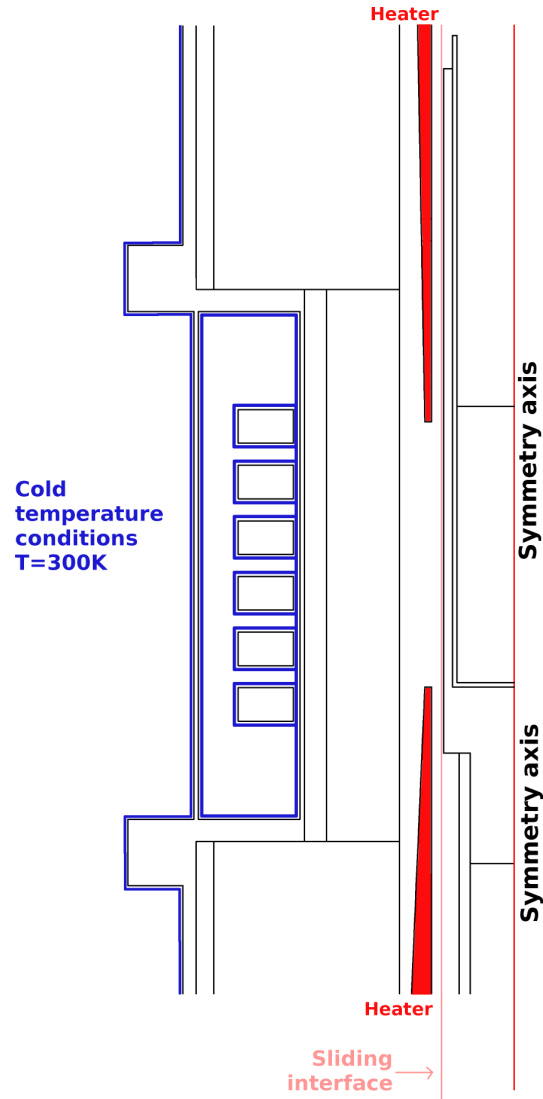


Figure 3.11: Close-up view on the central part of the model geometry. Highlighted temperature boundary conditions, heaters and sliding interface.

Once the geometry is defined, the meshing process can begin. A progressive quadrilateral mesh was used to pave the different regions. In the central area of the furnace a fine mesh is desired in order to obtain a detailed description of the involved phenomena, while towards the external boundaries, less detailed mesh can be used. Figure 3.12 presents the mesh on the entire geometry (left side) and focusing on the central region (right side). The cell size far from the solidification region is $20mm$, in the electromagnet area the size is reduced to $4mm$ and in the solidification region the cells have a size of $1mm$. Furthermore, in the silicon area, a boundary layer mesh was added at the contact with the crucible wall. For this meshing configuration the total number of mesh cells is ≈ 20000 . As it can be observed in Figure 3.12, by using an interface type

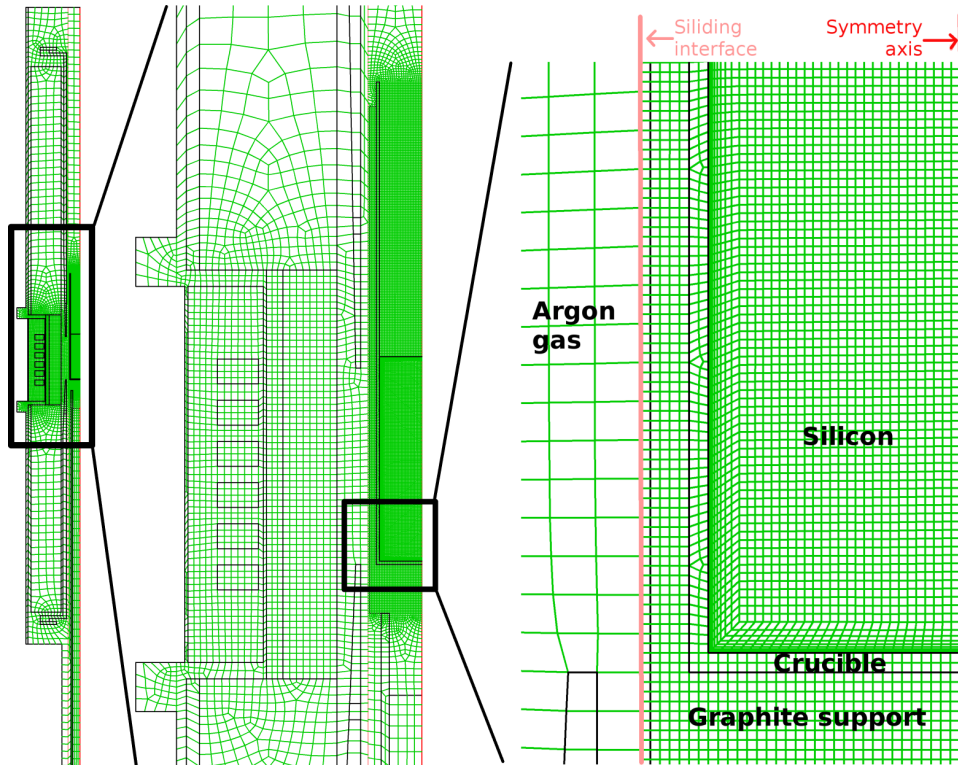


Figure 3.12: Numerical model mesh in different regions of the furnace and crucible. Total number of mesh cells is ≈ 20000 .

boundary (the sliding interface in the figure) the mesh can be different on each side of the interface. Fluent software is able to work with such cases if a coupled condition is set on the interface. These types of interfaces are also surrounding the silicon region when the SIMaP/EPM solidification module is used. In this configuration, the mesh in the solidification region resembles the one presented in Figure 3.4, while the mesh in the rest of the furnace remains unchanged.

3.5 Thermal model validation

The approach for the numerical model validation was a direct comparison with the experimental set-up. In the experiments conducted for this purpose the furnace was heated at high temperatures (similar with solidification experiments), but no crucible and no silicon was used. However, the graphite support was kept in place. The same reference temperature $1623K$ was imposed in both heaters (at positions TcR_{top} and TcR_{bottom} shown in Figure 2.8a). The simulation was conducted in the same conditions as during the experiments, with no crucible and no silicon. The heaters temperature for the simulation

was decreased with $\Delta T = 50K$ compared to the experiment. The ΔT value represents the temperature difference between the real temperature of the resistor and the temperature measured by a C type thermocouple, in a quartz tube near the heater. Other thermocouples were attached to the graphite support at different heights to measure the temperature inside the furnace, between the two heaters. During these experiments, the temperature imposed in the heaters was kept constant for several hours, in order to reproduce the steady state mode computed by the numerical model.

As previously described in section 2.1.1, a monitoring system was developed in order to measure the heat dissipation on external water cooled walls of the furnace. The system mainly consists in J type thermocouples and water flow meters installed at the outputs of the furnace cooling system. The heat dissipated on each part of the furnace (see Figure 3.13b) is estimated by using the water temperature difference between output and input and the flow rate measurements. Additionally to the computed total dissipated power, the electrical power injected in the heaters was available by measurements at the output of the electrical generators.

For the validation experiment, the total electrical power injected into both heaters was measured at $\approx 9.8KW$, while the total dissipated power was measured at $\approx 8.5KW$. The differences between the measured powers can be accounted for by the fact that several aspects have not been considered, like: power losses between the generators outputs and the heaters, as well as heat losses in pipes between the furnace and the measurement points for water flow rate and temperature. The simulation results indicated a total power in the furnace of $\approx 9.1KW$ for the imposed temperature of $1623K - \Delta T$ in each heater element. It can be easily observed that this value approximates the mean of the two previously measured powers. Figure 3.13a presents a comparison of the simulated and experimentally obtained power dissipation on the various regions of the furnace, while the analysed regions are identified on the furnace in Figure 3.13b.

The electrical connections indicated as well in Figure 3.13a refer to the connection parts between the heaters (see Figure 3.10a) and the electrical power supply. They are located at the extremities of the heaters and they are also water cooled.

Using thermocouples attached to the graphite support at different heights, the temperature inside the furnace was measured. The measured temperatures inside the furnace and the simulated temperatures are compared in Figure 3.14.

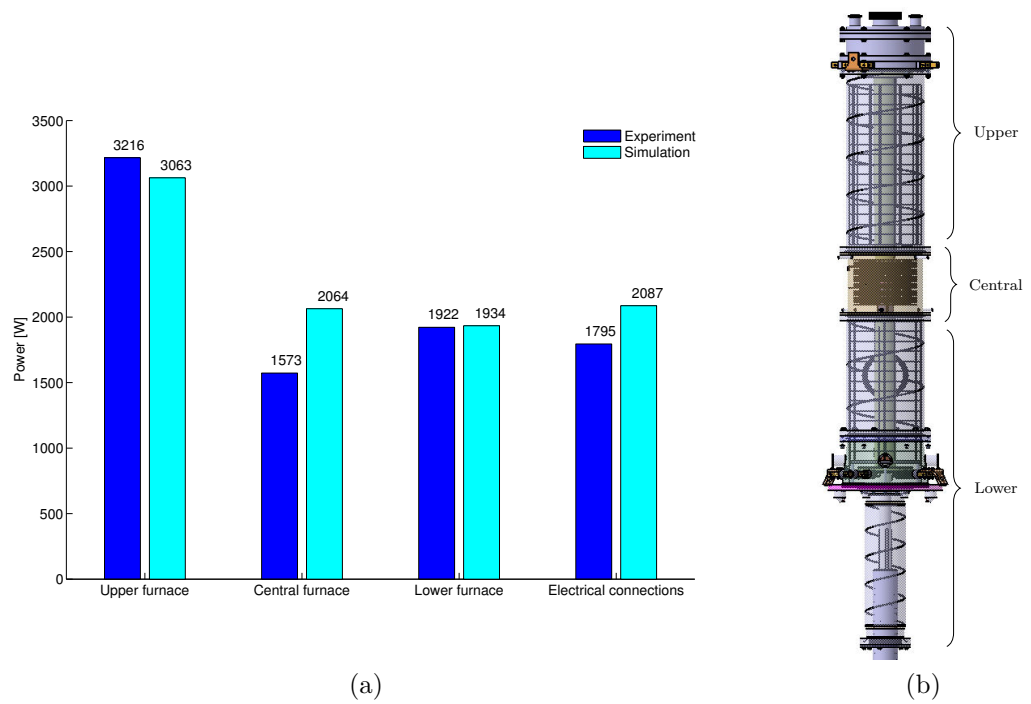


Figure 3.13: Comparison of experimentally measured dissipated powers and simulated ones (3.13a) and the analysed regions of the furnace (3.13b).

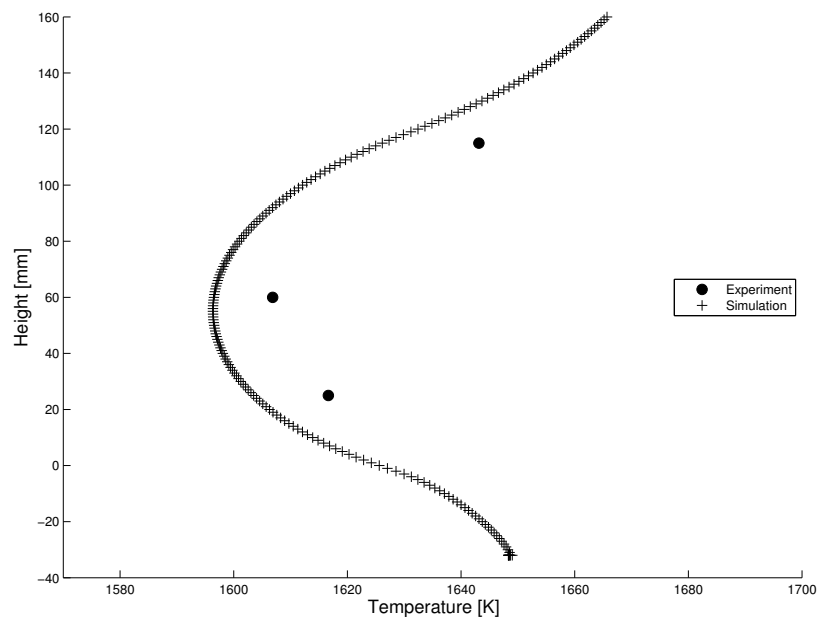


Figure 3.14: Comparison of experimentally measured temperatures and simulated ones on the graphite support wall.

The $0mm$ position corresponds to the upper end of the lower heater while the distance between the heaters is $120mm$. The lower heat source is positioned below $0mm$ while the upper heater is above $120mm$ and consequently the temperature is higher in these regions. Between the heaters a drop in temperature is expected, with the lowest temperature point located at half distance. The temperature difference between experimental and simulated values, at given heights, is $\approx 10K$, while the temperature distribution is similar. With acceptable differences between experimental and simulated temperatures and for the power differences presented in Figure 3.13a, the numerical model is considered to be a close representation of the experimental furnace.

«The great tragedy of science - the slaying of a beautiful hypothesis by an ugly fact.»
— Thomas Huxley

Chapter 4

Interface shape and crystal macro structure

4.1 Objectives and approach

Applied Travelling Magnetic Field (TMF) during the solidification process creates a forced convection in the melt by induced Lorentz forces [30, 37]. The direction of the time averaged force along the vertical axis is imposed by the orientation (upward or downward) of the magnetic field. In a cylindrical crucible surrounded by cylindrical electromagnet windings, the induced force density is axisymmetric. For the magnetic field frequency of $50Hz$ and for the physical properties of liquid silicon, the electromagnetic skin depth was computed at $\delta = 6, 24cm$. This shows how deep the magnetic field penetrates into the liquid silicon. The solid silicon is considered as electrically insulating, leaving it unaffected by the electromagnetic field. For a crucible with a diameter of $\approx 5cm$, the magnetic field can induce Lorentz forces in the melt as far as the center of the ingot. The induced current density, therefore the induced force density is the highest close to the crucible walls and decreases towards the center of the melt. The liquid flow patterns in the molten silicon, generated by the induced force, presents a toroidal shape with a flow direction (close to the crucible walls) imposed by the induced force direction. Figures 4.1b and 4.1c depict in a 2D vertical cut, the flow patterns that could be imposed by a travelling magnetic field, for two different orientations.

The induced flow patterns are decreasing the thermal gradient inside the melt by transporting liquid at high temperature from the top of the bulk towards the solidification interface. The high temperature liquid once in the interface vicinity, creates a partial remelting of the solid. Depending on the

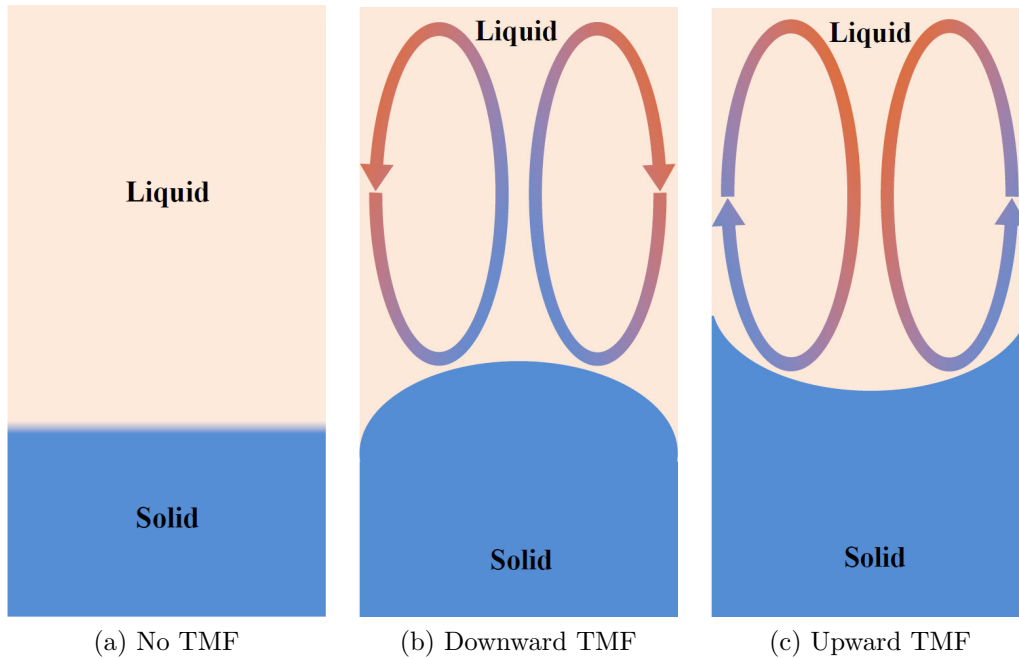


Figure 4.1: Solidification interface shapes and flow patterns during the solidification process for various magnetic field orientations.

liquid flow patterns, the hot liquid can be brought at the solidification interface in the center of the ingot (Upward TMF) or near the crucible walls (Downward TMF). This ultimately changes the solid-liquid interface shape in a concave or a convex one. As seen from the solid, a concave interface is shown in Figure 4.1b, while a convex one is presented in Figure 4.1c. As a consequence, the flow patterns in the melt influence the solid-liquid interface shape [31]. In a directional solidification process where no magnetic field is used, the interface shape should remain flat or present very small deflection (Figure 4.1a) due to radial thermal gradients in the silicon. A radial thermal gradient in the melt creates natural convection coupled to the solidification front deflection [19]. The shape of the interface has an influence over the grains macro-structure of the ingot and also on the impurity distribution along it. For a flat interface, grains that nucleate at the bottom of the crucible are expected to grow vertically towards the top and a columnar structure is to be expected (see Figure 4.2a). However, if the solidification front presents a significant curvature, the grains that nucleate on the crucible walls grow towards the center of the ingot, being in competition with the one nucleated at the bottom of the crucible. In this case, the resulting structure presents what will be further referred to as elongated grains (see Figure 4.2b).

Generally in the photovoltaic industry, a columnar structure of the grains is

preferred over the elongated one. The crystal structure with elongated grains presents a reduced average grain size compared to the columnar structure, therefore the grain boundaries density is increased. The grain boundaries can act as defects in the crystal and if solar cells are to be made using such materials, the cell efficiency will decrease. By inducing a forced convection in the melt the impurity chemical segregation process is improved (see Chapter 5) but the interface shape and the grain macro-structure changes. One possible approach to reduce the influence of the forced convection over the solidification front shape is to alternate the magnetic field orientation during the solidification. A periodic change of the TMF orientation periodically changes the flow orientation inside the melt. This flow changes should have an equal impact over the solidification front remelting in the center of the crucible as well as close to the crucible walls. The solid-liquid interface shape in this case is expected to be similar to the one where no magnetic field is used. This procedure where the travelling magnetic field orientation is periodically interchanged will be further on referred to as *Alternating TMF*.

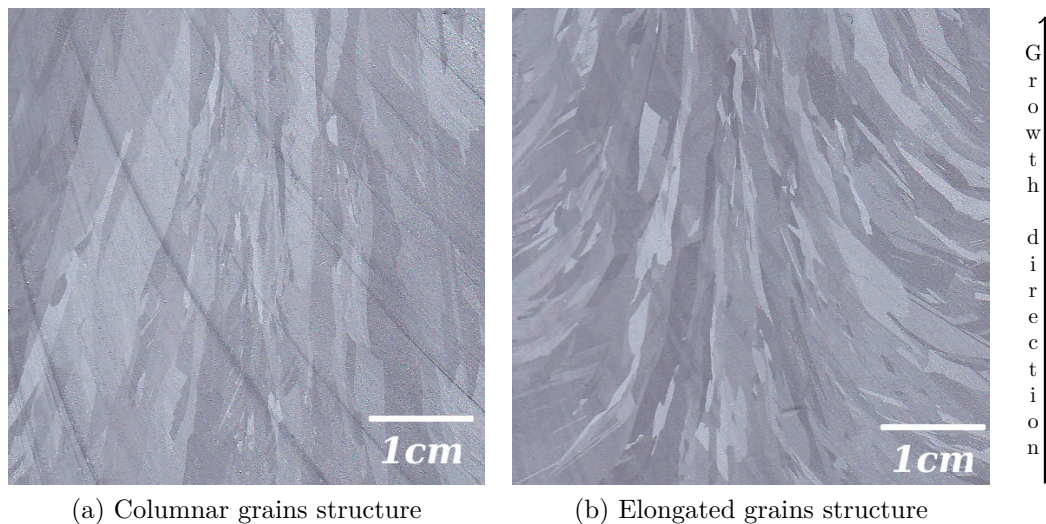


Figure 4.2: Grain structures obtained in experiment set I.

4.2 Experimental and numerical results

4.2.1 Solidification interface shape during the solidification process

A series of three experiments was conducted in order to observe the TMF influence on the S-L interface morphology and metallic impurities segregation along the height of the ingot. In this chapter only the results related to the interface shape for these experiments are presented. The results regarding the impurities segregation for these experiments are presented in Chapter 5. A vertical thermal gradient was created in the ingot by the two resistors heated at different temperatures. In order to obtain a controlled directional solidification (from the bottom to the top of the ingot), a constant cooling rate of $36K/h$ was imposed to the heating elements for all performed experiments. When travelling magnetic field was used, the imposed magnitude of the magnetic field was $4mT$ but the induced forces had a different orientation for each one of them. Table 4.1 presents all the main conditions of these experiments.

Table 4.1: Experiment set I

Experiment number	Raw material	Imposed ΔT	Cooling rate $[K/h]$	TMF Intensity $[mT]$	TMF orientation
I.1	Si-A	150	36	0	-
I.2	Si-A	150	36	4	Upward
I.3	Si-A	150	36	4	Downward
I.4	Si-A	150	36	4	Alternating

As presented in Table 4.1, for all experiments the same temperature difference $\Delta T = 150K$ was imposed between the heaters. The same raw material (*Si - A*) was used as well, for all experiments in this set. Details about the impurities levels for the used silicon can be fined in Chapter 2 Section 2.2 Table 2.1. For Experiment I.1 no travelling magnetic fields was used. This experiment was performed in order to obtain different references, like the interface shape, which are to be compared to the results obtained from the other experiments in this set. For Experiment I.2 the travelling magnetic field configuration had an upward orientation and induced Lorentz forces oriented upwards in the liquid silicon near the crucible. In Experiment I.3 the travelling magnetic field orientation was oriented downwards but the intensity was similar to the previous experiment. During experiment I.4 the orientation of

the TMF was alternated by interchanging two of the three phases that supply the electromagnet. TMF orientation was changed with a period of $t = 30s$.

Further on the obtained results for these experiments are analysed considering several aspects like the velocity in the liquid, flow patterns, solid-liquid interface and grain structure. This analysis takes into account the results from both numerical simulations and experiments. For the results presented in this section, numerical simulations in transient mode were conducted using the numerical model described in Chapter 3. In order to compute the solidification interface the *Solidification and Melting* module proposed by Fluent (Section 3.2.3) was used.

For a magnitude of the magnetic field of $4mT$, the induced Lorentz force density is computed (using *EPM Induction* module for Fluent) at around $60N/m^3$, at the beginning of solidification when only liquid silicon was present in the crucible. These forces are increasing the liquid velocity up to $\approx 3.5 \cdot 10^{-2}m/s$. The flow patterns present a toroidal vortex with the rotation direction related to the TMF orientation and they are capable of considerably decreasing the thermal gradient in the melt. A toroidal vortex is presented as two symmetrical vortices on a vertical cross-section of the ingot for 2D axisymmetric simulations, as seen in Figures 4.3 to 4.6.

In the first experiment the velocity in the liquid is driven by buoyancy forces and no forced convection is applied and as a result the maximum velocity in the liquid has an order of magnitude of $10^{-3}m/s$. Figure 4.3 presents the numerical results of flow patterns and the distribution of the liquid velocity during the solidification process for this experiment. It can be observed that the computed maximum velocity in the liquid is located into the vortex created above the solid.

For the second experiment, after a first layer of solid appears close to the crucible wall, the Lorentz forces induced in the liquid decrease from $60N/m^3$ to around $40N/m^3$. Figure 4.4 describes the flow patterns created in the melt and the velocity achieved in the liquid for the Experiment I.2. As it can be observed, the maximum velocity reaches about $2.5 \cdot 10^{-2}m/s$ at the centre of the ingot. At $t_1 + 0.5h$ (Figure 4.4), the solid-liquid interface presents an extremely convex shape (seen from the solid) and this is mainly due to the hot liquid brought from the top of the ingot to the centre of the solidification front. The heat loss towards the lateral thermal insulation around the crucible adds to this curvature effect of the solidification interface. It has been shown [19] that the solid-liquid interface curvature increases with higher lateral thermal

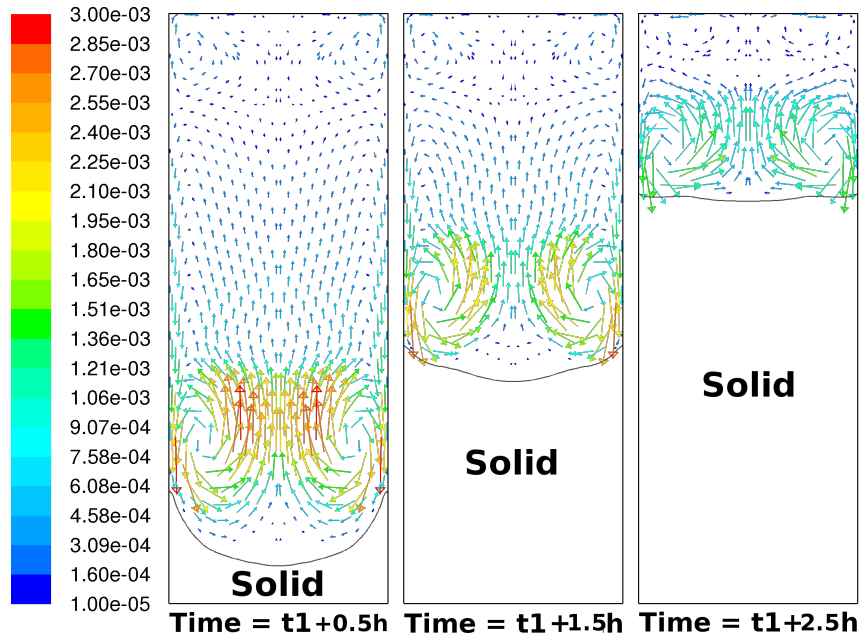


Figure 4.3: Experiment I.1. Numerical results of liquid velocity distribution on vertical cross-section expressed in m/s, at different instants during the solidification process. Ingots are 2 inches in diameter. At t_1 the solidification process began.

conductivity of the side insulation. Further on, the solidification front advances from the bottom to the top of the ingot and remains convex during the whole solidification process. Nonetheless the interface curvature decreases towards the end of the solidification.

A slow decrease of the liquid velocity can be observed with time for this experiment, as well as for all the others where magnetic field is used. Towards the end of the solidification process, the induced forces decrease in the remaining liquid volume, which results in lower liquid velocities and less efficient stirring of the melt. This phenomena is revealed by the simulations in which the crucible position is kept constant (similar position of the crucible as indicated in Figure 2.8a) and a cooling rate is imposed into the heaters. In this configuration, the liquid volume towards the end of the solidification is at the upper end of the physical geometry of the electromagnet. The solidification interface curvature is reduced towards the end of the solidification, as a result of the decreased velocity of the liquid.

For Experiment I.3 the flow patterns (Figure 4.5) are reversed and the liquid from the top is brought to the side of the interface, close to the crucible wall. This is due to downward oriented Lorentz forces. The liquid velocity reaches a maximum value of $3.4 \cdot 10^{-2} m/s$ at the centre of the ingot. The solid-liquid

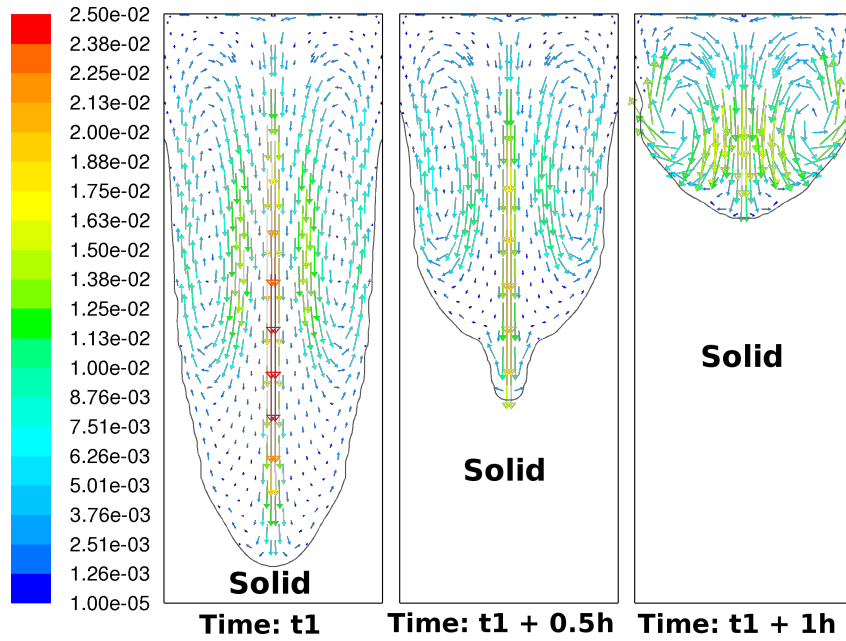


Figure 4.4: Experiment I.2. Numerical results of liquid velocity distribution on vertical cross-section expressed in m/s, at different instants during the solidification process. Ingots are 2 inches in diameter.

interface presents a concave shape in the middle part. The influence of the heat loss towards the lateral thermal insulation is reflected in the exterior part of the interface. Compared to Experiment I.2, the interface shape presents

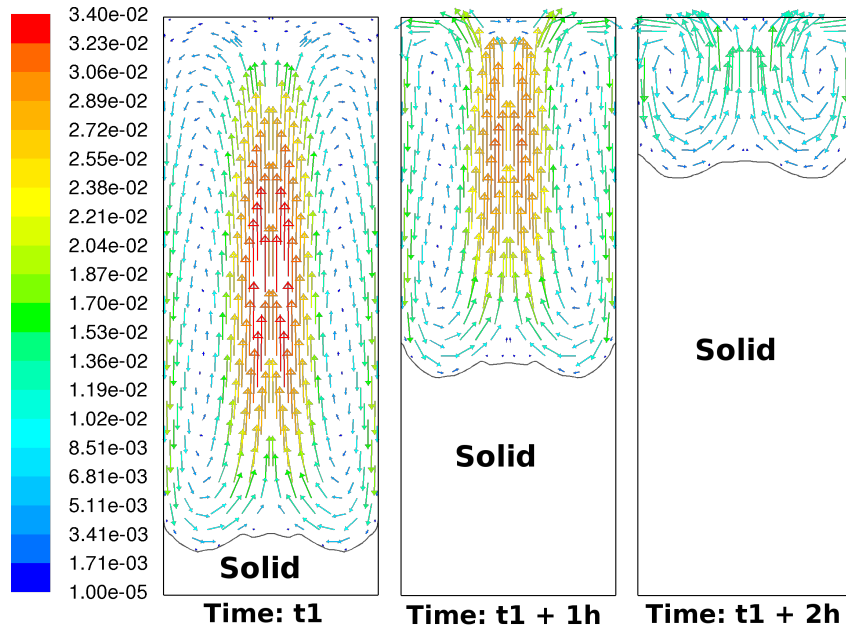


Figure 4.5: Experiment I.3. Numerical results of liquid velocity distribution on vertical cross-section expressed in m/s, at different instants during the solidification process. Ingots are 2 inches in diameter.

very small variations during the solidification process.

For the last experiment (I.4) in this set, the magnetic force orientation was alternated each 30s. Considering that it takes about 15s to obtain a stable flow inside the melt (according to the numerical simulation), a time period of 30 seconds between magnetic force direction changes was chosen. As a result of the relatively short period for each TMF orientation, the interface shape should present weak deformations. The general interface shape evolution during the complete solidification process should not be affected by the stirring. Reversing the direction of the induced forces creates a shift of 180° in the vortices rotation direction for each time period. The liquid velocity (Figure 4.6) reaches a maximum of $3.3 \cdot 10^{-2} m/s$ for both the periods of upward and downward induced forces. The solid-liquid interface shape is convex (seen from the solid) with a curvature of about $20mm$ at t_1 (Figure 4.6) and gradually decreases towards the end of the solidification process. For this experiment the interface shape in the middle of the ingot is almost flat.

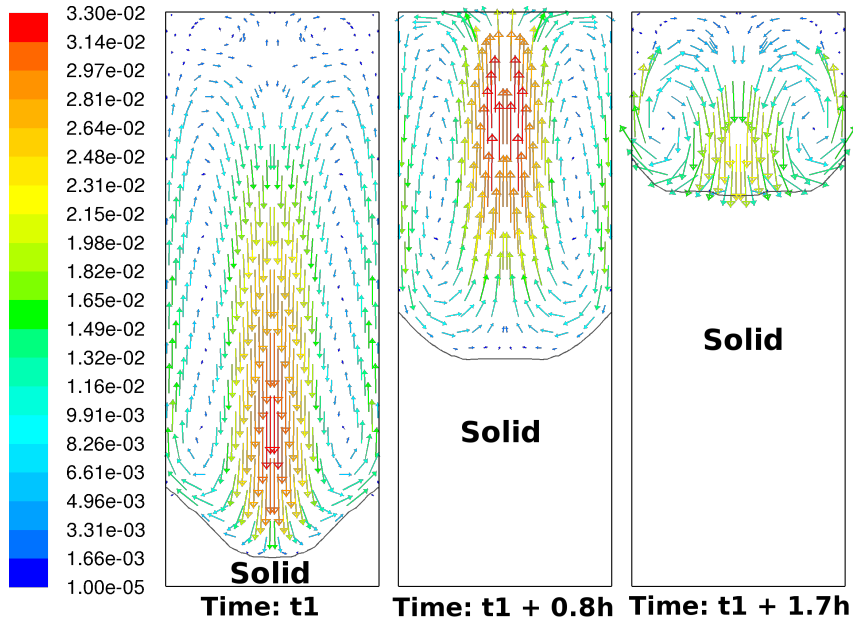


Figure 4.6: Experiment I.4. Numerical results of liquid velocity distribution on vertical cross-section expressed in m/s, at different instants during the solidification process. Ingots are 2 inches in diameter.

Figure 4.7 presents the grain macro-structure on vertical slices for all the performed experiments. The computed solidification front at different instants in time is superimposed on the images with the grains structure. The solid-liquid interface shapes and positions were recovered from the numerical simulations. The grain structure for these experiments seems to be influenced by

the solidification front shape. Especially for the experiments I.2 and I.4, a tendency of the grains to grow perpendicularly to the computed interface can be observed.

In Experiment I.1, according to numerical results, a higher radial thermal gradient was present in the ingot at instant $t1 + 1h$ than at $t1 + 3h$ (see Figure 4.7a). As a result, the S-L interface has a convex shape with a deflection of approximately $15mm$ in the first instants of solidification ($t1 + 1h$). Later during the solidification, the solid-liquid interface curvature decreases towards the end of the solidification. The main reason for this behaviour is the heat loss towards the lateral thermal insulation. The impact of lateral thermal conductivity of the side insulation on the solid-liquid interface shape is discussed in [19].

The grain macro-structure for the Experiment I.3 shows that inside the melt, the two vortices were not equal in size, probably because of non-uniformly distributed Lorentz forces around the crucible. This is a first indication of a possible experimental non-axisymmetric flow in the melt. As a result, in this experiment the grains generated at the left side and the grains generated at the right side of the ingot are not intersecting each other in the center of the ingot. A study of grains crystallographic orientations and grain boundaries

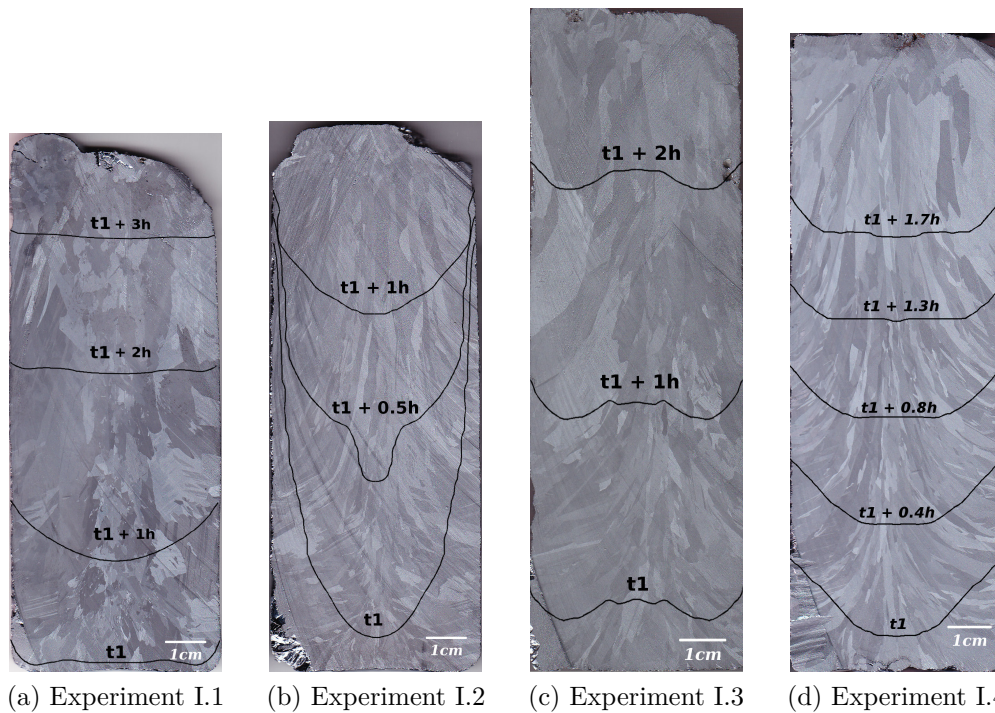


Figure 4.7: Grain macro-structure on vertical slices and computed solid-liquid interface shapes and positions during the solidification process

angles along the interfaces should be conducted in order to offer more precise information regarding the impact of interface shape on the grain structure.

Having the solidification front position and the solid fraction at different moments in time for each experiment, an average growth rate can be computed for each experiment. Experiment I.2 presented the fastest growth velocity at $\sim 16 \cdot 10^{-6} m/s$. In the case of the Experiment I.3, the computed growth rate ($\sim 12 \cdot 10^{-6} m/s$) was about 25% smaller compared to the second experiment. For the last experiment an average growth velocity was computed at $\sim 14 \cdot 10^{-6} m/s$ which represents an average growth rate of the two previous experiments. In the case of the second experiment a considerable difference could be observed regarding the growth rate at the centre of the ingot and near the edges, while the third experiment does not show the same behaviour. For Experiment I.4 the flatter part of the interface in the ingot centre becomes larger toward the end of the ingot and advances faster than the external part.

4.2.2 Interface marking by Peltier effect

For the experiments presented in Section 4.2.1, the solidification interface was computed using the Fluent solidification module. In this section an experiment with interface marking by Peltier effect was conducted. The aim was to experimentally obtain the solidification front shape. The method, graphically represented in Figure 4.8, involves injecting a direct current in the sample during the crystallization process. In the experimental procedure a power supply was needed to inject the electrical current during the solidification process. The electrical resistance in the circuit had to be decreased to a minimum value in order to obtain a high value for the electrical current in the sample. Therefore the electrical connections between silicon bulk and the graphite components of the electrical circuit had to be designed. From the top a mobile graphite rod was introduced in the melted silicon only when the markings were performed and removed immediately after. This action was necessary in order to avoid a further contamination with carbon of the silicon melt and to avoid the rod being trapped in the solid silicon at the end of the process. Moreover, the fused silica crucible has a significant electrical resistance compared to the silicon or graphite. In order to decrease the resistance, a contact had to be made directly between the silicon and the graphite support. This was achieved in the experiment by creating an electrical connection between the silicon and the graphite support through the bottom part of the crucible.

When the current passes through the crystal, thermal phenomena depend

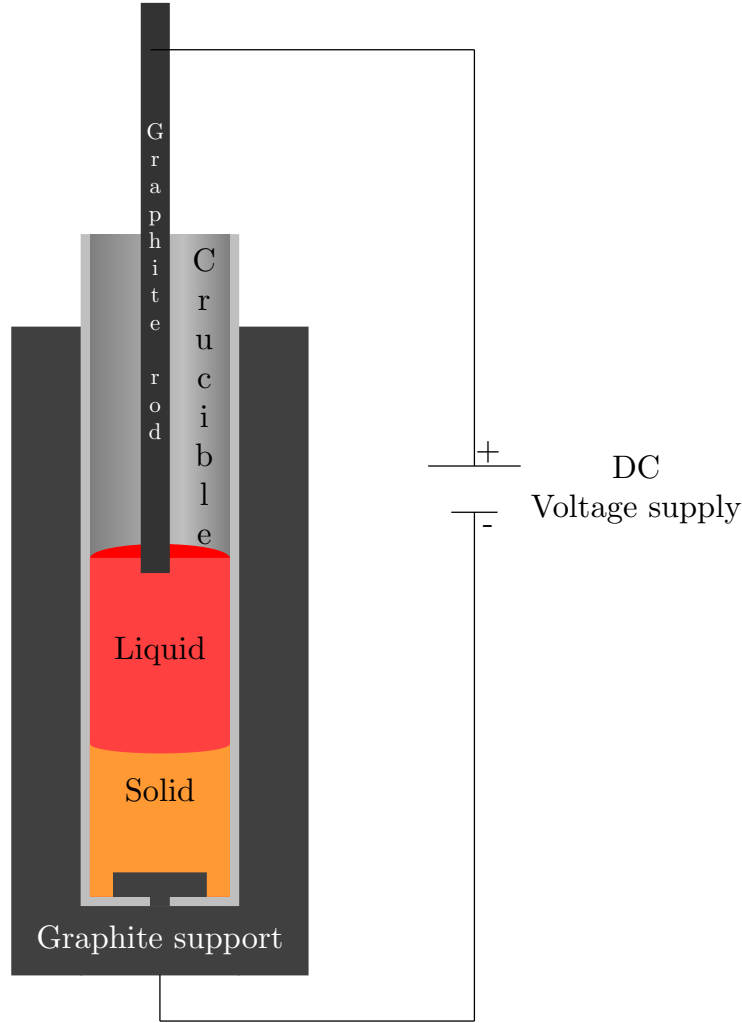


Figure 4.8: Principle of interface marking with Peltier effect.

on source terms due to the Thomson effect (Equation 4.1), the Joule effect (Equation 4.2) and the Peltier effect (Equation 4.3). As a result of those effects, a fast temperature variation at the solidification interface appears. This leads to a fast variation in the position of the solidification front. The direction of the current is important in this case. Indeed, the Peltier and Thomson effects are proportional to the current density and depend on the sign (direction) of current density, whereas the Joule heating effect only depends on the square of the current intensity [45]. For the Thomson effect, the generated heat sign also depends on the sign of the axial thermal gradient.

Thomson source term:

$$q = \mu J \frac{\partial T}{\partial x} \quad (4.1)$$

where q represents the generated heat, J is the electric current density, μ is the Thomson coefficient and $\frac{\partial T}{\partial x}$ is the temperature gradient.

Joule power density:

$$q = \rho J^2 \quad (4.2)$$

where ρ is the resistivity of the material.

Peltier source term:

$$q = \Pi J \quad (4.3)$$

where Π is the Peltier coefficient.

The temperature variation at the solidification interface depends on the current direction through the interface surface. This could lead either to a fast temporary solidification when the interface will advance into the liquid, or to a partial remelting. This fast variation of the temperature changes the growth rate of the crystal, causes micro segregations, and may also locally modify the structure of the crystal [45]. Those differences in the crystal structure and the different doping concentrations at the interface allow the marking by this method. In order for these marks to become visible, additional post processing is required once the solidification process ends. After a vertical cut of the ingot the crystal surface must be polished and submitted to a chemical etching process. During the chemical etching of the crystal surface, the local variation in the dopant levels and the changes in the crystal structure are revealed.

An experiment was conducted in order to mark the solidification interface by using Peltier effect. Since the electric current density J is a very important parameter, a crucible with a reduced diameter was used, in order to increase J for a fixed electrical current at the DC supply output. The ingot diameter for this experiment was 3.3cm , whereas for all other experiments the crucible had an internal diameter of $\approx 5\text{cm}$. The electrical current injected in the ingot was $\approx 75\text{A}$ which resulted in a mean value for the current density of $\approx 0.09\text{A}/\text{mm}^2$. Table 4.2 presents other important information regarding the experimental conditions as the type of raw material used, ΔT and pulling velocity. The raw material was chosen such that the $\approx 600\text{ppm}$ of aluminium contained as impurities are acting as dopant in this experiment. Details about the others impurities levels for the used silicon can be fined in Chapter 2 Section 2.2 Table 2.1. For this experiment the thermal gradient in the silicon was generated by imposing a temperature difference ΔT in the heaters. The heaters temperature was kept constant and no cooling rate was imposed. Instead, the crucible was moved downward at a constant pulling velocity of $10^{-6}\text{m}/\text{s}$.

The solidification interface was successfully marked several times during

Table 4.2: Experiment where Peltier effect was used for solid-liquid interface marking.

Experiment number	Raw material	Imposed ΔT	Pulling velocity [m/s]	TMF intensity [mT]	Current density [A/mm ²]
P.1	Si-B	330	10 ⁻⁶	0	0.09

this experiment and was revealed by chemical etching. One of these marks, is presented in Figure 4.9a. The image was created by stitching multiple pictures obtained with an optic microscope. The growth direction is from the bottom towards the top of the ingot. Figure 4.9b presents the same image with the same marked interface emphasized with white color. The missing emphasized interface on the right side of the picture in Figure 4.9b is the first indication of the drawbacks for these method. Although this solidification interface marking method offered some interesting results, none of the marks are clear along the whole width of the ingot. On the right side of this picture the mark become less and less visible until disappears. Another observed fact is the thickness of the mark which is of a few hundreds μm .

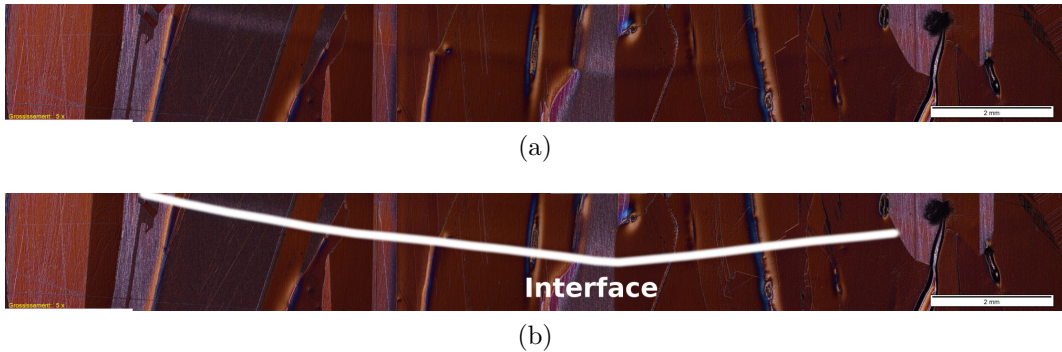


Figure 4.9: Interface marked using Peltier effect (4.9a) and emphasized interface (4.9b). The scale presented on the image is 2mm.

As a conclusion, the Peltier method can be successfully used to perform solid-liquid interface markings but some aspects must be taken into consideration. The electrical current density used, must be adjusted to the crystal surface and this can quickly lead to the need of a huge power supply. Moreover, the dopant could play an important role in this process. So far in this study only aluminium was used as dopant and other elements must be further investigated. In this experiment the interface was not marked in the crucible walls vicinity but the shape in the central region of the ingot was successfully recovered.

4.2.3 Interface marking by TMF effect

In this section another method for marking the solidification front is presented. The approach aims at obtaining the same effect as Peltier method, meaning to produce thermal variations at the interface for short periods of time. The consequences should be similar as in the case of the previous method: local changes in the crystal structure and variations in the dopant/impurities concentration. Following the same post processing steps, cutting the ingot, polishing the surface and finishing by a chemical etch, the marked interfaces should also become visible.

In order to obtain temperature variations in the solidification front vicinity, the forced convection induced by the magnetic field can be used. During the solidification process where no magnetic field is used, by turning on the magnetic field for short periods of time, hot liquid from the top of the melt is brought to the interface. This produces a partial remelting of the solid upper layer. Once the magnetic field is turned off again, the vertical thermal gradient increases in the liquid and the solidification front is cooled down at the previous temperature. The reverse but comparable method is applied when the TMF is switched off for a short period during experiments where the magnetic field is normally turned on.

In order to test the interface marking procedure using TMF, another set of experiments (Table 4.3) was conceived. The set was designed similar to the experiments presented in Section 4.2.1 regarding the silicon type, TMF orientations and intensities. The crucibles used in these experiments have an internal diameter of $\approx 5\text{cm}$. However, an important difference is that for these experiments (Set III) the temperature field remains unchanged during the solidification process and the crucible is pulled down at a precise pulling velocity. This pulling velocity in the case of experiments III was set constant at $4 \cdot 10^{-6}\text{m/s}$. A lower ΔT was imposed in the experiments with TMF than

Table 4.3: Experiment set III

Experiment number	Raw material	Imposed ΔT	Pulling velocity [m/s]	TMF intensity [mT]	TMF orientation
III.1	Si-A	400	$4 \cdot 10^{-6}$	0	-
III.2	Si-A	350	$4 \cdot 10^{-6}$	4	Downward
III.3	Si-A	350	$4 \cdot 10^{-6}$	4	Upward
III.4	Si-A	350	$4 \cdot 10^{-6}$	4	Alternating

in the one without TMF, by reducing the temperature imposed in the upper heater. The reason for this is to retrieve a comparable experiment duration despite the fact that the forced convection tends to homogenize the liquid temperature. In other words, if the liquid is overheated, the crucible pulling takes longer to solidify the silicon inside.

In all experiments an upgraded metallurgical grade silicon was used. In addition to the performed experiments, numerical simulations were conducted. For all experiments the solid-liquid interface was marked several times and compared with the computed shapes.

The grain macro-structure on vertical cross sections for the performed experiments is presented in Figure 4.10. The lightened pictures embedded in each photo are microscopic close-ups on one of the interface markings. In the case of Experiment 1 (without TMF), the magnetic field was turned on for 60s at 2 hours time interval. For the other experiments (with TMF) the process was inverted and the magnetic field was turned off for 60s at 2 hours time interval.

In order to capture the interface on all the ingot width, a panorama image was constructed by stitching multiple small scale images obtained with an

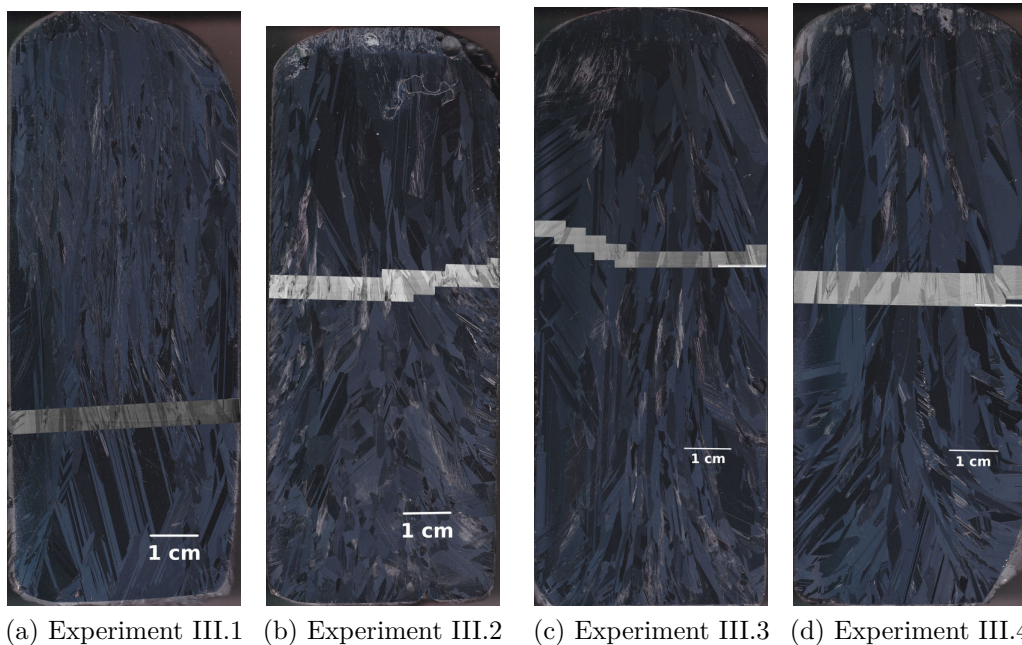
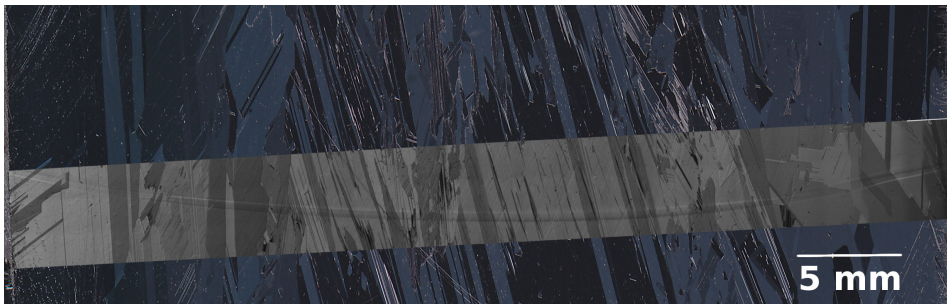


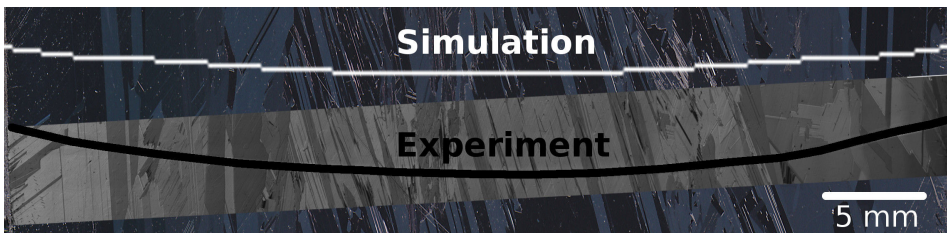
Figure 4.10: Grains macro-structure on vertical slices of the obtained ingots for: Experiment III.1 (without TMF), Experiment III.2 ($4mT$ downward oriented TMF), Experiment III.3 ($4mT$ upward oriented TMF) and Experiment III.4 ($4mT$ alternated orientation of TMF).

optical microscope. This was later overlaid on a scanned image of the ingot in order to present its position in the resulting ingot.

Figure 4.11a presents a close-up of a marked interface in the Experiment III.1. The marking thickness is $\approx 300\mu m$. The interface curvature was estimated at less than $3mm$ in this case. In Figure 4.11b the experimental interface is emphasised (black) and the computed interface (white) was added. At the same instant when the interface was marked experimentally, the numerical model computed an interface position only $5mm$ above. The experimental and computed interfaces basically have the same shape.



(a) Close-up interface image



(b) Simulation interface and emphasised experimental interface

Figure 4.11: Experiment III.1 macro-structure on vertical slice and marked interface (4.11a). Comparison between experimental and simulation results (4.11b) at the same instant during the solidification process.

For this first experiment, the solidification interface was marked 4 times and the numerical results showed that the computed interface was shifted with less than $5mm$ for each one of the markings. This result proves a good correlation between experimental set-up and numerical model. For a pulling velocity of $4 \cdot 10^{-6}m/s$, the computed growth rate and the experimentally measured one were at $\approx 5 \cdot 10^{-6}m/s$.

Figure 4.12a presents the computed temperature distribution inside the silicon melt at the moment of marking the interface presented in Figure 4.11. The temperature at the top of the liquid is $\approx 40K$ above the melting temperature and a vertical thermal gradient of about $500K/m$ is present in the melt. The negligible value of the horizontal thermal gradient leads to a moderate natural

convection. The velocity vectors in the liquid are depicted in Figure 4.12b on a vertical cross section. A toroidal vortex appear close to the interface and another one close to the liquid surface rotating in an opposite direction compared to the one from the bottom. The toroidal vortex in the upper part of the liquid is the result of the top heater surrounding and heating the upper part of the crucible. Close to the solidification interface the maximum computed liquid velocity is about $10^{-3}m/s$.

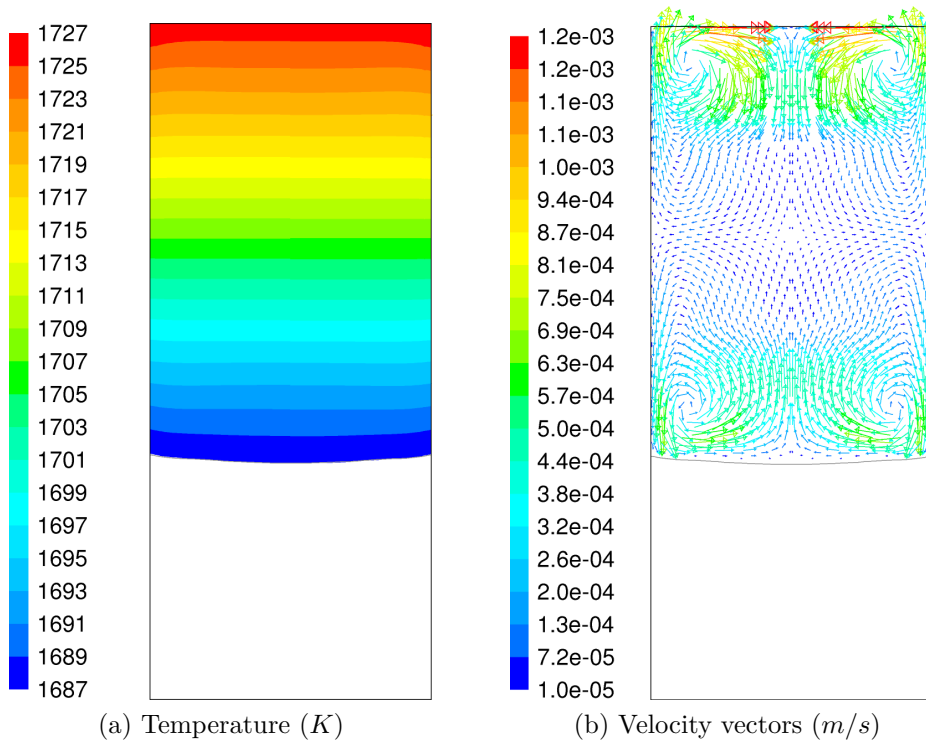


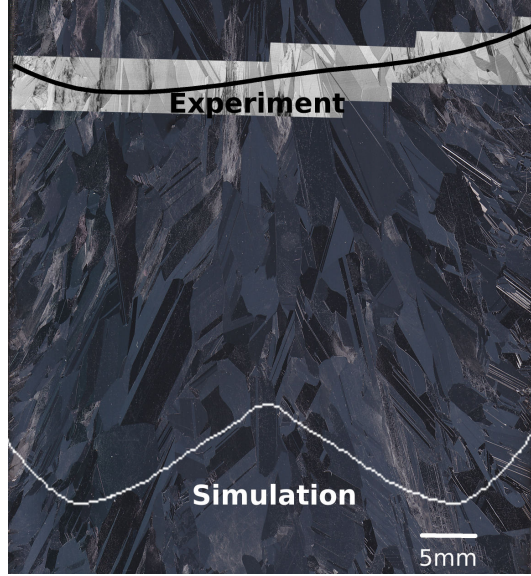
Figure 4.12: Experiment III.1; Temperature field (4.12a) and liquid velocity (4.12b) in the silicon melt.

Experiment III.2 was conducted in similar experimental conditions as Experiment III.1, with the major difference being the applied magnetic field. For this experiment a $4mT$ downward oriented TMF was used during the solidification. As in the above experiment, the solidification front was marked several times. Figure 4.13a presents an image with one of the marked interfaces during this experiment. A second simulation that corresponds to Experiment III.2 was also performed and a comparison of experimental and numerical results regarding the interface shape and position at the same time is presented in (Figure 4.13b).

Both numerical and experimental interfaces are presented at the same time during the solidification process. The model suggested that the interface was



(a) Close-up interface image



(b) Simulation interface and emphasised experimental interface

Figure 4.13: Experiment III.2 macro-structure on vertical slice and marked interface (4.13a). Comparison between experimental and simulation results (4.13b) at the same instant during the solidification process.

$\approx 35mm$ below the real position at the exact same instant. The experimentally observed interface displays a curvature of $\approx 5mm$ and a non-axisymmetric shape that suggests non-axisymmetric flow patterns in the melt. For the same pulling velocity as in the previous experiment ($4 \cdot 10^{-6}m/s$), the experimentally observed growth rate was $6 \cdot 10^{-6}m/s$. The numerical model computed the same crystal growth rate as in the experiment ($6 \cdot 10^{-6}m/s$).

Due to the high liquid velocity ($\approx 3 \cdot 10^{-2}m/s$) induced by the TMF, the computed thermal gradient in the melt near the solidification interface is reduced almost 10 times compared to Experiment III.1. The computed thermal field in the liquid for this experiment is depicted in Figure 4.14a. The highest temperature in the liquid is computed at the top of the melt near the crucible and is just $\approx 3K$ above the melting temperature. The computed velocity vec-

tors which describe the liquid flow patterns induced by the magnetic field are presented in Figure 4.14b. As a result, the liquid temperature becomes very sensitive to the temperature imposed in the heater elements. Slight variations in the imposed temperatures will have an increased impact on the computed position of the interface. Therefore, differences of just a few degrees between the real temperatures of the heaters, during the experiment, and the imposed temperatures in the simulation can result in a significant error in the computation of the interface position.

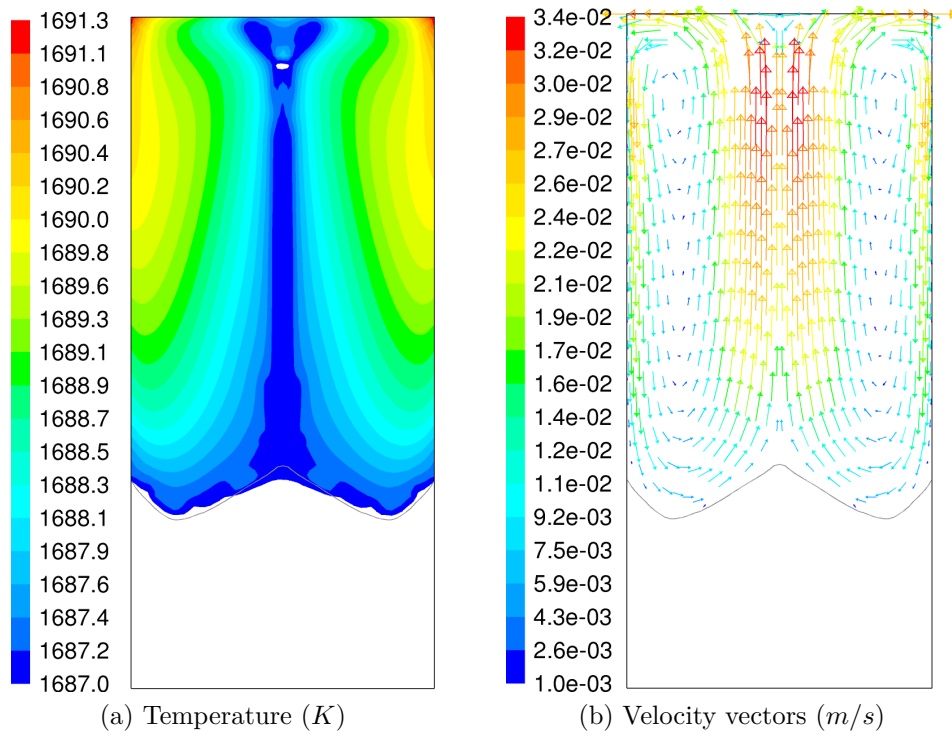
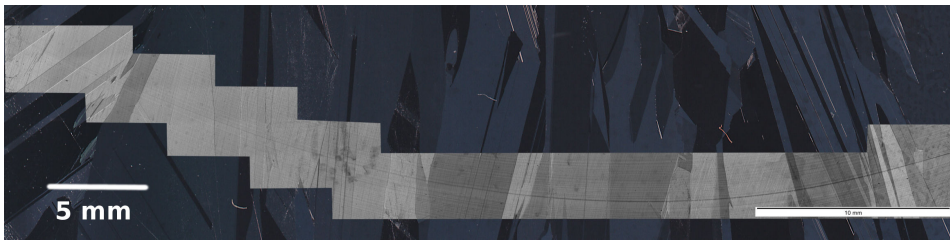


Figure 4.14: Experiment III.2; Temperature field (4.14a) and liquid velocity (4.14b) in the silicon melt.

The numerical model can only describe an axisymmetric flow, therefore only an axisymmetric interface shape can be computed. The central peak presented by the simulated interface is due to an upward flow in the center of the ingot, according to numerical simulation. The non-axisymmetric experimental interface (Figure 4.13) indicates non-axisymmetric flow patterns in the melt during the experiment. This asymmetry of the experimental solidification front can be also observed for the following experiments.

The third experiment was carried out with the same conditions as Experiment III.2, the only difference being the orientation of the TMF. This time the TMF was upward oriented. As for the previous experiments, the interface

was marked multiple times and Figure 4.15a presents an image with one of the marked interfaces during Experiment III.3. Experimental and numerical results regarding the interface shape and position are different (Figure 4.15b). As it can be observed, the experimental interface still presents a non-axisymmetric shape and a deflection of $\approx 8\text{mm}$. In this case the model computed the position of the interface even further down compared to the previous experiments, at $\approx 50\text{mm}$ below the position found in the experimental ingot. For this scenario the computed interface has a different shape compared to Experiment III.2. The hot liquid from the melt top is brought by the liquid flow in the center of



(a) Close-up interface image



(b) Simulation interface and emphasised experimental interface

Figure 4.15: Experiment III.3 macro-structure on vertical slice and marked interface (4.15a). Comparison between experimental and simulation results (4.15b) at the same instant during the solidification process.

the ingot and creates a convex shape of the solidification front. As in the case of Experiment III.2, the experimental interface asymmetry cannot be reproduced by the numerical simulation with a 2D axis symmetric geometry. The crystal growth velocity for this experiment was also computed at $6 \cdot 10^{-6} m/s$.

Figure 4.16a depicts the computed temperature in the molten silicon for the Experiment III.3. The thermal gradient is close to zero and the melt temperature is uniform around the melting temperature $1687K$. The velocity vectors (Figure 4.16b) indicate a reversed flow compared to the one in Experiment III.2, which is to be expected for an upward oriented TMF. The maximum computed liquid velocity is $\approx 3.2 \cdot 10^{-2} m/s$ in the center of the crucible.

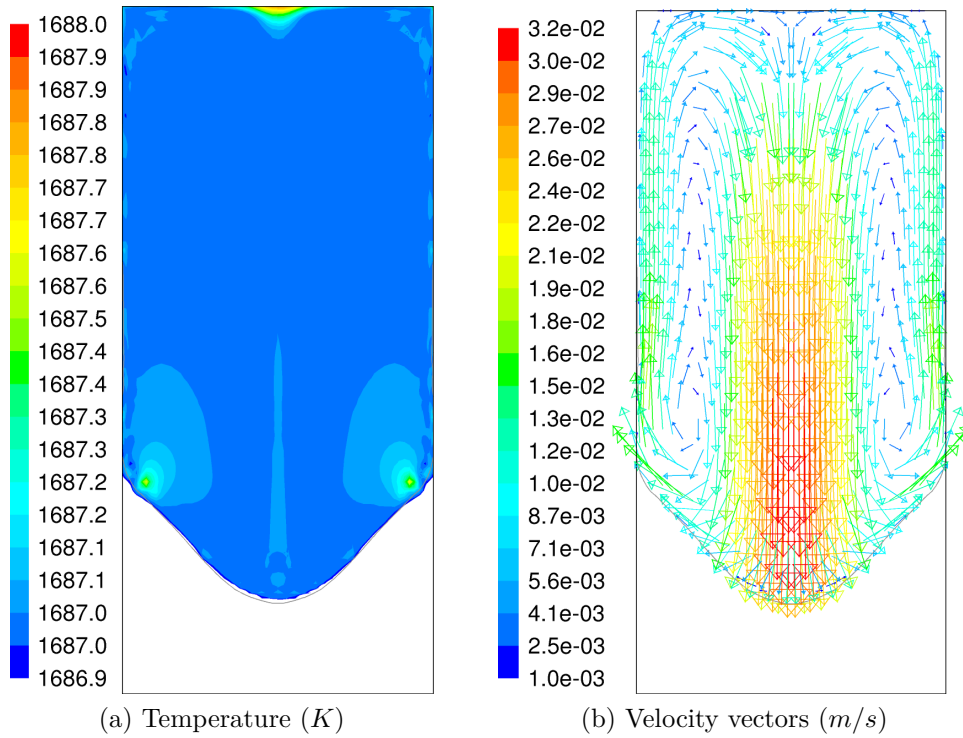
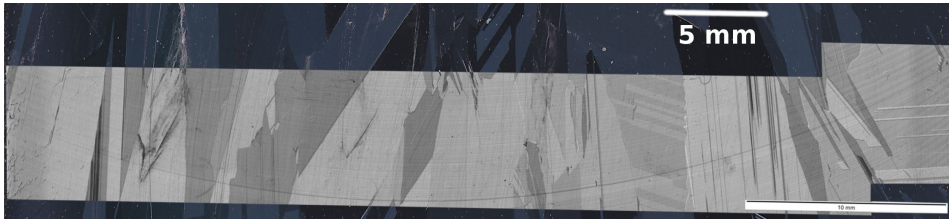


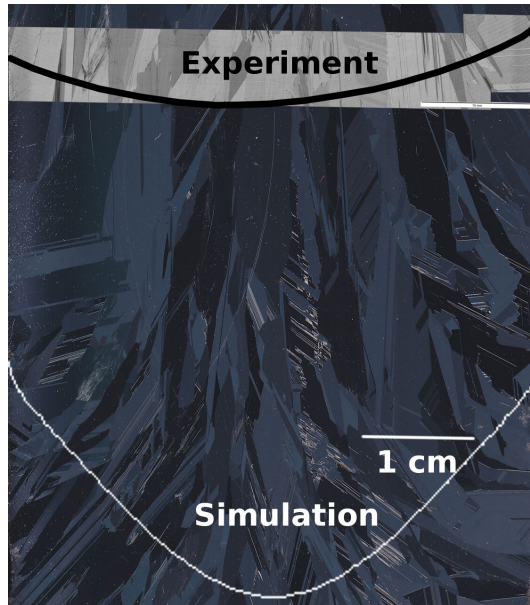
Figure 4.16: Experiment III.3; Temperature field (4.16a) and liquid velocity (4.16b) in the silicon melt.

Interfaces observed in Experiment III.2 and III.3 presented different non-axisymmetric shapes. Therefore, Experiment III.4 aimed to verify if an axisymmetric shape can be re-established by alternating the TMF orientation during the solidification process. The same intensity of the magnetic field was used for both orientations as in the previous experiments ($\approx 4mT$). The orientation was changed every $30s$.

Figure 4.17a presents an image with one of the marked interfaces during Experiment III.4. The interface deflection is $\approx 7mm$ and the growth velocity was



(a) Close-up interface image



(b) Simulation interface and emphasised experimental interface

Figure 4.17: Experiment III.4 macro-structure on vertical slice and interface at a precise moment (4.17a). Comparison between experimental and simulation results (4.17b) at the same time during the solidification process.

computed at $6 \cdot 10^{-6} m/s$. A comparison of experimental and numerical results regarding the interface shape and position is presented in Figure 4.17b. The computed position of the interface is $\approx 40mm$ below the observed one. The experimental interface still presents a non-axisymmetric shape. Nonetheless the experimental observations for this particular experiment indicate that by alternating the TMF orientation, the non-axisymmetric shape of the interface can be slightly reduced.

The computed solidification front for Experiment III.4 has a pronounced convex shape with a deflection comparable with the one obtained in Experiment III.3. This result lead to the observation that the fluid flow created with an upward TMF is more efficient in reshaping the solidification interface than the one generated by a downward TMF. The 30s time period, for each TMF orientation used for this experiment, is long enough to create flow patterns in

the melt similar to the ones computed for experiments III.2 and III.3 (Figures 4.14b and 4.16b). The temperature profile in the melt resembles as well with the ones presented in Figures 4.14a and 4.16a for each TMF orientation.

All the experiments in set III showed that obtaining the solidification front shape and position during the solidification process of multi-crystalline silicon, can be achieved using the magnetic field. Using this technique, interfaces are marked across the whole ingot width (even near the crucible walls) which was not achieved using the Peltier effect (Section 4.2.2). A few advantages are quickly observed from these results: the time evolution of the solidification front shape can be experimentally observed, the experimental growth velocity can be quantified at different heights of the ingot. Moreover, the furnace thermal insulation quality is reflected in the interface deflection when no magnetic field is applied.

The asymmetric shape of the experimentally observed interfaces for the experiments where the magnetic field was applied, indicate a non-axisymmetric flow in the liquid. This was further investigated in Section 4.3 where the flow patterns in a liquid metal at room temperature are analysed.

4.3 Flow patterns and liquid velocity analysed in GaInSn

The need for a better understanding of the results obtained in Section 4.2.3 regarding the non-axisymmetric shapes of the experimentally observed interfaces lead to this section where flow patterns in the liquid were studied. In order to characterise the liquid flow patterns generated by an induced TMF, in the same experimental set-up with the Bitter electromagnet, a liquid metal at room temperature GaInSn(68.5% Ga, 21.5% In, 10% Sn) replaced the silicon in the crucible. The liquid velocity measurements were performed with an Ultrasonic Doppler velocimeter DOP1000¹ that allows the measurement of particle velocities inside the liquid. Physical properties of the alloy [46] were used to configure the operating parameters of the measurement equipment.

A two inches crucible was partially filled (60mm height) with GaInSn. A downward orientation of the TMF was chosen to induce the forced convection. The probe measures the vertical component of the velocity for particles found at different depths. The measurements are performed in a cone shaped volume

1. DOP1000 is a registered trademark of Ultrasonic Doppler Velocimeter Signal Processing SA, Savigny, Switzerland.

in the liquid in front of the probe. Figure 4.18a provides a 2D description of the probe position during one measurement in a vertical cross section. The cone shape of the analysed volume in the liquid is also indicated in Figure 4.18a. The probe was positioned at half distance between the crucible centre and the wall. In order to obtain a 3D aspect of the flow, 6 different measurements shifted by 60° were taken. A top view of the probe positioning, as well as the measured liquid orientation, is presented in the Figure 4.18b. The positions marked with a cross are the ones where the flow was moving away from the probe and the ones marked with a dot are the positions where the probe indicated that the flow was moving towards it.

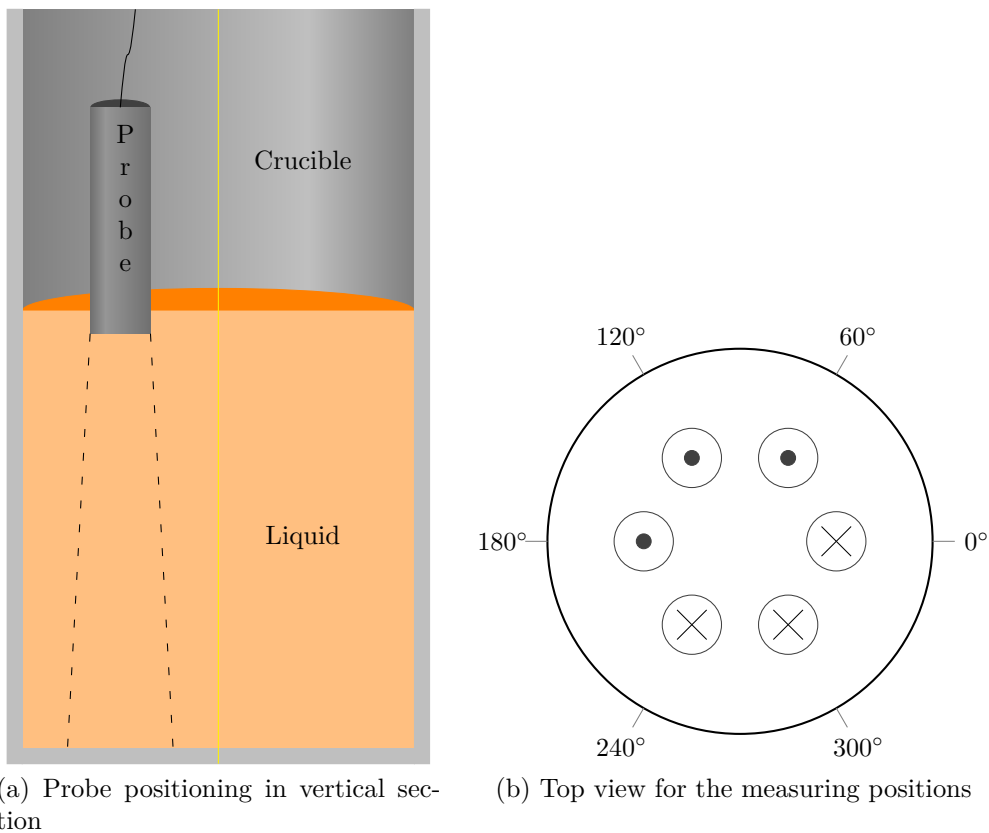


Figure 4.18: Velocity measurement procedure. Cross-section view (4.18a) and top view of liquid orientation (4.18b). Reconstruction of experimental measurements. A cross marks downward oriented flow. Dot marks upward oriented flow.

As indicated in Figure 4.18b, the measured flow orientation indicates a non axis symmetric flow pattern in the liquid. For half of the measurement positions the flow is upward (towards the probe) and for the other half, the flow is in an opposite direction. View from one side (perspective from Figure 4.18a), the liquid flow can be seen as only one predominant vortex across

the crucible width and not a toroidal one, as it was presented for example in Figures 4.1b or 4.1c.

Furthermore, a simulation of this configuration was conducted using the same numerical model. Even if a 2D axisymmetric model is not capable of computing the 3D flow found in the experimental measurements, a comparison between the numerical results and the experimental ones can be made regarding the achieved velocities in the liquid. For this simulation, the silicon was replaced with 60mm height GaInSn and the TMF intensity was the same as the one used during the measurements. The computed velocity vectors, which represents the flow patterns and liquid velocities, are presented in Figure 4.19. The cone shape of the probe measurement field was reconstructed in the simulation. For each depth, inside the cone shaped area, a mean value of the vertical component of the velocity was computed.

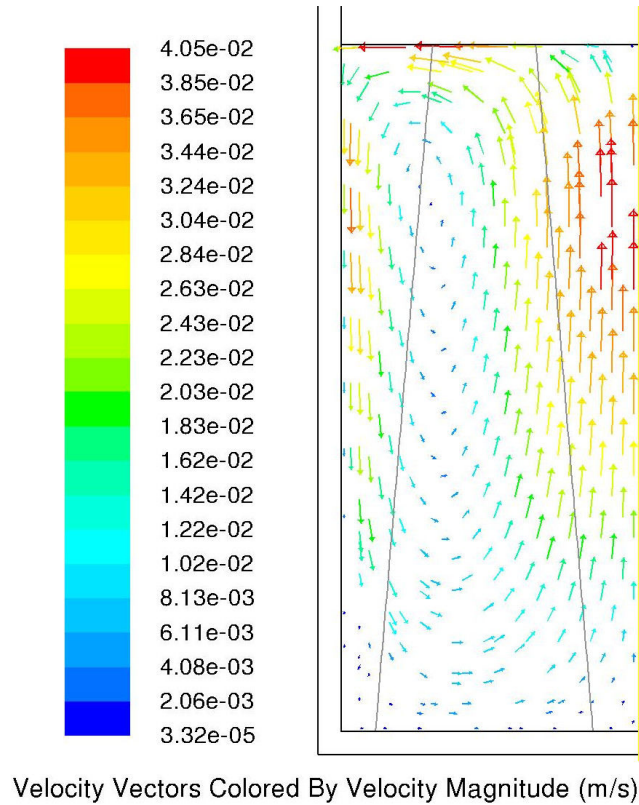


Figure 4.19: Computed liquid velocity of GaInSn, presented on a vertical cross section.

The experimental measurements and computed velocities are presented in Figure 4.20. The negative velocity value represents an upward oriented fluid flow and a positive value represents a downward oriented flow. Upward oriented flow is mainly observed starting from position at 30° up to 210° (see

Figure 4.18b). The other half of the melt mainly presents downward oriented velocities. Simulation results show that in the analysed area the main fluid orientation was upward even if the TMF orientation was downward. This result is due to the vortex centre being positioned closer to the wall rather than at half distance between crucible wall and symmetry axis.

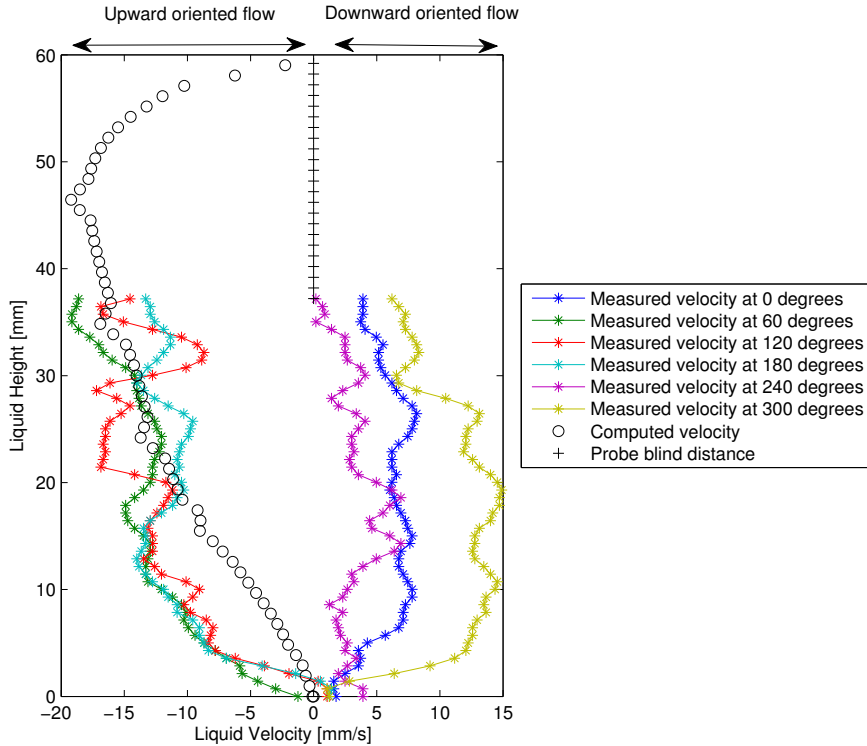


Figure 4.20: Axial liquid velocities in GaInSn.

In order to provide an explanation for the experimentally observed flow patterns, the stability criterion of the basic axisymmetric flow proposed by [47] was analysed. According to this criterion, for the specificities of VB2 furnace, during the experiments with TMF, the flow was not stable and different non-axisymmetric perturbations could occur when the aspect ratio of the liquid zone $A = \frac{\text{height}}{\text{radius}}$ changes during the solidification. The mode with an azimuthal wave number of 1 per turn, as observed experimentally was predicted by the linear stability analysis in [47] for $A = 3$ and a configuration close to our velocity measurements.

For an aspect ratio higher than 1, [48] indicates a critical forcing parameter and a critical Reynolds number smaller than the computed ones for the Experiments III.2, III.3 and III.4. This indicates an unstable flow during the experiments where TMF was used.

According to [28] the current supply connections could also affect the in-

duced flow patterns and trigger asymmetry. In the case of VB2 furnace the current supplies are positioned between 300° and 0° while the windings interconnections are positioned between 120° and 180° (see figure 4.18b).

It has been shown [49] also that a travelling magnetic field driven flow is sensitive to axial alignment. Differences as small as one or two millimetres between the axial center of the crucible and the magnetic field one, can switch the flow from a axisymmetric one to a 3D one.

4.4 Conclusions

In this chapter, experimental and numerical results for multiple series of experiments were presented, with focus on the shape of the solid-liquid interface. In the first set of experiments different orientations of the electromagnetic stirring were used. Numerical simulations for these experiments were conducted as well, in order to obtain more precise information such as temperature maps, flow patterns, liquid velocity in the silicon melt and their influence over the shape of the solidification front. The interface shape evolution during the solidification was computed for all the performed experiments. The orientation of the grains observed in the experimentally obtained ingots showed a strong correlation to the shape of the computed solid-liquid interface.

In order to confirm the observations made in the first set of experiments, the decision to experimentally mark the solidification interface was made. In order to achieve this, two methods were used. The first approach was to use the Peltier effect in order to mark the interface. This method offered relatively good results. However, limitations such as the reduced crucible diameter (1.3 inches) had to be considered. The interface marks obtained with this procedure are not clearly visible on the edges of the ingot, close to the crucible walls.

In the last set of experiments using silicon as raw material, marking of the interface was attempted using another approach. This time variations of the magnetic field intensities were used to perform the marking on normal sized ingots (2 inches in diameter). The obtained images indicated clear markings of the solidification interface on the entire ingot width. For these experiments, different orientations of the travelling magnetic field were used, and numerical simulations were performed. The experimentally obtained markings of the interface were compared to the ones computed for the same time. The observed differences between the interfaces obtained experimentally and through simulation indicated the possibility of a non-axisymmetric flow in the melt.

In order to verify the hypothesis of a non-axisymmetric flow in the melt induced by the magnetic field, the flow in the crucible was analysed using a liquid metal (GaInSn) at room temperature. This study was presented in the last part of this chapter and indicates a very high sensitivity of the flow stability when the magnetic field is used. The obtained results confirmed the possibility of a non-axisymmetric flow in the melt. The bibliographic study [47, 48, 49] triggered by these results showed that the liquid flow can easily become unstable, for the specificities of VB2 furnace and the TMF intensities used in the solidification experiments. Moreover, imperfections in the geometrical symmetry of the furnace components can also lead to a non-axisymmetric flow in the melt induced by the TMF.

Chapter 5

Segregation under travelling magnetic field (TMF)

5.1 Theoretical aspects of the segregation process

For a segregation coefficient smaller than 1 ($K_0 < 1$), the solute concentration in the liquid decreases with the distance from the solidification interface in an exponential fashion. This is generally representing a solute boundary layer. In [33], the author define the boundary layer thickness, for a diffusive case as

$$\bar{\delta} = \frac{C_L^* - C_L}{-dC/dx|_{x=0}} \quad (5.1)$$

where

C_L^* represents the concentration at the interface in the liquid

C_L represents the solute concentration in the bulk (far in the liquid)

x represents the crystallization direction

A graphical representation of $\bar{\delta}$ is presented in Figure 5.1.

A convecto-diffusive parameter $\bar{\Delta}$ [33] can be defined as

$$\bar{\Delta} = \frac{R\bar{\delta}}{D} \quad (5.2)$$

where R represents the crystal growth rate or in this case the solidification interface velocity and D represents the solute diffusion coefficient.

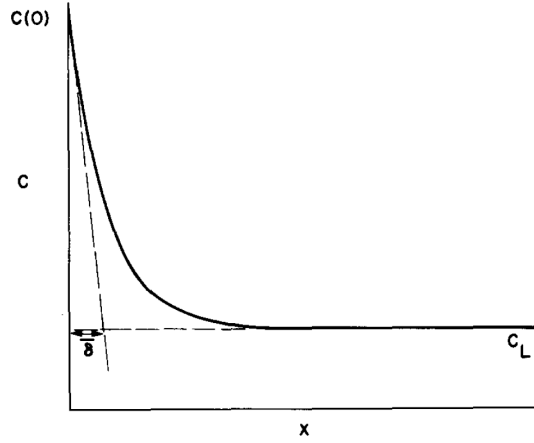


Figure 5.1: Definition of the boundary layer thickness $\bar{\Delta}$ [33]. (The concentration at the interface in the liquid C_L^* is referred to as $C(0)$ by the author)

According to Wilson [33], the Burton, Prim and Slichter's formula for the effective segregation coefficient [32] is equivalent to

$$K_{eff} = \frac{K_0}{1 - (1 - K_0)\bar{\Delta}} \quad (5.3)$$

where K_0 represents the equilibrium distribution coefficient, also known as the segregation coefficient.

The solute concentration at the interface in the solid (C_S^*) is related to the concentration at the interface in the liquid (C_L^*) by the formula

$$C_S^* = K_0 C_L^* \quad (5.4)$$

In a purely diffusive case, where no convective mixing is taking place in the liquid, $\bar{\Delta} \rightarrow 1$ and the effective segregation coefficient $K_{eff} \rightarrow 1$. The solute concentration in the solid (C_S) reaches the initial concentration C_0 after the initial transient period. The initial transient (Equation 3.34 [43]) appears at the beginning of the solidification process, when the solute boundary layer is formed. The initial transient duration depends on the species diffusive coefficient D , segregation coefficient K_0 and the crystal growth velocity. An estimation of the initial transient duration [43] (for the diffusive case) is $4D/RK_0$. Once the steady state is reached, the concentration in the solid stays at C_0 as long as the solute concentration in the far liquid (C_L) at $x \rightarrow \infty$ remains equal to C_0 . For a 1D analytical solution, Figure 5.2 depicts the axial solute distribution in steady state, at two different instants in time, for a pure diffusive case.

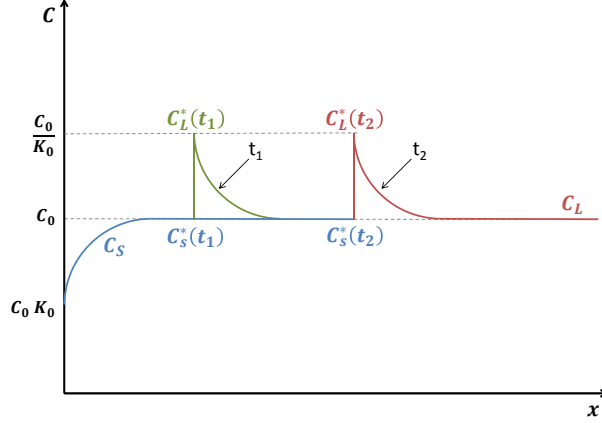


Figure 5.2: Segregation process for a pure diffusive case. t_1 and t_2 represents two different instants in time where the solidification interface is at a different position along the crystallization direction x .

When the effect of the convection in the liquid significantly overcomes the effect of the diffusion and the solute is homogeneously distributed in the liquid, $\bar{\Delta} \rightarrow 0$ and the effective segregation coefficient $K_{eff} \rightarrow K_0$. This second scenario will be referred to as the perfectly mixed case, where the solute boundary layer thickness $\bar{\delta} \rightarrow 0$. For a perfectly mixed case, the evolution of the solute concentration in the solid (C_S) along the axial component of the ingot is given by the Scheil-Gulliver law [50].

$$C_S = C_0 K_0 (1 - f)^{K_0 - 1} \quad (5.5)$$

For the perfect mixing scenario, Figure 5.3 depicts the solute distribution along the crystallization direction x with the interface at two different positions at two different instants in time (t_1 and t_2). Due to the perfect mixing of the liquid, the solute is homogeneously distributed in the bulk, the concentration at the interface (C_L^*) will be the same as in the far liquid. This time the concentration in the liquid C_L at $x \rightarrow \infty$ is no longer C_0 compared to the diffusive case. Therefore the concentration in the liquid at the interface is decreased compared to the diffusive scenario. The concentration in the solid C_S follows the Scheil-Gulliver law (Equation 5.5) computed with a segregation coefficient K_0 , and remains for a longer distance below the initial concentration.

In a more realistic scenario (Figure 5.4) with partial mixing, the diffusion and convection effects must be both taken into account. In the steady state the concentrations in the solid C_S should follow Scheil-Gulliver law but this

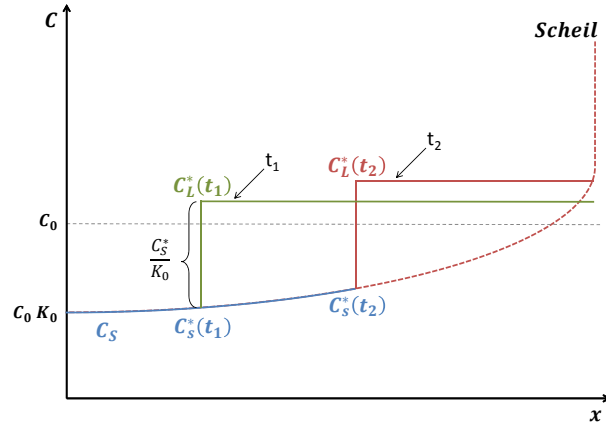


Figure 5.3: Segregation process for a perfect mixing case. t_1 and t_2 represents two different instants in time where the solidification interface is at a different position along the crystallization direction x .

time computed with K_{eff} which differs from K_0 . The initial transient as well as the diffusion boundary layer are present in this case. For a solute with a segregation coefficient K_0 below unity, $K_{eff} \rightarrow K_0$ if the diffusion influence is insignificant or $K_{eff} \rightarrow 1$ if the convection influence is insignificant.

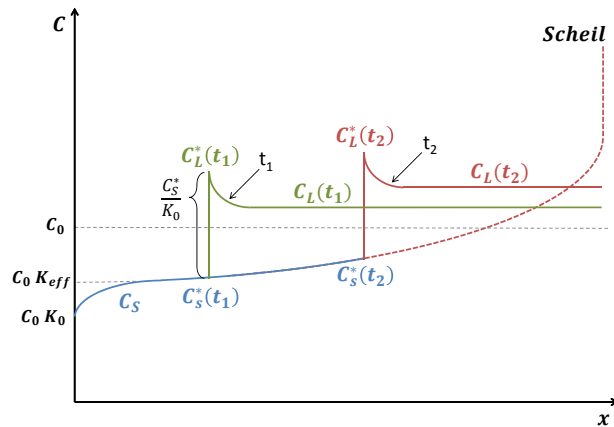


Figure 5.4: Segregation process for a convecto-diffusive case. t_1 and t_2 represents two different instants in time where the solidification interface is at a different position along the crystallization direction x .

5.2 Experimental and numerical results

5.2.1 Overview of the analysis methodology

Studying the impurity distribution in the obtained silicon crystals is one of the main tasks of this work. Experimental, as well as numerical, results regarding the chemical segregation of impurities are discussed in this chapter. Multiple series of experiments were conducted mainly in order to study the effect of the electromagnetic stirring over the segregation process. In the obtained ingots, impurity levels were recorded at different positions, especially in the center of the ingot. The impurity levels in the resulted ingots were measured by the inductively coupled plasma (ICP) method. A $5mm$ thick slice was removed from the central part of each of the obtained ingots and was afterwards cut in smaller samples. An example of the slice cutting procedure is depicted in Figure 5.5, where the samples in lightgrey are the ones used for ICP analysis. As the image indicates, the analysed samples are mainly removed from the center of the slice in order to obtain a description of the impurity concentration evolution along the solidification length. Due to the fact that the entire ingot volume could not be analysed, the resulting mean value of the measured samples is not equal to the initial concentration of that impurity in the ingot. Some of the samples, depicted in darkgrey color in Figure 5.5, were used for observations using an optical microscope as well as a scanning electron microscope (SEM) in order to provide more precise information about the experimental results.

Multiple series of experiments were conducted in order to study the segregation phenomena in a directional solidification process. Two different types of silicon were used for these experiments and the impurity contamination levels for each of these are presented in Table 5.1. The material *Si – A* presents low levels of aluminium, iron and phosphorus for a metallurgic grade silicon, while *Si – B* presents similar iron and phosphorus concentrations but an increased concentration in aluminium.

Table 5.1: Impurities levels for the raw silicon used in the performed solidification experiments

Material reference	Aluminium [ppm]	Iron [ppm]	Phosphorus [ppm]
Si-A	6.8	10	9.6
Si-B	600	13.2	2.76

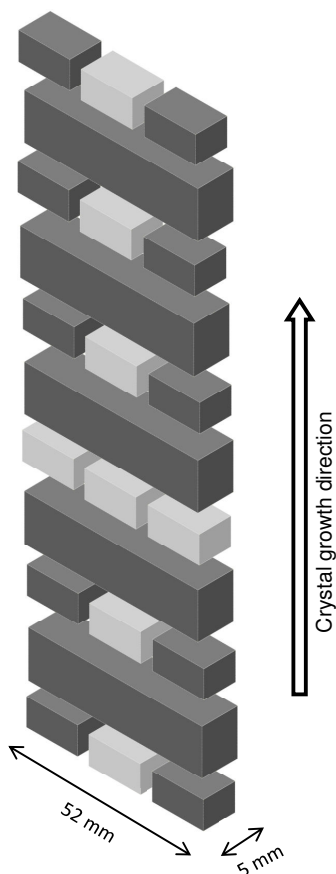


Figure 5.5: Vertical slice from the center of the ingot and cutting procedure. The samples depicted in lightgrey are used for impurity analysis. The samples depicted in darkgrey observed at microscope.

The theoretical values [44] for the segregation coefficient K_0 for all the followed impurities in this study are presented in Table 5.2.

Table 5.2: Segregation coefficient for the impurities of interest.

	Aluminium	Iron	Phosphorus
K_0	$2 \cdot 10^{-3}$	$8 \cdot 10^{-6}$	0.35

In this chapter the experiments from sets I to III are presented. Details regarding the condition in which each experiment was conducted as well as the furnace configurations have been presented in Chapter 2 Section 2.2. For experiments from set I and III more details and results from numerical simulations have been presented in Chapter 4 Section 4.2.

5.2.2 Results on experiments set I

Four experiments were conducted in set I and as presented in Table 5.3, the same material *Si-A* was used and the same temperature difference $\Delta T = 150K$ was imposed between the heaters in order to obtain a vertical thermal gradient in the silicon. The crucible was kept at the same position for all the experiments and the same cooling rate was imposed to trigger the solidification process. The main difference between experiments from this set consists in the different orientations used for the travelling magnetic field for each experiment. For the alternating TMF (Experiment I.4) the magnetic field orientation was changed at an interval of $\Delta t = 30s$.

Table 5.3: Experiment set I

Experiment number	Raw material	Imposed ΔT	Cooling rate [K/h]	TMF intensity [mT]	TMF orientation
I.1	Si-A	150	36	0	-
I.2	Si-A	150	36	4	Upward
I.3	Si-A	150	36	4	Downward
I.4	Si-A	150	36	4	Alternating

According to the numerical results for these experiments, presented in Chapter 4, the maximum velocity in the liquid has a magnitude order of $10^{-3}m/s$ for Experiment I.1, driven by buoyancy forces. When external forces are applied (Experiments I.2, I.3 and I.4) the numerical model computed a velocity of the liquid up to $3.5 \cdot 10^{-2}m/s$.

Multiple samples were taken from the centre of each ingot at different heights (see Figure 5.5) and had their average impurities concentrations measured. Furthermore, a value of the solid fraction was associated to the measurement position in accordance with the numerical results for each experiment. The numerical simulations from which the solidification interface position was recovered were conducted using ANSYS FLUENT solidification module.

Figure 5.6 presents the evolution of measured levels of aluminium, normalised to the initial concentration C_0 , versus the solidification fraction for the experiments conducted in this set. Moreover, the aluminium concentration versus the solid fraction, given by the Scheil-Guliver law (Equation 5.5), was added to the figure. The Scheil-Guliver law represents the perfectly mixed case (computed with a theoretical value K_0 for the segregation coefficient) and does not depend on the solidification front shape. The detection limit of this

method is also indicated in Figure 5.6 as *ICP detection limit*. The given value for the *ICP detection limit* represents the lowest concentration value that can be detected using this method.

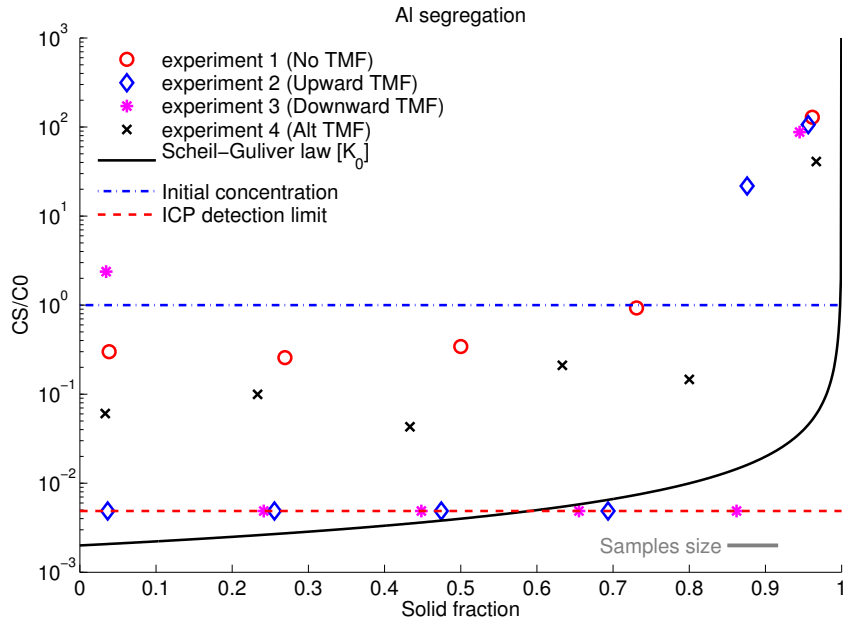


Figure 5.6: Aluminium axial segregation along the ingot centre for experiments in set I.

For the Experiment I.1 (without TMF) the aluminium concentration measured in the first half of the ingot was ≈ 8 times smaller than C_0 . Only after 80% of the ingot solidified, the concentration in the solid reaches the initial concentration C_0 and increases up to a hundred times C_0 towards the end of the solidification process.

The axial distribution of aluminium (Figure 5.6) concentrations for the Experiments I.2 and I.3 reached the ICP precision limit (of $0.05ppm$) for 85% of the ingots' heights. However towards the end of the solidification, the measured quantities were up to 100 times higher than the initial concentration C_0 . The I.2 and I.3 experiments indicate a low aluminium presence in most of the ingot and are close to the theoretical limit represented by Scheil-Guliver law.

Compared to the second and third experiments, the Experiment I.4 presents higher concentrations of impurities but still below C_0 values for more than 90% of the ingot's height. In the case of aluminium, the measured concentration in the solid was 10 times lower than C_0 which indicates an improvement compared to Experiment I.1.

The measured iron levels for all experiments in set I are presented in Figure 5.7 along with Scheil law and the detection limit. The axial distribution

of iron along the solid fraction presents a similar evolution as the aluminium one. The recorded iron concentration in Experiment I.1 was ≈ 8 times lower than C_0 for 80% of the ingot. For experiments I.2 and I.3 the detection limit was reached again which suggest the possibility to have a concentration close to the Scheil-Guliver law at least for 70% of the ingot. For Experiment I.4 the measured iron concentration was ≈ 100 times lower than C_0 for 80% of the ingot. For the last 20% of the ingot the measured iron levels were up to 100 times higher than the initial concentration C_0 .

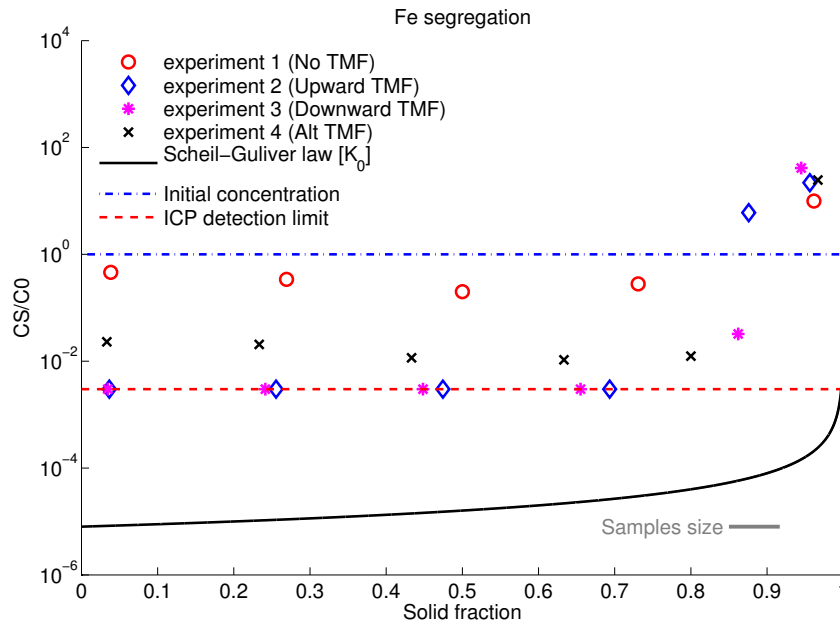


Figure 5.7: Iron axial segregation along the ingot centre for experiments in set I.

Because of a higher value of K_0 for phosphorus compared to aluminium or iron (see Table 5.2), the segregation process is not as efficient in this case. The measured concentration for phosphorus are presented in Figure 5.8. For experiments I.1 and I.4 the phosphorus levels remained unchanged and close to the initial concentration value for most of the ingot and presented a slight increase towards the end. In the case of Experiment I.3 the measured values basically followed the Scheil-Guliver law. Experiment I.2 presented three measurement points below Scheil values and another three that corresponds to the law. The detection limit was far below any of the measurement values and an indication of it on the figure was not required.

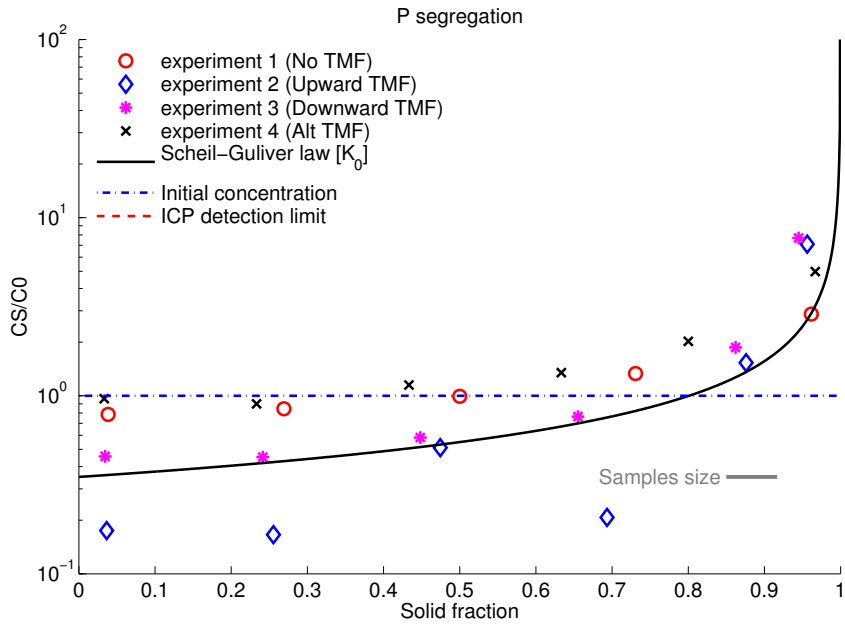


Figure 5.8: Phosphorus axial segregation along the ingot centre for experiments in set I.

The samples removed from the ingots (see Figure 5.5) and not used for segregation analysis were carefully observed using a scanning electron microscope (SEM). For some of the samples, in order to be able to observe the surface topography, a chemical etching of the surfaces was required after the polishing process. The procedure used was similar to the one used for revealing interface demarcations, presented in Chapter 4. Figure 5.9 depicts the surface of one of the analysed samples, where crystal defects were found. The image presents two grains, one on the left and another on the right side, separated by a vertical boundary. On the left hand side grain a high density of defects, with sizes of $\approx 3\mu m$, was detected. The grain boundary acted as a barrier and so, in the grain from the right side of the picture, the number of observed defects is significantly decreased. The observed defects on this image appear to be dislocation pits. Thermal stress along with impurities presence in the material could easily lead to defects in the crystal structure which ultimately results in a decreased quality of the crystal [30].

Different impurities contaminating the silicon could also lead to the formation of precipitates in the resulting crystal. The precipitation of different impurities could occur if their local concentration reaches the eutectic point on the phase diagrams. This will allow in certain cases a new phase to form (i.e. $FeSi_2$ for iron) or in other cases the precipitation of pure pollutants (i.e. for aluminium). The pollutant concentration reached at the solidification in-

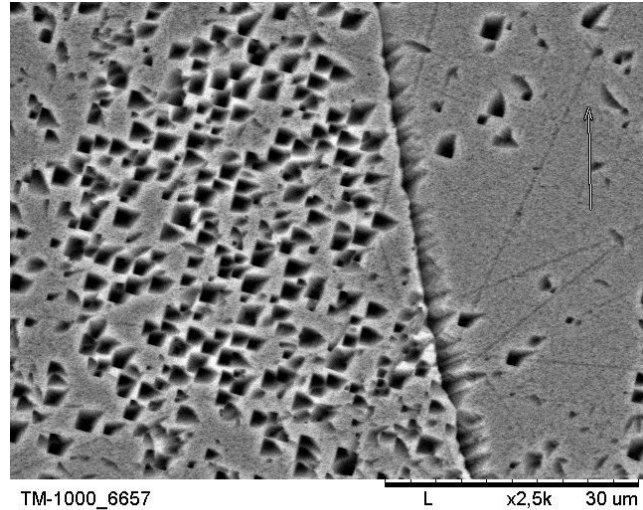
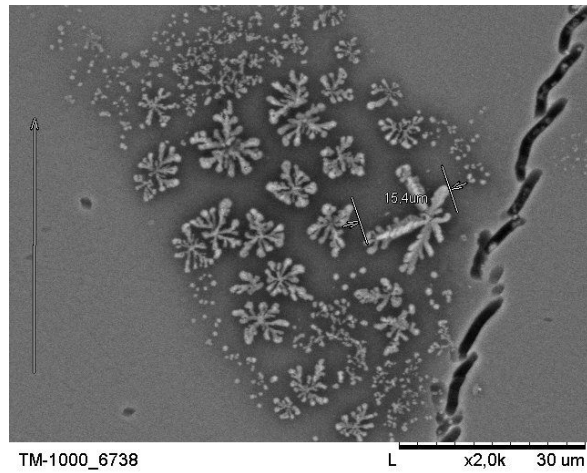


Figure 5.9: Sample surface (experiment I.2) obtained with a scanning electron microscope (SEM) using secondary electrons (SE) and dislocation etch pits observed at the surface.

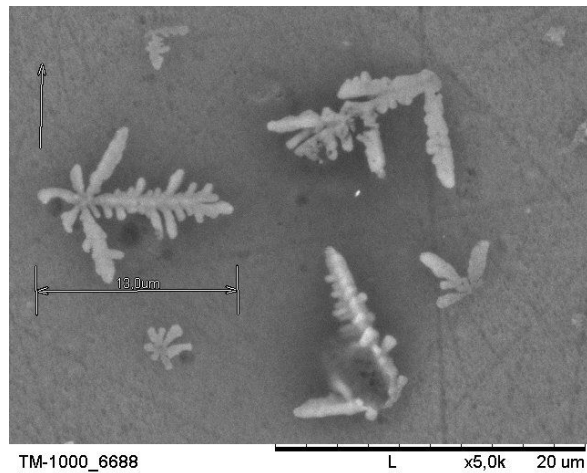
terface is related to the solute boundary layer. This boundary layer is defined by the initial level of pollutant and the solidification process parameters such as thermal gradient, growth velocity and liquid velocity. If multiple contaminants are present in the silicon, during the solidification process they could also interact with each other at different concentrations and temperatures forming various other compounds that are incorporated in the solid as impurity precipitates.

Figure 5.10 depicts such precipitates observed on the upper part of ingots obtained from experiments conducted in set I. These images were obtained with a scanning electron microscope (SEM) using backscattered electrons (BSE). The growth direction of the crystal was from the bottom of the image towards the top. Figure 5.10a presents a cluster of snowflake like precipitates. In the central area, the precipitates size can reach up to $15\mu m$ and decreases towards the edges of the cluster. Figure 5.10b presents another such cluster where precipitates with the same shape and similar sizes were found. The dendrite like precipitates were observed on these samples before the chemical etching process and they are to be found at a grain boundary or inside the grain.

By using energy dispersive X-ray spectroscopy (EDS) for some of the precipitates found in the samples, the constituent elements were determined. Figure 5.11 presents the EDS spectrum most frequently found in this investigation and it corresponds to an aluminium precipitate. This indicates that the majority of the precipitates found were aluminium precipitate. In order to obtain



(a) Experiment I.4



(b) Experiment I.1

Figure 5.10: Dendrite like precipitates observed on the surface of a sample obtained from experiments in set I. Images presenting sample's surface obtained with a scanning electron microscope (SEM) using backscattered electrons (BSE).

such precipitates, according to the Al-Si phase diagram (see Appendix C), the local aluminium concentration in the solid must reach 12.6 mass fraction. Figure 5.12 presents another observed EDS spectrum which indicates a ternary phase containing aluminium and iron. The formation of a variety of such phases is possible and in order to determine the exact conditions in which they formed, the phases must firstly be identified. In this research work no further investigations were made regarding the observed precipitates.

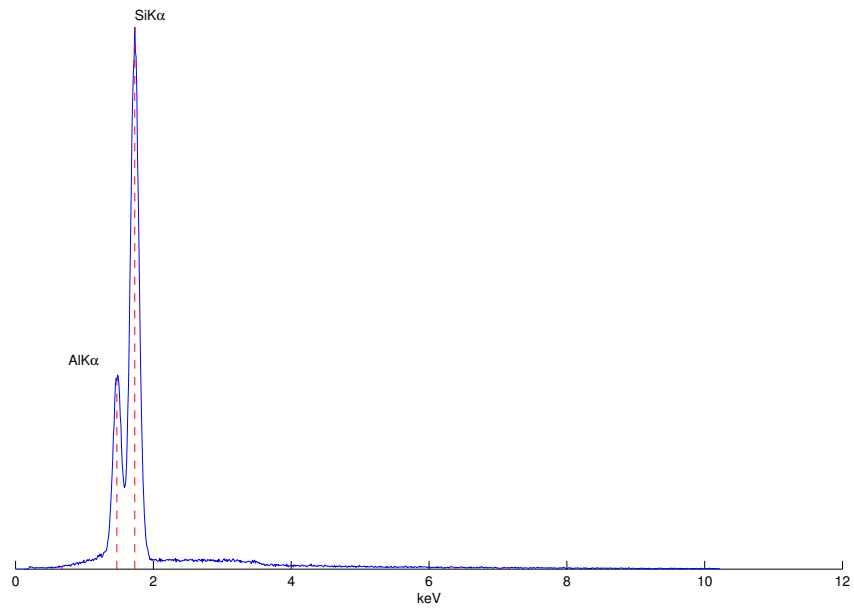


Figure 5.11: EDS spectrum of Al and Si observed on samples from experiments in Experiment I.1 at the level of a dendrite like defect.

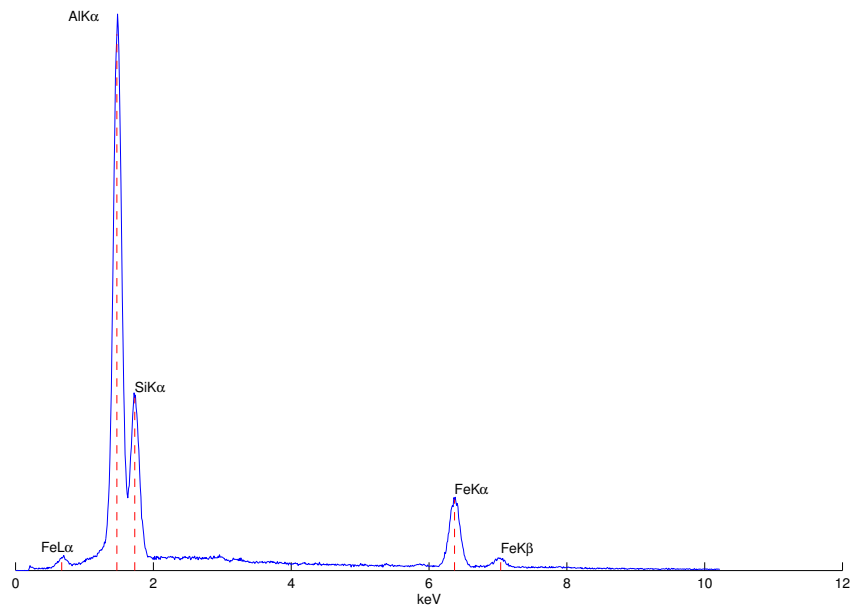


Figure 5.12: EDS spectrum of Al, Si and Fe observed on samples from experiments in Experiment I.1 at the level of a dendrite like defect.

5.2.3 Results on experiments set II

A second set of experiments was conducted to observe the effect of the magnetic field over the segregation process, this time on a more polluted material. As specified in Table 5.1 *Si-B* used for these experiments presents a high concentration of aluminium ($\approx 600ppm$). Details about experiments conducted in this set are presented in Table 5.4. Only two experiments were conducted, one without TMF and another one with a downward oriented TMF. The main solidification process parameters such as imposed ΔT and cooling rate are similar to the ones used in experiments set I. However, due to an increased contamination with aluminium for this case, an increased value of the TMF intensity was considered. In experiment II.2 the magnetic field intensity was set to $7mT$.

Table 5.4: Experiment set II

Experiment number	Raw material	Imposed ΔT	Cooling rate [K/h]	TMF intensity [mT]	TMF orientation
II.1	Si-B	150	36	0	-
II.2	Si-B	150	36	7	Downward

Vertical slices of the obtained ingots with the grain macro-structure for each experiment are depicted in Figure 5.13. For the experiments conducted with this material, a generally poor quality of the ingots upper part was observed. For the last half of the ingot obtained in Experiment II.1, the border presents irregular shapes. The same phenomena can be also observed for Experiment II.2 but only in the upper quarter of the ingot. This poor quality of the ingot may be related to the the aluminium presence in the final ingot, subject which will be discussed in the following paragraphs. For Experiment II.2 rather elongated grains (see Section 4.1) are observed in the first (70%) of the ingot by comparison to Experiment II.1 which presents smaller grains without a precise orientation.

A vertical slice was removed from the center of each ingot. The slice was separated into small samples (see Figure 5.5) to measure their impurity concentrations. A similar procedure as the one presented for experiments in set I was followed. The measured levels of aluminium in the center of the ingots are presented in Figure 5.14 along with the theoretical values for the Scheil-Guliver law. Due to the high levels of aluminium present in this experiments, the detection limit was below any of the measurement values and an indication

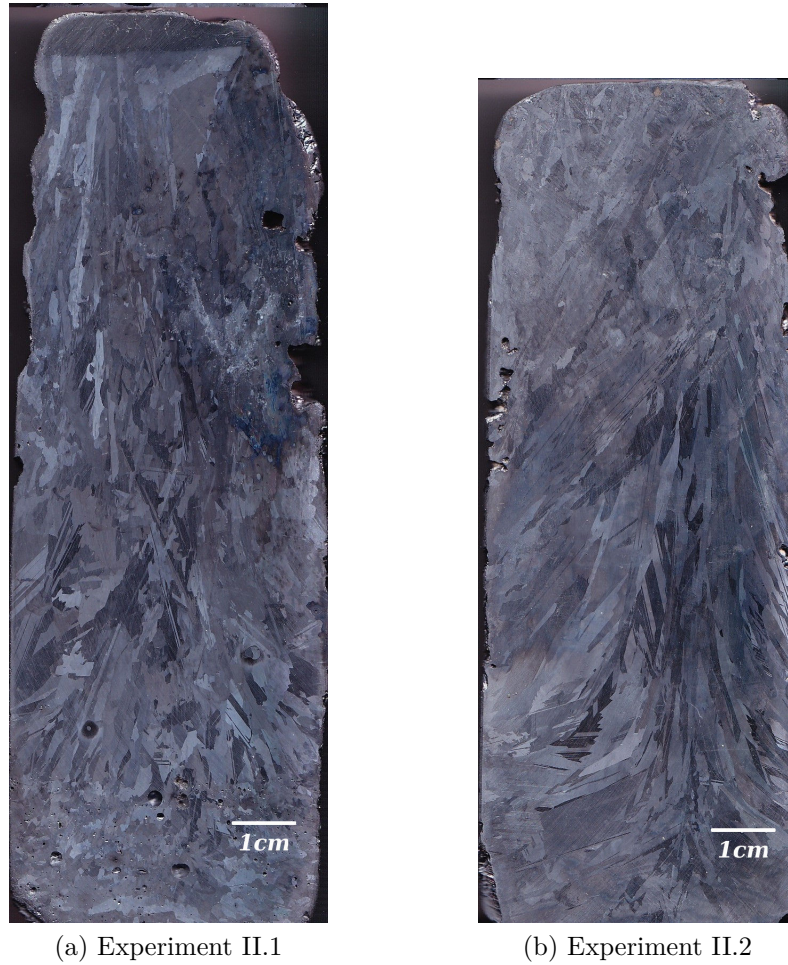


Figure 5.13: Grain macro-structure on vertical slices for experiments from set II.

of it on the figure was not required.

For Experiment II.1, the measurements for the first position (solid fraction = 0.05), which correspond to the bottom of the ingot, indicated a higher concentration compared to the initial one C_0 . In fact, the first 2cm at the bottom of the ingot (Figure 5.13a) indicate that the melting process was not complete. This could be related to the fact that the measured levels of impurities in that area are higher than the initial concentrations values, but a proper explanation for this phenomena can not be provided. For the next half of the ingot, up to 0.7 of solid fraction, the average amount of aluminium found in the ingot is equal to the initial concentration C_0 . In the last 0.3 of the solid fraction an increase of the aluminium presence was observed. The fact that the total amount of pollutant measured is higher than C_0 is related to the fact that all the measurements were performed in the central area of the ingot. The flow

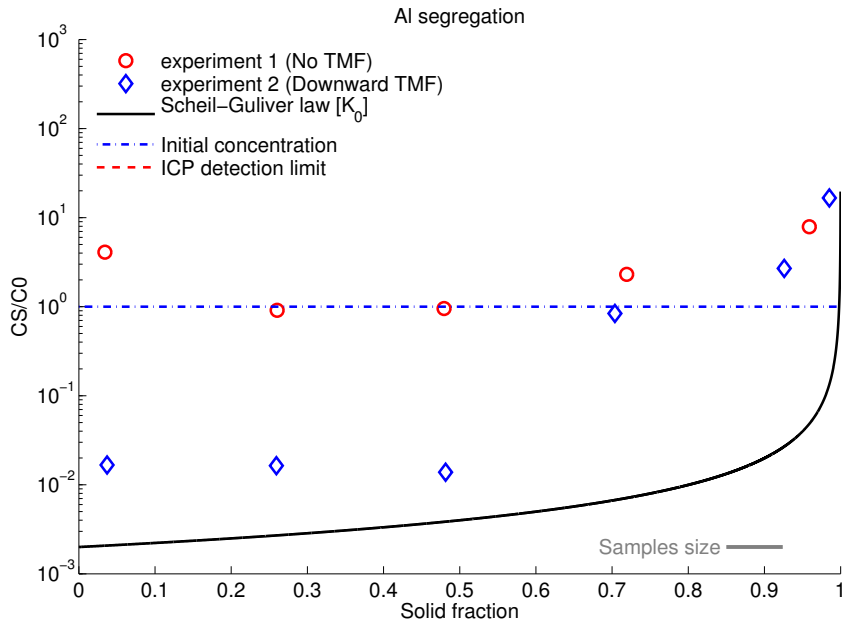


Figure 5.14: Aluminium axial segregation along the ingot centre for experiments in set II.

patterns in the liquid, generated by the natural convection are sufficient to partially transport the impurities towards the centre of the ingot. The flow patterns, as well as the liquid velocities for this experiments, are discussed in the following paragraphs.

The measured aluminium distribution along the solid fraction for the second experiment (II.2) is also presented in Figure 5.14. In the first 70% of the ingot, the recorded levels were 100 times lower than C_0 , which indicates a good separation of aluminium from the silicon. This region in the ingot corresponds to the one where the elongated grains are observed (see Figure 5.13b). For the upper part of the ingot (from 0.7 to 1 of the solid fraction) the aluminium presence increases dramatically above C_0 and the grains structure changed to smaller grains. This results will be further detailed in the following paragraphs.

The iron distribution along the solid fraction for this two experiments (Figure 5.15), present the same characteristics as the aluminium ones. For Experiment II.1, the first measurement position gives a value above C_0 followed by a plateau slightly below C_0 and an increase towards the end of the ingot. The measurements for Experiment II.2 reached the detection limit in the first 70% of the ingot and then suddenly increase above C_0 towards the end of the solidification.

The phosphorus distribution (Figure 5.16) in the first experiment shows values close to the initial concentration, apart from the first measurement

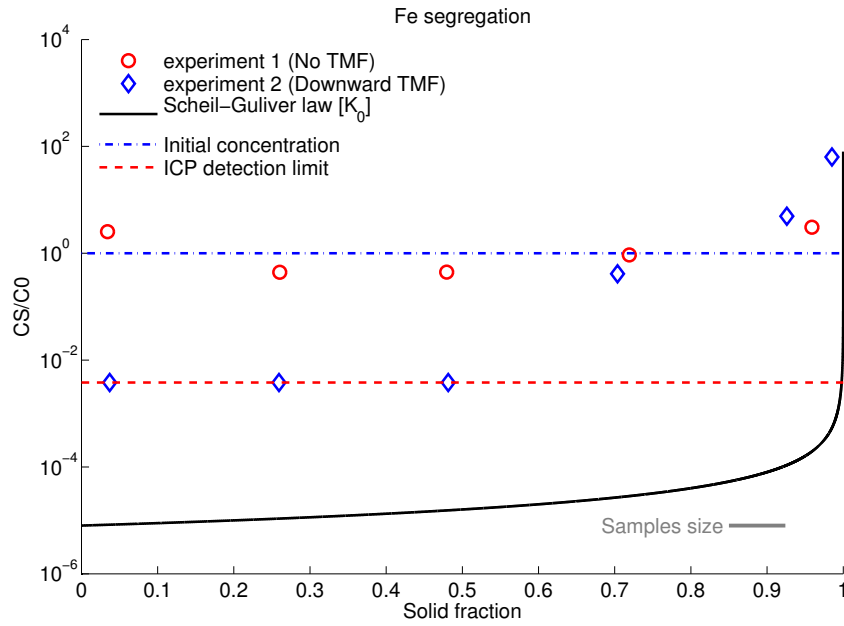


Figure 5.15: Iron axial segregation along the ingot centre for experiments in set II.

position. The second experiment however presented almost a perfect match with the Scheil-Guliver law.

In order to obtain more information regarding the experiments conducted in set II, numerical simulations were performed using ANSYS FLUENT solidification module. Figure 5.17 presents for both experiments the computed velocity vectors, on a vertical cross section, at three different instants during the solidification.

In the first experiment the velocity in the liquid is driven by buoyancy and no external forces are applied. As it is described in Figure 5.17a, the maximum velocity in the liquid was computed at $2.7 \cdot 10^{-3} m/s$ and the flow patterns suggest the presence of a small toroidal vortex in the melt above the solid-liquid interface. The solidification front presents a convex shape in the first part of the ingot and becomes flatter towards the end of the ingot.

For the second experiment, the induced forces create a toroidal vortex in the whole melt, capable of considerably decreasing the thermal gradient in the liquid. For a magnitude of the magnetic field of $7mT$, the maximum values for the induced Lorentz forces are computed at $170N/m^3$. Figure 5.17b describes vertical cross-sections of the flow patterns and the velocities achieved in the liquid for different instants during the solidification process. The velocity reaches a maximum value of $\approx 6 \cdot 10^{-2} m/s$ in the centre of the ingot.

The liquid velocity in the bulk has a direct influence on the solute bound-

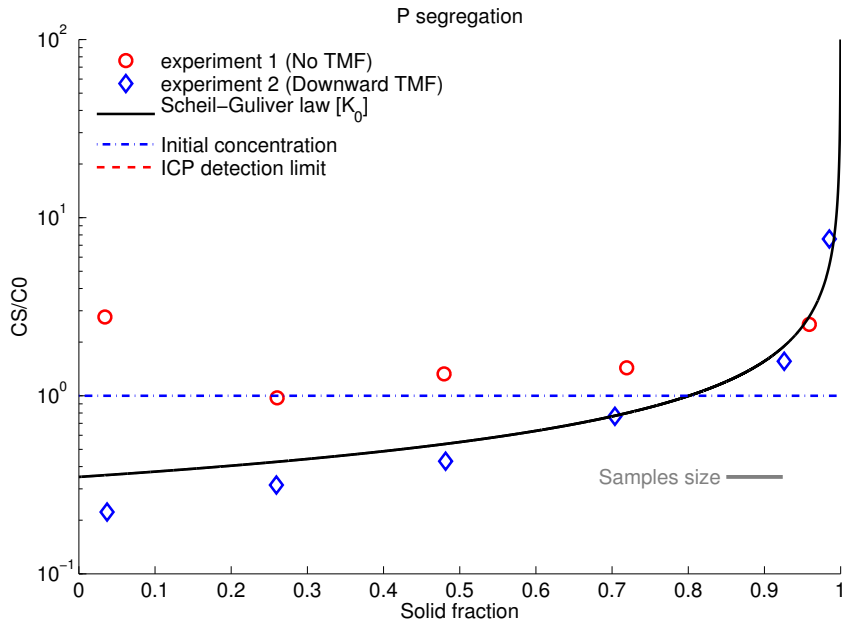
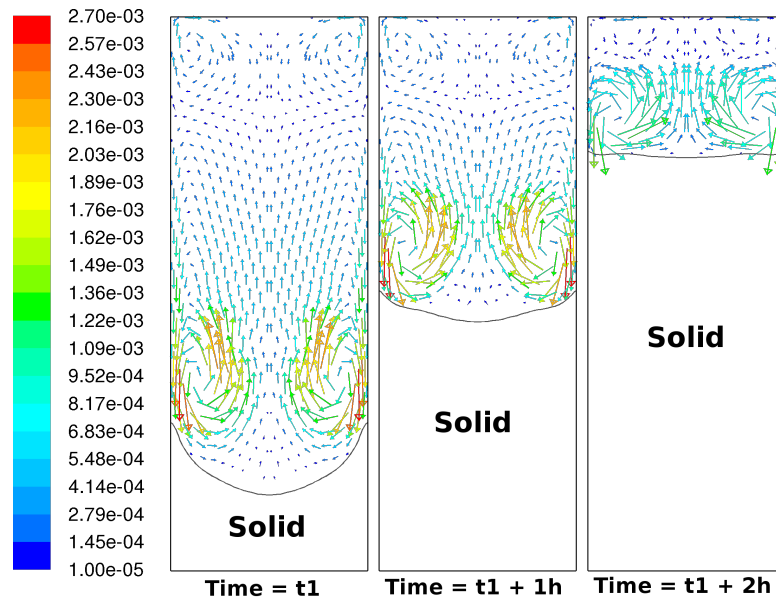


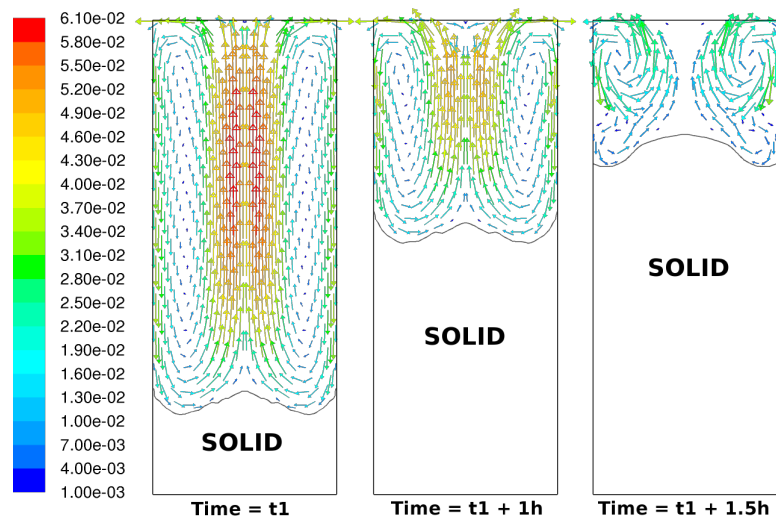
Figure 5.16: Phosphorus axial segregation along the ingot centre for experiments in set II.

ary layer, therefore on the impurities levels at the solidification interface. The higher the velocity is, the lower the impurity concentration at the interface is. In Figure 5.17b, a decrease of the liquid velocity can be observed towards the end of the solidification. This phenomena is related to the fact that at the end of the solidification process, the liquid quantity is reduced and with that the forces induced by the magnetic field are decreasing as well. In Figure 5.18 the maximum computed velocity, for different positions of the solid fraction, is presented for both experiments. For both experiments, the liquid velocity decreases when the solid fraction equal to 0.5 is reached. A sudden increase of the impurity concentrations between 0.5 and 0.7 of the solid fraction was experimentally observed for experiment II.2 (see Figures 5.14 and 5.15). It is hard to quantify the exact effect of the liquid velocity over the measured impurity concentrations, therefore it is not clear if this velocity decrease can explain the concentration increase. However, the abrupt concentration increase can be due to a destabilization of the solidification interface, triggered by the concentration increase at the interface. An analysis of the solidification interface morphological instability for Experiment II.2 is presented in Appendix D.

Similar to the experiments in set I, the ingots surfaces are analysed using an optic microscope, as well as a SEM one. Images obtained with an optic microscope in the upper part of the ingot from Experiment II.2 are presented in Figure 5.19. Column-like traces at the crystal surface are observed in Fig-



(a) Experiment II.1



(b) Experiment II.2

Figure 5.17: Numerical results of liquid velocity distribution on vertical cross-section expressed in m/s, at different instants during the solidification process. Ingots are 2 inches in diameter.

ure 5.19a. The solidification direction is from the bottom towards the top of the image. At the upper end of these columns impurity precipitates are usually found. The sample surface was subjected to a very short (only few seconds) chemical etching process, so that most of the precipitates found at the surface remained in place. For some of these structures, like the one in the center of the Figure 5.19a, a precipitate tail of about $500\mu m$ can be observed. In some other case, like the one presented in Figure 5.19b, the precipitates formed a

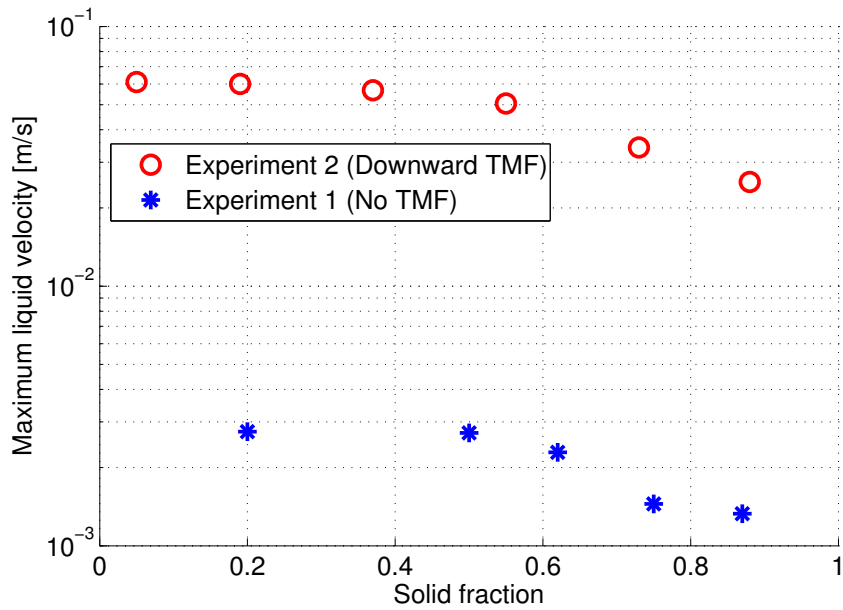


Figure 5.18: The maximum computed liquid velocity at different positions of the solidification interface.

long line of $\approx 2\text{cm}$ in the crystallization direction.

Similar structures were also analysed using a scanning electron microscope (SEM). Figure 5.20 presents images of the upper end of similar column-like structures observed on the sample surface using secondary electrons (SE). The column tip is surrounded by micro pits which represent crystal defects similar to the ones presented in Figure 5.9. This could indicate a high level of stress being applied to the crystal by the precipitates at the end of these columns. An interesting fact is that inside the column no such defects are observed.

The precipitates usually are ending up at the grains boundary being rejected there by the crystallographic structure of each silicon grain. Such a situation is presented in Figure 5.21. Another similar example is depicted in Figure 5.22.

The measured levels of impurities increased in the last 30% of the ingot obtained in Experiment II.2. The measurements represent average values for samples ($10 \times 10 \times 5 \text{ mm}$) coming from the same region where structures like the ones presented in figures 5.19, 5.21 and 5.22 were found. The decrease of the flow velocity, computed in the same part of the ingot, seems to significantly influence the precipitants distribution in the final ingot.

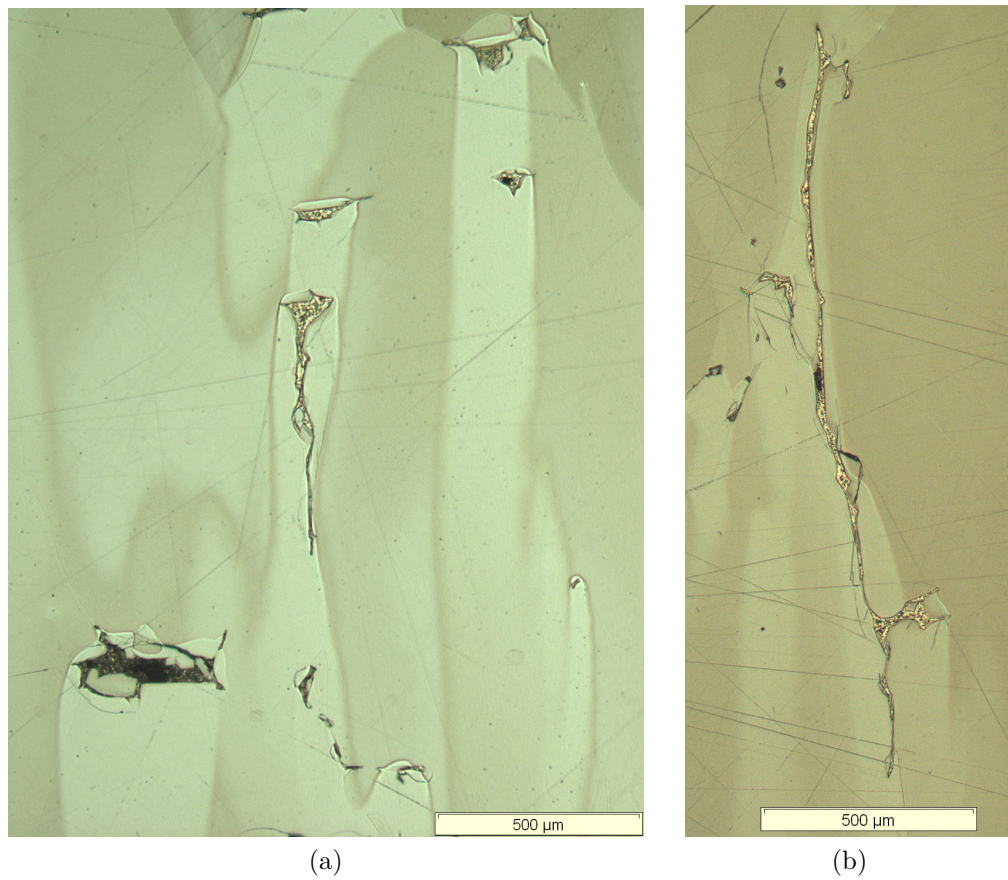


Figure 5.19: Example of column like traces observed on the surface of a sample obtained from experiments in set II. Solidification direction is from the bottom towards the top. Image obtained with an optical microscope.

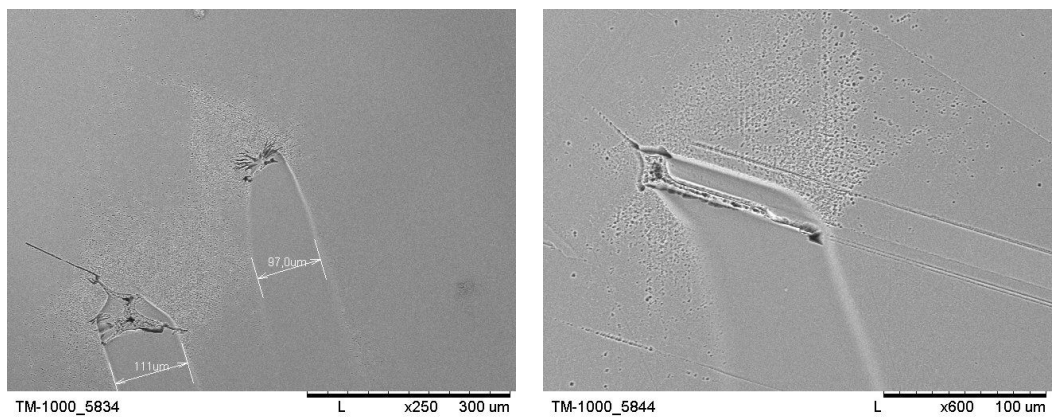


Figure 5.20: Example of column like traces observed on the surface of a sample obtained from experiments in set II. Solidification direction is from the bottom towards the top. Image presenting sample surface topography obtained with a scanning electron microscope (SEM) using secondary electrons (SE).

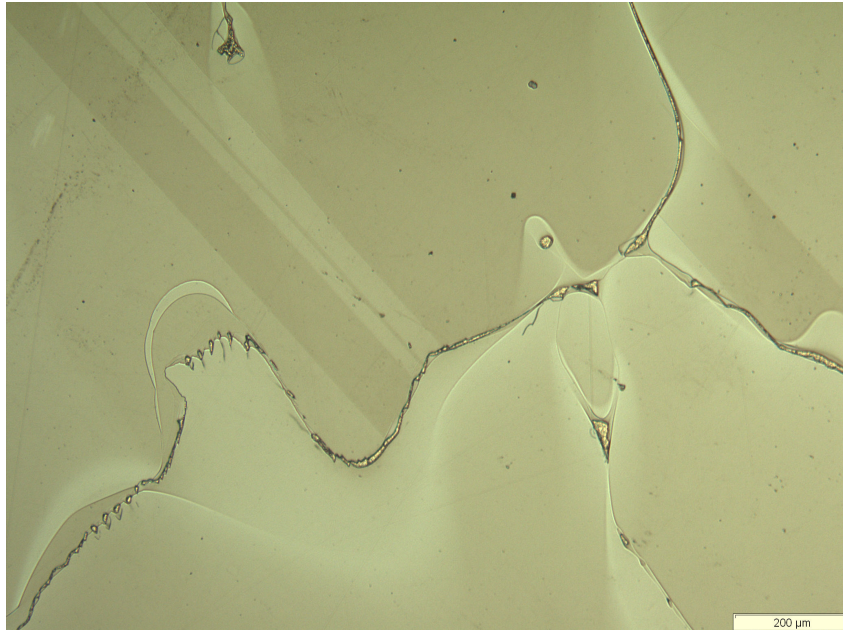


Figure 5.21: Precipitates observed on the surface of a sample obtained from experiments in set II. Solidification direction from the bottom towards the top of the image. Image obtained using an optical microscope.

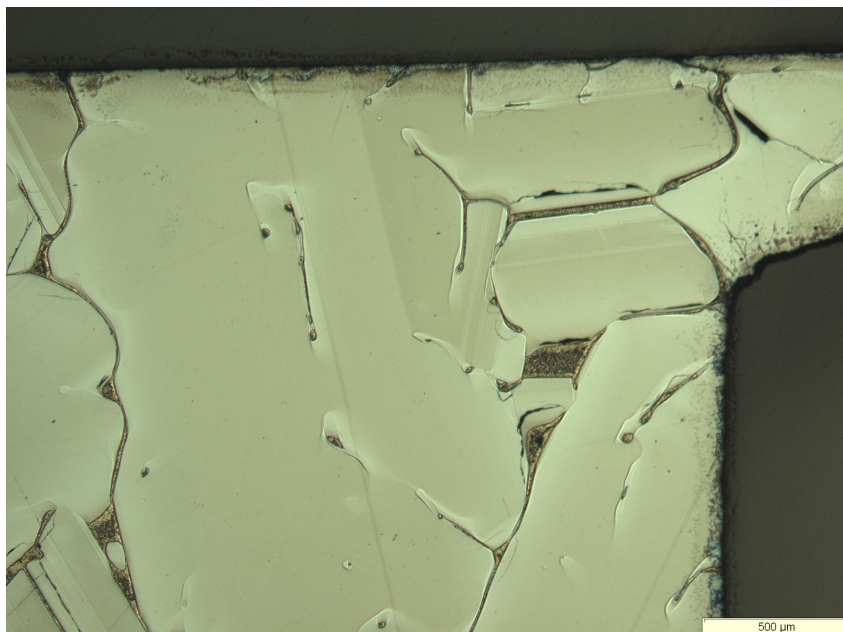


Figure 5.22: Precipitates observed on the surface of a sample obtained from experiments in set II. Solidification direction from the bottom towards the top of the image. Image obtained using an optical microscope.

5.2.4 Results on experiments set III

Experiment set III consists in another four performed experiments. The experimental conditions are summarised in Table 5.5. More details about the experimental conditions for this set are specified in Chapter 4 where results regarding the demarcation of the solidification interface as well as numerical simulations results are presented.

Table 5.5: Experiment set III

Experiment number	Raw material	Imposed ΔT	Pulling velocity [m/s]	TMF intensity [mT]	TMF orientation
III.1	Si-A	400	$4 \cdot 10^{-6}$	0	-
III.2	Si-A	350	$4 \cdot 10^{-6}$	4	Downward
III.3	Si-A	350	$4 \cdot 10^{-6}$	4	Upward
III.4	Si-A	350	$4 \cdot 10^{-6}$	4	Alternating

The secondary objective for these experiments, besides marking the solidification interface, was to observe the impurity segregation for different magnetic field orientations. The main difference between experiments in set I and III is that in the first one the crucible remains in a fix position and the heaters were cooled at a constant rate while in the set III, the thermal field remains unchanged and the crucible is pulled downwards with a constant velocity.

The impurity concentrations evolution along the ingot height was obtained with the same method as for the previous experiments. Several silicon samples were removed from the ingot at different heights and had the average concentration of different impurities measured using ICP method. The results obtained for aluminium, iron and phosphorus are presented in Figures 5.23, 5.24 and 5.25. For aluminium (Figure 5.23), the measured values for all experiments are slightly below the initial concentration C_0 for about 80% of the ingot height. This indicates that the magnetic field used in experiments III.2, III.3 and III.4 had a very small influence on the segregation process. Moreover, at the top of the ingot, the measured values increase with a factor of 100 for all experiments.

The iron distribution (Figure 5.24) presents a striking resemblance to the aluminium one. About 80% of the ingot height revealed concentrations close to C_0 for all experiments and in the last 10%, the measured values increase more then 100 times for three out of four experiments.

The phosphorus concentration distribution (Figure 5.25) shows a constant value around C_0 for most of the ingot height for all experiments. At the end

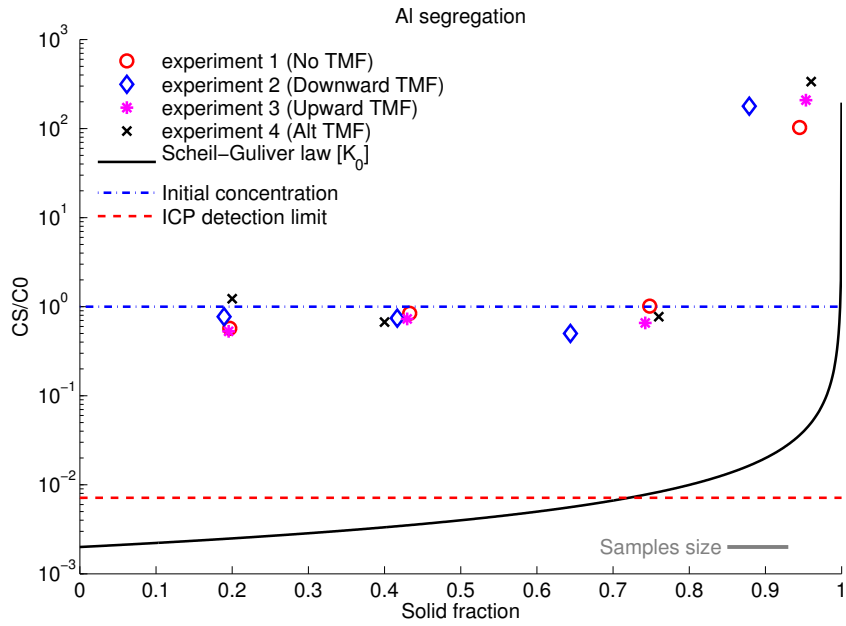


Figure 5.23: Aluminium axial segregation along the ingot centre for experiments in set III.

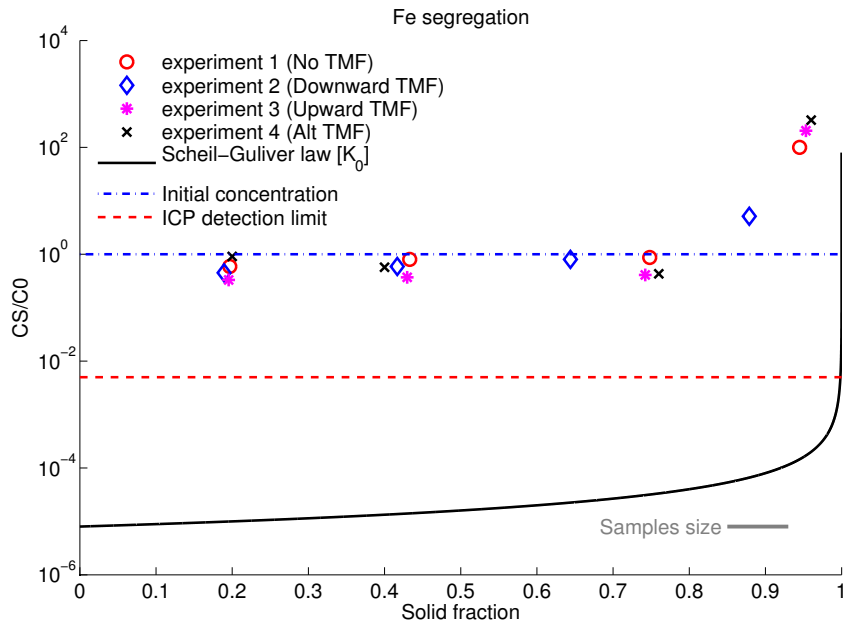


Figure 5.24: Iron axial segregation along the ingot centre for experiments in set III.

of the solidification up to 10 times higher values than C_0 are observed for experiments III.1, III.3 and III.4. However, for Experiment III.2 the phosphorus levels was recorded at ≈ 0.9 of the solid fraction to be almost 100 times higher than C_0 .

For the first numerical simulations, the ANSYS FLUENT solidification

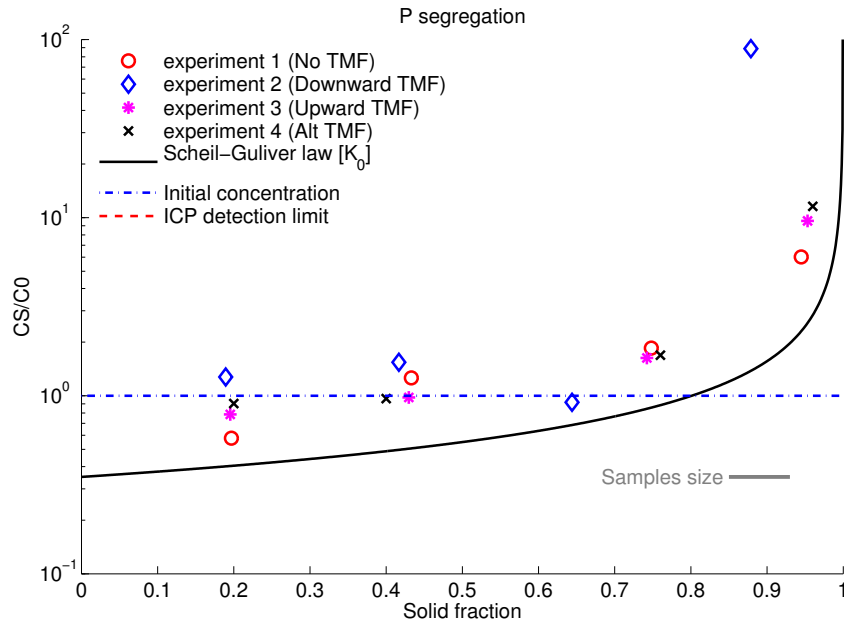


Figure 5.25: Phosphorus axial segregation along the ingot centre for experiments in set III.

module was used to compute the solidification interface and the results are presented in Chapter 4. In order to also consider the impurity segregation, in the new simulations, the SIMAP/EPM solidification model was used. Details about the solidification module can be found in Chapter 3 Section 3.3. The experiments for which numerical simulations were conducted are Experiments III.1 and III.2.

The flow patterns and liquid velocities obtained in this simulations are identical with the ones presented in Chapter 4 Figures 4.12b and 4.14b. The computed interface shape and positions are the same for both solidification modules in the case of Experiment III.1 and in Chapter 4 was shown that they are also in concordance with the experimentally observed ones. However, for Experiment III.2 the interface position is computed at about the same position in the new simulations as in the old ones but the shape is different. Figure 5.26 depicts a comparison between the experimentally observed interface, the interface computed with ANSYS FLUENT solidification module (Simulation 1) and the one computed with the SIMAP/EPM module (Simulation 2) at the same time. The interface computed in Simulation 2 indicates that the flow patterns have less impact on the interface shape than Simulation 1 suggested. This could indicate that the Fluent solidification module used in Simulation 1 may have some difficulties in computing a correct shape for the solidification interface. Unfortunately, both computed shapes correspond to an axisymmet-

ric flow while the experimentally observed one has a 3D liquid flow.

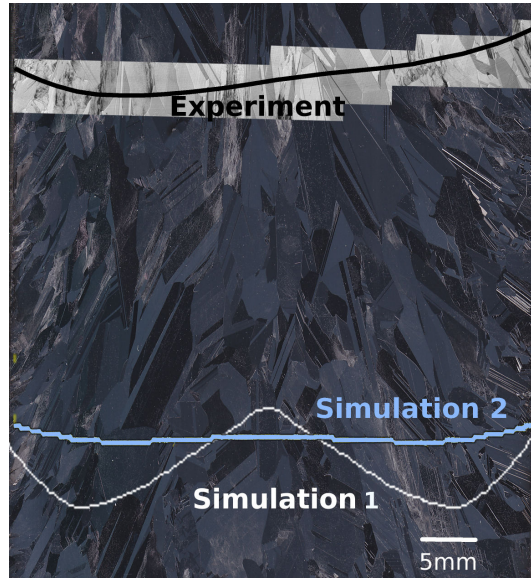


Figure 5.26: Comparison of experimental and computed interfaces for experiment III.2. Simulation 1 is obtained with ANSYS FLUENT solidification module while Simulation 2 is obtained with SIMAP/EPM solidification module.

The impurities considered for this simulations are aluminium and iron with an identical initial concentration $C_0 = 10^{-5}$ mass fraction (10ppm). The computed aluminium distribution in the liquid at different instants in time during Experiment III.1 is depicted in Figure 5.27. Computed values as small as $10^{-3}m/s$ for the liquid velocity are enough to redistribute the aluminium along the solidification interface. The highest aluminium concentrations are computed in the center of the ingot and it can go up to 10 times the initial concentration at about 80% of the ingot height. The bulk mean concentration goes from C_0 in the beginning to just about 3 times higher at a solid fraction of 0.8. The flow patterns for this experiment (see Figure 4.12b) presents two toroidal vortices, one close to the interface and another in the upper part of the liquid, turning in opposite directions. With this particularity of the flow, the boundary between the two vortices, acts like a barrier for the solute distribution in the melt. This is the main reason for the presence of the two regions, with different solute concentrations.

The computed aluminium distribution in the liquid at different instants in time during Experiment III.2 is depicted in Figure 5.28. Because of the magnetic field, the liquid velocity is significantly increased which leads to a more homogeneous distribution of the solutes in the liquid. Due to the fact

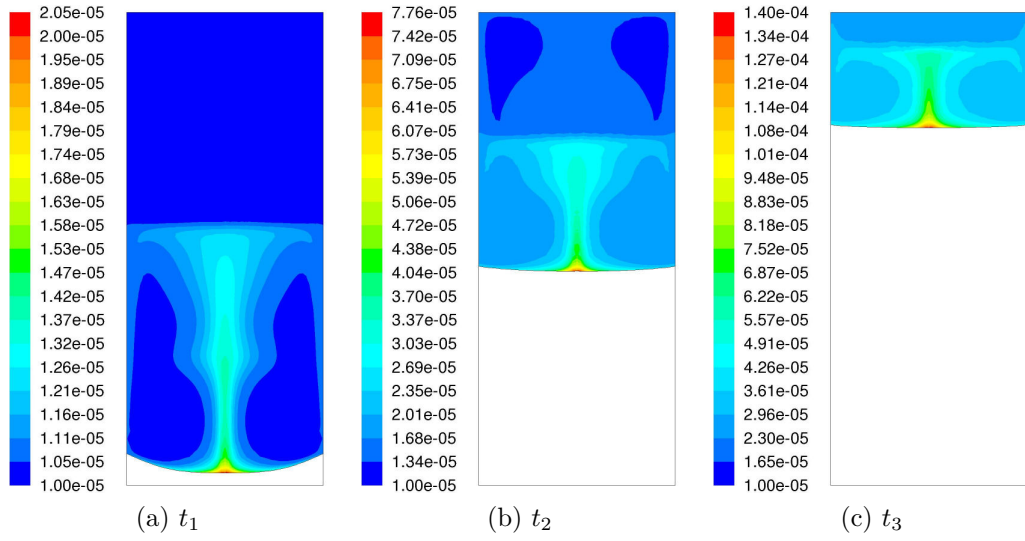


Figure 5.27: Evolution in time of the aluminium distribution in liquid silicon for Experiment III.1. Colour map values are expressed in mass fraction.

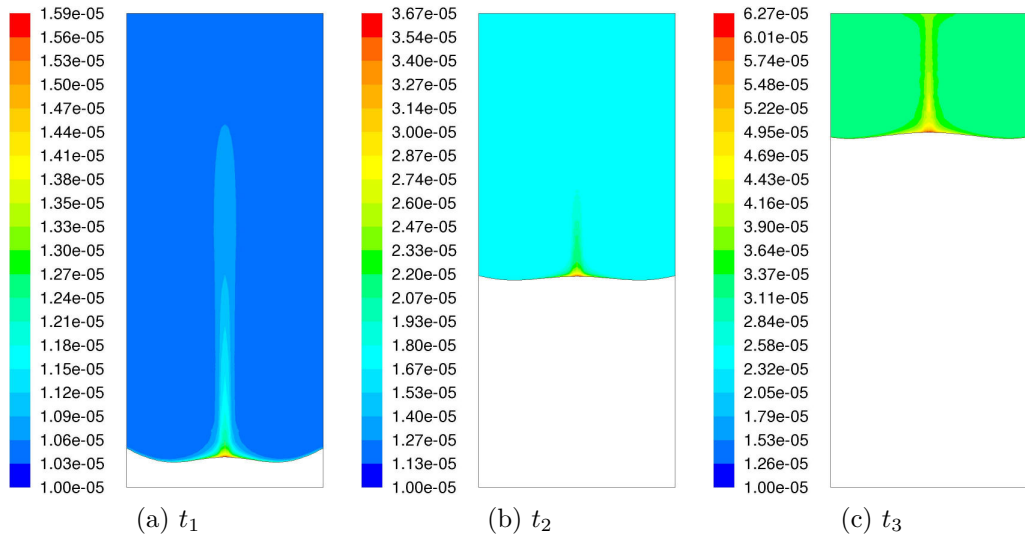


Figure 5.28: Evolution in time of the aluminium distribution in liquid silicon for Experiment III.2. Colour map values are expressed in mass fraction.

that near the interface, the liquid flow patterns in the first experiment as well as in the second one have the same orientation (see Figures 4.12b and 4.14b), the solvents presents the same distribution pattern along the interface for both experiments. The impurity concentration in the center of the ingot is higher than on the borders, near the crucible walls. For Experiments III.1 and III.2, the aluminium radial distribution at the interface, in the liquid, is depicted in Figure 5.29. The values of the solid fraction, at which the C_l is presented, corresponds to the instants t_1, t_2 and t_3 from Figures 5.27 and 5.28. For

Experiment III.1 the numerical model computed higher aluminium concentration at the interface compared to the Experiment III.2, at the same solid fraction. For both experiments, at the center of the ingot, the concentration was significantly increased compared to the edges, close to the crucible walls.

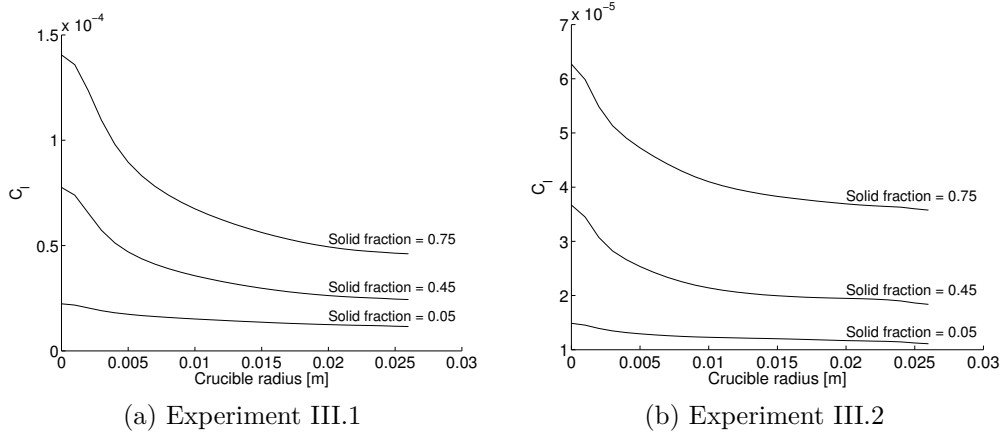


Figure 5.29: Simulated aluminium distribution in liquid silicon at the interface.

By multiplying the aluminium values in the liquid, at the interface, with the segregation coefficient K_0 , the aluminium levels in the solid, at the interface (C_s) can be estimated. Dividing C_s by the mean concentration in the liquid bulk (C_{bulk}), an effective segregation coefficient along the interface radius can be determined, for the performed simulations. Figure 5.30 presents the K_{eff} values, computed as C_s/C_{bulk} , along the interface, for three different positions (solid fraction). For both experiments, at any of the solid fraction value, the K_{eff} computed in the center of the ingot is higher than on the edges. Close to the crucible walls the computed values for K_{eff} for all solid fractions, are close to the theoretical value of the aluminium segregation coefficient $K_0 = 2 \cdot 10^{-3}$. However, at the ingot center, smaller values of K_{eff} are computed for Experiment III.2, compared to III.1 for the same value of the solid fraction. For any of the performed simulations, at a constant radius, a variation of the K_{eff} with the solid fraction is observed, especially at the beginning of the solidification. This indicates that the K_{eff} does not have a constant value during the entire solidification process.

Figure 5.31 presents for both experiments, the computed maximum aluminium concentration in the solid (ingot center), normalised to the initial concentration, along the solid fraction. Using a constant value for K_{eff} (computed at 0.45 solid fraction in the center of the ingot), a Scheil-Guliver law was added on the figure for each experiment. In these case, the Scheil-Guliver law

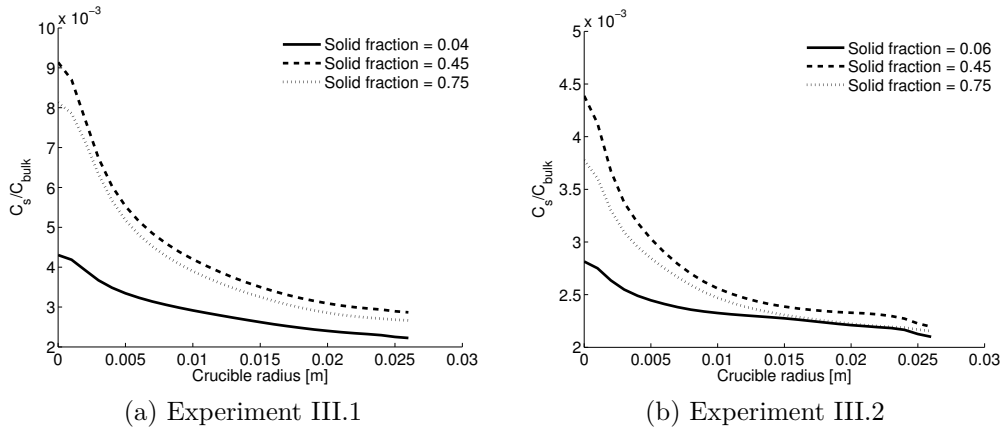


Figure 5.30: Computed K_{eff} for aluminium along the solidification interface.

is representing the theoretical axial distribution of the aluminium, obtained for previously computed values of K_{eff} in the center of the ingot at a given value of the solid fraction. The reader should be aware that with an axial and radial variation of K_{eff} (see Figure 5.30), the representation of the Scheil-Guliver law in Figure 5.31, computed as described above, does not represent the correct description of the theoretical solution. For the second experiment, where TMF was used, lower aluminium concentrations were computed at the center of the ingot compared to the first experiment, where no TMF was used. In the first 20% of the solidification, the computed aluminium concentration for each experiment seems to describe the initial transient (first presented in Section 5.1), after which a steady regime is reached. However, the Scheil-Guliver law does not include the initial transient. Therefore, the comparison of the computed concentrations with the Scheil-Guliver law, can be analysed for a solid fraction, greater than 0.2, for each experiment.

Figure 5.32 presents the axial concentrations using the minimum computed aluminium values at the interface (at the ingot border). The Scheil-Guliver law was computed this time using the theoretical K_0 for aluminium, which is close to the computed K_{eff} (see Figure 5.30).

The simulation results regarding aluminium axial distribution (Figures 5.31 and 5.32) seems to be rather different from the ones observed experimentally (Figure 5.23). The numerical model seems not to describe all the experimental conditions. For instance, a relevant difference between the model and the real experiment, is the crystal grain structure. The numerical model does not describe the grain boundaries while in reality, most of the impurities are trapped in there.

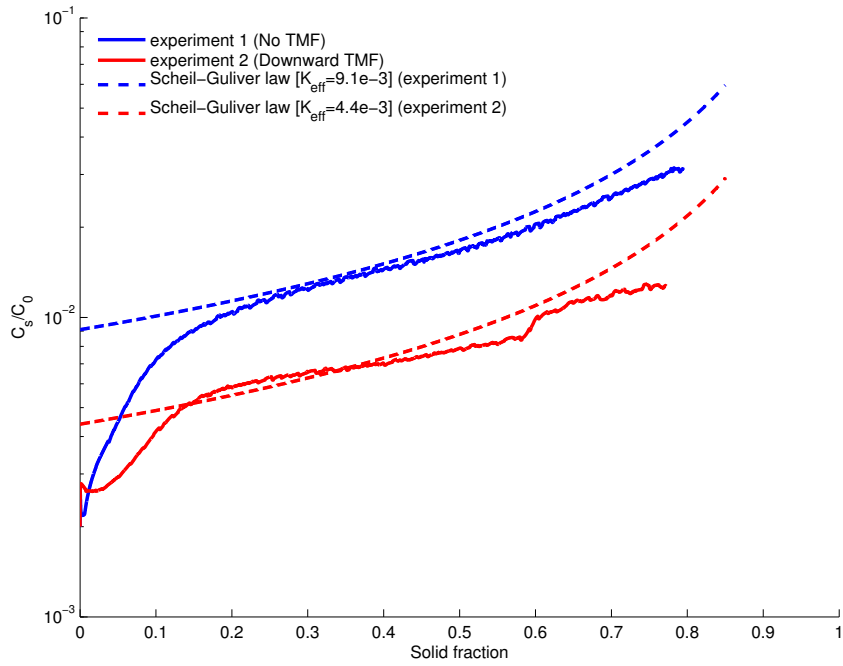


Figure 5.31: Computed maximum values of aluminium at the interface (liquid side) for experiments in set III. Aluminium axial segregation at the center of the ingot.

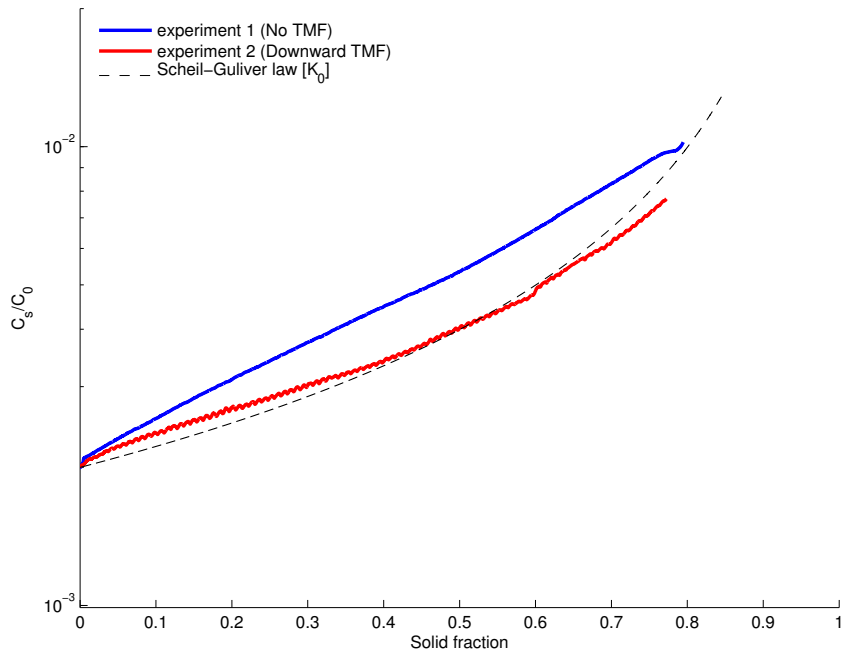


Figure 5.32: Computed minimum values of aluminium at the interface (liquid side) for experiments in set III. Aluminium axial segregation on the edges of the ingot.

The simulation results regarding the iron and phosphorus segregation for these experiments are presented in Appendix E .

5.3 Conclusions

This chapter was completely dedicated to the chemical segregation during a directional solidification process under the influence of a travelling magnetic field. At the beginning of the chapter, the theoretical aspects regarding these phenomena were presented. Most of the chapter content focuses on experimental results, in parallel with numerical simulations. After presenting an overview of the analysis methodology used for the experiments, the results are divided into three experimental sets.

The initial results for the first set of experiments (the same first set from Chapter 4), where different orientations of the travelling magnetic field were used, present the measured impurity concentration along the height of the obtained ingots. In this study, the analysed impurities were aluminium, iron and phosphorus. These results clearly indicate an improvement of the segregation efficiency with the increased intensity of the magnetic field, for all analysed impurities. Using a scanning electron microscope (SEM), the crystal surface was also analysed, relating the amount of the observed precipitates with the impurity concentrations measured.

In the second set, experiments using highly contaminated silicon were conducted. An interface breakdown, due to a possible morphological instability, was observed and analysed. The evolution of impurities along the height of the ingots was also measured. The images obtained with the scanning electron microscope revealed important precipitate agglomerations at the tip of unusual column-like structures and at the grain boundaries.

The last set of experiments presented in this chapter consisted in multiple experiments with different orientations of the travelling magnetic field. Measurements of the impurity concentrations along the height of the ingots were performed as well, but for these experiments, the focus was on the numerical results. For some of these experiments, numerical simulations were conducted using the SIMaP/EPM solidification module to simulate the segregation phenomena. The last part of this chapter is dedicated to these numerical results, which are analysed in detail. The numerical results regarding the axial segregation of impurities do not seem to correctly describe the experimentally obtained ones, most probably due to an incomplete description in the model

of all the involved phenomena, such as the presence of the grain boundaries at the solidification interface.

General conclusions and perspectives

The objectives of this thesis were to study and improve the segregation process efficiency in a directional solidification process of silicon by using a travelling magnetic field, as well as controlling the solidification interface shape. These aspects of the solidification process represent important steps in obtaining high quality photovoltaic modules. By improving the efficiency of these steps, the production cost for photovoltaic modules can be reduced.

In this study, an experimental set-up consisting in a Bridgman type solidification furnace, equipped with an electromagnet stirrer, was used. The Bitter type electromagnet, able to create a travelling magnetic field, was used to stir the melt during the solidification process, directly influencing the segregation process, as well as the solidification interface shape. Multiple experiments were conducted where the main varying parameter was the orientation of the travelling magnetic field. In these experiments, upward and downward orientations were selected as well as alternating these orientations in some of the experiments. Measurements of the impurity distribution along the height of the ingot were performed for each experiment, and for some of them the solid-liquid interface was marked.

In parallel to the experimental study, a numerical model has also been developed using the commercial software ANSYS FLUENT. The model, covering the entire furnace geometry, was designed to provide information complementary to the experimental data. The simulations give detailed temperature maps of the furnace, as well as important information regarding the solidification process, like flow patterns, liquid velocities and the solid-liquid interface shape and relative position during the solidification process. To complete the model, a new solidification module able to simulate the segregation process for such processes was developed in SIMaP/EPM laboratory.

In some of the performed experiments, demarcation of the solid-liquid in-

interface during the solidification are performed, using two techniques. The marks obtained using Peltier effect were not clearly visible close to the crucible walls. Another problem encountered with this method was the limitation in diameter of the used crucibles. By creating variations of the magnetic field intensities, demarcations of the interface on normal sized ingots (2 inches in diameter) were performed, in a series of experiments which allowed a comparison of these marks with the interface computed by the numerical model. While the computed interfaces and the experimentally obtained ones matched for the case without the use of the magnetic field, differences were observed for the cases which used TMF. The experimentally obtained demarcations of the interface indicated the possibility of a non-axisymmetric flow in the melt, which was further studied, using a liquid metal (GaInSn) at room temperature. This study indicated a very high sensitivity of the flow stability, inside the crucible, when the magnetic field is used and also confirmed the possibility of a 3D flow in the melt.

The thickness of the interface marks, obtained with both procedures, was measured at $\approx 300\mu m$. With this performance, the demarcations can be successfully used to observe the flow impact on the shape of the interface or to improve numerical models by comparing results. However, the marks are too thick to observe details such as facets on the interface. Therefore, the possibility of improving the quality of the demarcations, by reducing their thickness, can be further analysed. For these further studies, some suggestions can be made. If Peltier method is used, decreasing the durations of injected electrical current while increasing its intensity, should produce thinner marks. If a travelling magnetic field is used to perform the demarcations, various combinations of its intensity, orientation and duration should be tested. What dopant material is better to use and in which concentration is another important question to answer in this case, regardless of the used procedure.

Regarding the flow instability observed in GaInSn and indirectly in the silicon melt, through the performed demarcation of the interface, further analysis is required. There are multiple possible causes for an induced flow to become unstable in an axisymmetrical configuration. The bibliographic study triggered by these results showed that the liquid flow can easily become unstable, for the specificities of VB2 furnace and the TMF intensities used in the solidification experiments. Moreover, imperfections in the geometrical symmetry of the furnace components can also lead to a non-axisymmetric flow in the melt induced by the TMF. The sources of the non-axisymmetric flow,

related to the symmetry of the furnace components, must be eliminated. Once this is done, experimental considerations for which the flow remain axisymmetric should be identified. In a regained 2D axisymmetrical flow, the influence of the alternated TMF on the segregation phenomena and the interface shape must be re-analysed. In this study, different durations for each orientation of the TMF must be considered.

The segregation phenomenon was also considered by this study and measurements of the impurity concentrations (aluminium, iron and phosphorus) were done along the height of the ingots from all performed experiments. In some of these experiments, a significant decrease of the impurity concentration in the ingots was observed as a consequence of the electromagnetic stirring. Most of the ingots were also analysed using a scanning electron microscope (SEM), which revealed various precipitates and crystal defects. In some experiments, where highly contaminated silicon was used, an interface breakdown, due to a possible morphological instability, was observed and analysed. Numerical simulations, using the SIMaP/EPM solidification module was used to simulate the segregation phenomena. These numerical results were analysed in details in the last chapter. These results concerning the axial segregation of impurities, are comparable with the experimental ones obtained under TMF. However, they do not seem to correctly describe the experimental results obtained under natural convection, where the liquid velocity was considerably smaller. The presence of the grain boundaries at the solidification interface, not taken into account by the model, could be one of the reasons for these differences. Therefore, the segregation results provided by the new solidification model could be experimentally validated in a mono-crystalline ingot, where the grain boundary presence at the interface is eliminated.

The solidification module can be further developed. The influence of a more precise description of the solidification interface details (i.e. including facets) over the solute accumulation in the liquid, in various experimental conditions, can be tested. The goal is to improve the numerical simulations by finding and correcting the current differences. The module can also be tested for other types of crystallization methods such as Czochralski, floating zone or continuous casting processes.

Bibliography

- [1] G. Masson, S. Orlandi, M. Reking, Global market outlook for photovoltaics 2014-2018, Tech. rep., European Photovoltaic Industry Association (EPIA) (2014).
URL <http://www.epia.org/news/publications/>
- [2] H. Ossenbrink, T. Huld, A. J. Waldau, N. Taylor, Photovoltaic electricity cost maps, Tech. Rep. JRC 83366, European Commission Joint Research Centre Institute for Energy and Transport (2013).
URL <http://iet.jrc.ec.europa.eu/remea/photovoltaic-electricity-cost-maps>
- [3] A. Campoccia, L. Dusonchet, E. Telaretti, G. Zizzo, An analysis of feed-in tariffs for solar pv in six representative countries of the european union, Solar Energy 107 (0) (2014) 530 – 542. doi:<http://dx.doi.org/10.1016/j.solener.2014.05.047>.
- [4] National Renewable Energy Laboratory (NREL) (2014). [link].
URL <http://www.nrel.gov/ncpv/>
- [5] S. Pizzini, Towards solar grade silicon: Challenges and benefits for low cost photovoltaics, Solar Energy Materials and Solar Cells 94 (9) (2010) 1528 – 1533, {PVSEC} 18. doi:<http://dx.doi.org/10.1016/j.solmat.2010.01.016>.
- [6] K. Nakajima, N. Usami, S. O. service), Crystal Growth of Si for Solar Cells, Advances in Materials Research,, Springer Berlin Heidelberg,, Berlin, Heidelberg :, 2009. doi:<http://dx.doi.org/10.1007/978-3-642-02044-5>.
- [7] Y. Delannoy, Purification of silicon for photovoltaic applications, Journal of Crystal Growth 360 (0) (2012) 61 – 67, 5th International Workshop on Crystal Growth Technology. doi:<http://dx.doi.org/10.1016/j.jcrysgr.2011.12.006>.

- [8] N. Nakamura, H. Baba, Y. Sakaguchi, Y. Kato, Boron removal in molten silicon by a steam-added plasma melting method, *Materials Transactions* 45 (3) (2004) 858 – 864.
- [9] B. Wu, N. Stoddard, R. Ma, R. Clark, Bulk multicrystalline silicon growth for photovoltaic (pv) application, *Journal of Crystal Growth* 310 (7-9) (2008) 2178 – 2184, the Proceedings of the 15th International Conference on Crystal Growth (ICCG-15) in conjunction with the International Conference on Vapor Growth and Epitaxy and the US Biennial Workshop on Organometallic Vapor Phase Epitaxy. doi:http://dx.doi.org/10.1016/j.jcrysgro.2007.11.194.
- [10] M. Trempa, C. Reimann, J. Friedrich, G. Müller, The influence of growth rate on the formation and avoidance of c and n related precipitates during directional solidification of multi crystalline silicon, *Journal of Crystal Growth* 312 (9) (2010) 1517 – 1524. doi:http://dx.doi.org/10.1016/j.jcrysgro.2010.02.005.
- [11] H. E. Ghitani, M. Pasquinelli, S. Martinuzzi, Influence of dislocations on photovoltaic properties of multicrystalline silicon solar cells, *Journal de Physique III France*, EDP Sciences 3 (10) (1993) 1941 – 1946. doi:http://dx.doi.org/10.1051/jp3:1993251.
- [12] Y. Miyamura, H. Harada, K. Jiptner, J. Chen, R. Prakash, S. Nakano, B. Gao, K. Kakimoto, T. Sekiguchi, Crystal growth of 50 cm square mono-like si by directional solidification and its characterization, *Journal of Crystal Growth* 401 (0) (2014) 133 – 136, proceedings of 17th International Conference on Crystal Growth and Epitaxy (ICCGE-17). doi:http://dx.doi.org/10.1016/j.jcrysgro.2014.03.016.
- [13] M. Trempa, C. Reimann, J. Friedrich, G. Müller, D. Oriwol, Monocrystalline growth in directional solidification of silicon with different orientation and splitting of seed crystals, *Journal of Crystal Growth* 351 (1) (2012) 131 – 140. doi:http://dx.doi.org/10.1016/j.jcrysgro.2012.04.035.
- [14] V. Pupazan, R. Negrila, O. Bunoiu, I. Nicoara, D. Vizman, Effects of crucible coating on the quality of multicrystalline silicon grown by a bridgman technique, *Journal of Crystal Growth* 401 (0) (2014) 720 – 726, proceedings of 17th International Conference on Crystal Growth and Epitaxy (ICCGE-17). doi:http://dx.doi.org/10.1016/j.jcrysgro.2014.02.038.

- [15] Y. Wong, C. Hsieh, A. Lan, C. Hsu, C. Lan, The effect of silica nucleation layers on grain control of multi-crystalline silicon in directional solidification, *Journal of Crystal Growth* 404 (0) (2014) 59 – 64. doi:<http://dx.doi.org/10.1016/j.jcrysgro.2014.06.047>.
- [16] C. Reimann, M. Trempa, T. Jung, J. Friedrich, G. Müller, Modeling of incorporation of o, n, c and formation of related precipitates during directional solidification of silicon under consideration of variable processing parameters, *Journal of Crystal Growth* 312 (7) (2010) 878 – 885. doi:<http://dx.doi.org/10.1016/j.jcrysgro.2009.11.070>.
- [17] N. Mangelinck-Noël, T. Duffar, Modelling of the transition from a planar faceted front to equiaxed growth: Application to photovoltaic polycrystalline silicon, *Journal of Crystal Growth* 311 (1) (2008) 20 – 25. doi:<http://dx.doi.org/10.1016/j.jcrysgro.2008.10.011>.
- [18] M. Beaudhuin, Étude expérimentale et numérique de la précipitation d'impuretés et de la formation des grains dans le silicium photovoltaïque, Ph.D. thesis, Institut polytechnique de Grenoble (2009).
- [19] M. Bellmann, H. Dalaker, M. Syvertsen, S. Gouttebroze, M. M'Hamdi, Optimization of silicon crystallization in a bridgman growth furnace by numerical modeling, *Journal of Crystal Growth* 362 (0) (2013) 38 – 41, the 5th Asia Conference on Crystal Growth and Crystal Technologies. doi:<http://dx.doi.org/10.1016/j.jcrysgro.2011.12.093>.
- [20] M. Bellmann, E. Meese, L. Arnberg, Impurity segregation in directional solidified multi-crystalline silicon, *Journal of Crystal Growth* 312 (21) (2010) 3091 – 3095. doi:<http://dx.doi.org/10.1016/j.jcrysgro.2010.07.052>.
- [21] F. Santara, Y. Delannoy, A. Autruffe, Electromagnetic stirring and retention to improve segregation in silicon for photovoltaics, *Journal of Crystal Growth* 340 (1) (2012) 41 – 46. doi:<http://dx.doi.org/10.1016/j.jcrysgro.2011.11.074>.
- [22] S. Dumitrica, D. Vizman, J.-P. Garandet, A. Popescu, Numerical studies on a type of mechanical stirring in directional solidification method of multicrystalline silicon for photovoltaic applications, *Journal of Crystal Growth* 360 (0) (2012) 76 – 80, 5th International Workshop on Crystal Growth Technology. doi:<http://dx.doi.org/10.1016/j.jcrysgro.2012.01.011>.

- [23] P. Rudolph, Travelling magnetic fields applied to bulk crystal growth from the melt: The step from basic research to industrial scale, *Journal of Crystal Growth* 310 (7–9) (2008) 1298 – 1306, the Proceedings of the 15th International Conference on Crystal Growth (ICCG-15) in conjunction with the International Conference on Vapor Growth and Epitaxy and the US Biennial Workshop on Organometallic Vapor Phase Epitaxy. doi:<http://dx.doi.org/10.1016/j.jcrysgro.2007.11.036>.
- [24] S. Yesilyurt, S. Motakef, R. Grugel, K. Mazuruk, The effect of the traveling magnetic field (tmf) on the buoyancy-induced convection in the vertical bridgman growth of semiconductors, *Journal of Crystal Growth* 263 (1–4) (2004) 80 – 89. doi:<http://dx.doi.org/10.1016/j.jcrysgro.2003.11.066>.
- [25] N. Dropka, C. Frank-Rotsch, P. Rudolph, Comparison of stirring efficiency of various non-steady magnetic fields during unidirectional solidification of large silicon melts, *Journal of Crystal Growth* 365 (0) (2013) 64 – 72. doi:<http://dx.doi.org/10.1016/j.jcrysgro.2012.12.009>.
- [26] N. Dropka, C. Frank-Rotsch, P. Rudolph, Numerical study on stirring of large silicon melts by carousel magnetic fields, *Journal of Crystal Growth* 354 (1) (2012) 1 – 8. doi:<http://dx.doi.org/10.1016/j.jcrysgro.2012.05.037>.
- [27] D. Vizman, K. Dadzis, J. Friedrich, Numerical parameter studies of 3d melt flow and interface shape for directional solidification of silicon in a traveling magnetic field, *Journal of Crystal Growth* 381 (0) (2013) 169 – 178. doi:<http://dx.doi.org/10.1016/j.jcrysgro.2013.06.023>.
- [28] K. Dadzis, D. Vizman, J. Friedrich, Unsteady coupled 3d calculations of melt flow, interface shape, and species transport for directional solidification of silicon in a traveling magnetic field, *Journal of Crystal Growth* 367 (0) (2013) 77 – 87. doi:<http://dx.doi.org/10.1016/j.jcrysgro.2012.12.135>.
- [29] D. Vizman, J. Friedrich, G. Mueller, 3d time-dependent numerical study of the influence of the melt flow on the interface shape in a silicon ingot casting process, *Journal of Crystal Growth* 303 (1) (2007) 231 – 235, proceedings of the Fifth Workshop on Modeling in Crystal Growth IWMCG-5. doi:<http://dx.doi.org/10.1016/j.jcrysgro.2006.11.317>.
- [30] F.-M. Kiessling, F. Büllesfeld, N. Dropka, C. Frank-Rotsch, M. Müller, P. Rudolph, Characterization of mc-si directionally solidified in travelling

- magnetic fields, *Journal of Crystal Growth* 360 (0) (2012) 81 – 86, 5th International Workshop on Crystal Growth Technology. doi:<http://dx.doi.org/10.1016/j.jcrysgro.2012.03.017>.
- [31] N. Dropka, C. Frank-Rotsch, W. Miller, P. Rudolph, Influence of travelling magnetic fields on s–l interface shapes of materials with different electrical conductivities, *Journal of Crystal Growth* 338 (1) (2012) 208 – 213. doi:<http://dx.doi.org/10.1016/j.jcrysgro.2011.10.007>.
- [32] J. A. Burton, R. C. Prim, W. P. Slichter, The distribution of solute in crystals grown from the melt. part i. theoretical, *The Journal of Chemical Physics* 21 (11) (1953) 1987–1991. doi:<http://dx.doi.org/10.1063/1.1698728>.
- [33] L. O. Wilson, On interpreting a quantity in the burton, prim and slichter equation as a diffusion boundary layer thickness, *Journal of Crystal Growth* 44 (2) (1978) 247 – 250. doi:[http://dx.doi.org/10.1016/0022-0248\(78\)90199-9](http://dx.doi.org/10.1016/0022-0248(78)90199-9).
- [34] A. Ostrogorsky, Effective convection coefficient for porous interface and solute segregation, *Journal of Crystal Growth* 348 (1) (2012) 97 – 105. doi:<http://dx.doi.org/10.1016/j.jcrysgro.2012.03.049>.
- [35] B. Gao, X. Chen, S. Nakano, K. Kakimoto, Crystal growth of high-purity multicrystalline silicon using a unidirectional solidification furnace for solar cells, *Journal of Crystal Growth* 312 (9) (2010) 1572 – 1576. doi:<http://dx.doi.org/10.1016/j.jcrysgro.2010.01.034>.
- [36] Influence of traveling magnetic field on the crystallization of multicrystalline Silicon, the 4th International Workshop on Science and Technology of crystalline Si Solar Cells, Taipei, Taiwan, Proceedings on CD-ROM, published by the Industrial Technology Institute of Taiwan.
- [37] K. Zaïdat, T. Ouled-Khachroum, G. Vian, C. Garnier, N. Mangelinck-Noël, M. Dupouy, R. Moreau, Directional solidification of refined al-3.5 wt% ni under natural convection and under a forced flow driven by a travelling magnetic field, *Journal of Crystal Growth* 275 (1–2) (2005) e1501 – e1505, proceedings of the 14th International Conference on Crystal Growth and the 12th International Conference on Vapor Growth and Epitaxy. doi:<http://dx.doi.org/10.1016/j.jcrysgro.2004.11.182>.
- [38] ANSYS FLUENT Theory Guide, Release 14.5 October 2012. [link].
URL <http://www.ansys.com>

- [39] Y. Delannoy, C. Alemany, K.-I. Li, P. Proulx, C. Trassy, Plasma-refining process to provide solar-grade silicon, *Solar Energy Materials and Solar Cells* 72 (1-4) (2002) 69–75. doi:[10.1016/S0927-0248\(01\)00151-9](https://doi.org/10.1016/S0927-0248(01)00151-9).
- [40] F. R. Menter, Two-equation eddy-viscosity turbulence models for engineering applications, *Aiaa Journal* 32 (1994) 1598–1605. doi:[10.2514/3.12149](https://doi.org/10.2514/3.12149).
- [41] V. Voller, C. Prakash, A fixed grid numerical modelling methodology for convection-diffusion mushy region phase-change problems, *International Journal of Heat and Mass Transfer* 30 (8) (1987) 1709 – 1719. doi:[http://dx.doi.org/10.1016/0017-9310\(87\)90317-6](http://dx.doi.org/10.1016/0017-9310(87)90317-6).
- [42] A. Bianchi, Y. Fautrelle, J. Etay, *Transferts thermiques*, Presses Polytechniques et Universitaires Romandes, Lausanne, 2004.
- [43] W. Kurz, D. J. Fisher, *Fundamentals of solidification*, 1986.
- [44] H. Kodera, Diffusion Coefficients of Impurities in Silicon Melt, *Japanese Journal of Applied Physics* 2 (1963) 212–219. doi:[10.1143/JJAP.2.212](https://doi.org/10.1143/JJAP.2.212).
- [45] S. Corre, T. Duffar, M. Bernard, M. Espezel, Numerical simulation and validation of the peltier pulse marking of solid/liquid interfaces, *Journal of Crystal Growth* 180 (3–4) (1997) 604 – 614, modelling in Crystal Growth. doi:[http://dx.doi.org/10.1016/S0022-0248\(97\)00257-1](http://dx.doi.org/10.1016/S0022-0248(97)00257-1).
- [46] X. Wang, Y. Fautrelle, J. Etay, R. Moreau, A periodically reversed flow driven by a modulated traveling magnetic field: Part i. experiments with gainsn, *Metallurgical and Materials Transactions B* 40 (1) (2009) 82–90. doi:[10.1007/s11663-008-9176-0](https://doi.org/10.1007/s11663-008-9176-0).
- [47] A. Y. Gelfgat, On three-dimensional instability of a traveling magnetic field driven flow in a cylindrical container, *Journal of Crystal Growth* 279 (3–4) (2005) 276 – 288. doi:<http://dx.doi.org/10.1016/j.jcrysgro.2005.02.030>.
- [48] I. Grants, G. Gerbeth, Stability of melt flow due to a traveling magnetic field in a closed ampoule, *Journal of Crystal Growth* 269 (2–4) (2004) 630 – 638. doi:<http://dx.doi.org/10.1016/j.jcrysgro.2004.05.090>.
- [49] A. Cramer, J. Pal, K. Koal, S. Tschisgale, J. Stiller, G. Gerbeth, The sensitivity of a travelling magnetic field driven flow to axial alignment, *Journal of Crystal Growth* 321 (1) (2011) 142 – 150. doi:<http://dx.doi.org/10.1016/j.jcrysgro.2011.02.020>.
- [50] E. Scheil, Bemerkungen zur schichtkristallbildung, *Zeitschrift für Metallkunde* 34 (1942) 70–72.

Appendix A

Multilayer thermal insulation

For the multilayer thermal insulation, two different materials were used in order to increase the overall thermal conductivity. The insulation was positioned around the crucible. Values of the thermal conductivity and the maximum allowed temperatures for the materials are presented in Table A.1. A top and side view of the insulation, as well as geometrical dimensions are presented in Figure A.1.

Table A.1: Thermal conductivity and the maximum allowed temperatures for the materials in the multilayer insulation. Catalogue values obtained from the manufacturer (FINAL MATERIALS).

	Thermal conductivity [W/mK]	Maximum allowed temperature [$^{\circ}C$]
External insulation (Nano T High)	0.025	1050
Internal insulation (ALZ 1645)	0.16	1650

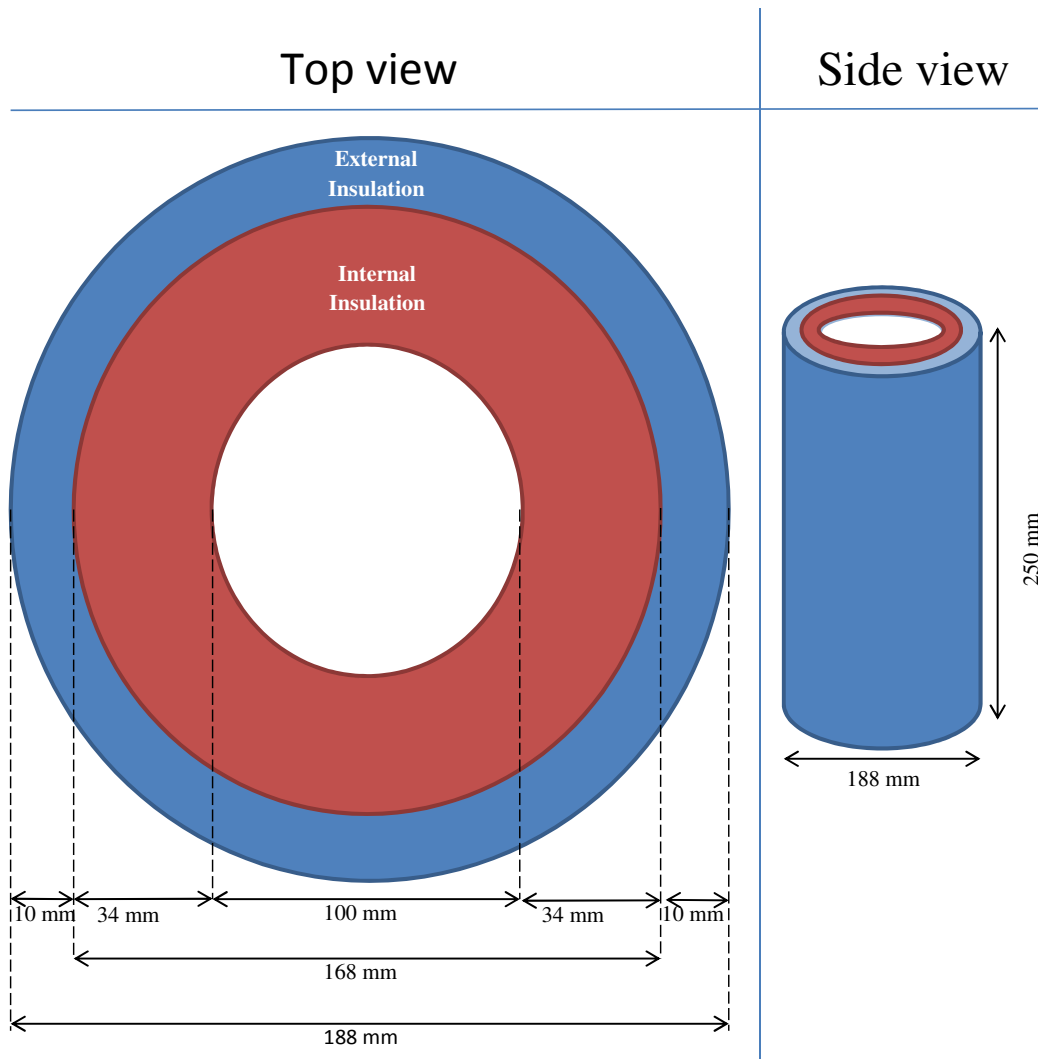


Figure A.1: Multilayer insulation, dimensions and perspectives.

Appendix B

Silicon properties

Table with the physical properties of the silicon¹:

	Symbole	Silicium solide ($T_f - \epsilon$)	Silicium liquide ($T_f + \epsilon$)	Unités
Masse volumique	d	2310	2560	$kg.m^{-3}$
Masse atomique	M	$28,0855(3) \cdot 10^{-3}$	$28,0855(3) \cdot 10^{-3}$	$kg.mol^{-1}$
Volume molaire	V_m	$1,22 \cdot 10^{-5}$	$1,12 \cdot 10^{-5}$	$m^3.mol^{-1}$
Résistivité électrique	ρ_{el}	Fonction du dopage	50 – 80	$\mu\Omega.cm$
Viscosité dynamique	μ		0,75	$mPa.s$
Viscosité cinématique	ν		$2,9 \cdot 10^{-7}$	$m^2.s^{-1}$
Tension de surface	σ		$7,31 \cdot 10^{-1}$	$N.m^{-1}$
Température de fusion	T_f		$1414 \pm 0,9$	$^{\circ}C$
Chaleur massique	C_p	1,032		$J.g^{-1}.K^{-1}$
Conductivité thermique	k	19	56,5	$W.m^{-1}.K^{-1}$
Diffusivité thermique	α		$2,2 \cdot 10^{-5}$	$m^2.s^{-1}$
Énergie de fusion	ΔH_f		$50,693 \pm 3\%$	$kJ.mol^{-1}$
Émissivité	ϵ	0,6	0,2	
Expansion Thermique	β	$4,6 \cdot 10^{-6}$	$1,1 \cdot 10^{-4}$	K^{-1}

1. Mickaël BEAUDHUIN, *Étude expérimentale et numérique de la précipitation d'impuretés et de la formation des grains dans le silicium photovoltaïque*, PhD thesis, Institut polytechnique de Grenoble, 2009.

Appendix C

Phase diagrams

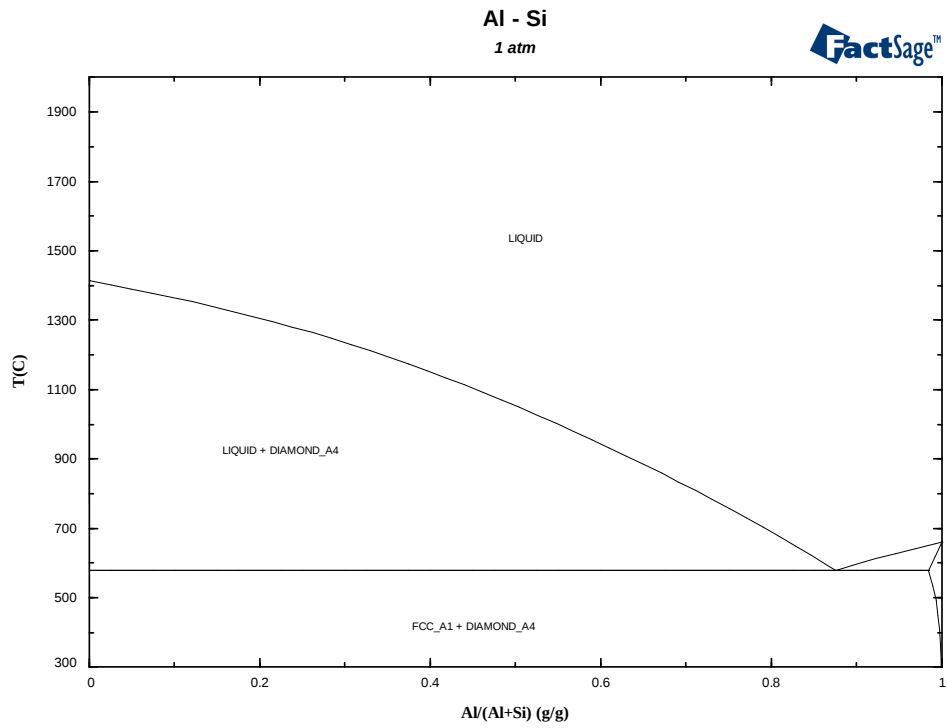


Figure C.1: Phase diagram for aluminium-silicon .

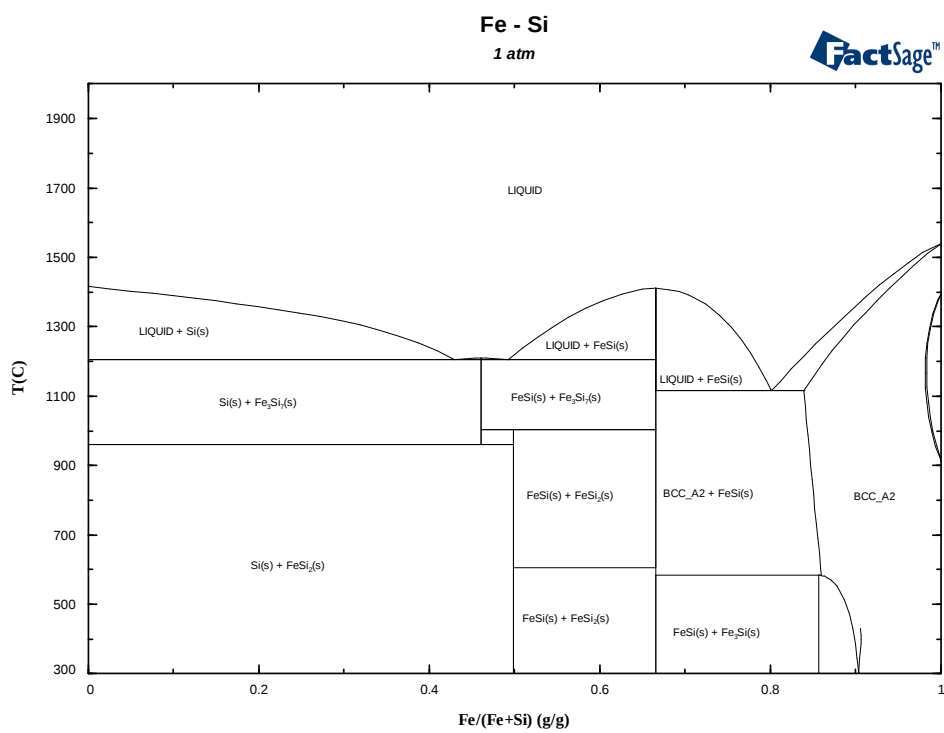


Figure C.2: Phase diagram for iron-silicon.

Appendix D

Interface stability criterion

The morphological instability of the solidification interface¹ is related to a critical velocity of the interface. During the solidification process, if the crystal growth rate became higher than the critical velocity, the interface becomes morphologically unstable. The critical velocity $v_{critical}$ is computed as

$$v_{critical} = \frac{D\nabla T}{-m_l C_l^* (1 - K_{eff})} \quad (D.1)$$

where

D is the diffusion coefficient

∇T is the solid thermal gradient at the interface, perpendicular to the interface

m_l is the liquidus slope

C_l^* is the solute concentration at the interface in the liquid

K_{eff} is the effective segregation coefficient

Using Equation D.1, critical velocity was computed for Experiment II.2 and compared to the crystal growth velocity. The diffusion coefficient of aluminium is known from literature², and for aluminium impurities $D = 7 \cdot 10^{-8} m^2/s$. The liquidus slope was estimated from the Al-Si phase diagram at $m_l = -0.0005$. A value for the effective segregation coefficient was recovered from the experimentally measured aluminium concentration in the first part of the ingot (Figure 5.14, Experiment 2). The K_{eff} is estimated at 10^{-2} and according to Equation 5.3 contains information about the boundary layer and the liquid velocity through term $\bar{\Delta}$. A value for the thermal gradient ∇T perpendicular to the interface, cannot be easily recovered from the numerical simulations, due to

1. W. Kurz, D.J. Fisher, *Fundamentals of solidification*, 1986

2. Hiroshi Kodera, *Diffusion Coefficients of Impurities in Silicon Melt*, Japanese Journal of Applied Physics, vol. 2, no.4, pp. 212-219, 1963

the interface curvature. ANSYS Fluent provides only axial and radial thermal gradients, not perpendicular gradients to the interface. The average value for the axial thermal gradient, according to the simulations is $\nabla T \approx 1300K/m$, but this value cannot be considered more than an approximation of the real gradient. The experimental recorded temperatures in the crucible vicinity can be used to estimate an axial thermal gradient in the ingot at $\nabla T \approx 1000K/m$.

The evolution of the solute concentration at the interface in the liquid (C_l^*) along the solid fraction can be estimated from concentration in the solid, given by the Scheil-Guliver law (Equation D.2).

$$C_s = C_0 K_{eff} (1 - f)^{K_{eff}-1} \quad (D.2)$$

where C_0 represents the initial solvent concentration, $600ppm$ or $6 \cdot 10^{-4}$ mass fraction in the studied case (Experiment II.2).

Equation D.3 indicates the formula used to compute the solute concentration at the interface in the liquid (C_l^*).

$$C_l^* = \frac{C_s}{K_0} \quad (D.3)$$

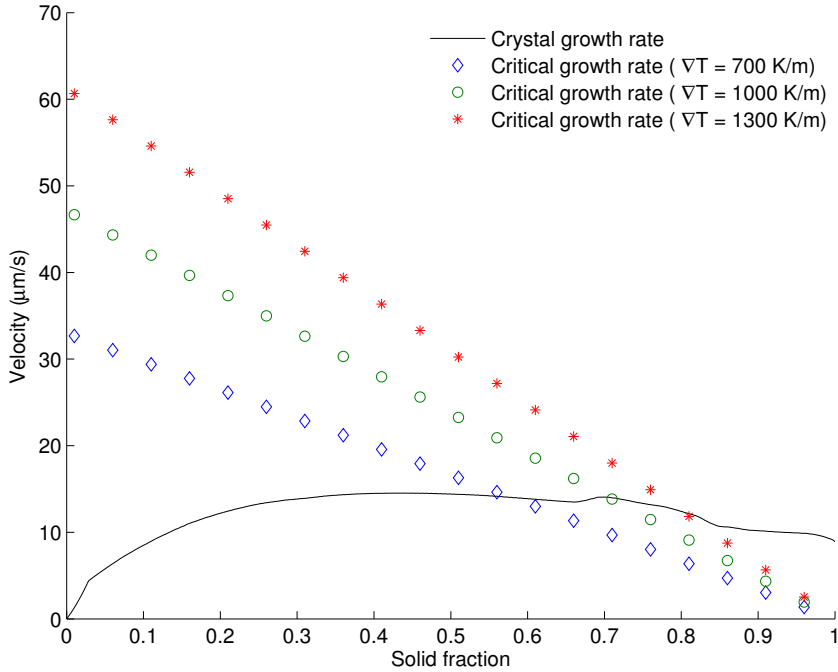


Figure D.1: Computed critical velocity.

FigureD.1 depicts the comparison of the crystal growth rate and the critical growth velocity. The crystal growth rate was recovered from the numerical

simulation. Moreover, using the experimentally recorded temperatures during the experiments, the interface position and velocity can be estimated based on the thermal balance at the interface. The experimental estimation of the crystal growth rate in this particular case was $\approx 13\mu m/s$, which is similar with the one computed by the numerical model. Due to a lack of exact information regarding the thermal gradient at the solidification interface, multiple values for the critical velocity were computed, using Equation D.1, for different values of ∇T .

In all cases, the growth rate exceeds the critical velocity after some limit solid fraction. This indicates the solid fraction from where the solidification interface may become morphological unstable. For a thermal gradient $\nabla T = 700K/m$ the interface instability may occur above a solid fraction of 0.6, while for a higher value of ∇T the instability is further delayed. This result indicates that for a $\nabla T \approx 700K/m$, which is a plausible value, the solidification interface instability may happen in the same region of the ingot where the drastic increase of the impurity concentration was experimentally observed. This can indeed explain the experimental observations regarding the axial distribution of impurities in the ingot from Experiment II.2.

The interface stability criterion consideration can be applied to Experiment II.1 as well. For this experiment, based on the measured levels of aluminium (see Figure 5.14), $K_{eff} \rightarrow 1$. With this assumption, using Equation D.1 the critical velocity $v_{critical} \rightarrow \infty$ which indicates that the interface is stable for the whole duration of the solidification process. However, the possibility of an early morphological destabilization of the interface must be considered as well. In this case the impurity levels measured from the beginning will probably be at the initial concentration C_0 , as it was indicated in the last part of the Experiment II.2. If this was the case, then a value for K_{eff} cannot be retrieved from the experimental measurements, in order to properly apply the stability criterion on Experiment II.1

Appendix E

Simulation results for iron and phosphorus

In this appendix, results obtained from the numerical simulation, of the segregation of iron and phosphorus for the experimental set III, are presented. The simulations were conducted using the SIMaP/EPM solidification module. The results regarding aluminium segregation in these simulations are presented and discussed in Chapter 5 Section 5.2.4. In this appendix, the images with results regarding iron and phosphorus segregation are presented but without further comments.

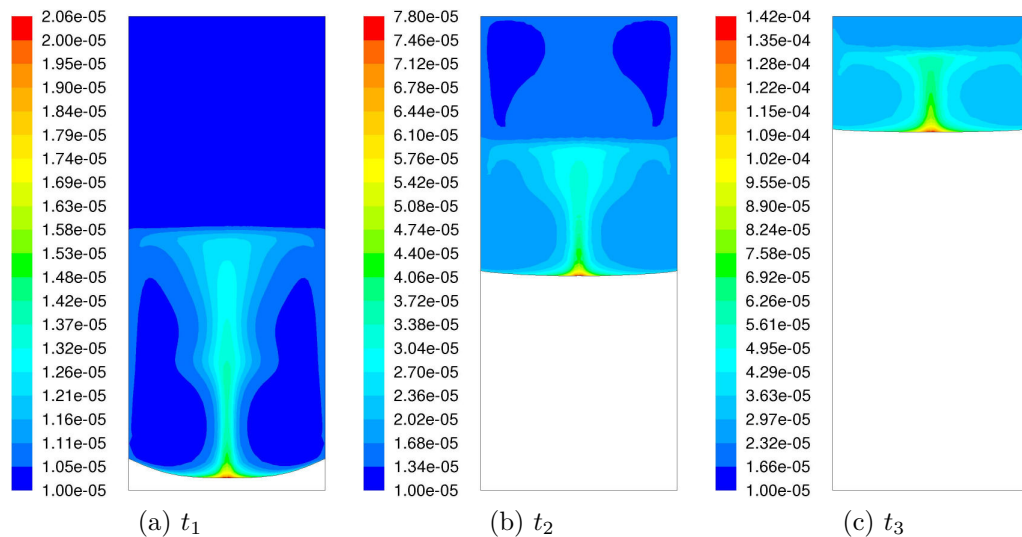


Figure E.1: Evolution in time of the iron distribution in liquid silicon for Experiment III.1.

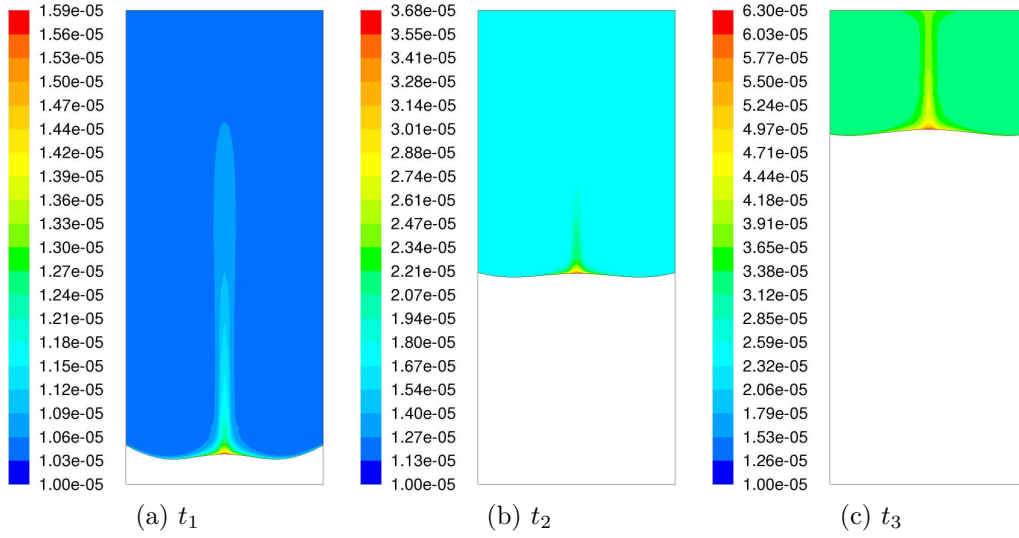


Figure E.2: Evolution in time of the iron distribution in liquid silicon for Experiment III.2.

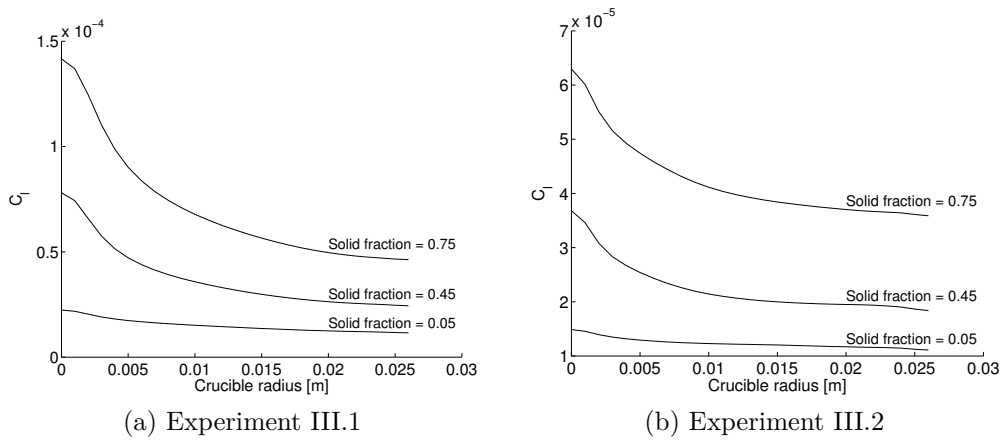


Figure E.3: Iron distribution in liquid silicon at the interface.

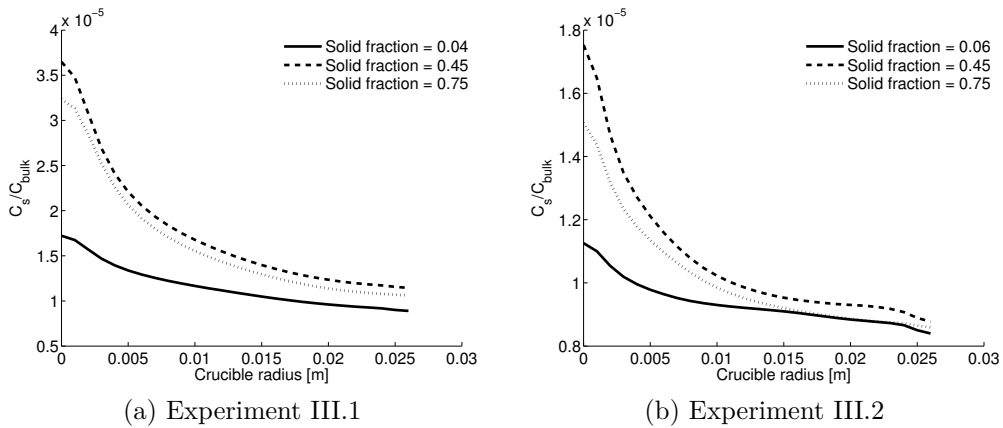


Figure E.4: Computed K_{eff} for iron along the solidification interface.

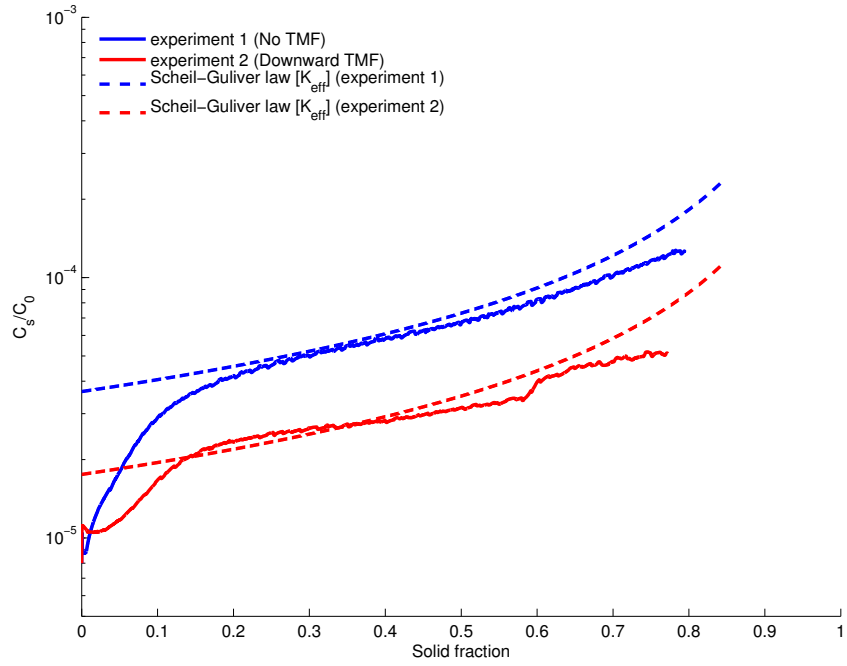


Figure E.5: Computed maximum values of iron at the interface (liquid side) for experiments in set III. Iron axial segregation in the center of the ingot

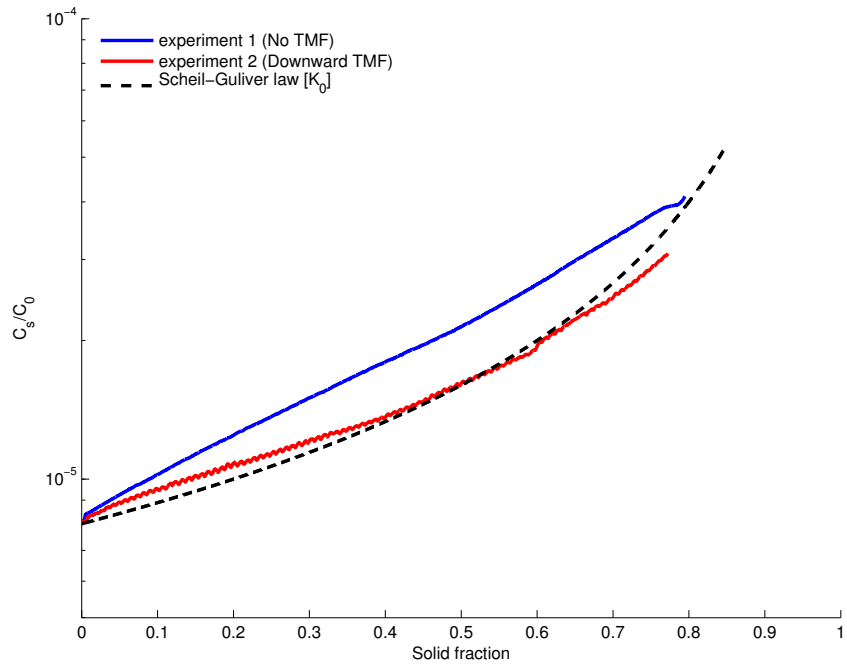


Figure E.6: Computed minimum values of iron at the interface (liquid side) for experiments in set III. Iron axial segregation on the border of the ingot.

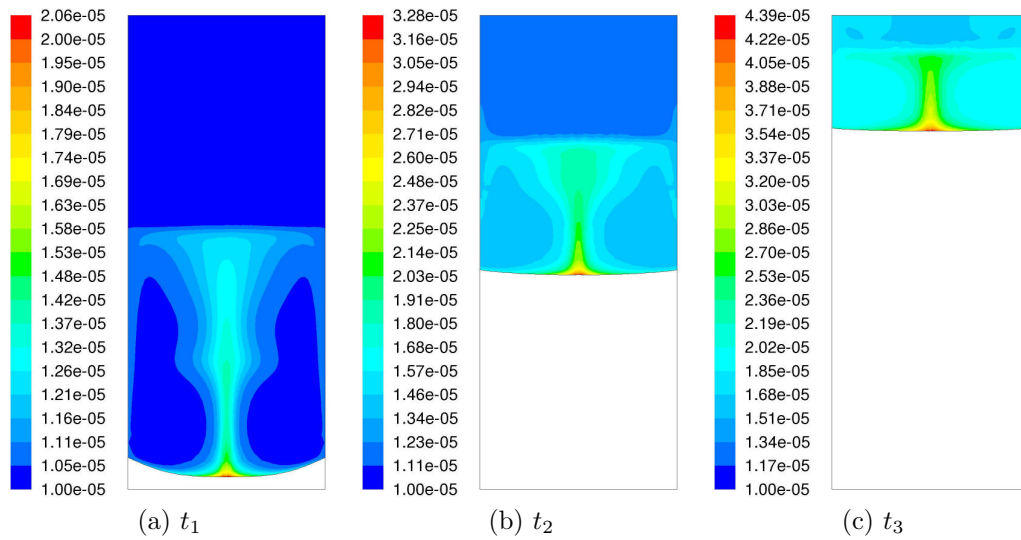


Figure E.7: Evolution in time of the phosphorus distribution in liquid silicon for Experiment III.1.

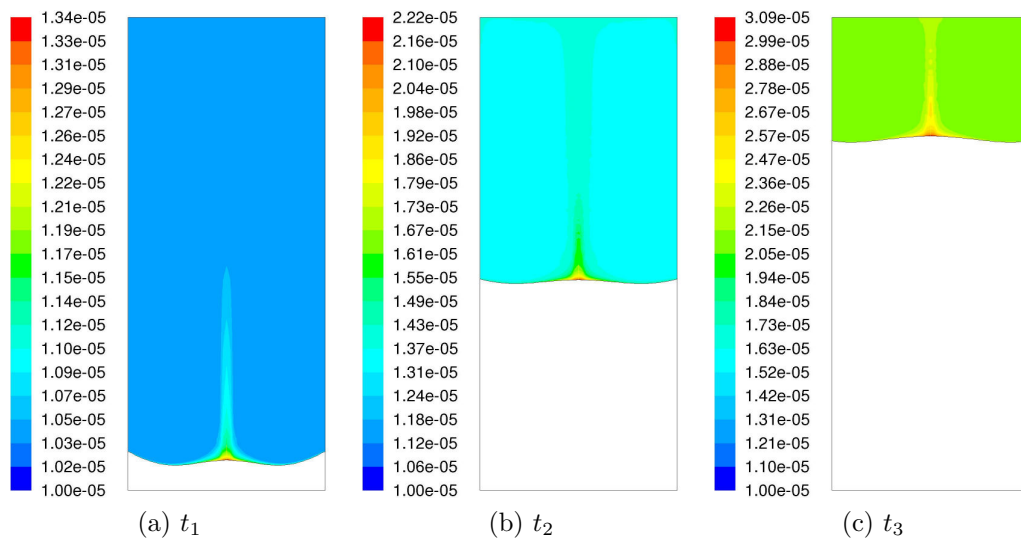


Figure E.8: Evolution in time of the phosphorus distribution in liquid silicon for Experiment III.2.

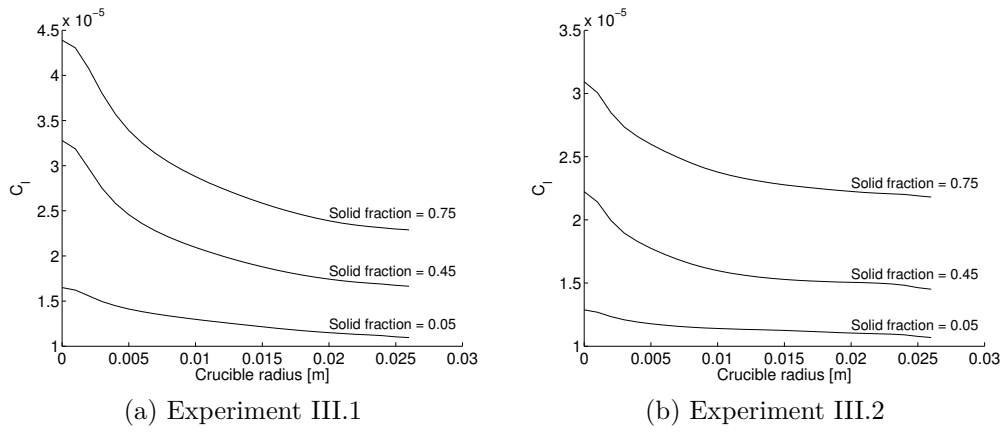


Figure E.9: Phosphorus distribution in liquid silicon at the interface.

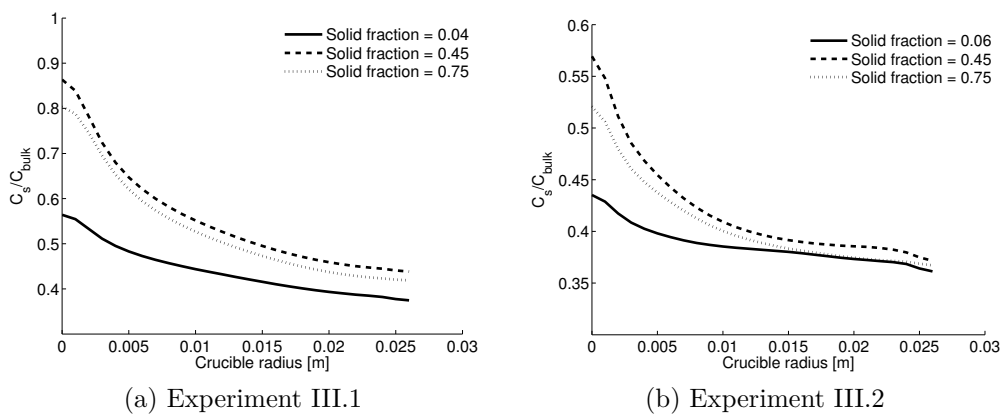


Figure E.10: Computed K_{eff} for phosphorus along the solidification interface.

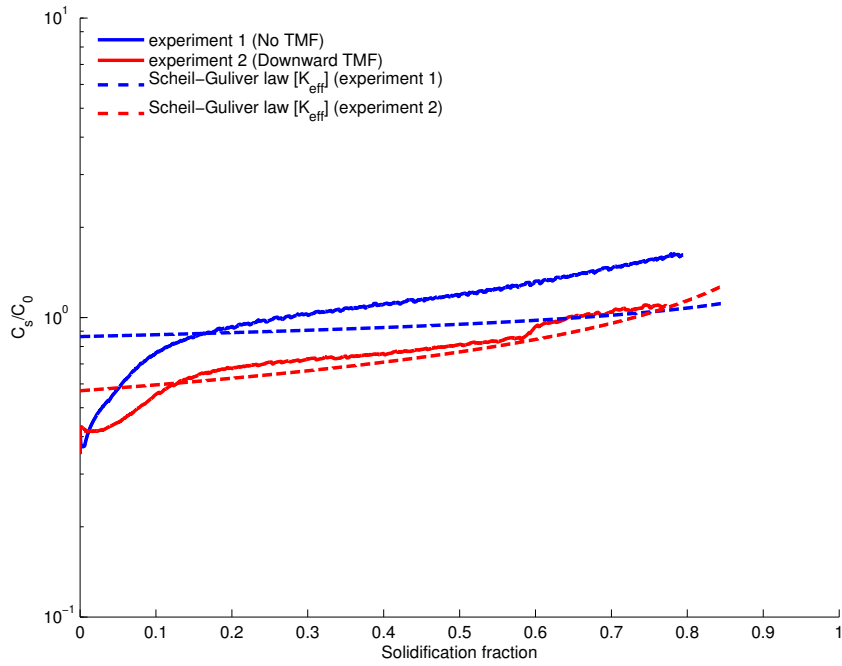


Figure E.11: Computed maximum values of phosphorus at the interface (liquid side) for experiments in set III. Phosphorus axial segregation in the center of the ingot

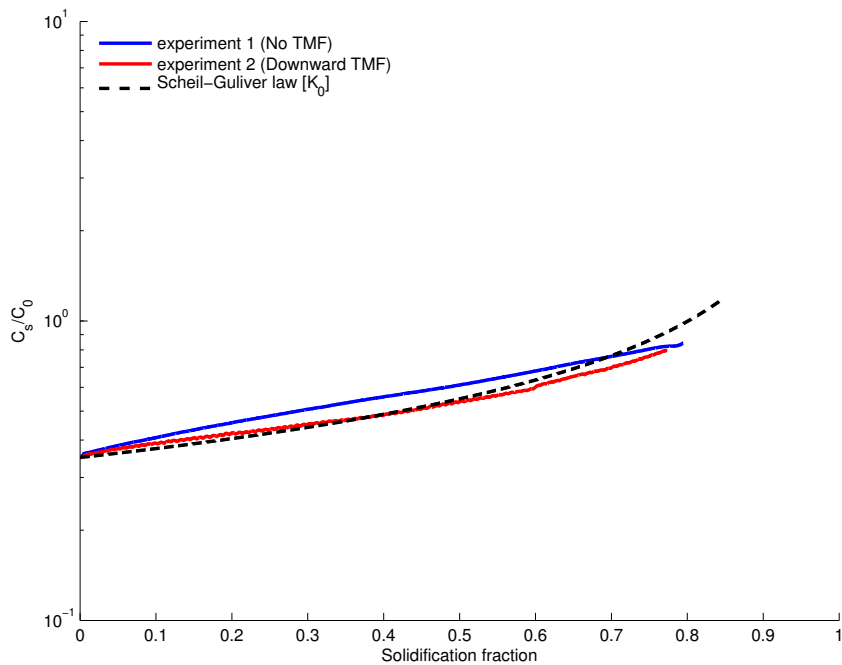


Figure E.12: Computed minimum values of phosphorus at the interface (liquid side) for experiments in set III. Phosphorus axial segregation on the border of the ingot.

Appendix F

Résumé

Table des matières

1	Introduction	147
2	État de l'art	148
3	Description de l'installation expérimentale	151
4	Description du modèle numérique	155
5	L'interface de solidification et la structure des grains	157
6	La ségrégation chimique sous champ magnétique glissant	164
7	Conclusions	167

1 Introduction

Dans les prochaines années, une augmentation significative des installations photovoltaïques est prévue. La plupart des modules photovoltaïques produits sont à base de silicium et aucun autre matériau ne pourra remplacer efficacement le silicium dans un avenir proche. L'efficacité électrique des modules photovoltaïques est reliée en grand partie à la qualité des plaquettes de silicium (ou wafers) utilisées, c'est-à-dire à la qualité du lingot dont elles sont issues. La qualité des lingots du silicium dépend fortement du taux de défauts cristallins et de la quantité d'impuretés présentes dans le lingot. Les lingots de silicium (monocristallins et multicristallins) sont élaborés à l'aide de procédé de croissance cristalline où les principaux paramètres tels que la vitesse de croissance et le gradient de température sont contrôlés avec précision. La solidification est un procédé de croissance à partir d'un bain fondu que l'on refroidit de manière contrôlée. Durant ce processus, les impuretés ayant un coefficient de ségrégation $K_0 < 1$ sont extraites du silicium grâce au phénomène de ségrégation chimique. L'écoulement dans le bain liquide influe fortement sur la ségrégation. L'utilisation d'un champ magnétique permet de contrôler l'écoulement dans la zone liquide durant la solidification des lingots de silicium.

Pour l'étude expérimentale, nous utilisons un four Bridgman équipé d'un brasseur électromagnétique qui permet de générer une convection forcée par champ glissant. Les impuretés rejetées à l'interface solide-liquide (rejet de soluté) sont redistribuées dans le liquide en présence de convection forcée. La décroissance du taux d'impuretés dans le liquide à proximité de l'interface, c'est-à-dire dans la couche limite, tend à diminuer la quantité d'impuretés incorporées dans le solide. Ainsi, les impuretés sont localisées dans la fin du lingot de silicium. La convection forcée a aussi un effet sur la courbure de l'interface solide-liquide. La forme de l'interface a une influence sur la structure de grains du lingot multi-cristallin. La plupart des joints de grains sont considérés comme des défauts cristallins réduisant l'efficacité des cellules solaires. L'interface de solidification a été marquée pendant les expériences pour analyser l'influence du champ magnétique glissant sur sa forme.

Parallèlement à l'étude expérimentale, un modèle numérique des phénomènes mis en jeu dans le procédé de solidification sous champ a été développé en utilisant le logiciel commercial ANSYS FLUENT. Il permet, notamment, d'obtenir le champ de température dans le four et les vitesses dans le liquide. Les informations obtenues par le modèle viennent compléter les résultats expérimentaux et peuvent être exploitées pour améliorer le processus expérimental.

Pour simuler le procédé de ségrégation, nous avons conçu et développé dans ANSYS FLUENT un nouveau module de solidification. Ce nouveau module utilise la fonction de maillage dynamique de FLUENT. Cette approche permet de travailler avec deux domaines distincts (un pour le liquide et un pour le solide) et aussi de gérer les conditions aux limites à l'interface de solidification. Ensuite nous avons intégré ce module dans le modèle du procédé.

2 État de l'art

Dans un rapport¹ publié en 2014, l'EPIA² prévoit une installation photovoltaïque globale cumulée de plus de 400 GW en 2018 (Figure 1). Ceci correspond à une augmentation significative du marché photovoltaïque globale dans les prochaines années.

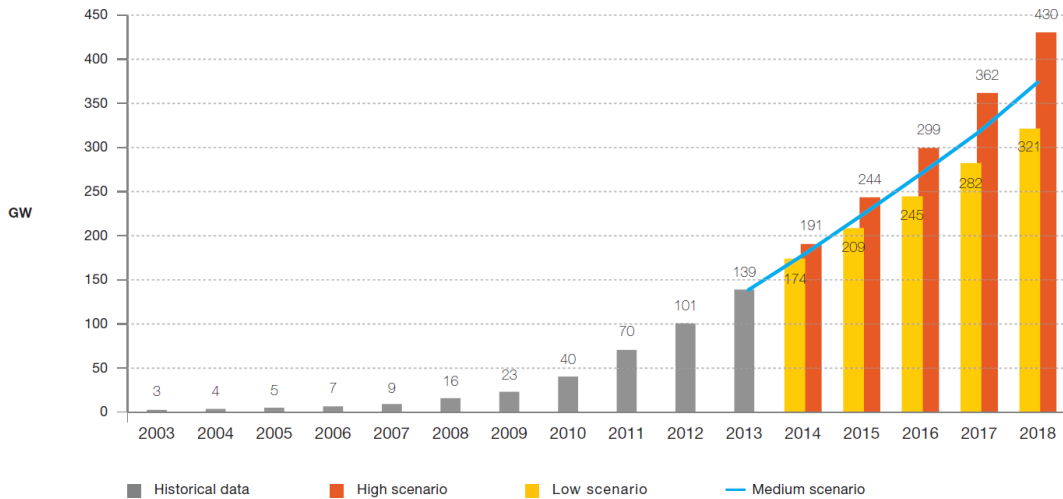


FIGURE 1: Prévisions sur l'installation photovoltaïque globale cumulée (Source : EPIA 2014)

La plupart des modules photovoltaïques produits sont à base de silicium et aucun autre matériau ne pourra remplacer efficacement le silicium dans un avenir proche. Dans la Figure 2 la chaîne de production des panneaux photovoltaïques est détaillée. La matière première, souvent nommée « feedstock » est utilisée pour obtenir des lingots de silicium suivant un procédé de solidification. La qualité des lingots de silicium dépend fortement du taux de défauts cristallins et de la quantité d'impuretés présentes dans le lingot. Les plaquettes ou « wafers » sont découpées dans le lingot obtenu. Elles sont ensuite utilisées

1. G. Masson, S. Orlandi, M. Reking, Global market outlook for photovoltaics 2014-2018, European Photovoltaic Industry Association (EPIA) (2014).

2. EPIA : European Photovoltaic Industry Association

pour la fabrication des cellules solaires. Enfin, les cellules sont assemblées en modules photovoltaïques. L'efficacité électrique des modules photovoltaïques est reliée en grande partie à la qualité des « wafers » de silicium utilisés et donc à la qualité du lingot dont ils sont issus. La qualité des lingots de silicium dépend du procédé de croissance cristalline où les principaux paramètres sont la vitesse de croissance, le gradient de température et aussi de la charge initiale, donc de la qualité du « feedstock ».

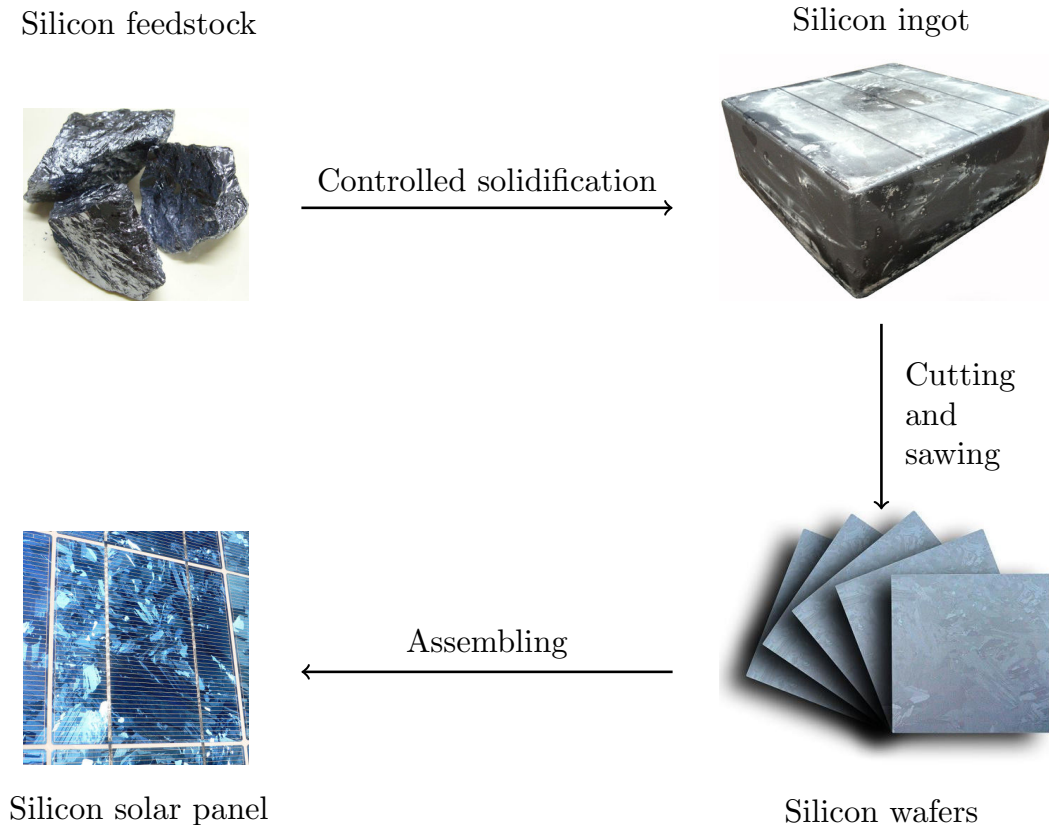


FIGURE 2: Étapes dans le processus de fabrication des modules PV

Pour une bonne qualité du lingot, le « feedstock » doit avoir une qualité solaire, qui suppose généralement un niveau d'impuretés au-dessous de 1 partie par million (ppm)³. Plusieurs méthodes sont utilisées pour améliorer la qualité du silicium métallurgique afin d'obtenir la qualité solaire. Ces méthodes de purification sont présentées dans la Figure 3. Les processus comme Siemens ou FBR se situent sur une voie chimique, tandis que la voie métallurgique suppose l'enchaînement de plusieurs étapes de solidification dirigée et d'autres processus comme celui mettant en oeuvre une torche à plasma.

3. S. Pizzini, Towards solar grade silicon : Challenges and benefits for low cost photovoltaics, Solar Energy Materials and Solar Cells 94 (9) (2010) 1528 – 1533, PVSEC 18.

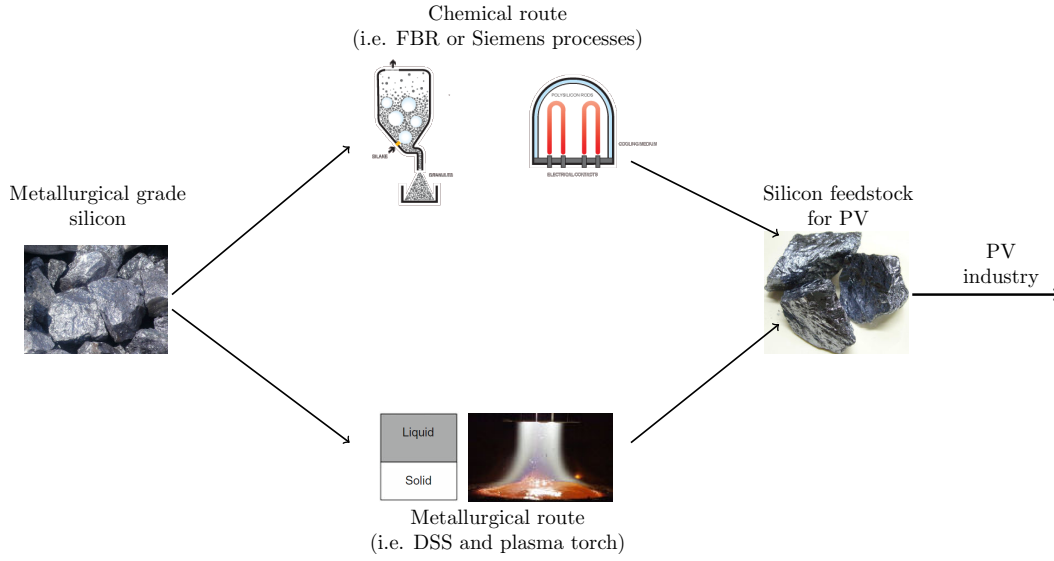


FIGURE 3: Routes de purification du silicium

Cette étude se positionne sur la voie métallurgique, où la solidification dirigée est utilisée pour la purification du silicium. Durant ce processus, les impuretés ayant un coefficient de ségrégation $K_0 < 1$ sont extraites du silicium solide grâce au phénomène de ségrégation chimique. L'installation expérimentale utilisée pour la solidification dirigée du silicium est un four de type Bridgman (Figure 4), qui permet le contrôle des paramètres comme la vitesse de croissance, le gradient de température et la charge initiale.

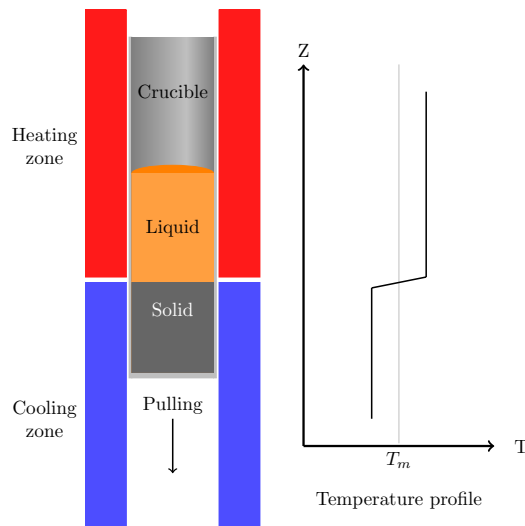


FIGURE 4: Schéma de la technique Bridgman-Stockbarger et profile de température sur Z

3 Description de l'installation expérimentale

La partie expérimentale de cette étude a été réalisée avec un four de solidification Bridgman verticale (VB2) présenté dans la Figure 5. Le four est équipé de deux éléments chauffants (résistances) contrôlés indépendamment, d'isolation thermique et d'un brasseur électromagnétique de type Bitter. Le brasseur produit un champ magnétique glissant qui génère un écoulement forcé dans le silicium liquide. Le silicium est positionné dans un creuset de 2 pouces de diamètre.

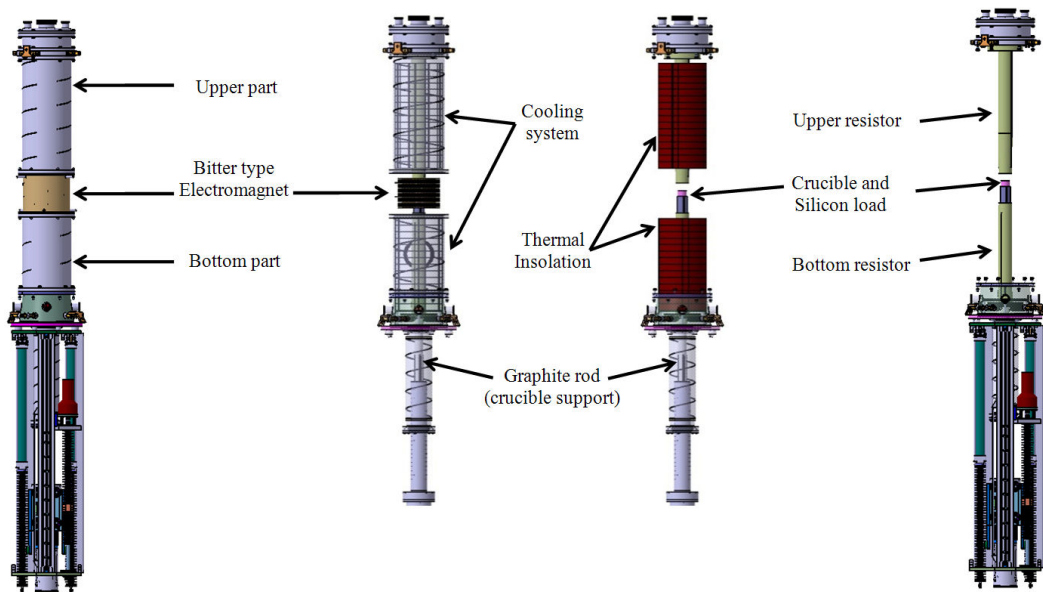


FIGURE 5: Four de solidification Vertical Bridgman 2 inches (VB2)

Une vue détaillée de la partie centrale du four où les principaux éléments sont mis en évidence, est présentée dans la Figure 6. Le brasseur électromagnétique est constitué de 6 enroulements et il est positionné autour du creuset. Le brasseur est alimenté en triphasé et il produit un champ magnétique glissant (TMF) vers le bas ou vers le haut. Une troisième possibilité est d'alterner le sens de glissement du champ magnétique. Nous appellerons cette configuration TMF alternatif.

Suivant le sens de glissement du TMF, l'orientation des forces induites et l'écoulement dans le liquide changent. La vitesse induite dans le liquide est proportionnelle à l'intensité du champ magnétique. Figure 7 montre les différents écoulements obtenus et les différentes formes de l'interface de solidification suivant les diverses configurations de champ glissant. La forme de l'interface est

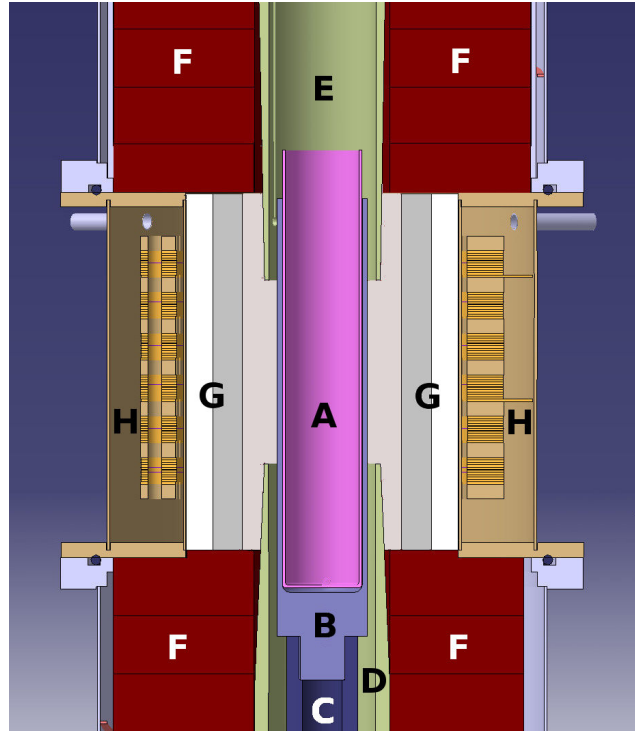


FIGURE 6: Vue sur la partie centrale du four VB2. A : Creuset, B : Portcreuset, C : Canne en graphite, D : Résistance chauffante basse, E : Résistance chauffante haute, F : Isolation thermique – feutre en graphite, G : Isolation thermique – multicouche, H : Brasseur Bitter.

influencée par l'écoulement⁴. Le liquide chaud, dans le haut du bain liquide, est transporté près de l'interface.

Un autre effet important de la convection forcée est son action sur la ségrégation chimique d'impuretés. Les impuretés rejetées à l'interface solide-liquide sont redistribuées dans le liquide en présence de convection forcée. La décroissance du taux d'impuretés dans le liquide à proximité de l'interface tend à diminuer la quantité d'impuretés incorporées dans le solide.

Dans cette étude trois séries d'expérience ont été réalisées. Deux types de matière première (feedstock de silicium), ayant différentes concentrations initiales d'impuretés (Tableau 1), ont été utilisés.

Les trois séries d'expérience effectuées sont détaillées dans les Tableaux 2, 3 et 4. La série I est composée de quatre expériences dans lesquelles la première a été conduite sans champ glissant et représente l'expérience de référence. Les trois autres (I.2, I.3 et I.4) ont été réalisées en présence de champ magnétique glissant de différentes orientations. Le but était d'étudier la forme de l'interface

4. N. Dropka, C. Frank-Rotsch, W. Miller, P. Rudolph, Influence of travelling magnetic fields on s-l interface shapes of materials with different electrical conductivities, *Journal of Crystal Growth* 338 (1) (2012) 208 – 213.

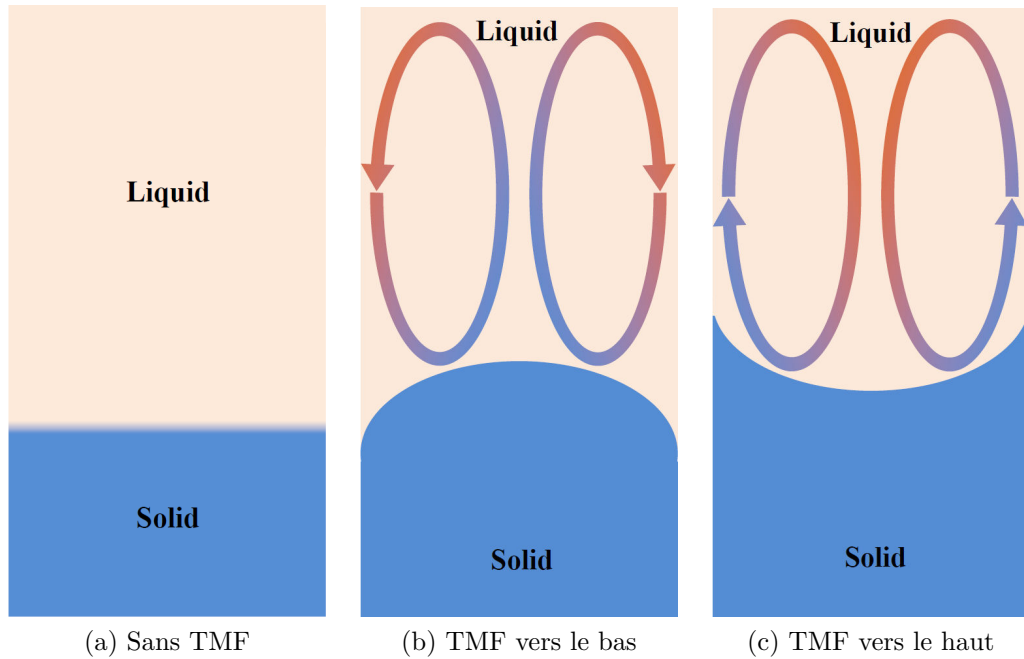


FIGURE 7: Écoulement induit par TMF et l'influences sur la forme de l'interface de solidification

TABLE 1: La concentration initiale d'impuretés

Référence	Aluminium [ppm]	Fer [ppm]	Phosphore [ppm]
Si-A	6.8	10	9.6
Si-B	600	13.2	2.76

et la ségrégation chimique avec champ glissant (sous TMF). Les résultats des expériences de la première série ont été obtenus en imposant une vitesse de refroidissement des résistances chauffantes.

La deuxième série (Tableau 3) a été réalisée toujours en imposant une vitesse de refroidissement dans les résistances mais cette fois la matière première utilisée est beaucoup plus chargée en aluminium. Dans cette série l'intérêt était d'étudier la ségrégation chimique sous TMF ayant une intensité plus élevée comparée à la série I.

La troisième série (Tableau 4) reprend la même structure que la série I mais la différence majeure est la vitesse de tirage imposé au creuset. Cette fois le champ de température est conservé constant et la solidification est contrôlée par le système de tirage.

TABLE 2: Expériences série I

Numéro d'expérience	Silicium utilisée	ΔT imposée	Vitesse de refroidissement [K/h]	Intensité du TMF [mT]	Orientation du TMF
I.1	Si-A	150	36	0	-
I.2	Si-A	150	36	4	Vers le haut
I.3	Si-A	150	36	4	Vers le bas
I.4	Si-A	150	36	4	Alternatif

TABLE 3: Expériences série II

Numéro d'expérience	Silicium utilisée	ΔT imposée	Vitesse de refroidissement [K/h]	Intensité du TMF [mT]	Orientation du TMF
II.1	Si-B	150	36	0	-
II.2	Si-B	150	36	7	Vers le bas

TABLE 4: Expériences série III

Numéro d'expérience	Silicium utilisée	ΔT imposée	Vitesse de tirage [mm/h]	Intensité du TMF [mT]	Orientation du TMF
III.1	Si-A	400	$4 \cdot 10^{-6}$	0	-
III.2	Si-A	350	$4 \cdot 10^{-6}$	4	Vers le bas
III.3	Si-A	350	$4 \cdot 10^{-6}$	4	Vers le haut
III.4	Si-A	350	$4 \cdot 10^{-6}$	4	Alternatif

4 Description du modèle numérique

Le logiciel commercial ANSYS FLUENT a été utilisé pour développer un modèle numérique des phénomènes mis en jeu dans le procédé de solidification sous champ. Il permet, notamment, d'obtenir le champ de température dans le four et les vitesses dans le liquide. Les informations obtenues par le modèle viennent compléter les résultats expérimentaux et peuvent être exploitées pour améliorer le processus expérimental.

Le modèle numérique est un modèle 2D axisymétrique qui contient la géométrie complète du four. La Figure 8 présente une vue de la partie centrale de la géométrie, où les principaux éléments du four sont mis en évidence. Une densité de puissance est imposée dans les deux résistances chauffantes afin de retrouver une température similaire avec celle imposée expérimentalement. Les parois extérieures sont refroidies et donc dans le modèle une condition limite froide est imposée. Dans les extrémités du four, la taille caractéristique des cellules du maillage est fixée à 20 mm. Le maillage s'affine vers la zone de solidification (Figure 9). A l'intérieur du creuset la taille caractéristique des mailles est de 1 mm.

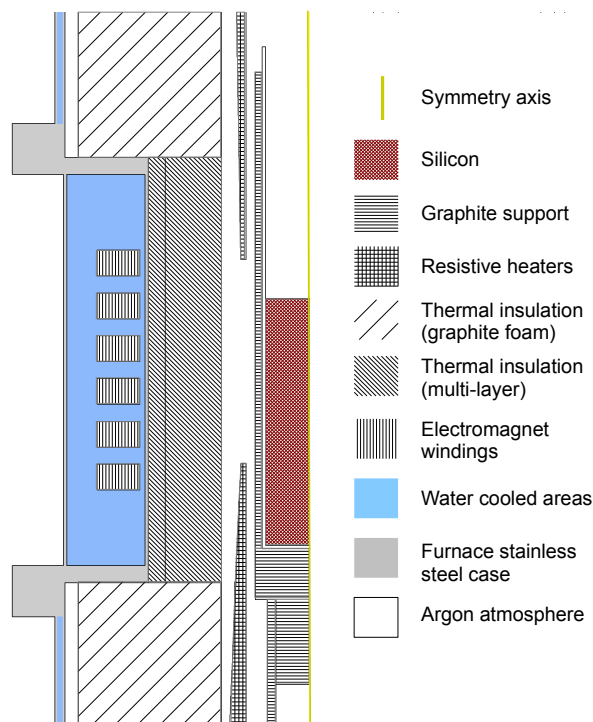


FIGURE 8: Éléments constitutifs, vue sur la partie centrale de la géométrie

Nous avons également conçu et installé dans l'équipement expérimental un système qui permet les mesures des puissances thermiques dissipées dans le

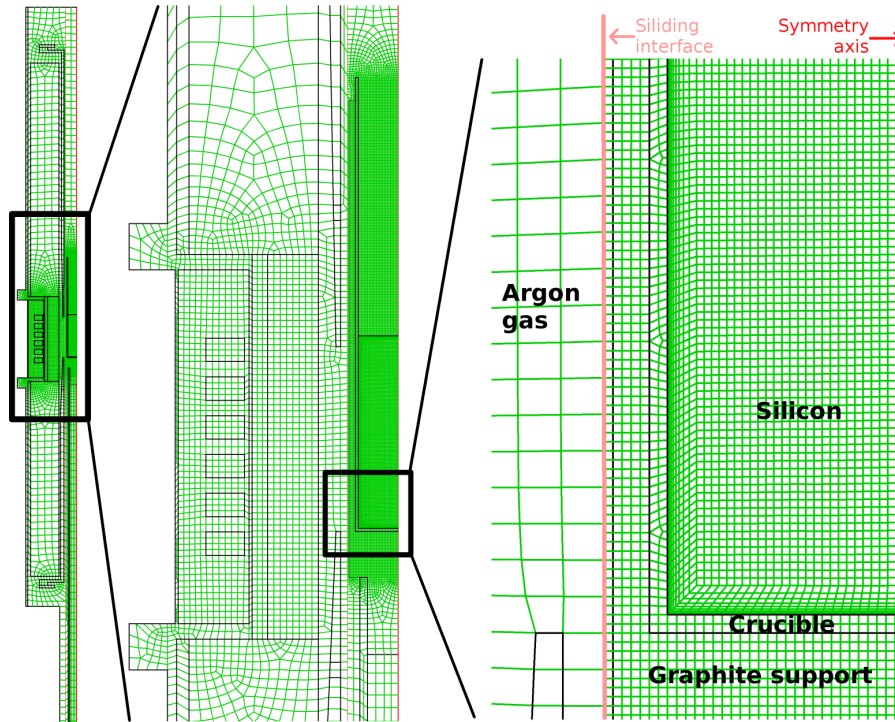


FIGURE 9: Maillage du four

système de refroidissement. Grâce à ce système, une validation en puissance du modèle numérique a été possible. De plus, la validation thermique du modèle a été complétée par des comparaisons des profils de températures au niveau du porte-crucible. Le modèle calcule un profil de température similaire avec celui mesuré expérimentalement.

Le modèle numérique a été continuellement amélioré tout au long de l'étude et un nouveau module de solidification a été développé dans la dernière partie de la thèse. Le nouveau module de solidification SIMaP/EPM permet d'effectuer des simulations de ségrégation. Ceci n'était pas possible dans notre cas (corps quasiment pur) avec le module de solidification FLUENT. Une validation théorique du module a été réalisée, en comparant les résultats du calcul avec une solution analytique⁵ (Figure 10).

5. A. Bianchi, Y. Fautrelle, J. Etay, Transferts thermiques, Presses Polytechniques et Universitaires Romandes, Lausanne, 2004.

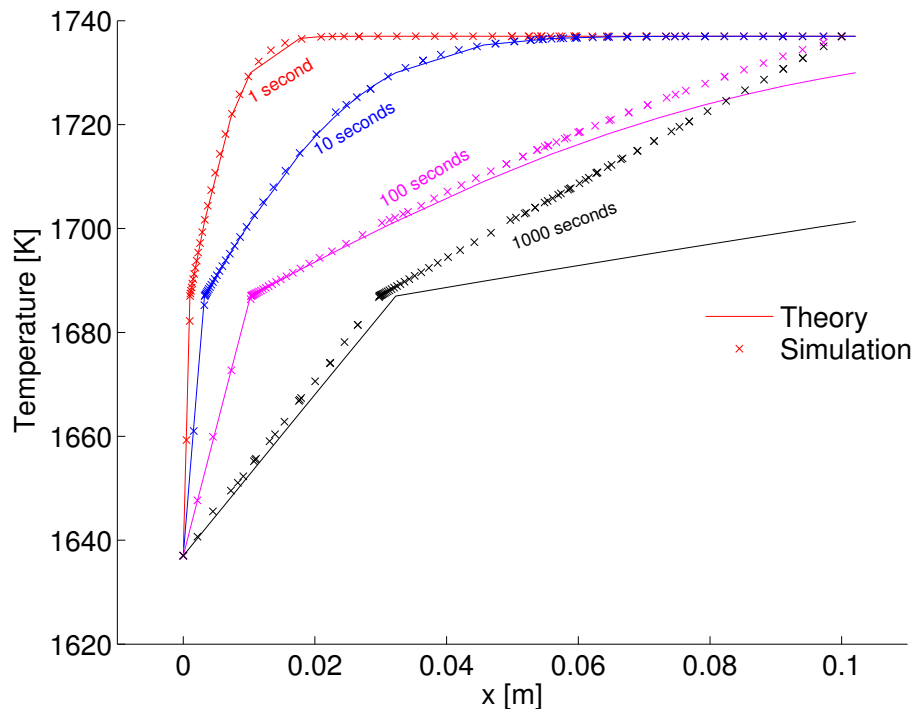


FIGURE 10: Validation thermique du module de solidification SIMaP/EPM

5 L'interface de solidification et la structure des grains

Un des principaux objectifs de la thèse est l'étude de la forme de l'interface de solidification sous champ magnétique glissant. Pendant cette étude deux procédures de marquage de l'interface ont été mises en oeuvre. La première méthode utilise l'effet Peltier et la procédure est présentée dans la Figure 11. Le principe consiste à envoyer des pulses de courant électrique dans la charge, pendant la solidification, afin de faire varier localement la concentration des impuretés dans le lingot.

Après une attaque chimique sur la surface du lingot, une trace qui représente la forme de l'interface au moment du marquage doit apparaître. Figure 12 présente un des marquages effectués avec cette méthode. Le principal désavantage de cette méthode réside dans le fait que les marquages d'interface ne sont pas visibles sur toute la largeur du lingot.

La deuxième méthode testée pour effectuer le marquage d'interface solide-liquide est d'utiliser le TMF. Une variation de l'intensité du TMF va produire des variations de la vitesse du liquide, qui en suite va impacter localement la ségrégation chimique des dopants. L'effet est le même avec celui de la première méthode, mais cette fois le paramètre contrôlé est l'intensité du TMF. Cette

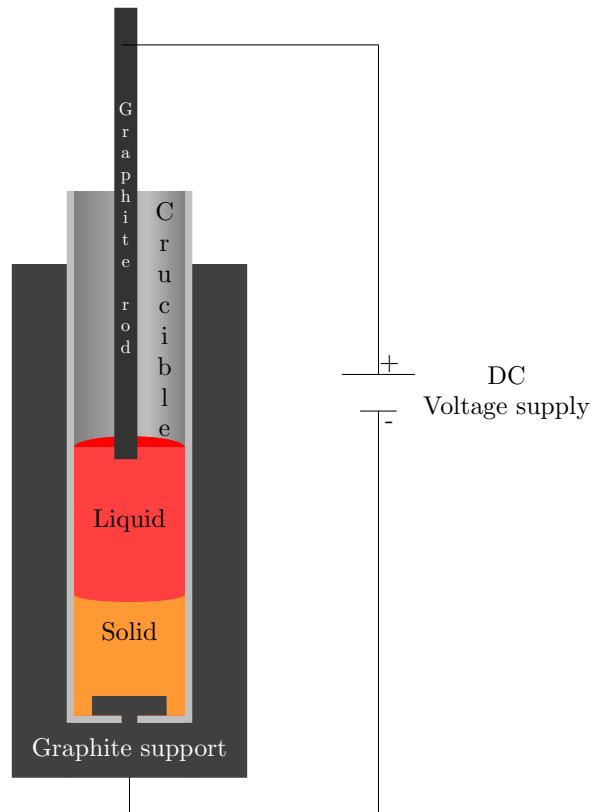
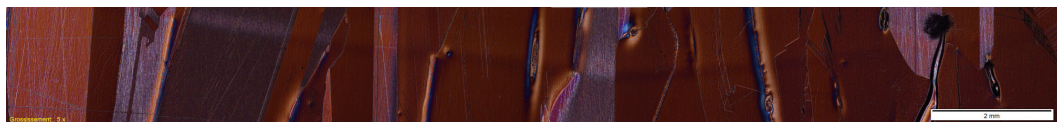


FIGURE 11: Schéma de principe de la procédure Peltier



(a) Interface de solidification



(b) Interface de solidification mis en évidence

FIGURE 12: Interface de solidification marquée à l'effet Peltier

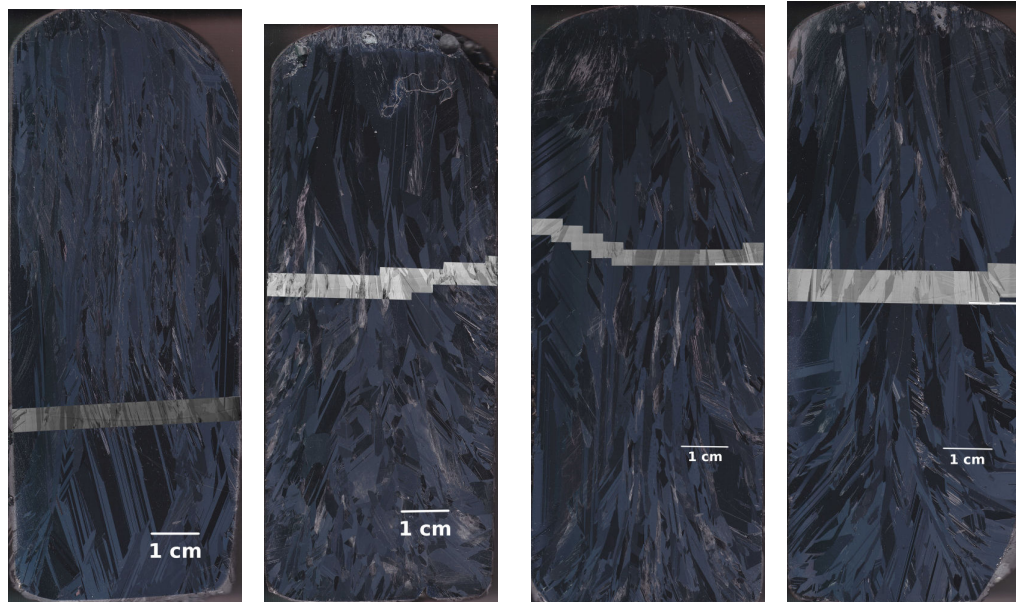
méthode a été utilisée avec succès dans toutes les expériences de la série III, où l'interface est maintenant marquée sur toute la largeur du lingot.

Dans la Figure 13, la structure des grains des lingots obtenus dans la série III est présentée en section verticale. Les zones gris claires sur chaque lingot sont des images de microscope qui détaillent le marquage de l'interface. Ces zones sont superposées sur l'image du lingot. Un zoom sur le marquage obtenu pour l'expérience III.1 ainsi qu'une comparaison avec les résultats du modèle sont présentés dans la Figure 14. L'expérience III.1 a été conduite sans TMF.

La Figure 15 présente une carte de température et le profil de vitesses

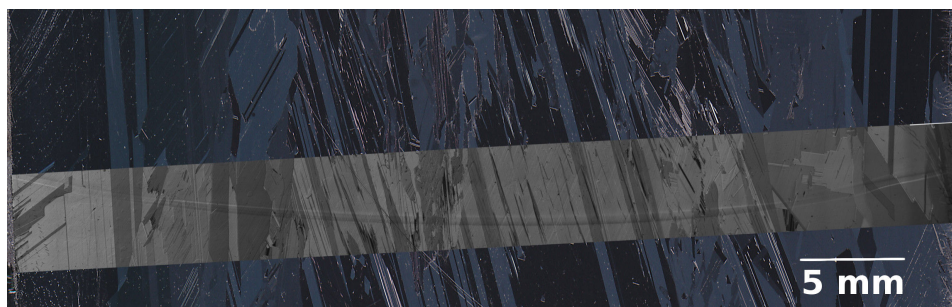
calculés pour l'expérience III.1. La vitesse calculée est voisine de 0.001 m/s et elle est due à la convection naturelle.

Le marquage obtenu pour l'expérience III.2 ainsi que la comparaison avec l'interface calculée par le modèle sont présentée dans la Figure 16. Le marquage

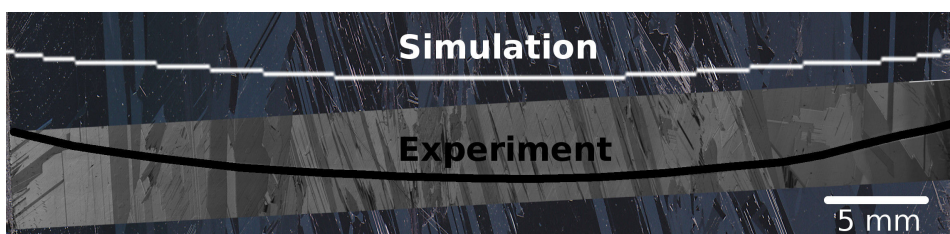


(a) Expérience III.1 (b) Expérience III.2 (c) Expérience III.3 (d) Expérience III.4

FIGURE 13: Structure des grains et marquages des interfaces dans la série III d'expériences



(a) Marquage d'interface expérience III.1



(b) Comparaison marquages expérience simulation

FIGURE 14: Marquage d'interface expérience III.1 et comparaison avec la simulation

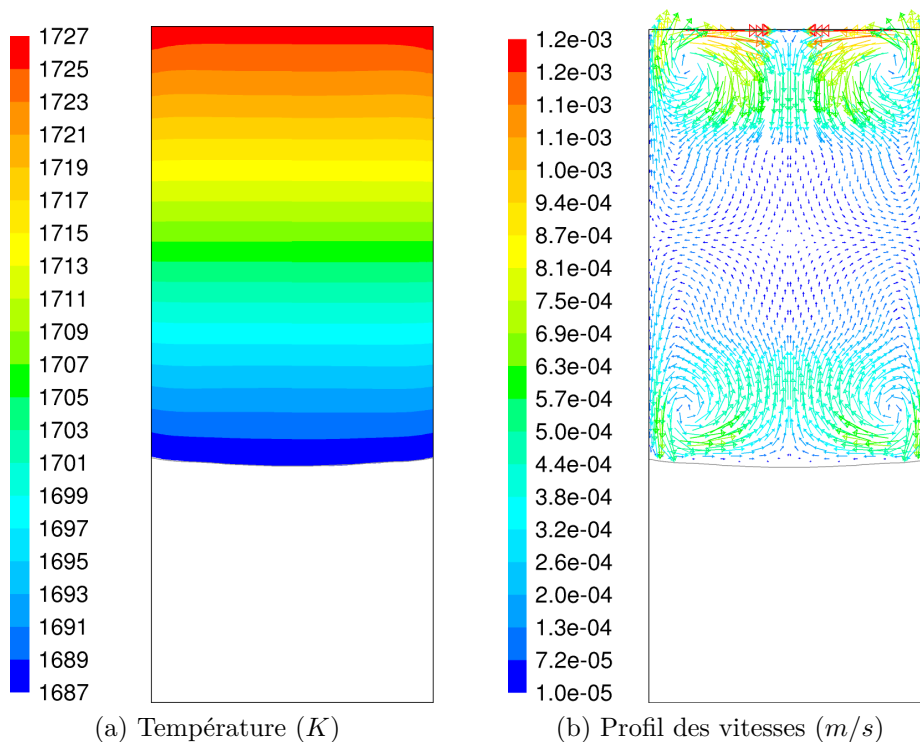


FIGURE 15: Expérience III.1 : Résultats numériques représentant une carte de température (a) et un profil des vitesses dans le liquide (b)

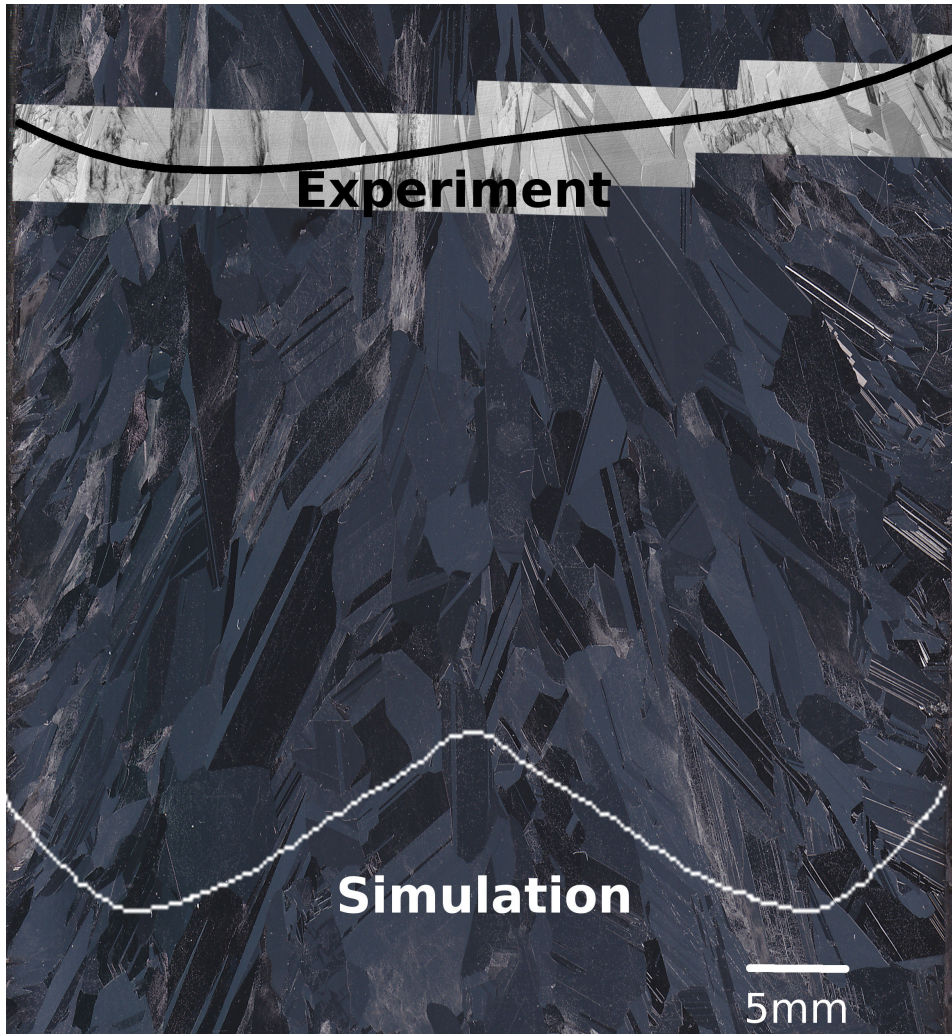
expérimental d'interface montre une forme asymétrique. Nous constatons ici que le modèle ne calcule pas une position très précise de l'interface. Dans le cas d'expérience III.2 le champ magnétique glissant a été utilisé pendant toute la durée de la solidification.

Le champ glissant ayant été utilisé dans cette expérience a pour conséquence la création de forces induites qui augmentent la vitesse du liquide jusqu'à plus de 0.03 m/s . La Figure 17 présente une carte de température et le profil de vitesse calculé pour l'expérience III.2. Nous pouvons observer que le gradient de température dans le liquide est fortement diminué par la grande vitesse dans le liquide. En conséquence les températures dans le liquide sont fortement influencées par les températures des résistances chauffantes. Autrement dit, une faible variation dans la température imposée dans les résistances chauffantes peut avoir une grande influence sur la position de l'interface.

La forme asymétrique de l'interface, observée expérimentalement pour toutes les expériences sous champ glissant dans la série III peut être la conséquence d'un écoulement asymétrique dans le liquide, induit par le brassage électromagnétique. Pour vérifier cette hypothèse, un creuset a été rempli avec un métal liquide à température ambiante (GaInSn), et mis sous TMF. Les vitesses in-



(a) Marquage d'interface expérience III.2



(b) Comparaison marquages expérience simulation

FIGURE 16: Marquage d'interface expérience III.2 et comparaison avec la simulation

duites par le champ magnétique ont été mesurées avec un vélocimètre Doppler. Un schéma explicatif du positionnement de la sonde de mesure est présenté sur la Figure 18.

Les profils de vitesses mesurés dans le GaInSn sont présentés dans la Figure 19. Ils montrent que l'écoulement est en fait asymétrique. Nous avons réa-

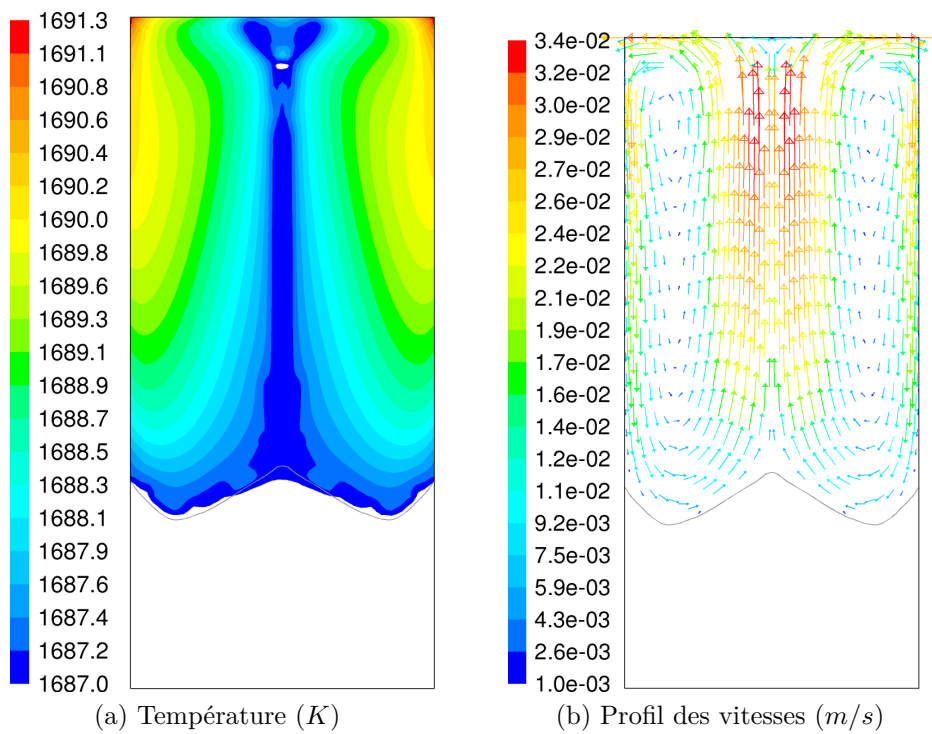
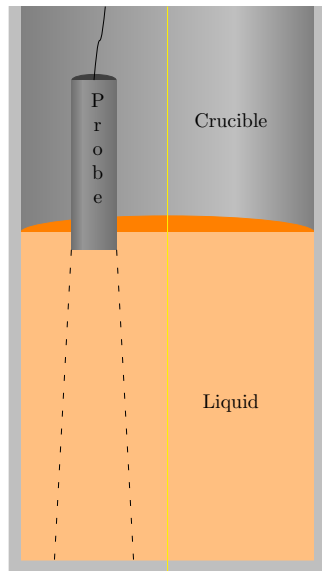
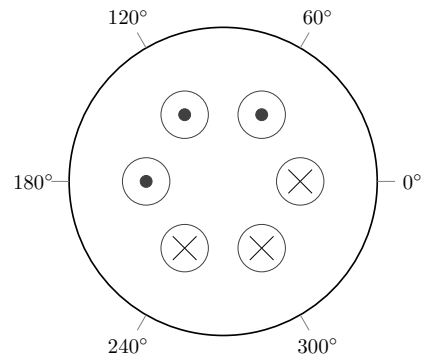


FIGURE 17: Expérience III.2 : Résultats numériques représentant une carte de température (a) et un profil des vitesses dans le liquide (b)

lisé une simulation qui correspond à la procédure expérimentale de ces mesures. Les résultats de la simulation indiquent que les vitesses calculées par le modèle ont des ordres de grandeurs comparables avec les mesures expérimentales. Par contre l'écoulement mesuré présente une configuration tridimensionnelle.



(a) Probe positioning in vertical section



(b) Top view for the measuring positions

FIGURE 18: Positionnement de la sonde pour les mesures des vitesses dans le GaInSn liquide. Vue en section verticale et vue par le haut

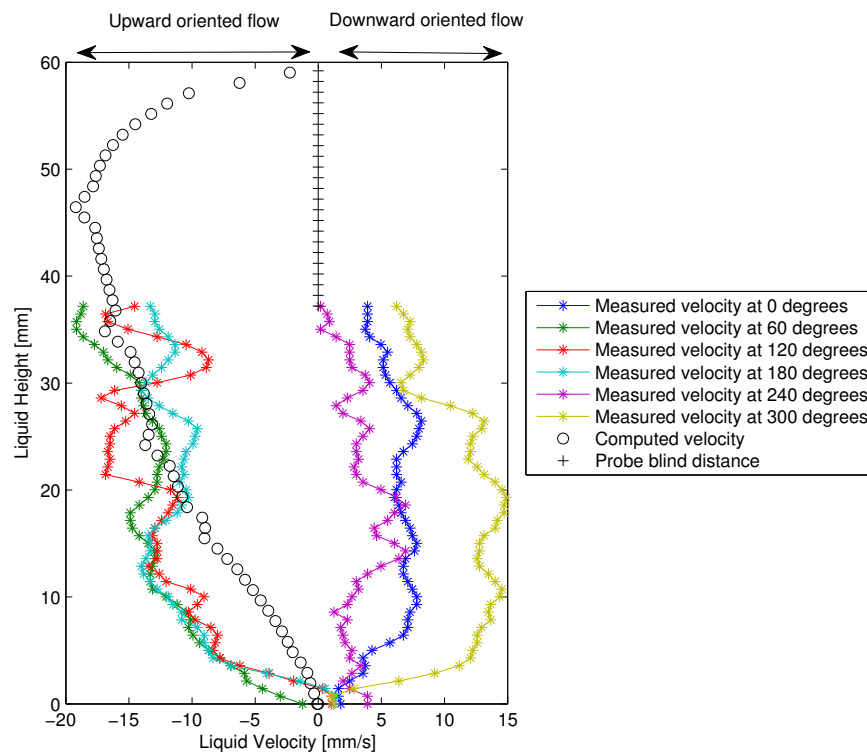


FIGURE 19: Profils de vitesses mesurées dans GaInSn et simulées. Valeurs représentant la composante verticale de la vitesse

6 La ségrégation chimique sous champ magnétique glissant

Au cours du processus de solidification dirigée, les impuretés ayant un coefficient de ségrégation $K_0 < 1$, qui se trouvent dans la charge initiale de silicium, sont rejetées dans le liquide au voisinage de l'interface, grâce au phénomène de ségrégation chimique. Plus le coefficient K_0 est petit, plus le liquide est enrichi en impuretés vers la fin de la solidification, et moins d'impuretés vont se retrouver dans la plus grande partie du solide. Le rejet de soluté à l'interface forme une couche limite solutale dans le liquide. L'écoulement dans le bain liquide influence fortement la ségrégation. Dans un liquide fortement brassé les impuretés sont homogénéisées, et l'épaisseur de la couche limite est diminuée. En conséquence la concentration d'impuretés trouvées dans le solide doit aussi diminuer. Les mesures expérimentales pour les expériences effectuées dans la série I (Figure 20) montre que pour toutes les expériences sous TMF la concentration d'aluminium est plus faible que dans le cas de l'expérience sans TMF.

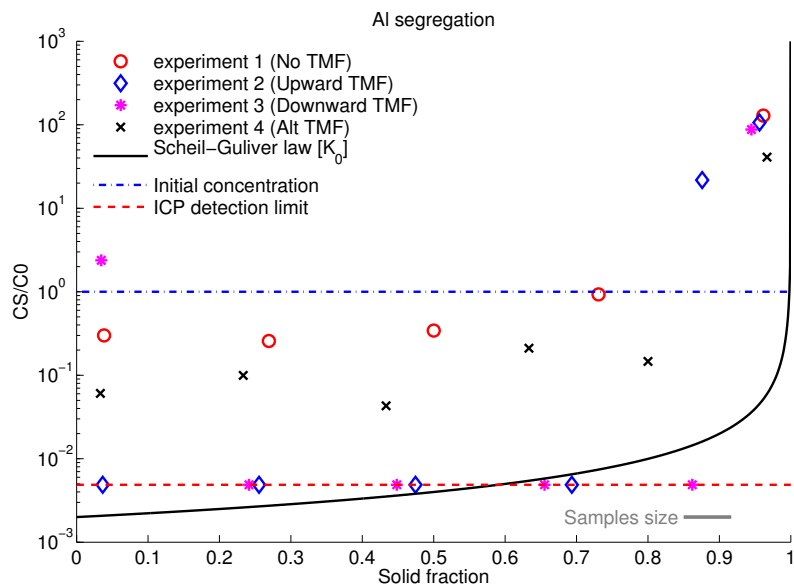


FIGURE 20: Série d'expériences I. Evolution de la concentration d'aluminium, dans le solide avec la fraction solide. Valeurs normalisées à la concentration initiale

Des simulations numériques ont été faites pour étudier la ségrégation des impuretés. Pour ces simulations le nouveau module de solidification (developpé dans le cadre de SIMaP/EPM) a été utilisé. Une première simulation avec des conditions de solidification équivalentes à l'expérience III.1 montre l'effet

de la convection naturelle sur la ségrégation. La distribution calculée de la concentration d'aluminium dans le liquide au cours de la solidification pour l'expérience III.1 est présentée dans la Figure 21. La deuxième simulation avec des conditions de solidification équivalentes à l'expérience III.2 montre l'effet du TMF sur la ségrégation et le calcul de la distribution d'aluminium dans le bain liquide est présenté dans la Figure 22.

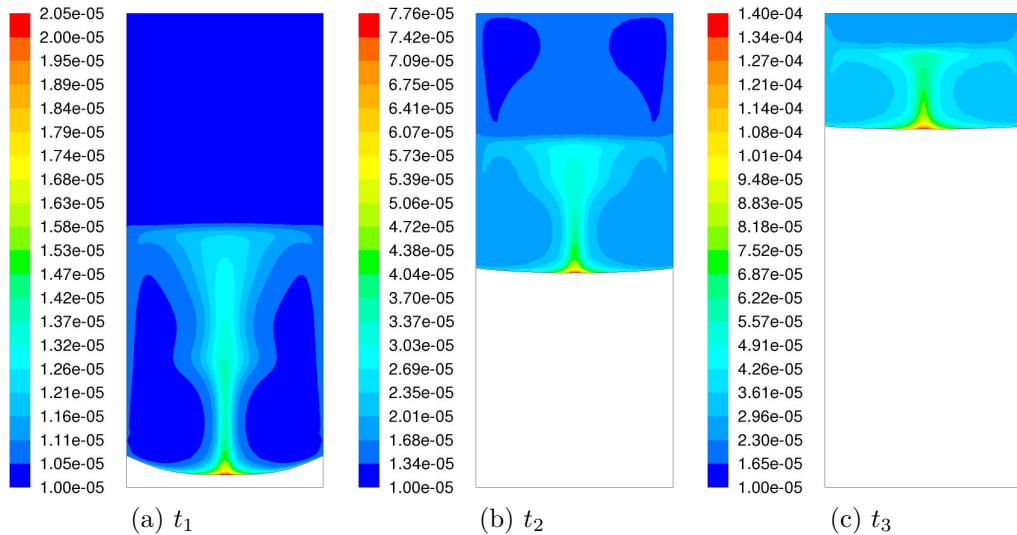


FIGURE 21: Simulation pour expérience III.1. Distribution de la concentration d'aluminium dans le liquide au cours de la solidification. Solidification sous convection naturelle

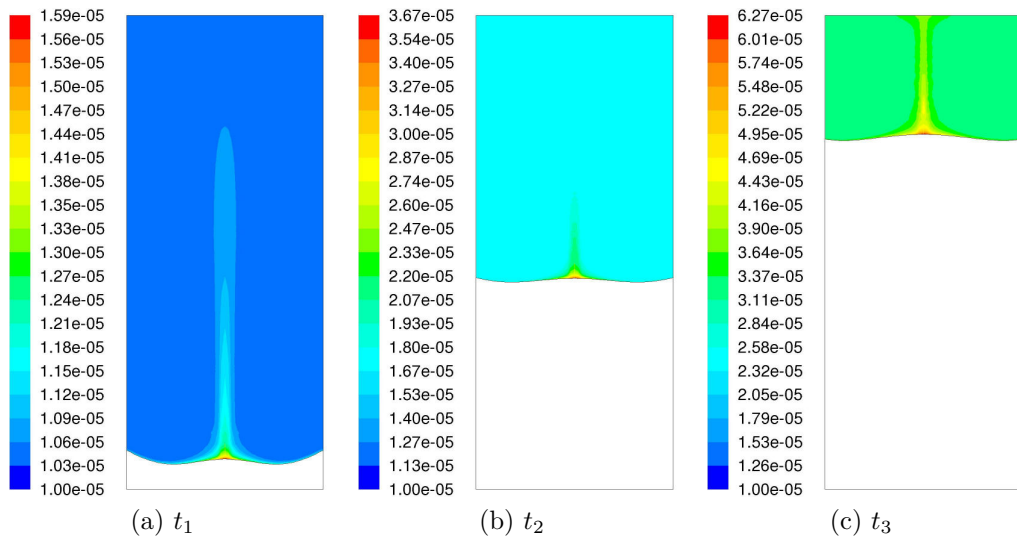


FIGURE 22: Simulation pour expérience III.2. Distribution de la concentration d'aluminium dans le liquide au cours de la solidification. Solidification sous TMF vers le bas

Le calcul de la distribution d'aluminium dans le liquide, pour les deux simulations présentées dans les Figures 21 et 22, montrent qu'une meilleure homogénéisation d'impuretés est obtenue sous TMF. L'augmentation des vitesses dans le liquide pour expérience III.2 est à l'origine de cette homogénéisation. Un autre effet du brassage est une décroissance de la concentration maximale calculée dans le liquide, qui est environ deux fois plus faible par rapport au cas sous convection naturelle. La concentration initiale d'aluminium pour les deux expériences est 10^{-5} fraction massique.

La distribution radiale d'aluminium à l'interface de côté liquide, pour les deux simulations est présentée dans la Figure 23. L'écoulement dans le liquide proche de l'interface est similaire dans les deux cas, ce qui fait que les impuretés s'accumulent au centre du lingot. Malgré tout, les vitesses plus importantes dans le liquide sous TMF font que le soluté est mieux dispersé dans le liquide dans la simulation III.2 et que la concentration à l'interface est diminuée par rapport à la simulation III.1.

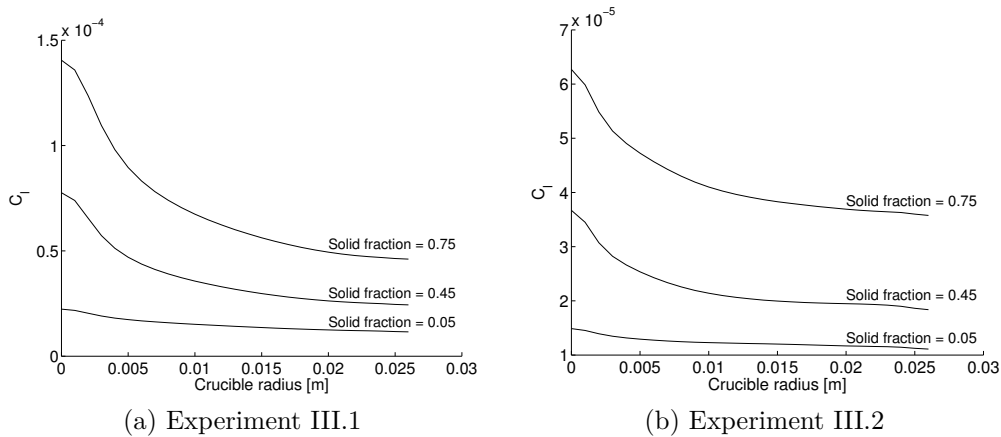


FIGURE 23: Simulations pour les expériences III.1 et III.2. Distribution radiale d'aluminium à l'interface coté liquide

A partir de la concentration d'aluminium à l'interface dans le solide (Figure 23) nous pouvons calculer l'évolution de la concentration dans le solide avec la fraction solide. Dans la Figure 24 cette évolution au centre des lingots, normalisée par la concentration initiale pour les deux simulations, est présentée. Nous observons que pour les deux cas, une bonne ségrégation (faible concentration d'aluminium) est calculée par le modèle. Cet observation nous indique que même les vitesses induites dans le liquide par la convection naturelle ($\approx 10^{-3}m/s$) sont suffisantes pour produire un effet similaire avec celui produit par les vitesses induites par le brassage ($\approx 10^{-2}m/s$), en ce qui concerne la

ségrégation. Les concentrations calculées par le modèle, dans les deux cas, se rapprochent des observations expérimentales pour les expériences sous TMF.

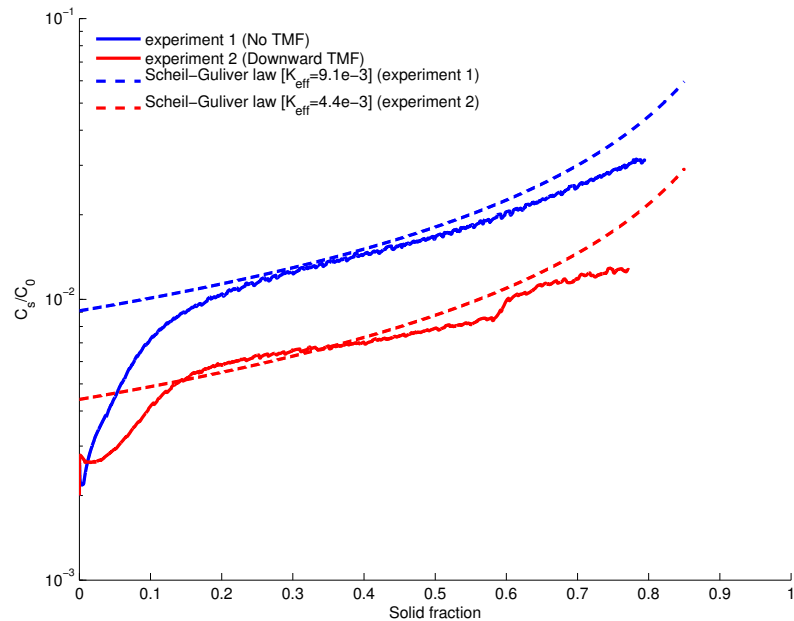


FIGURE 24: Simulations pour les expériences III.1 et III.2. Evolution de la concentration d'aluminium dans le solide, avec la fraction solide. Valeurs normalisée à la concentration initiale

De plus, dans la Figure 24 nous pouvons aussi observer le transitoire initial, c'est à dire l'évolution de la concentration entre les fractions solides 0 et 0.2. A partir de la fraction solide 0.2, un régime stationnaire s'installe et l'évolution de la concentration avec la fraction solide doit suivre une loi de Scheil si le coefficient de ségrégation effectif est constant. Une loi du Scheil a été calculée pour les deux cas et nous observons que la concentration après le transitoire initial est proche de la loi de Scheil calculée. Des différences peuvent être toutefois observées, ceci indique que le coefficient de ségrégation effectif varie pendant la solidification.

7 Conclusions

L'objectif de cette thèse était d'effectuer une l'étude sur l'influence du champ magnétique glissant, pendant la solidification dirigée du silicium multicristallin, sur la forme de l'interface de solidification et la ségrégation chimique d'impuretés. Une approche à la fois expérimentale et numérique ont été conduites au cours de cette étude. Le travail effectué pendant la thèse a été plutôt orienté sur la partie procédé. Une procédure pour marquer ex-

périmentalement les interfaces de solidification a été mise en place. Suite à l'observation d'interfaces asymétriques, une étude sur l'écoulement induit par le brassage électromagnétique a été effectuée. Les résultats de l'étude montrent qu'un écoulement asymétrique peut facilement être induit par le brassage dans le bain liquide, suite aux instabilités hydrodynamiques ou à une asymétrie géométrique des éléments du four.

L'instrumentalisation du four a été également développée durant la thèse. Un panneau d'eau qui permet des mesures de puissances dispersées sur les parois du four a été installé sur le circuit de refroidissement du four. Grâce à ces mesures, une validation thermique du modèle numérique a été effectuée.

Le modèle numérique a été complété avec un nouveau module de solidification, qui permet d'effectuer des simulations de ségrégation chimique au cours de la solidification. Les résultats obtenus avec ce nouveau module montrent une bonne corrélation avec les résultats expérimentaux pour les cas de solidification sous TMF mais des différences pour la solidification sous convection naturelle. Ces différences montrent qu'expérimentalement, les vitesses du liquide dues à la convection naturelle ne sont pas suffisantes, pour une bonne ségrégation d'impuretés, contrairement à ce que le modèle indique. Ces résultats montrent aussi que certains phénomènes physiques, comme par exemple l'encapsulation d'impuretés aux joints de grains, ne sont pas pris en compte dans le modèle.

Les perspectives de ce travail peuvent être séparées en deux grandes catégories. En ce qui concerne l'écoulement asymétrique induit par le TMF, l'étude déjà commencée doit être continuée, afin de trouver la source de l'asymétrie et si possible de l'éliminer. En ce qui concerne la ségrégation, et surtout les différents résultats expérimentaux et numériques pour la ségrégation sous convection naturelle, une étude pour déterminer tous les phénomènes physiques qui ne sont pas pris en compte par le modèle, doit être effectuée. De plus, une validation expérimentale complémentaire des résultats de ségrégation du modèle doit être effectuée. Pour cette validation est conseillé de comparer les résultats numérique avec la ségrégation expérimentale dans un mono cristal, pour éviter l'encapsulation d'impuretés aux joints des grains.

Abstract :

The photovoltaic modules are generally produced using silicon wafers. Their electrical efficiency is related to the crystal quality, which is influenced by the presence of pollutants in the ingots from which the wafers are cut. Silicon ingots are obtained as a result of solidification processes, which imply growing a crystal from melt. During this solidification process, impurities are separated from the silicon. The segregation process is greatly influenced by the melt velocity during the solidification process. The control of the melt flow during the crystallization process can be achieved using external magnetic fields. This thesis presents the results of the study on the influence of the forced convection induced by a travelling magnetic field (TMF) during the solidification process, using both an experimental set-up (VB2) and a numerical model.

Keywords : Multi-crystalline silicon, Directional solidification, Impurities segregation, Travelling magnetic field, Forced fluid flow, Solid-liquid interface

Résumé :

La plupart des modules photovoltaïques produits sont à base de silicium. L'efficacité de ces modules dépend fortement de la qualité cristalline du silicium utilisée ainsi que de la quantité d'impuretés présente dans le lingot d'origine d'où sont issus les modules. Les lingots de silicium sont obtenus au cours d'un procédé de solidification, durant lequel les impuretés sont extraites par phénomène de ségrégation. Le processus de ségrégation est influencé par l'écoulement dans le liquide durant l'étape de solidification. L'utilisation d'un champ magnétique externe permet le contrôle de l'écoulement dans le bain liquide. Dans cette étude, l'effet d'un écoulement forcé sur le processus de ségrégation est étudié. Pour cela un dispositif expérimental (VB2) et un modèle numérique ont été développés dans le but de comprendre le rôle de l'écoulement sur la forme de l'interface et sur la ségrégation des impuretés.

Mots clé : Silicium multi-cristalline, Solidification dirigée, Ségrégation des impuretés, Solid liquid interface, Champ magnétique glissant , Écoulement forcé, Interface solide-liquide